# Probing the distribution of cortical components, including PtdIns(4,5)P$_2$, during asymmetric division of *C. elegans* embryos

THÈSE N$^O$ 8735 (2018)

PRÉSENTÉE LE 31 AOÛT 2018
À LA FACULTÉ DES SCIENCES DE LA VIE
UNITÉ DU PROF. GÖNCZY
PROGRAMME DOCTORAL EN APPROCHES MOLÉCULAIRES DU VIVANT

ÉCOLE POLYTECHNIQUE FÉDÉRALE DE LAUSANNE

POUR L'OBTENTION DU GRADE DE DOCTEUR ÈS SCIENCES

PAR

## Melina Jasmin SCHOLZE

acceptée sur proposition du jury:

Prof. D. Constam, président du jury
Prof. P. Gönczy, directeur de thèse
Prof. M. Labouesse, rapporteur
Prof. A. Roux, rapporteur
Prof. G. van der Goot, rapporteuse

### EPFL
ÉCOLE POLYTECHNIQUE
FÉDÉRALE DE LAUSANNE

Suisse
2018

# Abstract

Asymmetric cell division is crucial for embryonic development and stem cell lineages. In the one-cell *C. elegans* embryo, a contractile cortical actomyosin network contributes to asymmetric division by segregating PAR proteins to discrete cortical domains. The anterior-posterior (AP) polarity established in this manner is maintained thereafter and translated into mechanisms that lead to asymmetric spindle positioning during mitosis, thus ensuring proper segregation of cell fate determinants and fate specification of the daughter cells.

Here, performing cortical live imaging using confocal spinning disk microscopy, we discovered that the plasma membrane lipid phosphatidylinositol 4,5-bisphosphate (PtdIns(4,5)$P_2$; PIP$_2$) forms polarized dynamic structures at the cell membrane of *C. elegans* zygotes, which distribute in a PAR-dependent manner along the AP embryonic axis. PIP$_2$ cortical structures overlap with filamentous actin (F-actin), and coincide with the actin regulators RHO-1, CDC-42 as well as ECT-2. Particle image velocimetry analysis revealed that PIP$_2$ and F-actin cortical movements are coupled, with PIP$_2$ structures moving slightly ahead of polymerizing F-actin bundles. Importantly, we established that the formation of PIP$_2$ cortical structure depends on F-actin and their movement on actin polymerization. Conversely, we found that decreasing or increasing the level of PIP$_2$ results in severe F-actin disorganization, revealing interdependence between these components. Moreover, increasing or decreasing the levels of PIP$_2$ revealed that the formation of CDC-42 and RHO-1 cortical structures depends on PIP$_2$, while PIP$_2$ structures formation is mostly independent of RHO-1 and CDC-42. Furthermore, we uncovered that PIP$_2$ and F-actin regulate the sizing of PAR cortical domains during the establishment and maintenance phases of polarization. Overall, our work establishes that a lipid membrane component, PIP$_2$, modulates actin organization and cell polarity in *C. elegans* embryos.

Furthermore, we found that the force generation mediators GPR-1 and LIN-5, as well as the negative force regulators CSNK-1 and GPB-1, distribute in cortical structures. While CSNK-1 and GPB-1 form elongated cortical structures during pseudocleavage overlapping with PIP$_2$ cortical structures, GPR-1 and LIN-5 form mostly cortical foci not overlapping with GPB-1 and PIP$_2$ cortical structures. The formation of GPB-1 cortical structures is independent of GPR-1 and vice versa. However, the formation and localization of GPB-1 cortical structures depends on PIP$_2$. Overexpressing GPR-1 increases the formation of GPR-1 cortical structures and PIP2/GPB-1 cortical structures, which overlap in large part. CSNK-1 regulates PPK-1 localization to the embryo posterior and is required for the formation of PIP$_2$ cortical structures on the anterior side.

Overall, this work reveals that many important players of asymmetric cell division in the one-cell stage *C. elegans* embryo distribute unevenly on the cortex in dynamic and polarized elongated structures and foci. Moreover, for the first time, the contribution of a plasma membrane lipid, PIP$_2$, to proper AP polarity establishment and maintenance is demonstrated.


Key words:     Development, *C. elegans* embryo, Asymmetric cell division,

Phosphoinositides, PIP$_2$, Actin, Polarity, Spindle positioning

# Zusammenfassung

Asymmetrische Zellteilung ist für die Entwicklung von Embryonen und für Stammzelllinien von entscheidender Bedeutung. Im einzelligen *C. elegans* Embryo trägt ein kontraktiles Aktin-Myosin-Netzwerk zur asymmetrischen Zellteilung bei, indem es PAR Proteine in diskrete kortikale Bereiche trennt. Nachdem die Polarität entlang der anterior-posterior (AP) Achse etabliert wurde, wird diese aufrecht erhalten und in Mechanismen übersetzt, welche während der Mitose zu einer asymmetrischen Positionierung der Spindel führen. Die exakte Positionierung der mitotischen Spindel ist ausschaggebend für die korrekte Trennung von Determinanten des Zellschicksals und die richtige Spezifikation der Tochterzellen.

Wir zeigen mittels konfokaler Spinning-Disk-Echtzeit-Mikroskopie, dass das Plasmamembranlipid Phosphatidylinositol 4,5-Bisphosphat (PtdIns(4,5)$P_2$; $PIP_2$) polarisierte dynamische Strukturen an der Zellmembran von *C. elegans* Embryonen bildet. Diese Structuren verteilen sich PAR-abhängig entlang der embryonalen AP Achse. Kortikale $PIP_2$-Strukturen überlappen teilweise mit filamentösem Aktin (F-Aktin) und vollständig mit den Aktinregulatoren RHO-1, CDC-42 sowie ECT-2. Eine „Particle Image Velocimetry" Analyse ergab, dass die kortikalen Bewegungen von $PIP_2$ und F-Aktin gekoppelt sind. Außerdem bewegen sich $PIP_2$-Strukturen etwas vor polymerisierenden F-aktin-Bündeln. Wir konnten zeigen, dass die Bildung von kortikalen $PIP_2$-Strukturen von F-Aktin und deren Bewegung von der Aktinpolymerisation abhängt. Umgekehrt haben wir festgestellt, dass eine Verringerung oder Erhöhung der gesamten zellulären Menge von $PIP_2$ zu einer schweren F-Aktin-Desorganisation führt, was die wechselseitige Abhängigkeit zwischen diesen beiden Komponenten belegt. Ebenfalls zeigten eine verringerte oder erhöhte $PIP_2$ Menge, dass die Bildung von kortikalen CDC-42- und RHO-1-Strukturen von $PIP_2$ abhängt, während die Bildung von $PIP_2$-Strukturen weitgehend unabhängig von RHO-1 und CDC-42 ist. Darüber hinaus haben wir entdeckt, dass $PIP_2$ und F-Aktin die Dimensionierung von kortikalen PAR Bereichen während der Etablierung und Erhaltung der Polarisation regulieren. Zusammenfassend zeigt diese Arbeit, dass eine Lipidmembrankomponente, $PIP_2$, die Organisation des kortikalen F-Aktin Cytoskeletts und die Zellpolarität in *C. elegans* Embryonen moduliert.

Außerdem haben wir festgestellt, dass die Krafterzeugungsmediatoren GPR-1 und LIN-5 sowie die negativen Kraftregulatoren CSNK-1 und GPB-1 ebenfalls in kortikalen Strukturen verteilt sind. Während CSNK-1 und GPB-1 eher längliche kortikale Strukturen während der Pseudospaltungsphase bilden, welche mit kortikalen $PIP_2$-Strukturen überlappen, formen GPR-1 und LIN-5 hauptsächlich kleine kortikale Foki, die nicht mit kortikalen GPB-1- und PIP2-Strukturen überlappen. Die Bildung von kortikalen GPB-1-

Strukturen ist unabhängig von GPR-1 und umgekehrt. Die Bildung und Lokalisierung von kortikalen GPB-1-Strukturen hängt jedoch von $PIP_2$ ab. Eine Überexpression von GPR-1 erhöht die Bildung von kortikalen GPR-1-Strukturen sowie GPB-1-Strukturen, welche größtenteils überlappen. Darüber hinaus reguliert CSNK-1 die Lokalisierung von PPK-1 zu kortikalen Strukturen auf der anterioren Seite und die Bildung von kortikaler $PIP_2$-Strukturen.

Insgesamt zeigt diese Arbeit, dass viele wichtige Akteure der asymmetrischen Zellteilung im einzelligen Stadium des *C. elegans* Embryo ungleichmäßig auf dem Zell-kortex verteilt sind und dynamische und polarisierte länglichen Strukturen und Foki bilden. Darüber hinaus wird zum ersten Mal der Beitrag eines Plasmamembranlipids, $PIP_2$, zu einer korrekten Bildung und Erhaltung der AP-Polarität gezeigt.

Stichwörter:   Entwicklung, *C. elegans* Embryo, Asymmetrische Zellteilung, Phosphoinositide, $PIP_2$, Aktin, Polarität, Spindelpositionierung

# Acknowledgments

First of all, I would like to thank Prof. Pierre Gönczy for taking me as a PhD student in his lab, giving me the opportunity to work on this great project in an exciting environment and for his outstanding supervision throughout my entire PhD. He was extremely supportive in every possible way and in all kinds of situations and scientific discussion with him are always exceptionally fruitful and motivating. Thank you, Pierre, for everything, you made me grow a lot and without your continuous amazing support I would have not succeeded to be, where I am now.

I also thank all past and present members of the UPGON laboratory I worked with, Coralie Busso, Isabelle Fluckiger, Tania Hübscher, Tatiana Favez, Niccolo Banterle, Marie Pierron, Jian Qiu, Georgios Hatzopoulos, Kerstin Klinkert, Alexandra Bezler, Akshari Gupta, Veronika Nemciková Villímová, Radek Jankele, Tessa Averink, Nils Kalbfuss, Eduard Ebberink, Aleksandar Salim, Benita Wolf, Alessandro De Simone, Nicola Dynes, Virginie Hamel Hachet, Paul Guichard, Sachin Kotak, Meritxell Orpinell, Fernando Balestra, Zoltan Spiro, Lukas Von Tobel, Aitana Neves, Zhou Fang, Michele Graciotti, and Christian Gentili for an inspiring, fun, and multi-cultural working environment and for all their always extremely helpful scientific input and so many great scientific discussions, as well as for numerous great activities done together outside of the lab. In particular, I would like to thank Sachin Kotak for the extremely great scientific support he provided me during my first year in the lab, helping me a lot to start my PhD, but also for all his friendship and support, together with his wife Sveta Chakrabarti, outside of the lab. Also Zoltan Spiro I thank for lots of help in the first months of my PhD to get my project and experiments started. Alessandro De Simone, I would like to thank especially for all his support doing image processing, analysis and quantifications in Matlab, which was extremely helpful and important for me, but also for becoming a great friend, always cheering me up in the lab and being a great and funny "opposite desk" mate. Georgios Hatzopoulos I would like to thank for his amazing experimental support, always being ready to share his huge amount of knowledge in conducting experiments and always having a very helpful answer or idea to all kinds of scientific questions. Alexandra Bezler and Marie Pierron I would like to thank specifically for all their help and input in working with *C. elegans* and doing injections. I also want to thank Kerstin Klinkert for many especially nice discussions about my project and for being always amazingly nice in sharing her microscopy time when I had an urgent experiment to do. I also want to thank Radek Jankele for being a great desk neighbor with so many very helpful scientific ideas and for the amazing time we spent together in England at the asymmetric cell division conference. I thank Coralie Busso, Isabelle Fluckiger, Tania Hübscher, Tatiana Favez for their experimental support mainly in doing all the routine maintenance in the lab. Moreover,

# Affidavit

I hereby confirm that my thesis entitled "Probing the distribution of cortical components, including PtdIns(4,5)$P_2$, during asymmetric division *C. elegans* embryos" is the result of my own work. All sources and materials applied are listed and specified in the thesis.

Parts of this thesis are published in the journal *Development*[1] with the following title:

**PI(4,5)$P_2$ forms dynamic cortical structures and directs actin distribution as well as polarity in *Caenorhabditis elegans* embryos**

Melina J. Scholze[(1)], Kévin S. Barbieux[(2)], Alessandro De Simone[(1,3)], Mathilde Boumasmoud[(1,4)], Camille C. N. Süess[(1)], Ruijia Wang[(1)], and Pierre Gönczy[(1)]

(1) Swiss Institute for Experimental Cancer Research (ISREC), School of Life Sciences, Swiss Federal Institute of Technology (EPFL), Lausanne, Switzerland
(2) Geodetic Engineering Laboratory (TOPO), Swiss Federal Institute of Technology (EPFL), Environmental Engineering Institute (IIE), Lausanne Switzerland

Present addresses:
(3) Department of Cell Biology, Duke University Medical Center, Durham 27710 USA
(4) Division of Infectious Diseases and Hospital Epidemiology, University Hospital Zürich, University of Zürich, Zürich, Switzerland

---

[1] http://dev.biologists.org/content/145/11/dev164988

# Table of Contents

# List of figures

# List of tables

# Abbreviations

| | |
|---|---|
| AB | Anterior Blastomere |
| ABP | Actin Binding Protein |
| ACT-1 | Actin-1 |
| ADF | Actin-Depolymerizing Factor |
| ADP | Adenosine Diphosphate |
| AIR-1 | Aurora A Kinase-1 |
| ANI-1 | Anilin-1 |
| ANTH | AP-180 N Terminal Homology |
| AP | Anterior Posterior |
| APC | Adenomatous Polyposis Coli |
| APC/C | Anaphase Promoting Complex |
| aPKC | Atypical Protein Kinase C |
| ARX | Aristaless Related Homeobox |
| AGS3 | Activator of G-protein Signalling 3 |
| ATP | Adenosine Triphosphate |
| bFGF | Basic Fibroblast Growth Factor |
| $Ca^{2+}$ | Calcium ion |
| Cas-9 | Caspase 9 |
| CAV-1 | Caveolin-1 |
| CCD | Charge-Coupled Device |
| CDC-42 | Cell Division Control Protein 42 Homolog |
| CDK-1 | Cyclin-Dependent Kinase 1 |
| CGEF-1 | *C. elegans* CDC-42 Guanine nucleotide Exchange Factor-1 |
| CHC-1 | Clathrin Heavy Chain-1 |
| CHIN-1 | Chimaerin-1 |
| CIB1 | Cryptochrome-Interacting Basic-Helix-Loop-Helix 1 |
| CIBN | N-terminus of CIB1 |
| CMOS | Complementary Metal-Oxyde-Semiconductor |
| CP | Capping Protein |
| CRISPR | Clustered Regularly Interspaced Short Palindromic Repeats |
| crRNA | CRISPR Ribonucleic Acid |
| CRY2 | Cryptochrome 2 |
| CRY2PHR | Cryptochrome 2 Photolyase Homology Region |
| CSNK-1 | Casein Kinase 1 |
| CYK-4 | Cytokinesis Defective-4 |
| DAG | Diacylglycerol |
| DEP | Dishevelled, EGL-10 and Pleckstrin |
| DIC | Differential Interference Contrast |
| DMSO | Dimethyl Sulfoxide |
| DNA | Deoxyribonucleic Acid |

| | |
|---|---|
| dsRNA | Double-Stranded Ribonucleic Acid |
| ECM | Extracellular Matrix |
| ECT-2 | Epithelial Cell Transforming-2 |
| EDTA | Ethylenediaminetetraacetic Acid |
| EGF | Epidermal Growth Factor |
| EGFR | Epidermal Growth Factor Receptor |
| EGTA | Ethylene Glycol Tetraacetic Acid |
| ENTH | Epsin N Terminal Homology |
| ER1 | Estrogen Receptor Positive |
| ERM | Ezrin, Radixin and Moesin |
| ES | External Sensory |
| GAP | GTPase Activating Protein |
| GDP | Guanine Diphosphate |
| GEF | Guanine Nucleotide Exchange Factor |
| GFP | Green Fluorescence Protein |
| GMC | Ganglion Mother Cell |
| GOA-1 | Guanine Nucleotide-Binding Protein G(o) subunit alpha-1 |
| GPA-16 | Guanine Nucleotide-Binding Protein alpha-16 |
| GPB-1 | Guanine Nucleotide-Binding Protein subunit beta-1 |
| GPC-2 | Guanine Nucleotide-Binding Protein subunit gamma-2 |
| GPCR | G-Protein Coupled Receptor |
| GPR-1/2 | G-protein Regulator-1 and -2 |
| GSK-3 | Glycogen Synthase Kinase-3 |
| GTBP-1 | GTPase-activating Protein SH3 Domain-Binding Protein-1 |
| IP3 | Inositol 1,4,5-trisphospate |
| KCl | Potassium Chloride |
| LGL-1 | Lethal Giant Larvae-like 1 |
| LGN | Leucine-Glycine-Asparagine Repeat Protein |
| MARK | MAP/microtubule Affinity-Regulating Kinases |
| meGFP | Monomeric Enhanced Green Fluorescence Protein |
| MES | 2-(N-morpholino)ethanesulfonic Acid |
| MgCl$_2$ | Magnesium Chloride |
| mGFP | Monomeric Green Fluorescence Protein |
| MLC-4 | Myosin Light Chain-4 |
| mNG | Monomeric Neon Green |
| MosSCI | mos1-mediated Single Copy Insertion |
| NEBD | Nuclear Envelope Breakdown |
| NG2 | Neuron-glial antigen 2 |
| NMY-2 | Non-Muscle Myosin-2 |
| NOP-1 | Pseudocleavage Protein NOP-1 |
| NUMA | Nuclear Mitotic Apparatus |
| N-WASP | Neural Wiskott–Aldrich Syndrome Protein |
| PAR | Partitioning-defective |
| PBS | Phosphate-Buffered Saline |
| PCK-3 | Protein Kinase C-like 3 |
| PDB | Protein Data Bank |
| PDGFR | Platelet-derived Growth Factor Receptor |
| PDZ | PSD-95/Discs-large/ZO-1 |
| PERM-1 | Permeable Eggshell-1 |

| | |
|---|---|
| PFN-1 | Profilin-1 |
| PH | Pleckstrin Homology |
| PI | Phosphatidylinositol |
| PI(3,4)P2 | Phosphatidylinositol 3,4-Bisphosphate |
| PI(4,5)P2 | Phosphatidylinositol 4,5-Bisphosphate |
| PI3K | Phosphatidylinositol 3-Kinase |
| PI3P | Phosphatidylinositol 3-Phosphate |
| PI4P | Phosphatidylinositol 4-Phosphate |
| PI4P5K | Phosphatidylinositol 4-Phosphate 5-Kinase |
| PI5P | Phosphatidylinositol 5-Phosphate |
| PIP | Phosphatidylinositol Phosphate |
| PIP$_2$ | Phosphatidylinositol 4,5-Biphosphate |
| PIP$_3$ | Phosphatidylinositol 3,4,5-Triphosphate |
| PIP4K | Phosphatidylinositol 5-phosphate 4-kinases |
| PIP5K | Phosphatidylinositol 4-phosphate 5-kinases |
| PIV | Particle Image Velocimetry |
| PLC | Phospholipases C |
| PPH-6 | Phosphatase-6 |
| PPIn | Phosphoinositides |
| PPK-1 | PIP Kinase-1 |
| PtdIns(4,5)P$_2$ | Phosphatidylinositol 4,5-bisphosphate |
| PTEN | Phosphatase and Tensin homolog |
| PyMOL | Python Molecule |
| RGA-3 | Rho GTPase Activating protein-3 |
| RGA-4 | Rho GTPase Activating protein-4 |
| RGS-7 | Regulator of G-protein Signaling-7 |
| RHO-1 | Ras-like GTP-binding protein-1 |
| RhoGAP | Rho GTPase Activating Protein |
| RhoGEF | Rho Guanine nucleotide Exchange Factor |
| RIC-8 | Resistance to Inhibitors of Cholinesterase 8 |
| RING | Really Interesting New Gene |
| RNA | Ribonucleic Acid |
| RNAi | Ribonucleic Acid Interference |
| SAPS-1 | Sit4p-associated proteins-1 |
| sgRNA | Single Guide Ribonucleic Acid |
| SNARE | Soluble NSF(N-ethylmaleimide-sensitive factor) Attachment Protein Receptor |
| SOP | Sensory Organ Precursor |
| SPD-2 | Spindle-Defective-2 |
| SPD-5 | Spindle-Defective-5 |
| STD | Standard Deviation |
| TAO | Thousand-And-One Amino Acids |
| TBA-2 | Tubulin-Alpha-2 |
| tracrRNA | Trans-Activating CRISPR Ribonucleic Acid |
| UNC | Uncoordinated |
| UTR | Untranslated Region |
| WASP | Wiskott–Aldrich syndrome protein |
| WSP-1 | Wiskott–Aldrich syndrome protein-1 |
| YFP | Yellow Fluorescent Protein |

# 1. Introduction

## 1.1 Asymmetric cell division

### 1.1.1 Types and common characteristics of asymmetric cell division

Asymmetric cell division is essential for stem cell lineages and the development of multicellular organisms. Asymmetric cell division is defined as any division that gives rise to two daughter cells with different fates, which includes differences in size, morphology, gene expression pattern, protein, RNA, organelle content or different cell progeny numbers in subsequent divisions (reviewed in Vertii et al., 2018). A particularly drastic example of asymmetric cell division occurs during polar body extrusion in metazoan oocytes, when the oocyte itself retains almost all of the cellular contents. Such dramatic asymmetry is achieved by asymmetric spindle positioning (Azoury et al., 2011; reviewed in Yi and Li, 2012).

The mechanisms of asymmetric cell division have been studied in a wide range of organisms from bacteria, yeast, worms (*Caenorhabditis elegans*), flies (*Drosophila melanogaster*) to mammals. Two principle mechanisms exist, one extrinsic and one intrinsic, which result in asymmetric division (reviewed in Horvitz and Herskowitz, 1992). In the extrinsic mechanism, the two daughter cells are initially equal, but then interact with different environments, which induces different fates. Intrinsically determined cell division occurs cell-autonomously, whereby cell intrinsic factors lead to the polarization of the cell (reviewed in Knoblich, 2010; Nung Jan and Yeh Jan, 1998). While intrinsically determined asymmetric cell divisions follow a precise developmental program, extrinsically caused divisions have more flexibility (reviewed in Knoblich, 2008). Intrinsically determined asymmetric cell division can be divided into four major steps (Figure 1) (reviewed in Gönczy, 2008). First, the symmetry of the cell is broken, after which the cell polarizes; then, fate determinants are segregated and, lastly, the mitotic spindle is aligned so that fate determinants are partitioned correctly into the two daughter cells upon division. Altogether, this sequence of events ensures that the two daughter cells have different fates (reviewed in Gönczy, 2008).
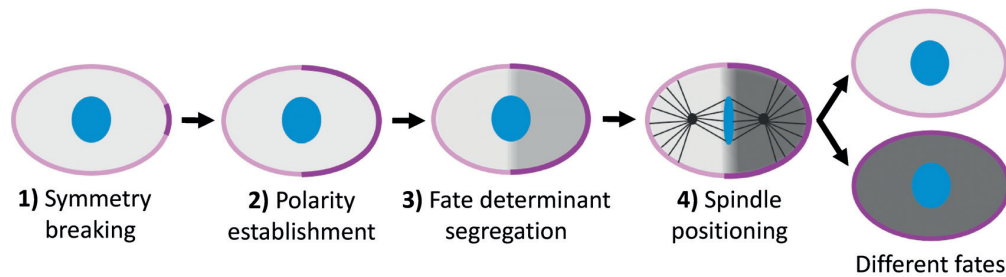
**Figure 1: Major steps of an intrinsically determined asymmetric cell division.** The four major steps that lead to an asymmetric cell division governing two daughter cells with different fates are (1) symmetry breaking, (2) polarity establishment, (3) fate determinants segregation and (4) positioning of the spindle in such a way that fate determinants are properly partitioned to daughter cells.

## 1.1.2 The history of studying asymmetric cell division

The hypothesis that a cell can divide into two daughter cells that differ from one another was postulated for the first time upon studies of leech cell lineages more than a century ago (Whitman, 1878). This hypothesis was supported shortly thereafter by studying muscle development of the ascidian *Styela partita* (Conklin, 1905; reviewed in Horvitz and Herskowitz, 1992). But only decades later, further breakthroughs led to the identification of fundamental mechanisms governing intrinsically determined cell division. These were for example the discovery of Numb, a general regulator of asymmetric cell division functioning in organisms from flies to mice (Rhyu et al., 1994; reviewed in Knoblich, 2010), or the identification of the *par* (partitioning defective) genes during asymmetric cell division of early *C. elegans* embryos (Kemphues et al., 1988). Originally, mostly unicellular organisms such as bacteria, algae, and yeast have been used to study the mechanisms of asymmetric cell division (reviewed in Horvitz and Herskowitz, 1992). However, most mechanisms in yeast turned out not to be conserved in metazoans, such that *Drosophila melanogaster* and *Caenorhabditis elegans* became the main model organisms of choice to study asymmetric cell division in metazoan organisms. Indeed, molecular players and pathways in these organisms turned out to be well conserved throughout metazoan evolution (reviewed in Gönczy, 2008; Neumüller and Knoblich, 2009). To summarize, the first indications for the existence of asymmetric cell division were discovered more than a century ago, whereas the underlying mechanisms were found more recently to be well conserved from worms and flies to vertebrates.

### 1.1.3 Asymmetric cell division in development

Asymmetric cell division contributes to the diversity of cell types in multicellular organisms. The *C. elegans* embryo is one of the best studied model systems for understanding how cells with different fates are generated in developing systems through intrinsically determined asymmetric division (detailed description see: 1.2.2, page 8) (reviewed in Gönczy, 2008). In *Drosophila*, one well-studied cell type undergoing asymmetric division are sensory organ precursor (SOP) cells in the peripheral nervous system that are the founders cells of external sensory (ES) organs (Figure 2) (reviewed in Gönczy, 2008; Knoblich, 2008; Neumüller and Knoblich, 2009). To generate the different cell types of the ES organs, SOP cells undergo three rounds of intrinsically determined asymmetric cell division. The first division gives rise to an anterior pIIa and a posterior pIIb cell. The pIIb cell divides into an apical pIIb cell and a basal glial cell that undergoes apoptosis. The two inner (neuron and sheath) and outer (hair and socket) cells of the organ are formed by terminal division of the pIIa and pIIIb cells, respectively (reviewed in Gönczy, 2008; Knoblich, 2008; Neumüller and Knoblich, 2009).
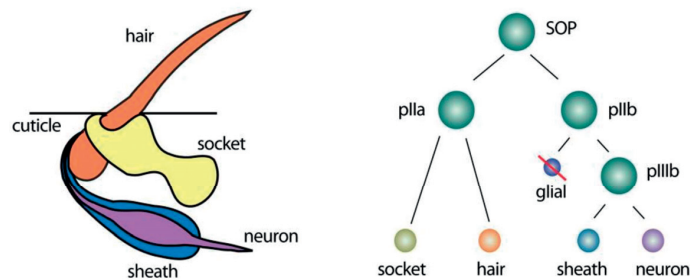


**Figure 2: Asymmetric division of *Drosophila* SOP cells to form ES organs.** Drosophila sensory organ precursor (SOP) cells undergo three rounds of asymmetric cell division (right) to form the different cell types of external sensory (ES) organs (left) (Neumüller and Knoblich, 2009) Copyright © 2009 by Cold Spring Harbor Laboratory Press.

Mechanisms of asymmetric cell division learnt from *C. elegans* and D. *melanogaster* show a partial conservation in many mammalian tissues, as for example in the cerebral cortex and the hematopoietic system (reviewed in Gönczy, 2008; Knoblich, 2008). As many examples of asymmetric cell divisions, also during development, are studied in stem cells, further examples and underlying mechanisms are described in the following section.

### 1.1.4 Asymmetric cell division in stem cells

Stem cells divide asymmetrically to give rise to a self-renewing stem cell and to a differentiating daughter cell. *Drosophila* neuroblasts are a well-studied example of stem cells undergoing an intrinsically determined asymmetric division and *Drosophila* ovarian stem cells one for an extrinsic division (reviewed in Knoblich, 2008). *Drosophila* neuroblasts divide several times in a stem-cell like manner. Each round of division gives rise to a large cell that retains the neuroblast stem-cell characteristics and a small cell called a ganglion mother cell (GMC) that differentiates further into neurons (reviewed in Knoblich, 2008). Unlike *Drosophila* neuroblasts, *Drosophila* ovarian stem cells in the reproductive system keep their stem-cell like behavior through diffusible signals obtained from surrounding cells (reviewed in Knoblich, 2008). The contact of the stem cell with this so-called stem cell niche is essential to maintain its ability to self-renew. During division, the mitotic spindle is oriented so that only one daughter cell stays in contact with the stem cell niche, while the other one loses this contact. The daughter cell that lost contact with the stem cell niche will differentiate in subsequent rounds of cell division, which will eventually lead to the formation of an oocyte (reviewed in Gönczy, 2008; Knoblich, 2008). As in *Drosophila*, asymmetric cell division is also a key feature of mammalian stem cells and evidence for asymmetrically dividing stem cells exists in the skin, muscle, gut, hematopoietic system, mammary glands and the developing brain (reviewed in Knoblich, 2008; Knoblich, 2010). Here, also stem cell niches have been identified, but the underlying mechanisms are less clear in general than in *Drosophila*. A well-studied model is neurogenesis in the mouse forebrain. Brain progenitors use their polarized surrounding to divide into an identical copy of themselves and into a daughter cell that will differentiate into a neuron (reviewed in Knoblich, 2008; Knoblich, 2010). Overall, asymmetric cell division is essential for stem cell lineages.

In the hematopoietic system, stem cell lineages are well established, but the underlying mechanisms of asymmetric cell divisions leading to these lineages are less clearly understood. Hematopoietic stem cells often reside in the vicinity of osteoblasts and endothelial cells of blood vessels, which thus have been suggested to act as a stem cell niche (Kiel et al., 2005). However, intrinsically determined aspects of asymmetric cell division also exist in the hematopoietic system (Schroeder, 2007; Wu et al., 2007a). One example are fetal hematopoietic stem cells that were shown to divide into one self-renewing and one differentiating cell in an intrinsic manner *in vitro* (Bowie et al., 2007; Zon, 2008). In later stages of hematopoiesis, T-lymphocytes upon encountering an antigen also undergo an asymmetric cell division to divide into one effector T-cell and one memory T-cell that keeps certain stem cell-like characteristics (Chang et al., 2007). Interestingly, the asymmetric division of T-lymphocytes provides another example where asymmetric cell division in vertebrates has a strong conservation of mechanisms with

*Drosophila* neuroblasts (Verbist et al., 2016). In both systems, the Par3 complex is involved in translating cell polarization into the correct segregation of fate determinants. Moreover, a complex containing the protein inscuteable dictates proper spindle positioning (Oliaro et al., 2010; Schober et al., 1999). Moreover, the transcription factor MYC is a regulator of proper asymmetric cell division in both systems (reviewed in Li et al., 2014). Overall, while the mechanisms underlying asymmetric cell divisions of stem cells are well understood for example in *Drosophila* neuroblasts, this is less the case for the hematopoietic system. However, a strong conservation between *Drosophila* neuroblasts and T-lymphocytes exists.

### 1.1.5 Asymmetric cell division and cancer

One important finding in recent decades is the connection between defective asymmetric cell division and tumorigenesis. Several genes, including *lgl* and *dlg*, which were found in a genetic screen for tumor formation in *Drosophila* (Gateff, 1978; Gateff, 1994), were later found to be key regulators of asymmetric cell division (Ohshiro et al., 2000; Peng et al., 2000). Furthermore, mutations in or overexpression of several other proteins involved in asymmetric cell division lead to tumor formation in *Drosophila* and mammary stem cells (Tosoni et al., 2015; reviewed in Knoblich, 2010). Altogether, these findings establish defective asymmetric cell division as a possible cause of tumorigenesis (reviewed in Knoblich, 2010). Moreover, key regulators of asymmetric cell division act as tumor suppressors (reviewed in Knoblich, 2010). One example for this was provided by mutants of Aurora A kinase (reviewed in Goldenson and Crispino, 2015; Marumoto et al., 2005). In *Drosophila* neuroblasts, Aurora A was established to act as a tumor suppressor (Lee et al., 2006; Wang et al., 2006) in contrast to its role as an oncogene in mammals (reviewed in Giet et al., 2005). Overall, in *Drosophila,* mutations in neuronal stem cells that lead to defective asymmetric cell division eventually give rise to tumors, with the whole process recapitulating several aspects of mammalian tumor formation (reviewed in Neumüller and Knoblich, 2009). Thus, *Drosophila* is a well-suited model to dissect tumor formation upon defective asymmetric cell division in stem cell lineages (reviewed in Neumüller and Knoblich, 2009). As described above, *Drosophila* neuroblasts divide into one self-renewing neuroblast that continues to proliferate, and one GMC cell that performs one terminal division into two neurons. All neuroblasts stop to proliferate in the pupal stage (Figure 3 A) (reviewed in Knoblich, 2008). Neuroblasts lacking regulators of asymmetric cell division functioning as tumor suppressors do not lose their ability to divide asymmetrically into one neuroblast and one GMC cell (reviewed in Knoblich, 2008). However, the GMC cell does not undergo a terminal division into two neurons, but instead continues to proliferate like a neuroblast (Figure 3 B). Thus, in this specific case, it is not defective cell polarity but instead defective cell-fate specification that leads to tumorigenesis (reviewed in Gönczy, 2008; Knoblich, 2008). Moreover, neu-

roblasts deriving from GMCs due to defective cell-fate specification do not proliferating (Figure 3 B). Hence, defects in asymmetric cell division have given rise to an immortal neuroblast-like cell type that does not exist in wild type (reviewed in Neumüller and Knoblich, 2009). Another connection between asymmetric cell division and cells adopting a stem cell-like character was found in human mammary stem cells. Here, Numb is partitioned into the daughter cell that retains the stem cell character where it stabilizes the key tumor suppressor protein p53 (Tosoni et al., 2015). In this way, asymmetric divisions act as tumor suppressors and might hinder the formation of putative tumor stem cells (reviewed in Vertii et al., 2018). Overall, it is now well established that defective asymmetric cell division can lead to tumorigenesis, but the underlying mechanisms are not entirely clear in most cases.
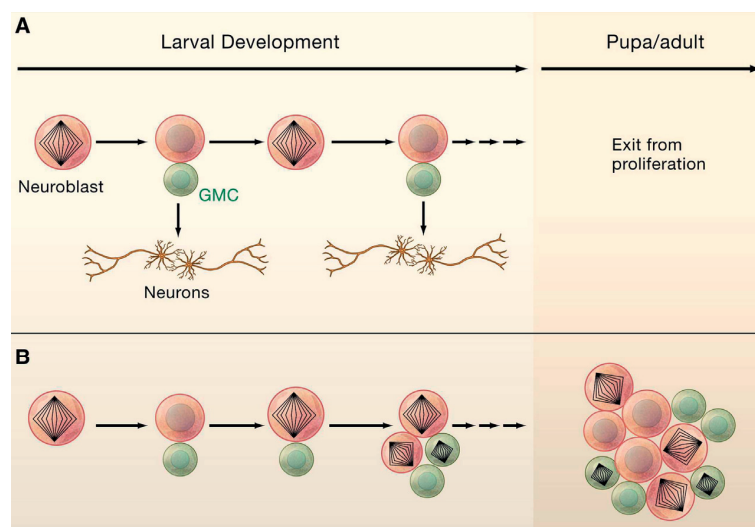


**Figure 3: Defective asymmetric cell division can lead to tumorigenesis in *Drosophila* neuroblasts.** (A) Drosophila *neuroblasts* usually divide into one renewing neuroblast (red) and one GMC (green) that undergoes one more terminal division into two neurons. During pupal stages all neuroblasts stop proliferating. (B) Defects during asymmetric cell division can result in GMC cells that keep proliferating like neuroblasts and in addition are immortalized, thus showing characteristics of tumor stem cells (reviewed in Knoblich, 2008). Reprinted by permission from Elsevier, Cell, Mechanisms of Asymmetric Stem Cell Division, Knoblich JA, 2008; © 2008 Elsevier Inc.

In addition to *Drosophila* neuroblasts, faulty asymmetric cell division is also involved in tumorigenesis in vertebrates. Glioma is a well-described example where defective asymmetric cell division leads to tumor formation (reviewed in Lewis and Petritsch, 2013). During gliogenesis, non-neuronal glia cells derive from neuronal stem cells. Glia cells then further differentiate into function-specialized glial lineages such as astrocytes and oligodendrocytes (reviewed in Gómez-López et al., 2014; Lewis and Petritsch, 2013). Oligodendrocyte precursor cells are characterized by the expression of

specific markers such as platelet derived growth factor receptor PDGFR alpha, neural/glial antigen 2 (NG2), and Oligo2. An oligodendrocyte precursor cell divides asymmetrically into one oligodendrocyte and another oligodendrocyte precursor (reviewed in Gómez-López et al., 2014; Lewis and Petritsch, 2013). During this division, epidermal growth factor receptor EGFR and EGF-dependent signaling is asymmetrically localized into the new oligodendrocyte precursor cell, which is driven by NG2 (Sugiarto et al., 2011). If NG2 positive oligodendrocyte precursor cells lose their potential to divide asymmetrically and EGFR signaling is constitutively active in all daughter cells, oligodendroglioma tumor formation takes place in the mouse (Sugiarto et al., 2011). Consistent with this result, in human glioma cells from patient tumors, the removal of the growth factors EGF and bFGF leads to an increase in asymmetric cell divisions (Lathia et al., 2011). Another example of a tumor suppressor role of asymmetric cell division was reported in estrogen receptor-positive (ER1) breast cancer cell. Here, estrogen inhibits asymmetric cell division, and upon inhibition of the estrogen receptor signaling pathway, the cells regain their ability to divide asymmetrically, which shifts them from a fast-dividing to a slow-dividing population (Dey-Guha et al., 2011; Russo et al., 2010). In summary, dissecting the mechanisms of asymmetric cell division is essential to understand the defects leading to tumorigenesis and the formation of putative cancer stem cells.

## 1.2 Asymmetric cell division in the early $C.\ elegans$ embryo

### 1.2.1 $C.\ elegans$ as a model system for asymmetric cell division

The *C. elegans* embryo has proven to be a very powerful model to study metazoan cell division. Most of the genes and pathways that regulate cell division in the embryo are well conserved and paradigms found in the worm can thus be applied to higher organisms including humans (reviewed in Oegema, 2006; Pintard and Bowerman, 2018). Moreover, *C. elegans* offers many practical advantages that facilitate the dissection of mechanisms of cell division. It is easy to cultivate in the laboratory, has a large brood size and a short life cycle, making it very useful for fast genetics (reviewed in Pintard and Bowerman, 2018). Moreover, the worm and its embryos are transparent and the one-cell stage *C. elegans* embryo is very large (50 x 30 μm), undergoing a fast cell cycle of approximately 20 minutes duration (reviewed in Pintard and Bowerman, 2018). Together, this makes the embryo a great tool for observing processes of cell division by live cell imaging (Gönczy et al., 1999). In addition, the syncytial gonad of *C. elegans* permits the usage of RNA interference to generate embryos depleted of maternally expressed proteins and thus to study the requirement of these proteins during cell divisions in the early embryo (Fire et al., 1991; Fire et al., 1998; Fraser et al., 2000; Gönczy et al., 2000; Guo and Kemphues, 1995; Kamath et al., 2001; Piano et al., 2000). Genome

wide RNAi screens have been conducted, which showed that approximately 2500 of the 20000 genes in the *C. elegans* genome are needed for embryo production and viability. Out of these 2500 genes, around 600 genes are essential for cell divisions in the early embryo as shown by phenotypic profiling using live imaging (Kamath and Ahringer, 2003; Sönnichsen et al., 2005). Moreover, genome editing can be performed in *C. elegans* in a targeted manner using CRISPR/Cas-9 (Paix et al., 2016; reviewed in Dickinson and Goldstein, 2016). All information available about *C. elegans* has been compiled in a database called WormBase[2] (Harris et al., 2010; Lee et al., 2018). To summarize, lessons learnt from the model organism *C. elegans* have proven to be widely applicable and useful do dissect fundamental biological processes, including asymmetric cell division.

## 1.2.2 Overview of events during asymmetric division in the one-cell stage *C. elegans* embryo

The one-cell stage *C. elegans* undergoes an intrinsically determined asymmetric division and this system has proven to be an excellent model to study the mechanisms of this process (see 1.2.1) (reviewed in Pacquelet, 2017; Rose and Gönczy, 2014). The first asymmetric division of the one-cell stage *C. elegans* embryo can be divided into the four typical steps that characterize an intrinsically determined asymmetric cell division generally (see 1.1.1) (reviewed in Pacquelet, 2017; Rose and Gönczy, 2014). The four steps are as follows: first, after fertilization, the symmetry of the embryo is broken, second, the embryo establishes and maintains polarization along the longitudinal axis, third, fate determinants are segregated and, fourth, the spindle is asymmetrically positioning. These four steps result in the asymmetric division of the one-cell stage zygote ($P_0$) into two daughter cells with different fates, the larger anterior blastomere (AB) and the smaller posterior blastomere ($P_1$) (reviewed in Pacquelet, 2017; Rose and Gönczy, 2014). Altogether, the early embryo undergoes five asymmetric divisions leading to six founder cells: AB, MS, E, C, D, and $P_4$, which then further differentiate into the different tissues of the adult worm (reviewed in Pacquelet, 2017; Rose and Gönczy, 2014). In the following sections, the steps of symmetry breaking, polarity establishment, polarity maintenance, and asymmetric spindle positioning in the one-cell stage embryo are explained in further detail, as those steps are important for the content of this thesis (Figure 4).

---

[2] www.wormbase.org
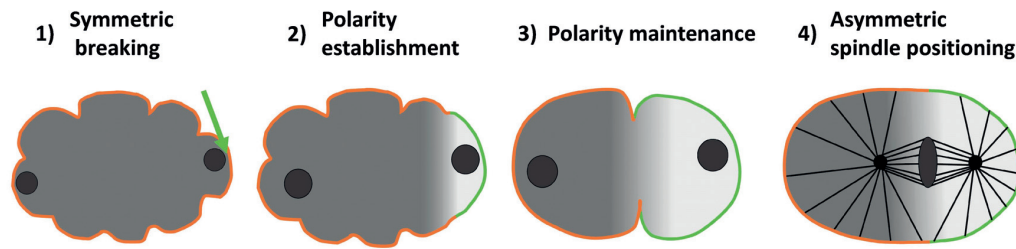
**Figure 4: Important events during the first asymmetric cell division of the one-cell stage _C. elegans_ embryo (middle plane).** After fertilization, the symmetry of the zygote is broken in the vicinity of the male pronucleus (green arrow) and an anterior (orange) – posterior (green) polarity is established and thereafter maintained. During mitosis, the spindle is asymmetrically positioning and the zygote will divide into two daughter cells with different sizes and fates.

### 1.2.3  Symmetry breaking

Oocytes in _C. elegans_ are fertilized in the spermatheca, almost invariably at the pole opposite from where the oocyte nucleus is located. The side of fertilization will usually be the future posterior pole and thus defines the anterior-posterior (AP) axis (Albertson, 1984; Goldstein and Hird, 1996). Shortly after fertilization, the embryo surface exhibits uniform contractions of the cortical actomyosin network located underneath the plasma membrane (Munro et al., 2004) (Figure 5, (1) symmetry breaking). These contractions are driven by non-muscle myosin 2 (NMY-2), which is enriched at the cortex shortly before the end of meiosis and forms a dynamic network of filaments and dense foci (Munro et al., 2004). When meiosis is completed, the sperm-derived centrosomes move close to the future posterior side of the cortex. This somehow leads to the clearance of ECT-2 and RHO-1 from this location, causing foci of NMY-2 to move rapidly away from there, as well and enriching on the anterior aide, which thus stays contractile while the posterior becomes non-contractile (Bienkowska and Cowan, 2012; Motegi and Sugimoto, 2006; Munro et al., 2004) (see 1.2.4 for further description). Anterior contractions culminate in a single constriction, called the pseudocleavage furrow (Hill and Strome, 1988; Rose et al., 1995) (Figure 5, (3) polarity maintenance). NMY-2 activity is regulated by the regulatory myosin light chain MLC-4 (Shelton et al., 1999). Early experiments showed already that cortical flows directed towards the anterior depend on F-actin but not on microtubules (Hird and White, 1993). The forces that NMY-2 generates lead to an anterior-directed cortical flow, which is transmitted to the cytoplasm where they generate a counter flow to the posterior (Goldstein and Hird, 1996; Hird and White, 1993; Niwayama et al., 2011). Position- and direction- dependent laser ablation experiments showed that cortical tension is anisotropic and strongest orthogonal to the AP axis. Together with modeling of cortical mechanics, these experiments revealed that the anisot-

ropy in cortical tension can be explained by cortical viscosity, which together with a gradient in actomyosin contractility can drive the long-ranged flow towards the anterior (Mayer et al., 2010). Overall, after meiosis, sperm-derived centrosomes cause an NMY-2-driven anterior-directed cortical flow away from the cortical area in their vicinity.

What is the cue that drives symmetry breaking of the *C. elegans* zygote? Although the exact nature of this cue is not clear yet, centrosomes have been shown to be key for breaking symmetry (Cowan and Hyman, 2004). This was established by laser ablation experiments physically removing the centrosome, as well as by the depletion of SPD-5 and SPD-2, which are essential centrosome components (Cowan and Hyman, 2004). Depletion of centrosomes completely abolished polarization and actomyosin cortical flows (Cowan and Hyman, 2004). These findings have been supported by later studies. Normally the centrosomes move closer to the cortex when polarity is initiated. If the distance of the centrosomes to the cortex is increased, polarity initiation is delayed (Bienkowska and Cowan, 2012). Defects in polarization were also observed in mutants in which the centrosomes remains far from the cortex, and these defects can be rescued by bringing the centrosomes back close to the cortex (Fortin et al., 2010; Lyczak et al., 2006; McCloskey and Kemphues, 2012). In contrast to the centrosome, symmetry breaking is independent of microtubules and the sperm pronucleus (Cowan and Hyman, 2004; Sadler and Shakes, 2000; Sonneville and Gönczy, 2004). Together, the centrosome and its closeness to the cortex are somewhat key to break symmetry.

### 1.2.4 Polarity establishment

Centrosomes induce the local disappearance in their vicinity of cortical ECT-2, a guanine nucleotide exchange factor (GEF) for RHO-1 (Bienkowska and Cowan, 2012; Cowan and Hyman, 2004; Motegi and Sugimoto, 2006). This results in local inactivation of the Rho GTPase RHO-1 and cortical flows away from this region, towards the future embryo anterior (Figure 5, (2) polarity establishment) (Bienkowska and Cowan, 2012; Cowan and Hyman, 2004; Motegi and Sugimoto, 2006). Both RHO-1 and ECT-2 are needed for MLC-4 phosphorylation and thus regulate NMY-2 contractility (Jenkins et al., 2006; Motegi and Sugimoto, 2006). How do centrosomes induce the local disappearance of ECT-2 in their vicinity and thus break symmetry and allow the onset of polarity establishment? It was proposed that the paternally contributed RhoGAP CYK-4 inhibits RHO-1 activity in the vicinity of centrosomes (Jenkins et al., 2006). However, during cytokinesis, CYK-4 was shown to also bind ECT-2 and activate RHO-1, and mutating the GAP domain of CYK-4 has no effect on polarization (Canman et al., 2008; Tse et al., 2012; Zhang and Glotzer, 2015). Together, the exact pathways through which centrosomes trigger polarization remain to be determined.

Further players involved in the formation of the actomyosin network and cortical contractility include NOP-1, a serine rich protein, PAR-4, a serine-threonine kinase, and the anillin ANI-1, a scaffolding protein (Fievet et al., 2013; Chartier et al., 2011; (Chartier et al., 2011; Maddox et al., 2005; Rose et al., 1995; Tse et al., 2012). NOP-1 contributes to proper cortical contractility possibly through activating RHO-1, maybe upstream of ECT-2 (Fievet et al., 2013; Rose et al., 1995; Tse et al., 2012). PAR-4 promotes proper cortical actomyosin flows by correctly localizing the anillin ANI-2, whereas the anillin ANI-1 is needed for proper cortical contractility by regulating the formation of NMY-2 foci (Chartier et al., 2011; Maddox et al., 2005; Tse et al., 2012). Moreover, negative regulators of RHO-1 and thus of actomyosin contractility were uncovered. These are the RhoGAPs RGA-3 and RGA-4, whose depletion leads to cortical hypercontractility and formation of a much small anterior domain compared to wild type embryos (Schmutz et al., 2007; Schonegg et al., 2007), and the TAO kinase KIN-18 (Spiga et al., 2013). In addition to the regulators described above, in an systematic RNAi screen, further genes essential for proper actomyosin flows were identified, including the ezrin *erm-1*, which remain to be characterized further (Fievet et al., 2013). Overall, while cortical flows leading to polarity establishment mainly depend on ECT-2 and RHO-1, numerous additional regulators have been characterized.

The anterior-directed actomyosin flow promotes PAR polarity establishment (Chartier et al., 2011; Cuenca et al., 2003; Fievet et al., 2013; Guo and Kemphues, 1996; Jenkins et al., 2006; Motegi and Sugimoto, 2006; Munro et al., 2004; Schonegg et al., 2007; Spiga et al., 2013). Directly after fertilization, both anterior and posterior PAR proteins localize throughout the entire cortex. At meiosis II, only anterior PAR proteins remain at the cortex, while posterior PAR proteins become cytoplasmic. As anterior PAR proteins are segregated towards the anterior side by actomyosin flows, posterior PAR proteins returns to the posterior cortical area that is now devoid of anterior PAR proteins (Boyd et al., 1996; Cuenca et al., 2003; Etemad-Moghadam et al., 1995; Hung and Kemphues, 1999; Munro et al., 2004). The diffusive properties of cortical anterior PAR proteins are such that actomyosin flows can induce their redistribution by advection (reviewed in Goehring and Grill, 2013). The RHO GTPase CDC-42 is essential to remove PAR-2 from the cortex and localize PAR-6 to the cortex during meiosis II (Schonegg et al., 2007). Finally, the PDZ domain containing proteins PAR-3 and PAR-6, as well as atypical protein kinase C-like 3 (PCK-3), are localized to the anterior side (Cuenca et al., 2003; Etemad-Moghadam et al., 1995; Hung and Kemphues, 1999; Tabuse et al., 1998; Watts et al., 1996). Moreover, the serine-threonine kinase PAR-1, the RING domain containing protein PAR-2, and Lethal Giant Larvae-like 1 (LGL-1) occupy the expanding posterior cortical domain (Beatty et al., 2010; Boyd et al., 1996; Cuenca et al., 2003; Guo and Kemphues, 1995). CDC-42 is also segregated to the anterior, where it stabilizes the actomyosin network and promotes PAR-6 association with the cortex (Kumfer et al., 2010; Motegi and Sugimoto, 2006; Schonegg and Hyman, 2006). Together, anterior-directed

cortical flows polarize the embryo by segregating PAR-3, PAR-6 and PCK-3 to the anterior, which allows occupancy of the expanding posterior domain by PAR-1, PAR-2, and LGL-1.

The *par* genes (partitioning defective genes) were found in a screen to identify regulators of asymmetric cell division in early *C. elegans* embryos (Kemphues et al., 1988). In the absence of one of the anterior PAR proteins, PAR-3, PAR-6 or PCK-3, the posterior PAR proteins PAR-1 and PAR-2 distribute throughout the entire cortex, the embryo divides symmetrically and both daughter cells behave like $P_1$ cells (Boyd et al., 1996; Etemad-Moghadam et al., 1995; Guo and Kemphues, 1995; Hung and Kemphues, 1999; Kemphues et al., 1988; Tabuse et al., 1998). The opposite scenario takes place upon depletion of PAR-2. Then, PAR-3, PAR-6 and PKC-3 distribute throughout the entire cortex, the embryo divides symmetrically as well, but both daughter cells behave like AB cells (Boyd et al., 1996; Etemad-Moghadam et al., 1995; Guo and Kemphues, 1995; Hung and Kemphues, 1999; Kemphues et al., 1988; Tabuse et al., 1998). How exactly PAR proteins interact with and attach to the cortex is not entirely clear. Some PAR proteins might bind to the membrane through interaction with phospholipids. In *C. elegans*, this was shown for PAR-2 (Motegi et al., 2011). Moreover, human PAR-1, PAR-3, and CDC-42, as well as *Drosophila* PAR-3, also interact with phospholipids (Horikoshi et al., 2011; Johnson et al., 2012; Krahn et al., 2010; Moravcevic et al., 2010; Wu et al., 2007b). Moreover, PAR proteins interact with and recruit each other to the cortex. Thus, PAR-2 recruits PAR-1 through direct interaction (Motegi et al., 2011). PAR-6, PAR-3 and PKC-3 form a complex, and PAR-3 is needed for cortical recruitment of PAR-6 and PKC-3, while PAR-6 and PKC-3 are required to localize each other (Hung and Kemphues, 1999; Li et al., 2010; Tabuse et al., 1998). However, PAR-6 colocalizes only partially with PAR-3 on the cortex, and a second population of PAR-6 exists, which is localized to the cortex by CDC-42, with which it directly interacts (Beers and Kemphues, 2006; Gotta et al., 2001; Robin et al., 2014). Moreover, PAR-3 forms clusters in a PCK-3-, CDC-42-, and actomyosin contractility-dependent manner, which is essential for proper polarity (Rodriguez et al., 2017; Wang et al., 2017). In addition to being established through actomyosin contractility, PAR polarity can be established in *C. elegans* zygotes through a partially redundant pathway, whereby microtubules nucleated from centrosomes bind and protect PAR-2 from PKC-3-mediated phosphorylation (Motegi et al., 2011). As phosphorylation of PAR-2 by PKC-3 prevents cortical localization of PAR-2, the interaction with microtubules allows PAR-2 association with phospholipids at the embryo posterior. Thereafter, PAR-2 recruits PAR-1, which then phosphorylates PAR-3 and thus excludes it from the posterior cortex (Hao et al., 2006; Motegi et al., 2011). Overall, PAR proteins interact with each other and the plasma membrane. Moreover, AP polarity can be established either through an actomyosin flow dependent or PAR-2 dependent pathway.
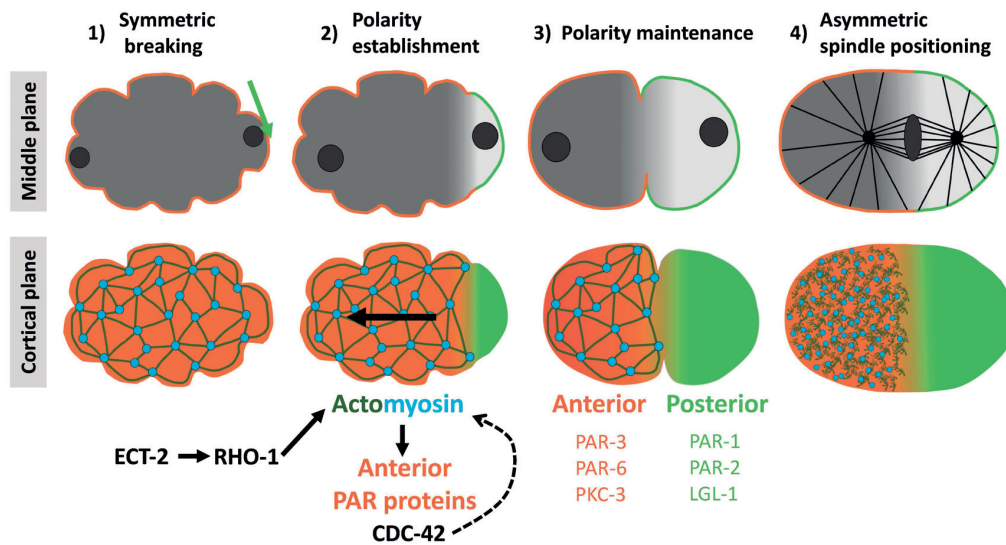
**Figure 5: Important events during the first asymmetric cell division of the *C. elegans* embryo (middle plane and cortical plane, as indicated).** (1) Symmetry breaking (2) polarity establishment, (3) polarity maintenance and (4) asymmetric spindle positioning shown in the middle plane (top) and cortical plane (bottom). After symmetry breaking (green arrow), the actomyosin network (actin: dark green, myosin: cyan) contracts towards the anterior side of the embryo (left) and takes anterior PAR proteins (orange) and the RhoGTPase CDC-42 with it. The posterior side of the embryo (right) gets occupied with previously cytoplasmic posterior PAR proteins (light green). Note that F-actin undergoes a morphological transition from a meshwork of microfilaments to an accumulations of foci during the first cell cycle (Velarde et al., 2007). Cortical contractions and the localization of the actomyosin network are regulated by the Rho GTPase RHO-1 and its GEF ECT-2 during the polarity establishment phase, as well as by the Rho GTPase CDC-42 during the polarity maintenance phase.

Except for PAR-2, which appears to be present only in nematodes, all other PAR proteins are highly conserved regulators of polarity across metazoans (Sailer et al., 2015; reviewed in Neumüller and Knoblich, 2009). In *Drosophila* neuroblasts and SOP cells, polarity is set up by the PAR-3 homolog Bazooka, PAR-6, and the PKC-3 homolog aPKC. In neuroblasts, the Bazooka/PAR-6/aPKC complex is localized at the apical site, whereas in SOP cells, it resides at the posterior side (Kuchinke et al., 1998; Petronczki and Knoblich, 2001; Wodarz et al., 2000; Rolls et al., 2003; reviewed in Neumüller and Knoblich, 2009). In *Drosophila*, Slmb, a E3 ubiquitin ligase, might play an analogous role to PAR-2 in *C. elegans* (Morais-de-Sa et al., 2014; Skwarek et al., 2014). Slmb also recruits PAR-1 to the posterior and is needed for polarity establishment in the *Drosophila* oocyte (Morais-de-Sa et al., 2014; Skwarek et al., 2014). Moreover, depletion of Slmb inhibits ectopic localization of the PAR-6/aPKC complex to the posterior and the Slmb depletion phenotype can be rescued by overexpression of Lgl (Morais-de-Sa et al., 2014; Skwarek et al., 2014). Other examples where PAR proteins are conserved are mammalian endothelial cells, *Xenopus* oocytes, and ascidian embryonic cells. Also in these cases, homologues of the PAR-3/PAR-6/PCK-3/CDC-42 complex are asymmetrically distributed and regulate cell polarity (Izumi et al., 1998; Joberty et al., 2000; Lin et al., 2000; Nakaya

et al., 2000; Patalano et al., 2006). To explain one of these examples in more detail, in mammalian epithelial cells, which are partitioned into three distinct domains, namely apical, basolateral, and junctional, Cdc-42, Par-6/aPKC are enriched at the apical domain, Par-3 at the junctional domain, and Par-1 and Lgl at the basolateral domain (reviewed in Rodriguez-Boulan and Macara, 2014). Although more complex, the molecular mechanisms underlying PAR polarity in mammalian epithelial cells are very analogous to those in *C. elegans,* emphasizing again the high conservation of the PAR protein machinery (reviewed in Lang and Munro, 2017)*.* The fact that mechanisms of polarity establishment during development are well conserved from the early *C. elegans* embryo to early mammalian embryos became also evident in a recent study in the early mouse embryo (Zhu et al., 2017). It has been known since a  long time that the mouse embryo breaks symmetry at the 8-cell stage, leading to the establishment of apical and basolateral domains (Ziomek and Johnson, 1980). However, the underlying mechanisms were only discovered recently. As in *C. elegans*, in the mouse embryo, after symmetry is broken, an actomyosin network becomes asymmetrically segregated to the apical side, and this is essential for the apical localization of the PAR protein complex and thus for proper polarity establishment (Zhu et al., 2017). The apical domain becomes enriched with the PAR-3/PAR-6/aPKC PAR protein complex (Vinot et al., 2005), and is essential for proper lineage specification (Korotkevich et al., 2017). To summarize, PAR proteins are central regulators of cell polarity conserved from *C. elegans* and *Drosophila* to mammals.

### 1.2.5   Polarity maintenance

After polarity establishment, the second phase of polarization of the one-cell stage *C. elegans* embryo starts, in which the established polarity has to be maintained (Figure 5, (3) polarity maintenance) (Cuenca et al., 2003). Mechanisms leading to their mutual exclusion are crucial and no physical barrier exists between anterior and posterior PAR domains (Cuenca et al., 2003; Goehring et al., 2011). These mechanisms include a mutually antagonistic negative feedback between anterior and posterior PAR proteins, which includes a local self-amplifying feedback-loop and long-range inhibition between the domains (reviewed in Goehring and Grill, 2013). PAR-1 and PAR-2 are excluded from the anterior domain n by phosphorylation through PKC-3 and vice versa, since PAR-1 phosphorylates PAR-3 and thus excludes it from the posterior domain (Hao et al., 2006; Motegi et al., 2011). Moreover, PKC-3 is essential for the posterior localization of LGL-1. LGL-1 itself supports PAR-2 in restricting anterior PAR proteins to the anterior (Beatty et al., 2010; Hoege et al., 2010). PAR-2 also prevents NMY-2 from spreading towards the posterior side in a CDC-42 dependent manner (Munro et al., 2004; Small and Dawes, 2017). CDC-42 plays further important roles during polarity maintenance. Thus, CDC-42 interacts with PAR-6 and restricts its localization to the anterior (Aceto et al., 2006; Gotta et al., 2001; Motegi and Sugimoto, 2006; Schonegg and Hyman, 2006). Vice versa, PAR-

6 is essential for the anterior localization of active CDC-42 (Aceto et al., 2006; Kumfer et al., 2010). Moreover, CDC-42 functions as an actomyosin regulator as it is required to maintain the localization of the actomyosin network at the anterior after polarity is established (Motegi and Sugimoto, 2006). CDC-42 is inhibited by the RhoGAP CHIN-1 and activated by the RhoGEF CGEF-1. CHIN-1 is excluded from the anterior by anterior PAR proteins (Kumfer et al., 2010; Sailer et al., 2015). Interestingly, polarity defects resulting from improper polarity establishment can be corrected during the polarity maintenance phase and also later during cytokinesis (Schenk et al., 2010; Schonegg et al., 2007; Spiga et al., 2013). In contrast to the established role of the actomyosin regulator CDC-42 and the mutual exclusion mechanisms of PAR proteins, the role of F-actin during polarity maintenance is somewhat controversial. Some studies show that disruption of the actomyosin network can destabilize already formed PAR polarity domains (Liu et al., 2010a; Severson and Bowerman, 2003). By contrast, others show that the maintenance of PAR polarity domains is independent of the actomyosin network (Goehring et al., 2011; Hill and Strome, 1990). Together, the mutual exclusion of anterior and posterior PAR domains is key for maintaining cell polarity, and polarity defects can be corrected until the very end of the first cell cycle. These facts likely contribute to the robustness of the first asymmetric cell division of the *C. elegans* zygote (reviewed in Pacquelet, 2017).

## 1.2.6   Asymmetric spindle positioning

The established and maintained AP polarity is then translated into proper positioning of centrosomes and the mitotic spindle (Figure 5, (4) asymmetric spindle positioning) (reviewed in Gönczy and Rose, 2005; McNally, 2013; Rose and Gönczy, 2014). Correct spindle positioning is essential to properly coordinate the placement of the cleavage furrow with segregation of cell fate determinants, together ensuring proper cell fate specification after asymmetric division (reviewed in Gönczy and Rose, 2005; McNally, 2013; Rose and Gönczy, 2014). Proper anaphase spindle positioning depends on the positioning of centrosomes before mitotic entry and of the spindle poles during mitosis. After fertilization, centrosomes are positioned at the posterior, attached to the male pronucleus (reviewed in Gönczy and Rose, 2005; McNally, 2013; Rose and Gönczy, 2014). Then, the centrosome-pronucleus complex migrates towards the anterior and meets the female pronucleus still in the posterior half of the embryo. Thereafter, the pronuclei with the attached centrosomes center in the middle of the embryo and rotate by 90° in a process called centration/rotation that positions the two centrosomes along the AP axis (reviewed in Gönczy and Rose, 2005; McNally, 2013; Rose and Gönczy, 2014). Upon mitotic entry, the spindle assembles in the center of the embryo and then gets positioned towards the posterior during metaphase and anaphase, with the posterior pole undergoing transverse oscillations during anaphase (reviewed in Gönczy and Rose, 2005;

McNally, 2013; Rose and Gönczy, 2014). The mechanisms lying behind proper centro-some and spindle pole positioning are described in the following sections.

Centrosomes and spindle poles are positioned by pulling forces generated through molecular motors connected to astral microtubules emanating from centro-somes and spindle poles (reviewed in Gönczy and Rose, 2005; McNally, 2013; Rose and Gönczy, 2014). During centration/rotation, pulling forces were proposed to be microtu-bule length dependent, with stronger forces acting on longer microtubules (Kimura and Kimura, 2011). These forces are generated by the minus-end directed molecular motor dynein, which is  distributed throughout the cytoplasm (Gönczy et al., 1999). Pulling forces during asymmetric spindle positioning in mitosis are exerted by cortical forces generated by dynein attached to the cortex (Figure 6) (Grill et al., 2001; Grill et al., 2003; Labbé et al., 2004). This was established by elegant laser ablation experiments severing the spindle (Grill et al., 2001) or fragmenting the spindle poles (Grill et al., 2003). Spindle poles or fragments liberated by the laser ablation move all the way to the cortex and this happens with higher velocity on the posterior side. These experiments revealed that pulling forces on aster microtubules are generated at the cortex and that net pulling forces are stronger on the posterior side, controlled by AP polarity cues (Grill et al., 2001; Grill et al., 2003; Labbé et al., 2004). These findings are supported by the observation that cortical pulling forces lead to membrane invaginations upon weakening of the cor-tical actomyosin network that are more pronounced on the posterior (Redemann et al., 2010).

Cortical pulling forces generated by the minus end directed motor dynein are mediated by a ternary complex (Couwenbergs et al., 2007; Kotak et al., 2012; Nguyen-Ngoc et al., 2007). The ternary complex is comprised of the two partially redundant Gα subunits, GOA-1 and GPA-16 (Gotta and Ahringer, 2001), the two essentially identical GoLoco con-taining proteins, GPR-1 and GPR-2, and the large coiled-coil protein LIN-5 (Figure 6) (Co-lombo et al., 2003; Srinivasan et al., 2003). LIN-5 binds to GPR-1/2 (Gotta et al., 2003; Srinivasan et al., 2003), which binds with its GoLoco motif to GDP-bound GOA-1/GPA-16 (Colombo et al., 2003; Gotta et al., 2003). The whole ternary complex is anchored to the plasma membrane by Gα myristoylation (Nguyen-Ngoc et al., 2007). The human homo-log of LIN-5, NUMA, can also directly bind to phospholipids in the plasma membrane (Kotak et al., 2014).

During mitosis, GPR-1/2 is distributed asymmetrically, being enriched at the pos-terior cortex in a manner that is regulated by AP polarity cues, and this is thought to cause higher net pulling forces on the posterior side (Figure 6) (Colombo et al., 2003; Gotta and Ahringer, 2001; Gotta et al., 2003; Srinivasan et al., 2003; Tsou et al., 2003). Consistent with this notion, during centration/rotation, when net pulling forces are higher on the anterior side, GPR-1/2 is enriched on the anterior cortex, which might imply that also during this process cortical forces are involved (Park and Rose, 2008).

The ternary complex anchors the minus end directed molecular motor dynein to the cortex, most likely through direct interaction of LIN-5 with dynein (Couwenbergs et al., 2007; Kotak et al., 2012; Nguyen-Ngoc et al., 2007). Dynein might then generate pulling forces by attempting to move towards the minus end of astral microtubules while being attached to the plasma membrane. In an alternative model, dynein could stay attached with the plus end of astral microtubules that depolymerize and generate pulling forces in this way (Couwenbergs et al., 2007; Kotak et al., 2012; Merdes et al., 1996; Nguyen-Ngoc et al., 2007; Schmidt et al., 2005). Supporting the second possibility, the microtubule associated protein adenomatous polyposis coli (APC) is localized at the anterior cortex in an anterior PAR protein-dependent manner, stabilizing microtubule plus ends and reducing microtubule catastrophe frequencies there, thus negatively regulating pulling forces (Sugioka et al., 2018). Together, proper asymmetric spindle positioning in mitosis is achieved by cortical pulling forces generated by a ternary complex anchoring dynein to the cortex, with net pulling forces being higher on the posterior possibly because of GPR-1/2 enrichment on this side.

Asymmetric spindle positioning in the one-cell stage embryo is tightly regulated by numerous positive and negative force regulators. The G-proteins Gβ, GPB-1, and Gγ, GPC-2 form a dimer that normally binds to the Gα G-proteins to form heterotrimeric complexes mediating G-protein coupled receptor (GPCR) signalling (Afshar et al., 2004; Afshar et al., 2005; Tsou et al., 2003). In the one-cell stage embryo, however, Gβγ compete with GPR-1/2 for Gα binding and thus negatively regulates forces. Depletion of GPB-1 or GPC-2 leads to exaggerated movements during centration/rotation and higher net pulling forces on the anterior (Afshar et al., 2004; Afshar et al., 2005; Tsou et al., 2003). GPB-1 negatively regulates GPR-1/2 cortical levels and GPR-1/2 localization at the anterior (Thyagarajan et al., 2011; Tsou et al., 2003). GPB-1 is itself asymmetrically distributed and enriched on the anterior side; this is mediated by GPB-1 trafficking through the endosomal system, which has been proposed to negatively regulate GPR-1/2 on the anterior side (Thyagarajan et al., 2011). In addition to Gβγ, Gα localization and function is also regulated by the GEF RIC-8 and the GAP RGS-7 (Afshar et al., 2004; Afshar et al., 2005; Couwenbergs et al., 2007; Hess et al., 2004; Miller and Rand, 2000). RIC-8 has GEF activity towards GOA-1 and regulates cortical enrichment of GPA-16 and thus positively regulates spindle pulling forces. In contrast, RGS-7 acts as a GAP for GOA-1 and hence negatively regulates spindle pulling forces on the anterior (Afshar et al., 2004; Afshar et al., 2005; Couwenbergs et al., 2007; Hess et al., 2004; Miller and Rand, 2000). Another negative regulator of forces is the Casein Kinase 1 (CSNK-1), which negatively regulates cortical levels of LIN-5 and GPR-1/2 (Panbianco et al., 2008). Depletion of CSNK-1 leads to exaggerated movements during centration/rotation and spindle positioning through increased cortical levels of GPR-1/2 and LIN-5, but polarity is not defective (Panbianco et al., 2008). CSNK-1 thus functions downstream of AP polarity cues. It has been suggested that CSNK-1 negatively regulates the localization of the type I phosphatidylinositol 4-phosphate 5-kinase (PI4P5K) PPK-1 at the anterior. PPK-1 converts PIP into PIP$_2$

(Panbianco et al., 2008). One hypothesis following from this result is that $PIP_2$ is enriched at the posterior cortex and positively regulates GPR-1/2 localization there. However, an asymmetric distribution of the $PIP_2$ biomarker GFP::PH$^{PLC1\delta1}$ was not reported in previous work (Audhya et al., 2005; Panbianco et al., 2008). Together, numerous positive and negative regulators of spindle pulling forces were discovered. While the underlying mechanisms for some, such as GPB-1, are well known, the exact mechanisms through which others, such as CSNK-1 and PPK-1 might regulate spindle positioning remain unclear.

An interesting link between AP polarity and asymmetric spindle positioning is provided by posttranslational modifications of LIN-5. PKC-3 phosphorylates four sites on LIN-5 and this negatively regulates spindle pulling forces at the anterior (Galli et al., 2011). In contrast, phosphorylation of LIN-5 at four other sites positively regulates pulling forces at both anterior and posterior sides (Portegijs et al., 2016). Two of these sites are phosphorylates by GSK-3 and Casein Kinase 1 (CSNK-1), and this promotes the interaction of LIN-5 with GPR-1/2. The other two sites are phosphorylated by CDK-1/cyclinB, which leads to the recruitment of the motor protein dynein (Portegijs et al., 2016). Thus, posttranslational modifications of LIN-5 give further insights into how the ternary complex is assembled and connected to dynein. Consistent with  posttranslational modifications playing a role, the phosphatase PPH-6 and its associated partner SAPS-1 positively regulate the cortical localization of GPR-1/2 and LIN-5, and thus spindle pulling forces (Afshar et al., 2010). However, which residues of GPR-1/2 and LIN-5 are involved in this mechanism and if PPH-6/SAPS-1 is counteracting PKC-3-mediated phosphorylation is not clear yet. Nevertheless, it has been shown that PPH-6/SAPS-1 functions upstream of the Aurora A kinase AIR-1 (Kotak et al., 2016). PPH-6/SAPS-1 negatively regulates the localization of AIR-1 at the cortex, where AIR-1 might negatively regulate spindle pulling forces, in turn explaining the positive force regulation of PPH-6/SAPS-1 (Kotak et al., 2016). A further regulator of GPR-1/2 localization is the DEP domain protein LET-99, which is localized at a lateral posterior band where it negatively regulates GPR-1/2 localization (Krueger et al., 2010; Park and Rose, 2008; Rose and Kemphues, 1998; Tsou et al., 2002). GRP-1/2 is thus enriched on the very posterior end, leading to stronger net pulling forces there. Together, the localization of GPR-1/2 to the very posterior by LET-99 is essential for proper spindle positioning (Krueger et al., 2010; Park and Rose, 2008; Rose and Kemphues, 1998; Tsou et al., 2002). Spindle displacement towards the posterior is also regulated in time by coupling to the cell cycle (McCarthy Campbell et al., 2009). It has been suggested that spindle displacement can only take place after the anaphase promoting complex (APC/C) has inactivated Cdk1 (McCarthy Campbell et al., 2009). Finally, also the cortical F-actin network is involved in negatively regulating spindle pulling forces. Acute depolymerisation of F-actin increases net pulling forces on the anterior (Afshar et al., 2010; Berends et al., 2013). Consistent with these results, a computer model revealed that force generation is reduced by increased cortical stiffness,

which increases the rate of detachment of force generators from the membrane (Kozlowski et al., 2007). Proper cortical tension on the anterior is regulated by the clathrin heavy chain CHC-1 (Spiro et al., 2014). Together, these results establish that the F-actin network negatively regulates spindle pulling forces on the anterior by increasing cortical rigidity. To summarize, AP polarity is translated into asymmetric positioning of the mitotic spindle towards the posterior, which ensures the proper segregation of cell fate determinants.

Just like PAR polarity proteins, members of the ternary complex, including their role in proper spindle positioning, are well conserved across metazoan organisms. In human cells, mammalian homologs of Gα (Gαi$_{1-3}$), GPR-1/2 (LGN and AGS3) and LIN-5 (NuMA) are also essential for proper positioning of the mitotic spindle (reviewed in Kotak and Gönczy, 2013). Another example is *Drosophila*, where the heterotrimeric G-protein Gαi, the GPR-1 homolog GoLoco proteins Pins and Loco, and a LIN-5 related dynein binding protein called Mud also form a ternary complex and control the position of the spindle during mitosis (Bowman et al., 2006; Izumi et al., 2006; Schaefer et al., 2001). In SOP cells, Pins and Gαi are localized on the anterior side, while the Par-3/Par-6/aPKC complex resides on the posterior side, which differs from *C. elegans* and results in only minor spindle displacement and the generation of two daughter cells of similar sizes (Bellaïche et al., 2001; Schaefer et al., 2001)*.* In *Drosophila* neuroblasts, both Pins-Loco/Mud/Gαi and Par-3/Par-6/aPKC complexes reside on the apical side and are connected by an adaptor protein called Inscuteable (Kraut et al., 1996; Schaefer et al., 2000; Siller et al., 2006; Yu et al., 2000), which leads to a large spindle displacement that generates a smaller basal cell (Bowman et al., 2006; Izumi et al., 2006; Yu et al., 2000). Altogether, not only during polarity establishment and maintenance, but also during spindle positioning, molecular players and mechanisms are well conserved from *C. elegans* to human.
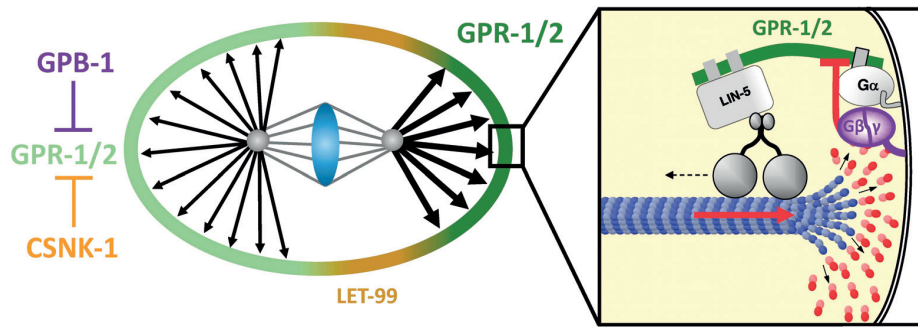
**Figure 6: Cortical force generation and regulation during asymmetric spindle positioning.** Pulling forces on aster microtubules of the mitotic spindle in the one-cell stage *C. elegans* embryo are generated by a ternary complex comprising Gα, GPR-1/2, and LIN-5, which links the minus end directed molecular motor dynein to the plasma membrane. LET-99 localizes at a posterior band and negatively regulates GPR-1/2 localization, leading to its enrichment at the very posterior end, which results in higher net pulling forces there. GPB-1 and CSNK-1 are negative regulators of forces on the anterior side. Further mechanisms and regulators of asymmetric spindle positioning are described in the text. (Ternary complex scheme on the right adapted from Rose and Gönczy, 2014).

## 1.2.7  Subcortical distribution of *C. elegans* PAR proteins and other cortical components

How cortical components distribute within their cortical domain and if this distribution is functional relevant is a question that in *C. elegans* has been investigated for PAR proteins so far. Interestingly, it has been found that PAR proteins are unevenly distributed within their respective cortical domain (Beers and Kemphues, 2006; Dickinson et al., 2017; Robin et al., 2014; Rodriguez et al., 2017; Wang et al., 2017). Thus, PAR-6 exists in two cortical populations, one diffuse and dependent on CDC-42, that it directly interacts with (Gotta et al., 2001), and one punctate and colocalizing with PAR-3 (Beers and Kemphues, 2006; Robin et al., 2014). PAR-3 forms cortical clusters dependent on actomyosin contractility (Wang et al., 2017). In addition, PAR cluster-formation depends on PCK-3, which also distributes in the same clusters, as well as on CDC-42, which localizes in ribbon shaped cortical structures that do not overlap with PAR-3/PCK-3 clusters (Rodriguez et al., 2017). The formation of PAR-3 clusters is crucial for proper segregation of PAR-3 to the anterior by cortical flows, and thus for proper polarity (Dickinson et al., 2017; Rodriguez et al., 2017; Wang et al., 2017). Moreover, PKC-3 can cycle between PAR-3 clusters, where it is held inactive but well segregated, and the CDC-42 pool, where it is active, but not well segregated (Rodriguez et al., 2017). Together, this results in an AP gradient of PKC-3 activity (Dickinson et al., 2017; Rodriguez et al., 2017). The finding that PAR proteins in *C. elegans* form discrete clusters and that this is essential for proper cell polarity is consistent with findings in fission yeast, where polarity proteins also form discrete cortical clusters that are crucial for spatio-temporal control of polarity at the

cell cortex (Dodgson et al., 2013). In *C. elegans*, a putative GAP of CDC-42, CHIN-1 (Kumfer et al., 2010), also forms cortical clusters (Sailer et al., 2015). In contrast to PAR-3 cortical clusters, CHIN-1 clusters form on the posterior during the polarity mainte-nance phase and this is important to stabilize the AP boundary (Sailer et al., 2015). In addition to CDC-42, RHO-1 and CSNK-1 were also observed to localize in ribbon shaped cortical structures on the anterior, but the functional relevance of these structures was not addressed (Motegi and Sugimoto, 2006; Panbianco et al., 2008; Schonegg and Hy-man, 2006). Overall, an uneven distribution was discovered for some cortical compo-nents in the early *C. elegans* embryo. However, the subcortical distribution and its po-tential functional relevance for many other cortical components, such as force genera-tion mediators and regulators during asymmetric spindle positioning, has not yet been investigated. Moreover, the cortical distribution and function of lipid membrane com-ponents, such as phospholipids, is unknown.

## 1.3 Phosphatidylinositol 4,5-bisphosphate and F-actin

### 1.3.1 Functions of $PIP_2$ at the plasma membrane

$PIP_2$ is involved in the regulation of numerous processes at the plasma membrane in many systems. These include exocytosis and endocytosis, phagocytosis, signal transduc-tion, and membrane transport, which are described in this section (Figure 7) (reviewed in De Craene et al., 2017; Di Paolo and De Camilli, 2006). Another essential function of $PIP_2$ at the plasma membrane is the regulation of actin cytoskeleton reorganization and F-actin polymerization (reviewed in De Craene et al., 2017; Di Paolo and De Camilli, 2006), which will be explained in the next section (see 1.3.3.2).
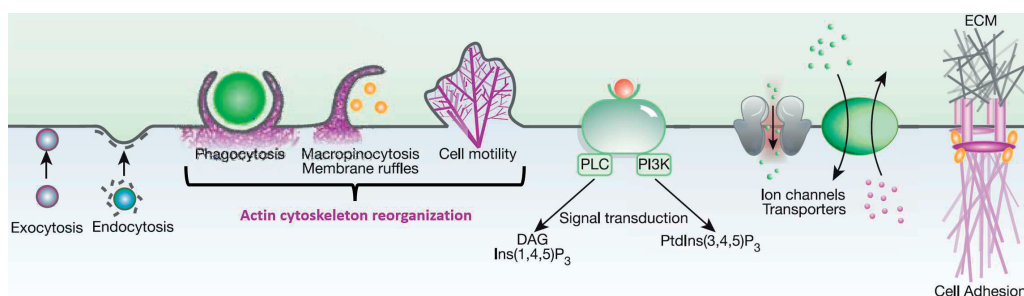
**Figure 7: Examples of PIP$_2$ functions at the plasma membrane.** For further description see text. ECM: extracellular matrix. Reprinted and adapted by permission from Springer Nature, Phosphoinositides in cell regulation and membrane dynamics, reviewed in Di Paolo G and De Camilli P, 2006; © 2006 Nature Publishing Group.

PIP$_2$ plays an important role in the transduction of extracellular signals. PIP$_2$ can execute this function either through its metabolites or through fluctuations in its own level (reviewed in Di Paolo and De Camilli, 2006). Cleavage of PIP$_2$ by phospholipases leads to metabolites and second messengers that can propagate and amplify extracellular signals (reviewed in Di Paolo and De Camilli, 2006). Dephosphorylation of PIP$_2$ by 5-phosphatases controls the steady state level of PIP$_2$ and can switch off PIP$_2$ signaling (reviewed in Di Paolo and De Camilli, 2006). As described below in Section 1.3.2, PIP$_2$ can also be converted to PIP$_3$ (reviewed in Cantley, 2002; Czech, 2003). PIP$_3$ normally exists only in very small amounts in the plasma membrane. However, upon growth receptor stimulation, PIP$_3$ can transiently increase dramatically and play important roles in processes such as migration, chemotaxis, differentiation, cell proliferation and metabolic changes (reviewed in Cantley, 2002; Czech, 2003). PIP$_2$ also regulates many steps during exocytosis and endocytosis (reviewed in Di Paolo and De Camilli, 2006). During exocytosis, for example, PIP$_2$ cooperates with SNARE pairing in marking the plasma membrane as an appropriate partner for vesicle fusion (Milosevic et al., 2005; Gong et al., 2005; reviewed in Di Paolo and De Camilli, 2006). During endocytosis, PIP$_2$ is involved in the recruitment and regulation of endocytotic proteins, such as clathrin adaptors and dynamin (Höning et al., 2005; Gaidarov and Keen, 1999; reviewed in Di Paolo and De Camilli, 2006). Many effector proteins of endocytosis contain domains that directly bind to PIP$_2$, such as ENTH (Epsin N-terminal homology), ANTH (AP-180 N-terminal homology) or PH (Pleckstrin homology) domains. If PIP$_2$ interact with the ENTH domain of Epsin1 for example, Epsin1 undergoes a structural rearrangement that induces membrane curvature that is needed to form endocytotic vesicles (De Craene et al., 2012; Ford et al., 2001; reviewed in Itoh and Takenawa, 2002; De Craene et al., 2017). During phagocytosis, PIP$_2$ is involved in reorganizing the actin cytoskeleton and thereby aid formation of the phagosome, a membrane protrusion needed for particle engulfment (reviewed in Botelho et al., 2004). PIP$_2$ also regulates many ion channels, transporters and exchangers in the plasma membrane. These include calcium channels and pumps, inward recti-

fier and voltage-gated potassium channels, transient receptor potential channels, epithelial sodium channels, and ion exchangers (reviewed in Hilgemann et al., 2001; Suh and Hille, 2005). Together, $PIP_2$ is involved in numerous processes at the plasma membrane.

## 1.3.2 Phosphoinositides (PPIn) and the phosphatidylinositol 4,5-bisphosphate ($PIP_2$) metabolism

Phosphoinositides are involved in various cellular processes, such as vesicle budding, membrane fusion and actin cytoskeleton dynamics (reviewed in De Craene et al., 2017). Phosphoinositides perform their function by recruiting and activating effector proteins regulating these processes (reviewed in De Craene et al., 2017). The synthesis and degradation of phosphoinositides involves numerous phosphorylating and dephosphorylating steps that are tightly regulated, and enzymes performing those steps are well conserved from yeast to human (reviewed in De Craene et al., 2017). Membrane bilayers contain five amphiphilic phospholipids: phosphatidylcholine, phosphatidylethanolamine, phosphatidylserine, sphingomyelin, and phosphatidylinositols (PPIn) (reviewed in De Craene et al., 2017; Spector and Yorek, 1985). Seven differently phosphorylated PPIn exist. The first suggestions for a PPIn metabolism pathway have been made in 1964 (Hokin and Hokin, 1964; reviewed in Payrastre et al., 2001). Since then, knowledge about the complexity of the PPIn metabolic network and the various enzymes involved is growing. Together, the PI metabolism network is a powerful system to control membrane signals in a spatially and temporally defined manner, and allow rapid and reversible formation of domains enriched in a certain PPIn species (Hokin and Hokin, 1964; reviewed in Payrastre et al., 2001).

Phosphatidylinositol (PI) consists of a glycerol moiety esterified in two positions by fatty acid chains and linked to an inositol ring by a phosphate group (reviewed in De Craene et al., 2017; Payrastre et al., 2001). The inositol ring can be phosphorylated at the positions 3,4, and 5 in different combinations leading to the possible generation of the following seven PPIn: phosphatidylinositol 3-phosphate (PI3P), phosphatidylinositol 4-phosphate (PI4P), phosphatidylinositol 5-phosphate (PI5P), phosphatidylinositol 3,4-bisphosphate ($PI(3,4)P_2$), phosphatidylinositol 3,5-bisphosphate ($PI(3,5)P_2$), phosphatidylinositol 4,5-bisphosphate ($PIP_2$), and phosphatidylinositol 3,4,5-trisphosphate ($PIP_3$) (reviewed in De Craene et al., 2017; Payrastre et al., 2001). PI provides the starting point for the whole PPIn metabolism network and all other seven PPIn are synthesized directly or sequentially from PI by diverse lipid kinases and phosphatases (reviewed in De Craene et al., 2017; Payrastre et al., 2001). An overview of the PPIn metabolic network including numerous biosynthesis and degradation pathways and some of the enzymes involved is

shown in Figure 8. As this is most relevant for this work, the biosynthesis and degradation of $PIP_2$ is described in more detail in the following paragraph.
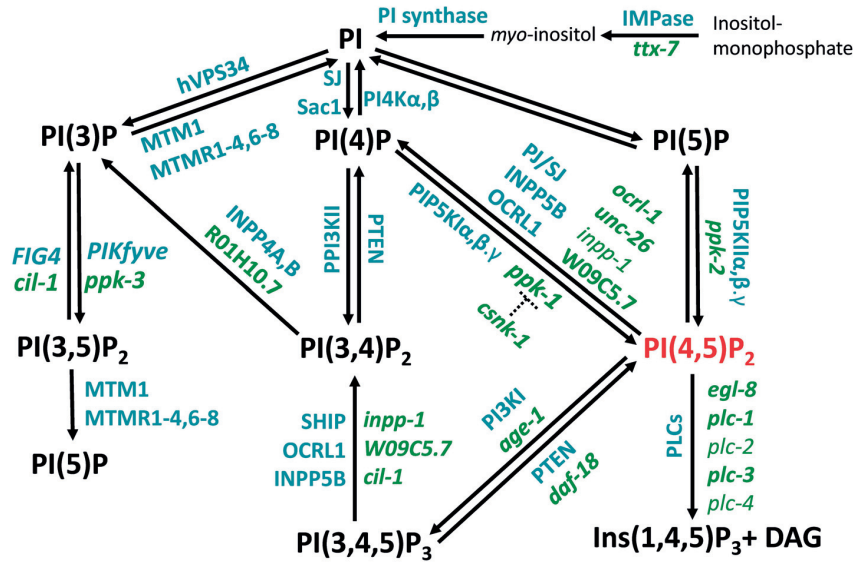
**Figure 8: Phosphoinositide biosynthesis and degradation pathways.** Human enzymes are depicted in blue on the left or top of *C. elegans* genes (green) encoding for a (putative) homolog enzyme. *C. elegans* genes that are not in bold exhibit only a very low expression level in the early embryo.

In eukaryotic cells, $PIP_2$ is kept at a steady state level at the inner leaflet of the plasma membrane where it is continuously phosphorylated and dephosphorylated (reviewed in Payrastre et al., 2001). Together with PI4P, $PIP_2$ is the most abundant PPIn and represents about 45% of total PPIn and about 90% of biphosphorylated PPIn (reviewed in De Craene et al., 2017; Di Paolo and De Camilli, 2006). In human cells, the type I phosphatidylinositol 4-phosphate 5-kinases (PIP5K) α, β, and γ generate $PIP_2$ from PI4P in the plasma membrane. $PIP_2$ can then be further phosphorylated to $PIP_3$ by a Phosphatidylinositol 3-kinase (PI3K) (Ishihara et al., 1998; Bunce et al., 2008; reviewed in Brown, 2015). Type II phosphatidylinositol 5-phosphate 4-kinases (PIP4K) are localized at the Golgi apparatus where they generate $PIP_2$ from PI5P (Clarke et al., 2008). Moreover, $PIP_2$ can also be produced by dephosphorylation of $PIP_3$ by PPIn 3-phosphatases such as PTEN (reviewed in Liu and Bankaitis, 2010). $PIP_2$ can be degraded by dephosphorylation to PI4P by PPIn 5-phosphatases such as OCRL1 and Synaptojanin (reviewed in De Craene et al., 2017). Alternatively, $PIP_2$ can be cleaved by various phospholipases C (PLC) into the second messengers diacylglycerol (DAG) and inositol 1,4,5-trisphospate ($IP_3$) (reviewed in De Craene et al., 2017; Liu and Bankaitis, 2010; Rhee and Bae, 1997).

In *C. elegans*, enzymes homologous to human PPIn kinases and phosphatases regulate $PIP_2$ generation and degradation. Thus, $PIP_2$ can be synthesized from PI4P *in*

*vitro* and *in vivo* by PPK-1, which is the sole *C. elegans* type I PIP5K (Weinkove et al., 2008). The localization of PPK-1 is negatively regulated by the Casein Kinase CSNK-1, which impacts proper spindle positioning (see 1.2.6 for more details) (Panbianco et al., 2008). There is also one type II PIP4K, PPK-2, but PPK-2 does not change the level of $PIP_2$, and *ppk-2* mutant worms are viable, suggesting that PPK-2 is not critical for $PIP_2$ generation in *C. elegans* (Weinkove et al., 2008). $PIP_2$ can be further phosphorylated to $PIP_3$ by AGE-1, the catalytic subunit of the *C. elegans* PI3K. AGE-1 null mutant worms lack PI3K activity and, hence, cannot form $PIP_3$, and arrest as dauer larvae exhibiting extreme longevity and stress resistance (Ayyadevara et al., 2016; Larsen et al., 1995; Morris et al., 1996; Tissenbaum and Ruvkun, 1998). Moreover, the expression of hundreds of genes is altered in *age-1* mutant worms (Ayyadevara et al., 2009; Shmookler Reis et al., 2012). In *C. elegans*, $PIP_2$ can also be generated by dephosphorylation of $PIP_3$ catalyzed by DAF-18, the lipid 3-phosphatase homolog of human PTEN (Gil et al., 1999; Mihaylova et al., 1999; Ogg and Ruvkun, 1998; Rouault et al., 1999). As DAF-18 catalyzes the opposite reaction to that mediated by AGE-1, it is not surprising that DAF-18 also plays an important role in L1 arrest, adult longevity, and dauer formation (Mihaylova et al., 1999; Solari et al., 2005). Mutants in *daf-18* show defects in dauer formation and can suppress the constitutive dauer formation and life extension phenotypes observed in *age-1* mutants (Ogg and Ruvkun, 1998; Rouault et al., 1999). $PIP_2$ can be either cleaved by phospholipases C (PLC) into $IP_3$ and DAG, or dephosphorylated to PI4P by lipid 5-phosphatases. In *C. elegans,* several PLC homologs of human PLC were found, such as *egl-8*, which is a homolog of human PLCβ (Lackner et al., 1999; Miller et al., 1999). Also, homologs of human 5-phosphatases exist. These include OCRL-1 and UNC-26. OCRL-1 hydrolyzes $PIP_2$ to PI4P, and its depletion leads to increased $PIP_2$ on *C. elegans* phagosomes (Cheng et al., 2015). UNC-26 is homologous to Synaptojanin, a polyphosphoinositide phosphatase that also hydrolyzes $PIP_2$ to PI4P. Impairment of UNC-26 results in vesicle trafficking defects and actin cytoskeletal abnormalities in the worm nervous system (Charest et al., 1990; Harris et al., 2000). Altogether, phosphoinositide biosynthesis and degradation is performed by a complex network of lipid kinases and phosphatases, of which many human homologs also function in *C. elegans*.

### 1.3.3 F-actin assembly and its regulation by PIP₂

#### *1.3.3.1 Mechanisms of actin filament assembly and disassembly*

Actin is very well conserved throughout evolution, originating from an ancient common ancestor, as bacteria, archaea, and all eukaryotes possess functionally and structurally related actin molecules (reviewed in Gunning et al., 2015; Pollard, 2016). Actin assembles into filaments in a reversible manner and thus forms one of the three major cytoskeletal polymers. Eukaryotic actin has four subdomains, with a deep cleft for ATP binding. Actin polymerization leads to a polarized helical filament with a so called "barbed"

end or plus-end, and a "pointed" end or minus-end (reviewed in Gunning et al., 2015; Pollard, 2016).

Actin polymerization of G-actin monomers bound to adenosine triphosphate (ATP) occurs spontaneously if a monovalent or divalent cation is present (reviewed in Kang et al., 2013). The bound ATP is then hydrolysed and the γ-phosphate dissociates, which prepares the actin filament for disassembly (reviewed in Kang et al., 2013). Actin polymerization starts with a lag period, which is the nucleation time needed to form small oligomers that can then be further elongated (Blanchoin and Pollard, 2002; reviewed in Pollard, 2016). The actin filament grows much faster on the barbed end than on the pointed end. Moreover, ATP bound actin monomers that are incorporated into a filament undergo a conformational change, which increases the hydrolysis rate of ATP to ADP (Blanchoin and Pollard, 2002; reviewed in Pollard, 2016). Different hypotheses exist as to how ATP is hydrolysed in the filament. It could be either hydrolysed in a zipper-like fashion along the filament or, as favoured now by most, randomly at different places in the filament (Jégou et al., 2011; reviewed in Korn et al., 1987). After hydrolysis, the phosphate only dissociates slowly and ADP-$P_i$-actin behaves as ATP-actin. By contrast, ADP-actin, when the cleaved phosphate is lost, dissociates much faster from both ends (Fujiwara et al., 2007). In the cytoplasm, ADP is exchanged for ATP at the actin monomer and the newly assembled ATP-actin can be incorporated into an actin filament again (Fujiwara et al., 2007). At steady state, the addition of actin monomers at the barbed end is balanced by their loss at the pointed end, a condition referred to as actin treadmilling (Fujiwara et al., 2007; reviewed in Pollard, 2016). At the pointed end, actin monomers associate and disassociate slower than on the barbed end. In addition, the affinity for phosphate is ten times weaker at the pointed end, leading to faster formation of ADP-actin, which then dissociates from the actin filament. Together, this explains why actin filaments polymerize faster at the barbed end (Fujiwara et al., 2007; reviewed in Pollard, 2016). Overall, F-actin polymerization takes place by the attachment of ATP-bound G-actin, followed by ATP hydrolysis in the filament to ADP, after which ADP-bound G-actin then detaches from F-actin.

Numerous proteins control the assembly and disassembly of F-actin (reviewed in Pollard, 2016). These proteins have various roles: they can exchange nucleotides on actin monomers, promote the dissociation of the phosphate, maintain G-actin available for polymerization, initiate polymerization by nucleation, and terminate elongation (reviewed in Pollard, 2016). Additionally, they are needed for end capping of the barbed or pointed end, filament cross-linking and severing of filaments (reviewed in Pollard, 2016). Some of these actin binding and regulating proteins are described in this paragraph. The actin monomer binding protein profilin is bound to the barbed end of actin monomers and inhibits elongation at the pointed but not at the barbed end (Courtemanche and Pollard, 2013). Moreover, by promoting the exchange of ADP for ATP at monomers, profilin increases the pool of ATP-actin ready for polymerization (Jégou et al., 2011; Mockrin

and Korn, 1980; Vinson et al., 1998). Cofilin, which was originally called actin-depoly-merizing factor (ADF) (Bamburg et al., 1980), binds to the side of F-actin and severs actin filaments (Cao et al., 2006). Cofilin can also bind to actin monomers and thereby inhibit the exchange of monomers at filaments, which can be overcome by profilin (Blanchoin and Pollard, 1998; Nishida, 1985). Another actin severing protein is gelsolin, which can also cap the barbed ends of actin filaments (reviewed in Nag et al., 2013). Also the initi-ation of F-actin polymerization is well regulated, as the arp2/3 complex regulates the formation of actin branches (reviewed in Rouiller et al., 2008), whereas formins initiate the polymerization of unbranched filaments (reviewed in Pollard, 2016). The arp2/3 complex consists of seven subunits, including arp2 and arp3 (reviewed in Rouiller et al., 2008). When the complex binds to the side of an actin filament, arp2/3 initiate the polymerization of a branched filament there. Thereafter, the barbed end of this new branched actin filaments growth, whereas the arp2/3 complex anchors the pointed end to the original actin filament (reviewed in Rouiller et al., 2008). The nucleation-promot-ing factors of the Wiskott-Aldrich Syndrome family (WASP), and other factors activate the arp2/3 complex (reviewed in Rottner et al., 2010). Formins nucleate unbranched actin filaments, possibly by stabilizing dimers, and they interact with the barbed end of filaments (Pring et al., 2003; reviewed in Paul and Pollard, 2009). Capping protein (CP) tightly binds barbed ends and thus the number of barbed ends available for growth be-comes limited (reviewed in Edwards et al., 2014). Another capping protein is tropomod-ulin, which binds to pointed ends and stabilizes them by blocking actin monomer addi-tion and loss (Rao et al., 2014). To summarize, actin assembly and disassembly is tightly regulated by numerous actin binding proteins.

### 1.3.3.2  Regulation of F-actin reorganization and polymerization by PIP$_2$

In systems from *S. cerevisiae* to *H. sapiens,* PIP$_2$ helps link the F-actin cortical network to the plasma membrane, is involved in cell adhesion, stimulates F-actin assembly and in-hibits F-actin disassembly (Figure 9) (reviewed in Brown, 2015; De Craene et al., 2017; Di Paolo and De Camilli, 2006; McLaughlin et al., 2002; Wu et al., 2014; Yin and Janmey, 2003; Zhang et al., 2012). The link of the plasma membrane to the underlying actin cy-toskeleton is provided in a regulated manner by proteins of the ERM family, which con-sists of ezrin, radixin and moesin. Direct binding of ERM proteins to PIP$_2$ is involved in their activation (reviewed in Tsukita et al., 1997; Wu et al., 2014). In addition to plasma membrane actin cytoskeleton linkage, PIP$_2$ is also involved in cell adhesion at the cell-substratum contact through its binding to talin (Martel et al., 2001). The ubiquitous cy-toskeletal protein talin concentrates at focal adhesions and cell-cell, as well as cell-sub-stratum contacts. Here, talin binds to β-tails of integrins and activates them (Burn et al., 1988; Burridge and Connell, 1983; Calderwood et al., 2002). The interaction of talin and integrins is enhanced by PIP$_2$ binding of talin *in vitro* (Martel et al., 2001). Moreover, PIP$_2$ is involved in F-actin polymerization and reorganization by activating F-actin assembly and inhibiting F-actin disassembly in numerous ways (Xian and Janmey, 2002; reviewed

in Wu et al., 2014). PIP$_2$ binds to the actin binding protein (ABP) gelsolin, which binds to the barbed ends of actin filaments, preventing monomer exchange and severing existing actin filaments (reviewed in Wu et al., 2014). The binding sites of PIP$_2$ and F-actin to gelsolin overlap and thus PIP$_2$ binding prevents gelsolin from binding to F-actin, and thus to cap or severe actin filaments (Xian and Janmey, 2002; Weeds et al., 1986; reviewed in Wu et al., 2014). PIP$_2$ also binds to cofilin/ADF, a family of ABPs that are related to gelsolins in a structural and functional manner (reviewed in Wu et al., 2014). Cofilin causes depolymerization at the minus end of F-actin and binds G-actin and F-actin, preventing the reassembly of G-actin and F-actin. Cofilin activity is inhibited by PIP$_2$ binding (Ojala et al., 2001; reviewed in Wu et al., 2014). Villin is another APB related to gelsolin and cofilin, which also severs actin filaments and is bound to and inhibited by PIP$_2$ (Meng et al., 2005; reviewed in Wu et al., 2014).
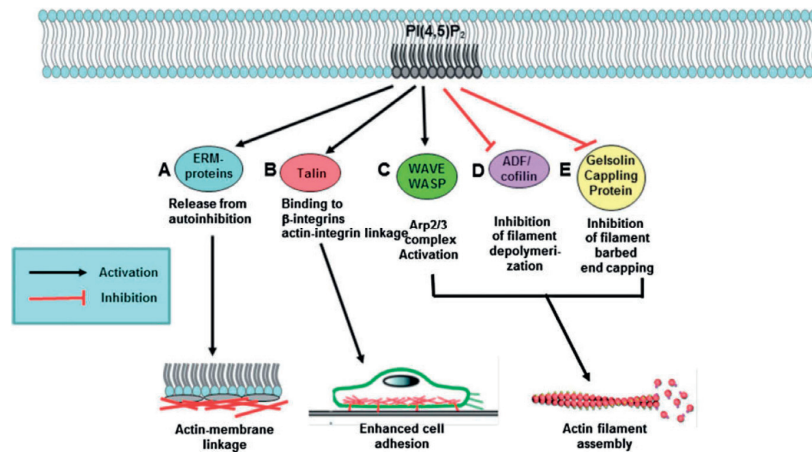


**Figure 9: Overview of possible regulation mechanisms of actin by PIP$_2$.** (A) PIP$_2$ regulates actin-membrane linkage by activating ERM-proteins. (B) PIP$_2$ binding to talin enhances the interaction of talin with integrins, which supports cell adhesion. (C-D) PIP$_2$ activates positive regulators of F-actin polymerization and branching and inhibits actin depolymerization and end capping factors (Wu et al., 2014). Reprinted by permission from John Wiley and Sons, British Journal of Pharmacology, The role of phosphoinositide-regulated actin reorganization in chemotaxis and cell migration, Wu C-Y *et al.*, 2014; © 2014 John Wiley and Sons.

An important pathway through which PIP$_2$ positively regulates F-actin assembly is mediated through the Wiskott–Aldrich Syndrome protein family proteins WASP and N-WASP (Higgs and Pollard, 2000; Prehoda et al., 2000; Wegner et al., 2008). In their inactive state, WASP and N-WASP exist in an auto-inhibited confirmation (Higgs and Pollard, 2000; Kumar et al., 2012). Upon cooperative binding of PIP$_2$ and Cdc42 to WASP or N-WASP, the protein undergoes a conformational change and gets activated. WASP then binds and activates the arp2/3 complex, which then nucleates F-actin (Higgs and Pollard, 2000; Kumar et al., 2012). N-WASP is already bound to arp2/3 in its autoinhibited state and cooperative binding of PIP$_2$ and Cdc42 leads to activation of already bound arp2/3, which then carries out actin polymerization (Humphries et al., 2014; Prehoda et al.,

2000; Wegner et al., 2008). PIP$_2$ can also activate F-actin polymerization by being phosphorylated to PIP$_3$ (reviewed in Chichili and Rodgers, 2009). PIP$_3$ then activates the guanine nucleotide exchange factor (GEF) Vav, which then can activate the Rho GTPases Cdc42, Rho, and Rac. Those in turn activate WASP family proteins, which then activate the arp2/3 complex as described, leading to F-actin polymerization and branching (Rozelle et al., 2000; Bustelo, 2000; reviewed in Chichili and Rodgers, 2009). Together, PIP$_2$ regulates F-actin cytoskeleton reorganization and linkage in numerous ways by recruiting and activating or inhibiting actin assembly and disassembly factors.

### 1.3.3.3 PIP$_2$ and actin cytoskeleton organization in C. elegans

In *C. elegans*, little is known about the role of PIP$_2$ in actin cytoskeleton reorganization. Overexpression of PPK-1 in developing neurons increases the level of PIP$_2$ and results in extended filopodial-like structures, probably through changes in the actin cytoskeleton (Weinkove et al., 2008). Also in the somatic gonad, PPK-1 is important for F-actin cytoskeletal organization and gonad contractility (Xu et al., 2007). In the developing *C. elegans* uterus, F-actin, F-actin regulators and PIP$_2$ are all enriched at the invasive membrane domain of anchor cells (Ziel et al., 2009). This suggests that PIP$_2$ could also reorganize actin at this location. Furthermore, the *C. elegans* gelsolin-like protein-1 (GSNL-1), which regulates the severing of actin filaments and barbed end capping, is inhibited by PIP$_2$ *in vitro* (Liu et al., 2010b; Liu et al., 2011). PIP$_2$, together with PI3P, has also been reported to transiently accumulate at phagosomes and to coordinate phagosome sealing in *C. elegans* (Cheng et al., 2015). As in other systems, PIP$_2$ contributes to phagocytosis through regulating a local increase in actin polymerization, which is needed for phagosome formation (reviewed in Botelho et al., 2004). In a systematic RNAi screen, the ezrin *erm-1* was identified as a putative regulator of actomyosin flows (Fievet et al., 2013). As in other systems, homologs of ERM-1 are essential for plasma membrane F-actin linkage. In other systems, ezrin proteins are activated by PIP$_2$ (reviewed in Wu et al., 2014), providing a first hint of PIP$_2$ involvement in F-actin reorganization in the early *C. elegans* embryo. Together, PIP$_2$ can regulate actin reorganization in the *C. elegans* gonad and nervous system, and probably also during phagocytosis and in anchor cells. But whether PIP$_2$ regulates cortical actomyosin network organization in the *C. elegans* embryo is not known.

## 1.3.4   Regulation of cell polarity by PIP$_2$.

In many systems, PIP$_2$ is well understood to regulate cell polarity through its ability to recruit PAR proteins, reorganize the actin cytoskeleton or start signaling cascades. One example where this has been well studied is *Drosophila* (Claret et al., 2014; Fabian et al., 2010; Gervais et al., 2008; Guglielmi et al., 2015; Tan et al., 2014). Here, in the follicular epithelium, PIP$_2$ is enriched at the apical plasma membrane and recruits PAR-3/Bazooka

there, thus defining the size of the apical domain. This process is crucial to maintain apical-basal polarity (Claret et al., 2014). Also in the oocyte, there is data suggesting that $PIP_2$ could mediate the interactions between different components that are essential for cell polarity, i.e., PAR proteins, the cytoskeleton and the plasma membrane (Gervais et al., 2008). This hypothesis is further supported by results showing that during oogenesis, $PIP_2$ production in the plasma membrane is crucial for actin organization and cell polarity (Tan et al., 2014). Not only during oogenesis, but also during spermatogenesis, $PIP_2$ is essential for polarity establishment and elongation of spermatids (Fabian et al., 2010). Moreover, during embryogenesis, loss of $PIP_2$ leads to clear loss of actin and of apical constriction (Guglielmi et al., 2015). Overall, $PIP_2$ is involved in the regulation of polarity in several tissues in *Drosophila*.

Besides Drosophila, $PIP_2$ is essential for proper cell polarity also in Zebrafish and yeast. In zebrafish, $PIP_2$, which is stabilized by the phosphatase Inpp5e, is involved in cell polarity in the renal epithelium (Xu et al., 2017). In *Saccharomyces cerevisiae*, $PIP_2$ was proposed to act in concert with the Rho GTPase Cdc42 to properly control polarized cell growth (Orlando et al., 2008). Moreover, in the fungus *Candida albicans* a steep $PIP_2$ gradient is crucial for asymmetric filamentous growth (Vernay et al., 2012). Another example where $PIP_2$ plays a role in cell polarization are motile cells, such as mammalian neutrophils or *Dictyostelium discoideum*, which are morphologically polarized with a leading edge and a trailing end. Here, $PIP_2$ regulates the reorganization of actin needed for cell motility (reviewed in Wu et al., 2014). Furthermore, $PIP_2$ induced actin assembly mediated by Cdc42 is also required for viability in early mammalian development, as demonstrated by inactivating Cdc42 in the mouse germline (Chen et al., 2000). During mouse oogenesis, PLC-mediated hydrolysis of $PIP_2$ is necessary and sufficient for symmetry breaking and proper polarity establishment. Here, as in *C. elegans,* polarity establishment starts with asymmetric segregation of an actomyosin network followed by asymmetric localization of PAR proteins, as described above (see 1.2.4) (Zhu et al., 2017). To summarize, in many systems $PIP_2$ is essential for F-actin reorganization and cell polarization but it remains to be investigated if this role is conserved in *C. elegans*.

### 1.3.5 Cortical PIP₂ domains

While the subcortical distribution and function of PAR proteins has been addressed in *C. elegans* (see 1.2.7), it is unclear what the situation is for phospholipids such as $PIP_2$. PAR-2 has been shown to directly bind to phospholipids, including $PIP_2$ (Motegi et al., 2011). Moreover, the human PAR-1 homolog MARK and the *Drosophila* and human PAR-3 homologues interact with phospholipids, including $PIP_2$ (Horikoshi et al., 2011; Krahn et al., 2010; Moravcevic et al., 2010; Wu et al., 2007b). The interaction of the *Drosophila* hom-

olog of PAR-3 Bazooka with phosphoinositides was suggested to couple plasma membrane polarity to cell polarity (Krahn et al., 2010). Moreover, the interaction of human PAR-3 with phospholipids is essential for epithelial cell polarization (Moravcevic et al., 2010). Furthermore, a CDC-42 homologue binds directly to $PIP_2$ (Johnson et al., 2012). Together, in other systems, phospholipids bind PAR proteins, which exhibit an uneven subcortical distribution, but the distribution of phospholipids such as $PIP_2$ themselves in the *C. elegans* zygote is unclear.

In other organisms and in *vitro,* $PIP_2$ can be unevenly distributed in the plasma membrane. In model membranes, $PIP_2$ is known to form electrostatic based clusters with $Ca^{2+}$ (reviewed in Brown, 2015). Generally, $PIP_2$ also accumulates in lateral domains in nascent phagosomes, membrane ruffles, and the leading edge of motile cells, which are all sites of actin reorganization (reviewed in McLaughlin et al., 2002; Zhang et al., 2012). Consistent with this fact, it was demonstrated that $PIP_2$ can stimulate actin polymerization in curved but not in flat model membranes, and this is dependent on Cdc42 (Daste et al., 2017; Gallop et al., 2013). $PIP_2$ domains and patches were also observed in cultured cells. Live imaging of NIH-3T3 cells revealed that $PIP_2$ forms domains at cell protrusions. Here, it has been suggested that transport of $PIP_2$ regulates actin polymerization and protrusion dynamics (reviewed in Chierico et al., 2015). In PC12 cells, $PIP_2$ assembles into patches at the leading edge dependent on Cdc42, N-WASP and actin cytoskeleton dynamics. These patches precede the accumulation of F-actin patches but also depend on F-actin (Golub and Caroni, 2005; reviewed in Golub and Pico, 2005). Also in *C. albicans*, a steep $PIP_2$ gradient depends on F-actin but not on microtubules (Vernay et al., 2012). Moreover it was suggested that the enrichment of actin filaments in the cortical cytoskeleton can drive clustering of rafts into $PIP_2$-containing macrodomains, which then regulate further actin polymerization and branching (reviewed in Chichili and Rodgers, 2009). Overall, $PIP_2$ can be distributed in subcortical domains and $PIP_2$ localization and F-actin polymerization exhibit reciprocal positive feedback regulation in several systems.

## 1.4  Aim of this thesis

Generally, this thesis aims to further analyze mechanisms regulating asymmetric cell division, and thus to improve our understanding of this fundamental process for the development of multicellular organisms and stem cell lineages. In particular, using the one-cell stage *C. elegans* embryo as a model, we aim to test the subcellular distribution of cortical components directly at that location, which is where they exert their function. In *C. elegans,* the question of how cortical components distribute within their cortical domain and if this distribution is functional relevant has already been investigated for PAR proteins, but it remains unknown for numerous other components. We thus aimed to investigate the cortical distribution and function of force generation mediators, negative force regulators and the membrane lipid component $PIP_2$.

Moreover, while the dependency of polarity in the *C. elegans* zygote on PAR proteins and the actomyosin network has been thoroughly investigated, the involvement in this process of plasma membrane components, such as phospholipids, has not yet been addressed much. In many systems, $PIP_2$ is essential for F-actin reorganization and cell polarization but it remains to be investigated if this role is conserved in *C. elegans*. We therefore aimed to also address the question whether $PIP_2$ is needed for reorganization and polymerization of F-actin and proper polarization in the early *C. elegans* embryo.

# 2. Materials and methods

## 2.1 Worm strains

Nematodes were maintained at 24°C using standard protocols (Brenner, 1974). The following strains were used: GFP::PH$^{PLC1\delta1}$ (OD58, *unc-119*(*ed3*) III; ltIs38[*pie-1*p::GFP::PH(PLC1delta1) + *unc-119*(+)]) (Audhya et al., 2005); mCherry::PH$^{PLC1\delta1}$ (OD70, *unc-119*(*ed3*) III; ltIs44[*pie-1*p::mCherry::PH(PLC1delta1) + *unc-119*(+)]V) (Audhya et al., 2005); GFP::PAR-2 (TH129) and GFP::PAR-6 (TH110) (Schonegg et al., 2007); GFP::NMY-2 (LP162, *nmy-2*(*cp13*[*nmy-2*::gfp + LoxP]) I) (Dickinson et al., 2013); CAV-1::GFP (RT688, unc-119(ed3) III; pwIs281[CAV-1::GFP, *unc-119*(+)]) (Sato et al., 2006); mNeon-Green::PH$^{PLC1\delta1}$ (LP274, cpIs45[P*mex-5*::mNeonGreen::PLCδ-PH::*tbb-2* 3'UTR + *unc-119*(+)] II; *unc-119*(*ed3*) III), mKate-2::PH$^{PLC1\delta1}$ (LP307, cpIs54[P*mex-5*::mKate2::PLCδ-PH(A735T)::*tbb-2* 3'UTR + *unc-119*(+)] II; *unc-119*(ed3) III) and mCherry::PH$^{PLC1\delta1}$ (LP308, cpIs55[P*mex-5*::mCherry::C1::PLCδ-PH::*tbb-2* 3'UTR + *unc-119*(+)] II; *unc-119*(ed3) III) (Heppert et al., 2016); Lifeact::mKate-2 (strain SWG001) (Reymann et al., 2016); GFP::RHO-1 (SA115, *unc-119*(*ed3*) III; tjIs1[*pie-1*::GFP::*rho-1* + *unc-119*(+)]) (Motegi et al., 2006); GFP::CDC-42 (SA131, *unc-119*(*ed3*) III; tjIs6[*pie-1*p::GFP::*cdc-42* + *unc-119*(+)]) (Motegi and Sugimoto, 2006); GFP::ECT-2 (SA125, unc-119(*ed3*) III; tjIs4[*pie-1*::GFP::*ect-2* + *unc-119*(+)]) (Motegi and Sugimoto, 2006); *unc-26*(*s1710*) (EG3027, *unc-26*(*s1710*) IV) (Charest et al., 1990); *age-1*(*m333*), (DR722, *age-1*(*m333*)/mnC1 *dpy-10*(*e128*) *unc-52*(*e444*) II) (Riddle, 1988); PPK-1::mGFP (PHX448, syb448[*ppk-1*::mGFP] I) (http://www.sunybiotech.com); GFP::GPR-1 (SV1569, he238[*fkbp*:: egfp::*gpr-1*] III) (Portegijs et al., 2016); GFP::LIN-5 (SV1589, (he244[egfp::*lin-5*] II) (Portegijs et al., 2016); GFP::GPB-1 (GZ789, *unc-119*(*ed3*) III; [*pie-1*::GFP::*gpb-1* + *unc-119*(+)]) (Thyagarajan et al., 2011); GFP::GPC-2 (GZ963, *unc-119*(*ed3*) III; [*pie-1*::GFP::*gpc-2* + *unc-119*(+)]) (Thyagarajan et al., 2011); YFP::GPR-1 (TH242, *unc-119*(ed3)III; ddIs32[pie-1::*gpr-1*(synthetic introns, CAI 1.0)::YFP; *unc-119*(+)] (Redemann et al., 2011); GFP::CSNK-1 (JA1354, *unc-119*(e2498); weIs12[*unc-119*(+):pie-1p:GFP:*csnk-1*]) (Panbianco et al., 2008); GFP::CHC-1 (*bIs5*[*GFP::CHC, rol-6(d)*] (Greener et al., 2001); GFP::AHPH (MG617 xsSi5[*pie-1*p::GFP::*ani-1*(AH+PH)::*pie-1* 3'UTR+Cbr-*unc-119*(+)]II] (Tse et al., 2012); GFP::WSP-1 (MOT471, temIs110[gfp::WSP-1] (Kumfer et al., 2010). DHC-1::GFP (CA1207, dhc-1(ie28[dhc-1::degron::GFP]) I.) (Zhang et al., 2015). Crosses were performed at 20°C to generate lines homozygote for all transgenes, which were then maintained at 24°C. For GFP::RHO-1 and mCherry::PH$^{PLC1\delta1}$ (only in Figure 21D), as well as GFP::PH$^{PLC1\delta1}$ and Lifeact::mKate-2, mCherry::PH$^{PLC1\delta1}$ and GFP::AHPH, mCherry::PH$^{PLC1\delta1}$

and PPK-1::mGFP worm lines were crossed and F1 progeny heterozygous for both transgenes imaged.

## 2.2 RNA interference

RNAi-mediated depletion was performed essentially as described (Kamath et al., 2001), using bacterial feeding strains from the Ahringer (Kamath et al., 2003) or Vidal library (Rual et al., 2004) (gift from Jean-François Rual and Marc Vidal). RNAi for *par-2* (Ahringer), *par-3* (Ahringer), *nmy-2* (Ahringer), *act-1* (Vidal), *tba-2* (Vidal), *rho-1* (Vidal), *cdc-42* (Vidal), *ocrl-1* (Ahringer), *csnk-1* (Ahringer), *gpb-1* (Ahringer) and *chc-1* (Ahringer) was performed by feeding L3-L4 animals with bacteria expressing the corresponding dsRNA at 24°C for 16-26 hours. RNAi for *pfn-1* (Vidal) and *arx-2*(Vidal) was performed by feeding L4 and young adults with bacteria expressing dsRNA at 24°C for 72-96 hours and imaging embryos of their offspring. RNAi for *gpr-1/2* (Vidal) was performed by feeding L1 and L2 worms with bacteria expressing dsRNA at 24°C for 48 hours. PERM-1 is a sugar modifying enzyme essential for forming the permeability barrier of the eggshell (Olson et al., 2012), and RNAi for *perm-1* (Ahringer) was performed by feeding L4 and young adults with bacteria expressing dsRNA at 20°C for 12-18 hours. Double RNAi for *ocrl-1* and *perm-1* was performed by mixing bacteria expressing *ocrl-1* dsRNA and *perm-1* dsRNA in the ratio 1:1, feeding L3 and L4 young adults 24-30 hours at 24 °C. The effectiveness of depletion was assessed phenotypically as follows: *par-2*(*RNAi*) and *par-3*(*RNAi*) -symmetric spindle positioning and equal cell division; *nmy-2*(*RNAi*) and *act-1*(*RNAi*) -absence of cortical ruffles, symmetric spindle positioning, no cytokinesis; *tba-2*(*RNAi*) -defective pronuclear meeting, no centration/rotation, no spindle assembly, misplaced cytokinesis furrow; *ocrl-1*(*RNAi*) -see 3.2.2, 3.2.3 and 3.2.4, *perm-1*(*RNAi*) -successful action of added drug; *pfn-1*(*RNAi*) -defective cortical F-actin network; *cdc-42*(*RNAi*) -partial loss of polarity during the maintenance phase; *rho-1*(*RNAi*) -absence of cortical ruffles; *csnk-1*(*RNAi*) -increased cortical contractions, increased spindle pulling forces, *gpb-1*(*RNAi*) -rocking of pronuclei during centration/rotation; *chc-1*(*RNAi*) sparse yolk granule density, *arx-2*(*RNAi*) -sterility of adult worms; *gpr-1/2*(*RNAi*) –symmetric cell division.

## 2.3 Molecular Biology

### 2.3.1 Generation of mGFP utilized for PPK-1::mGFP and CAAX::CIBN::mGFP

We utilized a sequence encoding GFP that was codon adapted and with synthetic introns for *C. elegans* (Dickinson et al., 2013). The A206K mutation was introduced using the QuikChange Site-Directed Mutagenesis Kit (Agilent) and the following primers (Microsynth): 5'-CTA CCT CTC CAC CCA ATC C**AA G**CT CTC CAA GGA CCC AAA C-3' (sense) and 5'-GTTTGGGTCCTTGGAGAG**CTT**GGATTGGGTGGAGAGGTAG-3' (antisense). Nucleotides introducing the mutation are marked in bold.

### 2.3.2 Generation of constructs for CRY2/CIBN optogenetic tool

Constructs used to set up an optogenetic tool (CIBN::CAAX, CIBN::mGFP::CAAX, mKate-2::CRY2PHR::OCRL-1) were assembled using Gibson Assembly (NEB) and then combined with the *pie-1* promoter and *pie-1* 3'UTR using the MultiSite Gateway Kit (ThermoFisher). As a destination vector, pCG150 containing an *unc-119* rescue fragment suitable for bombardment was utilized. For GFP and mKate-2, codon adapted versions with synthetic introns for *C. elegans* were utilized (Dickinson et al., 2013). The *pie-1* promoter and *pie-1* 3'UTR were obtained from the vectors pCM1.127 and pCM5.47 (Seydoux Lab – Third Generation Vector Kit, unpublished). CIBN::CAAX, CRY2PHR, and the 5-ptase domain of OCRL were amplified from the following vectors: pCIBN(deltaNLS)-pmGFP (Adgene, 26867), pCRY2PHR-mCherryN1 (addgene, 26866) and mCherry::CRY2-5ptaseOCRL (Adgene, 66836).

### 2.3.3 Generation of constructs for CRISPR/Cas9

Cloning of constructs for CRISPR/Cas9 and preparation of the injection mix were performed as described (Paix et al., 2014; Paix et al., 2016).The sgRNA was introduced into the Cas9 expression vector pDD162 using the Q5 Site-Directed Mutagenesis Kit (BioLabs). Repair templates containing GFP (Dickinson et al., 2013) were introduced into the subcloning vector pGEM-T (Promega) and then amplified in large amounts by PCR using Phusion Polymerase (NEB) to obtain linear repair templates for injection.

## 2.4 Live imaging

Gravid hermaphrodites were dissected in osmotically balanced blastomere culture medium (Shelton and Bowerman, 1996) and the resulting embryos mounted on a 2% agarose pad. DIC time lapse microscopy (Figure 10 A, C, E, G, I) was performed at 25°C ± 1°C with a 100× (NA 1.25 Achrostigmat) objective and standard DIC optics on a Zeiss Axioskop 2 microscope. Dual DIC and fluorescence time lapse microscopy (Figure 19A) was performed at 25°C ± 1°C with a 63x objective lens (NA 1.2 C Apo) using a Zeiss Axio Observer.D1 microscope equipped with a Andor Zyla sCMOS CCD camera. All other images were acquired at 23°C using an inverted Olympus IX 81 microscope equipped with a Yokogawa spinning disk CSU - W1 with a 63x (NA 1.42 U PLAN S APO) objective and a 16-bit PCO Edge sCMOS camera. Images were obtained using 488 nm and 561 nm solid-state lasers with an exposure time of 400 ms and a laser power of 20-60%. For cortical imaging, 3 planes at the cell cortex (each 0.25 µm apart) were acquired. Cell cycle stages were determined using transmission light microscopy, imaging the middle plane in parallel (data not shown).

## 2.5 Image Processing and analysis

Cortical images of GFP::PH$^{PLC1\delta1}$ used for quantification were processed as follows: the 3 cortical planes were z-projected using average intensity projection, after which a median filter of 1 pixel was applied. The background of the entire image was subtracted using the measured mean background in each frame. Signal intensity decay due to photobleaching was corrected with the Fiji plugin "bleach correction" using the exponential fitting method. The entire cortical region was segmented by applying a binary automated histogram-based threshold, followed by iterated morphological operations. Cortical structures were segmented by applying a binary intensity threshold, calculated by fitting the pixel intensity histogram with a Gaussian function and setting the threshold at 4 sigma from the Gaussian peak. The boundary between anterior and posterior domains was determined manually during pseudocleavage formation. Upon depletion of NMY-2 and ACT-1, where no pseudocleavage furrow forms, the boundary was set during mitosis. The fraction of the total area in each half covered by the segmented PIP$_2$ cortical structures was determined in each case.

Curves of normalized cortical structures sizes were fit with a sigmoidal model and synchronized, setting the sigmoid inflection point, which corresponded typically to the time of centration/rotation, as time t=0 s. Curves of normalized cortical structures sizes were aligned manually for *act-1*(*RNAi*) and *unc-26*(*s1710*) *ocrl-1*(*RNAi*) embryos using the clear landmark provided by Nuclear Envelope Breakdown (NEBD) as a reference,

because a sigmoid function could not be fit with the PH markers in these cases. Since the time separating centration/rotation from NEBD is typically 150 seconds, t=0 was set at -150 seconds prior to NEBD for *act-1*(*RNAi*) and *unc-26*(*s1710*) *ocrl-1*(*RNAi*) embryos.

The Elongation Index was calculated as follows: ((perimeter^2)/area)/4$\pi$ using the MATLAB image processing function "regionprops". The Elongation Index was then normalized by a factor of 1/$\pi$ such that a square of 2 x 2 pixels has an Elongation Index of 1.

For assessing the AP boundary of the segmented PIP$_2$ cortical structures (GFP::PH$^{PLC1\delta1}$) and of F-actin (Lifeact::mKate-2) (Figure 19), we automatically determined the extent of the PIP$_2$ and F-actin domains relative to the whole embryo length using a Matlab script. For Lifeact::mKate2, a histogram-based method was used to keep only the 95% brightest pixels.

Cortical images obtained by live confocal spinning disk imaging shown in the figures were processed as follows: the 3 cortical planes were z-projected using maximum intensity projection, then a median filter of 1 was applied. The grey value fluorescence intensity of some transgenes (GFP::PH$^{PLC1\delta1}$ as heterozygote, GFP::PAR-2, GFP::PAR-6, Lifeact::mKate-2, mCherry::PH$^{PLC1\delta1}$, mNeonGreen::PH$^{PLC1\delta1}$, GFP::GPB-1, YFP::GPR-1) was slightly variable, likely resulting from variable expression/folding of the fluorescent fusion protein. The brightness and contrast of images resulting from embryos expressing these transgenes was therefore adjusted accordingly. Such variability was especially pronounced in *unc-26*(*s1710*) *ocrl-1*(*RNAi*) embryos. Total cortical intensity was obtained as follows. 3 cortical planes, acquired as described above were z-projected by summing the intensity of all slices. Then, a Otsu threshold was first used to retrieve the brightest elements, retaining only the biggest blob, which corresponds to the embryo. Values outside the embryo were then averaged to obtain the mean background intensity, which was subtracted from the embryo pixel intensities. Thereafter, embryo pixel values were averaged to obtain the mean pixel intensity value.

## 2.6  Lipid delivery and injection

BODIPY® FL Phosphatidylinositol 4,5-bisphosphate (Echelon Bioscience, C-45F6) (end concentration: 10 µM) was delivered to *perm-1*(*RNAi*) embryos by adding it to the buffer in which gravid worms were dissected. Embryos were then mounted on a 2% agarose pad using Vaseline as a spacer to decrease the pressure exerted on the fragile *perm-1*(*RNAi*) embryos.

BODIPY® FL Phosphatidylinositol 4,5-bisphosphate (Echelon Bioscience, C-45F6) was injected into the syncytial gonad of young adult worms using a Eppendorf FemtoJet

*4i* Microinjector and Femtotips® II (Eppendorf, 930000043). 1mM EDTA (pH=7.0) was added to dried lipids to form a micelle suspension (500 µM stock solution). Lipids were sonicated for 30 sec in a bath sonicator to break micelles before each injection. Lipids were then diluted in ddH$_2$O to 100 µM and injected. Embryos of injected animals were imaged 2-4 hours after injection.

## 2.7 Cortical flow measurement and correlation analysis

### 2.7.1 Particle Image Velocimetry (PIV)

For Particle Image Velocimetry (PIV) analysis, cortical image sequences of mNeon-Green::PH$^{PLC1\delta1}$ and Lifeact::mKate-2 were prepared by performing a maximum intensity z-projection of a stack of 2 planes (0.25 µm apart) and applying a median filer of 1 pixel. PIP$_2$ cortical structures and the F-actin network were then segmented as follows: the embryo was first extracted from the background using a histogram-based automated threshold, keeping only blobs of a size superior to one third of the biggest blob. The resulting binary images were deemed to be the embryo area. We applied a morphological erosion to the mNeonGreen::PH$^{PLC1\delta1}$ movies with a large structuring element (a disk 30 pixels in radius) to calculate the average value of the pixels not corresponding to PIP$_2$ cortical structures; the PIP$_2$ cortical structures were then segmented as the pixels of intensity higher than the computed average value, times a scaling factor determined empirically (1.7). The extraction of the F-actin network was achieved simply by determining a histogram-based automated threshold on the morphological top-hat of the F-actin image. F-actin filaments and PIP$_2$ cortical structures were segmented prior to PIV analysis to ensure that only flow fields in the region of interest are measured.

PIV was then performed to measure cortical flows using the MATLAB based PIVlab toolbox (Thielicke and Stamhuis, 2014), which splits each image of a movie into a regular grid, for which the size of grid cells is given by the user. The position of each grid cell in the next image is estimated by finding the maximum normalized cell-to-cell cross-correlation of equivalent sizes in a geometrical neighborhood called interrogation area. Such PIV analysis was applied to mNeonGreen::PH$^{PLC1\delta1}$ and Lifeact::mKate-2 separately, after segmentation of the corresponding cortical structures. The choice of the grid cell sizes and interrogation areas resulted from a balance between two criteria: smaller cells allow to compute displacements with high spatial resolution, but excessively small cells do not contain enough information to be reliably correlated to other cells; the estimation of displacements of bigger cells is hence more reliable, but computed with lesser resolution. We found empirically 32 x 32 pixels for cell sizes, and 64 x 64 pixels for interrogation areas, to be a good compromise.

The PIV velocity fields output for both mNeonGreen::PH$^{PLC1\delta1}$ and Lifeact::mKate-2 signals were compared in terms of angles between colocalized features and correlation of the norms. For each movie, angles between velocity vectors of colocalized features were computed and plotted on a histogram. The average angle value for each time point and each movie was also computed to monitor the coherence between the two vector fields over time. Similarly, we computed the correlations of the norms of all velocities in the two movies, for the whole movie, and also for specific times. The cut-off angle is defined as the θ 0 parameter of the curve of equation y = a exp(-θ/θ 0) fitted to the histogram.

### 2.7.2 Cross-correlation analysis of PIP$_2$ structures and F-actin

Cross-correlation analysis was performed as follows. Movies used to calculate the cross-correlation were acquired by alternating the acquisition order of the red and green channels to prevent introducing a bias through the order of image acquisition. The colocalization of the thresholded PIP$_2$ cortical structures and F-actin network for a variety of time shifts was computed considering a time shift Δt (positive or negative), the colocalization of the segmented PIP$_2$ image at time t, and the segmented F-actin image at time t-Δt using the following formula:

Colocalization = (PIP$_2$(t) ∩ F-actin(t-Δt)/ PIP$_2$ (t)

Colocalization was computed in this manner from Δt = -(T-1) to Δt = (T-1), where T is the total duration of the movie. The Δt for which colocalization is maximal represents the time shift between PIP$_2$ and F-actin. The mean time shift and its error were computed as follows: we fitted a parabola of equation y = a + (t-t0)^2 + b to the local correlation as a function of the time shift. We calculated the best a, b and t0 parameters using a least-squares method, and input the standard deviations of the correlations to create a weight matrix used during the adjustment. The results were the mean time shift t0 = 9.3s and the standard deviation sigma_t0 = 1.5s.

## 2.8 Tracking

### 2.8.1 Tracking of PIP$_2$ cortical structures

To track PIP$_2$ structures (Figure 24E and Figure 26D, E), embryos expressing mNG::PH$^{PLC1\delta1}$ were imaged with an exposure time of 50 ms, a laser power of 60% and a 70 ms frame rate. PIP$_2$ structures were tracked manually on maximum intensity z-projection of the images containing the moving PIP$_2$ structures of interest. The length of the

track was obtained by reslicing it using the Fiji plugin "Reslice". The velocity was calculated from the corresponding number of time points and track length.

### 2.8.2   Tracking of spindle pole positioning

Spindle positioning tracks were generated by manually tracking spindle poles from NEBD to cleavage furrow formation using a MATLAB script that also computed the distance from the first to the last tracked point, providing the corresponding x- and y-coordinates and the maximum velocity in µm/sec. Tracks were automatically placed into ellipses fitted around the embryo. The end positions of the spindle poles were determined at cytokinesis onset.

## 2.9   Drug addition

The eggshell was permeabilized by performing *perm-1*(*RNAi*) as described above. Gravid hermaphrodites were dissected in a cell culture dish with a glass bottom, and the resulting embryos imaged with an inverted confocal spinning disk microscope (see above). Drugs were added under the microscope while imaging to precisely control the timing of drug addition. The following drugs and concentrations in solution were utilized: 30 µM Ionomycin (Calbiochem, 407950), 3-5 mM $CaCl_2$ (Sigma-Aldrich, C5080), 20 µM Cytochalasin D (AppliChem, 22144-77-0), 12.5 µM Latrunculin A (Sigma-Aldrich, 76343-93-6), 1 mM CK666 (Sigma-Aldrich, SML0006), 1 mM CK869 (Sigma-Aldrich, C9124). For control movies, DMSO at a concentration equivalent to the final DMSO concentration in the drug solutions was added to the buffer prior to dissection. For the drug delivery experiments shown in Figure 37, gravid hermaphrodites were dissected in either 250 nM or 500 nM Cytochalasin D (AppliChem, 22144-77-0) or 2.5 µM Jasplakinolides (AdipoGen, AG-CN2-0037). Embryos were then imaged acquiring 17 z-planes 0.5 µm apart starting every 30 seconds. For the experiments reported in Figure 33 and Figure 36, whenever embryos were dissected in the drug-containing solution, we ensured that the action of the drug (as monitored by $t_{1/2}$) took place > 6 min after polarity was established.

Successful drug action was determined for each embryo by the disappearance of the $PH^{PLC1\delta1}$ fluorescence signal from the plasma membrane (Ionomycin/$Ca^{2+}$, Latrunculin A) and of Lifeact::mKate-2 from the cell cortex (Cytochalasin D, Latrunculin A). The time between drug addition and drug action was variable, probably due to variations in eggshell permeability upon *perm-1*(*RNAi*). As a comparable reference time between embryos, we therefore determined the time $t_{1/2}$ (t inflection) when half of fluorescence at

the plasma membrane has disappeared, as follows. The total cortical region of the embryo was segmented by applying a binary automated histogram-based threshold; fluorescent values at a distance of 20 pixels from the edge were measured, and their mean fluorescence values plotted over time. The inflection point of a fitted sigmoid function was then determined as $t_{1/2}$.

After addition of Ionomycin/Ca$^{2+}$ to embryos expressing mCherry::PH$^{PLC1\delta1}$ /GFP::RHO-1 or mCherry::PH$^{PLC1\delta1}$ /GFP::CDC-42, the disappearance of the mCherry::PH$^{PLC1\delta1}$ signal from the plasma membrane was imaged over time, whereas GFP::RHO-1 and GFP::CDC-42 were not imaged continuously to prevent photobleaching. Instead, only one end point image was taken by acquiring 9 z-planes that were 0.5 µm apart.

## 2.10 Statistical analysis

The software packages JMP 13.2.0 (SAS Institute GmbH) and MATLAB 2016 were used to perform statistical analysis. Normal distribution of the data was tested using the Shapiro-Wilk test. Unless stated otherwise, statistical analysis was performed using non-parametric tests assuming non-normal distribution using the Wilcoxon Rank Sum test/Mann-Whitney test for two-group comparisons, and the Kruskal-Wallis test with a pairwise Wilcoxon Rank Sum test as a post-hoc test for three-group comparisons. In Figure 24B, unpaired t-test has been utilized to test the probability that two independent velocity fields result in the observed angle distribution. Values of $p \leq 0.05$ were considered statistically significant.

## 2.11 Immunofluorescence staining

Immunofluorescence staining was performed in solution as described (Aroian et al., 1997). First, worms were bleached for 5 min in bleaching solution (0.7 M NaOH, 28% Sodiumhypochlorite), then fixed in 3.8% Paraformaldehyde in cytoskeleton buffer (10 mM MES, pH=6.1, 138 mM KCl, 3 mM MgCl$_2$, 2 mM EGTA) and 8% Sucrose for 10 min at room temperature, and then in 100% Methanol for 5 min at -20°C. Embryos were permeabilized in 0.5% Triton X-100, or 0.5% Tween-20, or 0.5% Igepal in PBS for 12 min at room temperature. Primary antibodies were incubated over night at 4°C in washing solution (0.1% Triton X-100, or 0.05% Tween-20 in PBS). Primary antibodies used were goat polyclonal anti-Actin (I-19) (1:100, Santa Cruz) and rabbit anti-GFP (1:1000, kind gift from Viesturs Simanis). Secondary antibodies were added thereafter for 1 h at room temperature. Secondary antibodies used were donkey anti-rabbit-Alexa 488 (1:1000 Molecular

Probes (Invitrogen)) and donkey anti-goat-Alexa 568 (1:500 Molecular Probes (Invitrogen)). DNA was stained with 1 mg/ml Hoechst 33258 (Sigma) for 5 min at room temperature. Confocal images were acquired with a 63x objective lens (NA 1.40, Plan-Apochromat) using a Zeiss ALSM 700 microscope equipped with an Axiocam MRm (B/W) camera.

# 3. Results

## 3.1 Formation and movement of PI(4,5)P$_2$ cortical structures

### 3.1.1 The PIP$_2$ biomarker GFP::PH$^{PLC1\delta1}$ is present in dynamic polarized cortical structures in one-cell *C. elegans* embryos

While monitoring the distribution of components involved in asymmetric division of the *C. elegans* zygote with confocal spinning disk microscopy, we discovered that the PIP$_2$ biomarker GFP::PH$^{PLC1\delta1}$ (Audhya et al., 2005) forms distinct and dynamic structures at the cell cortex (Figure 10). The pleckstrin homology (PH) domain of mammalian phospholipase C1δ1 (PLC1 δ1) binds to PIP$_2$ *in vitro* and in cells with high specificity and affinity (Garcia et al., 1995; Lemmon et al., 1995; Várnai and Balla, 1998). Moreover, in vertebrate cells, the lateral diffusion of GFP::PH$^{PLC1\delta1}$ resembles that of PIP$_2$ (Golebiewska et al., 2008; Hammond et al., 2009), and membrane domains formed by fluorescently labeled PIP$_2$ overlap with those monitored by GFP::PH$^{PLC1\delta1}$ (reviewed in Chierico et al., 2015). Hence, GFP::PH$^{PLC1\delta1}$ is well suited to monitor PIP$_2$ dynamics in live cells.

Initially, when the cortical actomyosin network is contractile throughout the early *C. elegans* embryo, PIP$_2$ is present weakly and evenly on the cell cortex (data not shown). Thereafter, when the actomyosin network begins to move towards the anterior at the onset of polarity establishment, striking elongated cortical structures enriched in PIP$_2$ become apparent, primarily on the anterior side of the embryo (Figure 10 A, B, K; Figure 11 A, top; Movie 1[3]). Such PIP$_2$ cortical structures have an initial average area of ~2.5 μm$^2$ and elongate as the zygote progresses through the cell cycle (Figure 10 L, M). All elongated PIP$_2$ cortical structures move anteriorly during polarity establishment, becoming distributed in a clearly polarized manner at pseudocleavage, when they cover ~15% of the anterior cortical surface (Figure 10 C, D, arrow, K). During the centration/rotation stage that follows, PIP$_2$ cortical structures decrease in size (Figure 10 E, F, arrowhead), before disappearing almost completely, with some remaining small foci by the time of nuclear envelope breakdown (NEBD) (Figure 10 G, H, arrowheads). A few elongated cortical structures reappear during cytokinesis, primarily in the anterior (Figure 10 I, J).

---

[3] All movies can be found at the following link:
https://www.youtube.com/channel/UC8DaMJafa_Ase107jkeGbRg/videos
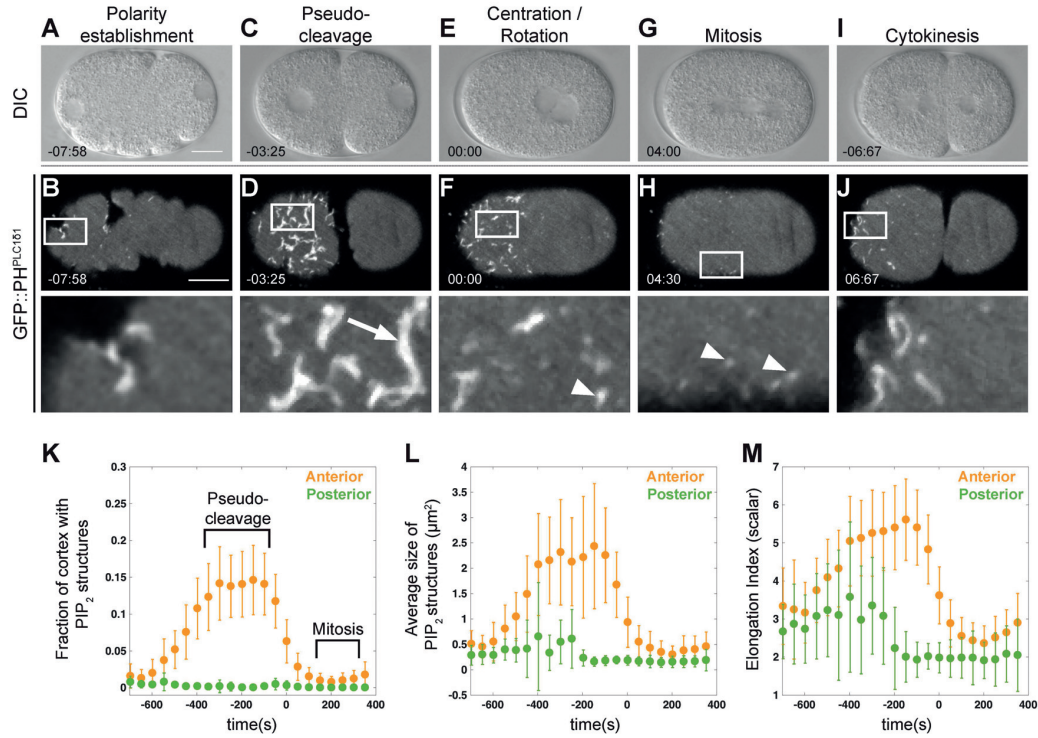
**Figure 10: The PIP₂ biomarker GFP::PH$^{PLC1\delta1}$ is enriched in dynamic cortical structures. (A-J)** Differential interference contrast (DIC) (A, C, E, G, I, middle plane) and spinning disk confocal imaging (B, D, F, H, J, cortical plane) of a different embryo at the corresponding stages, with boxed regions magnified below) of one-cell *C. elegans* embryos at indicated stages expressing GFP::PH$^{PLC1\delta1}$. See also Movie 1. Here and in subsequent figures, time is indicated in minutes:seconds, with 00:00 corresponding to the time of centration/rotation (t$_0$ in K-M). Here and in subsequent figures, the embryo anterior is to the left and the scale bar is 10 μm, unless indicated otherwise. **(K-M)** Fraction of cell cortex covered (K), average size (L) and Elongation Index (M, larger values correspond to more elongated shapes) of segmented PIP₂ cortical structures over time. The timing of pseudocleavage and mitosis are indicated. Here and in subsequent figures: quantification for anterior (orange) and posterior (green) embryo side is shown, with the mean and the standard deviation. N=39 embryos. See Materials and Methods for detailed description of how such graphs were generated.

In contrast to the structures visible when imaging the cortical plane, discrete PIP₂ entities are barely detectable as slight thickenings of the plasma membrane in the embryo middle plane (Figure 11, arrowhead), likely explaining why they were not noted previously (Audhya et al., 2005; Blanchoud et al., 2010; Panbianco et al., 2008). PIP₂ cortical structures tend to be drawn into plasma membrane invagination caused by cortical actomyosin contractions (Figure 11 arrow). To summarize, PIP₂ monitored with GFP::PH$^{PLC1\delta1}$ forms dynamic elongated cortical structures clearly detectable at the cortical plane but not the middle plane.
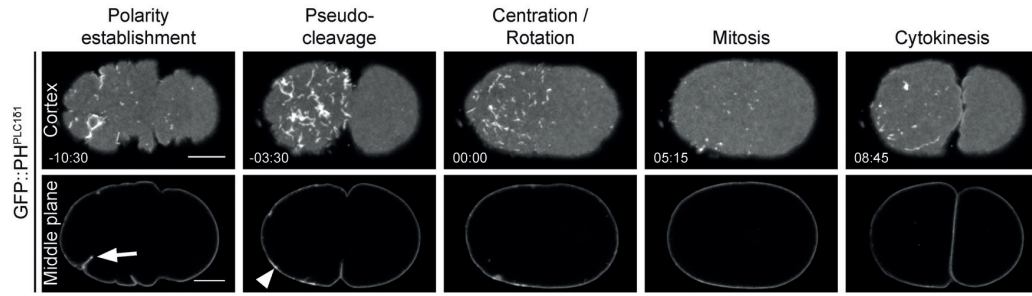
**Figure 11: PIP₂ cortical structures are barely detectable in the middle plane.** Images acquired at the indicated stages by spinning disk confocal imaging of embryos expressing GFP::PH$^{PLC1\delta1}$ (top: cortical plane, bottom: middle plane). Arrow: plasma membrane invagination caused by cortical actomyosin contractions, into which PIP₂ cortical structures are drawn. Arrowhead: cross-section of PIP₂ cortical structure seen as thickening of the plasma membrane in the middle plane.
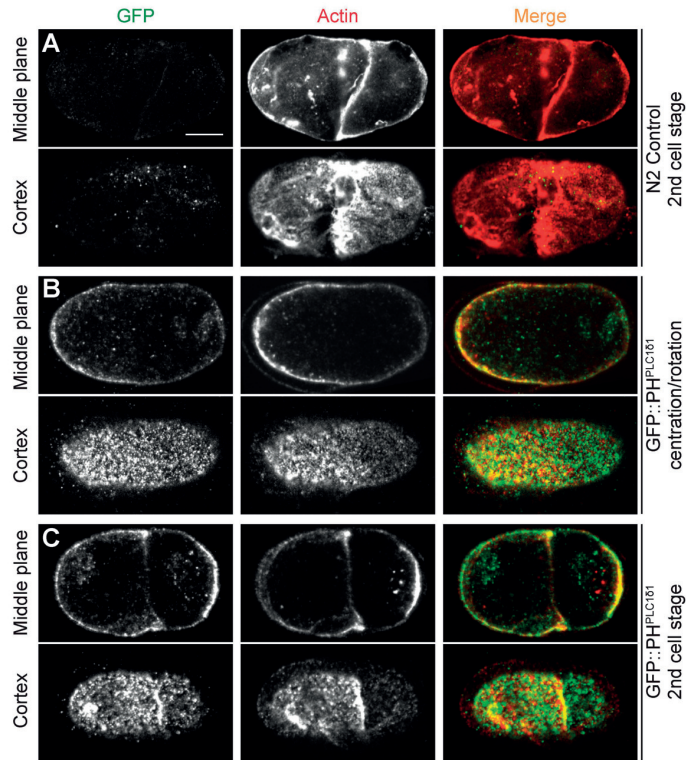


**Figure 12: PIP₂ cortical structures are not preserved by immunofluorescence staining. (A-C)** N2 control (A) and GFP::PH$^{PLC1\delta1}$ expressing embryos at centration/rotation (N=5) (B) or 2$^{nd}$ cell stage (N=4) (C) fixed and stained with GFP and Actin primary antibodies in solution. Middle and cortical planes are shown as indicated. Note: due to timing reasons when fixing in solution, one-cell stage embryos are difficult to obtain. As PIP₂ cortical structures reappear during the 2$^{nd}$ cell stage, embryos during the 2$^{nd}$ cell stage were also imaged. Note also clear overlap of PIP₂ and F-actin observed at the cortex of the middle plane (B and C, embryo periphery).

To verify that $PIP_2$ cortical structures monitored with GFP::PH$^{PLC1\delta1}$ represent cortical structures formed by endogenous $PIP_2$ in the plasma membrane, we set out to perform immunofluorescence staining (Figure 12). To set up the method with an appropriate control, we used GFP antibodies to stain $PIP_2$ cortical structures marked by GFP::PH$^{PLC1\delta1}$. First, we fixed and stained embryos according to standard procedures (Gönczy et al., 1999), but could not preserve any cortical structures (data not shown). As an alternative, we next utilized a method for fixing and staining embryos in solution, which is reported to preserve well the actin cortex (Aroian et al., 1997). Moreover, we sought to adjust the method by trying different detergents in different concentrations for permeabilization and washes. All in all, we successfully obtained cortical staining of F-actin comparable to that reported previously (Aroian et al., 1997) (Figure 12 B, C). However, we could not preserve the subcortical structures of GFP::PH$^{PLC1\delta1}$ that were observed by live imaging (Figure 12 B, C). This might be due to the fact that the permeabilization methods using organic solvents or detergents that remove lipids from the plasma membrane (Hobro and Smith, 2017; Jamur and Oliver, 2010) likely destroyed the subcortical distribution of $PIP_2$. Overall, we conclude that immunofluorescence staining is not suitable to detect endogenous $PIP_2$ cortical structures.

We set out to verify the cortical distribution revealed by GFP::PH$^{PLC1\delta1}$ using fluorescently labeled $PIP_2$. To this end, we first injected fluorescently Bodipy-FL-PIP$_2$ into the syncytial gonad of adult worms (Figure 13 A, B). The lipids got incorporated into oocytes and their future embryos, but there they did not reach the plasma membrane, since we could not detect any overlap with membrane mCherry::PH$^{PLC1\delta1}$ signal (Figure 13 B). In contrast, injected $PIP_2$ lipids were located in lipid droplets in the cytosol, perhaps corresponding to yolk-containing lipid storages (Figure 13 A, B) (Schmökel et al., 2016).
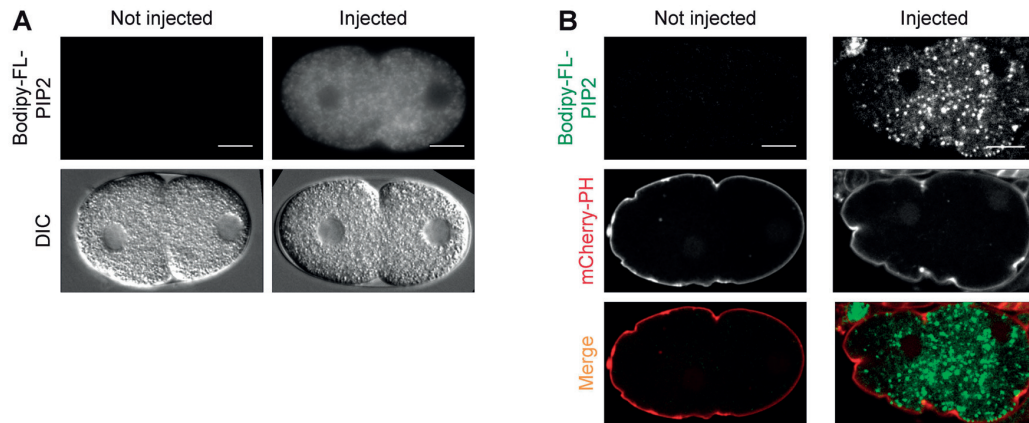
**Figure 13: Bodipy-FL-PIP₂ does not get incorporated into the plasma membrane after injection into the syncytial gonad. (A)** Widefield fluorescent images of the middle plane of embryos dissected from N2 wild type *C. elegans* worms injected with Bodipy-FL-PIP₂. Note that fluorescently labeled synthetic PIP2 injected in the syncytial gonad accumulates in the cytosol (N=3). **(B)** Confocal images of the middle plane of embryos expressing mCherry::PHPLC1δ1 dissected from *C. elegans* worms injected with Bodipy-FL-PIP2. Note fluorescently labeled synthetic PIP2 injected in the syncytial gonad accumulating in yolk granules (N=2). Note: As no Bodipy-FL-PIP₂ signal could be detected at the cell cortex, not the cortical plane, but the middle plane is shown to demonstrate the accumulation of Bodipy-FL-PIP₂ in the cytosol or yolk granules.

We thus set out to use another approach to deliver Bodipy-FL-PIP₂ into the plasma membrane, using one-cell stage embryos whose eggshell had been permeabilized using *perm-1*(*RNAi*) (Carvalho et al., 2011) (Figure 14 A-C). Importantly, we found that Bodipy-FL-PIP₂ delivered to otherwise wild type embryos distributes in dynamic polarized cortical structures akin to those observed with mCherry::PH$^{PLC1δ1}$ (Figure 14 A, B; Movie 2). Moreover, delivering Bodipy-FL-PIP₂ to embryos expressing mCherry::PH$^{PLC1δ1}$ established that the two components overlap (Figure 14 C). Overall, we conclude that GFP::PH$^{PLC1δ1}$ is a faithful marker of PIP₂ in one-cell *C. elegans* embryos, where it is present in dynamic and polarized structures at the plasma membrane.
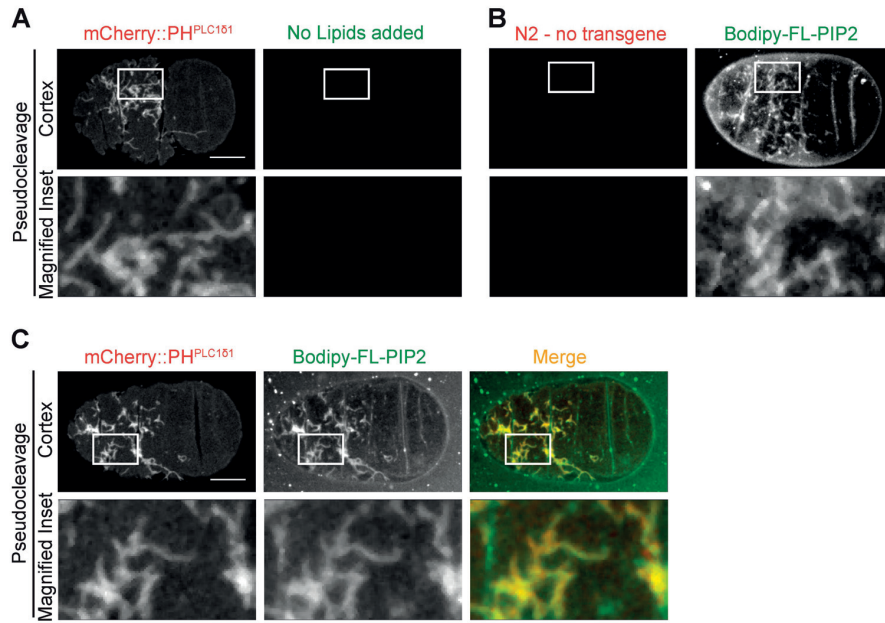
**Figure 14**: **Fluorescently-labeled PIP₂ distributes like mCherry::PH^PLC1δ1.** *perm-1*(*RNAi*) embryos with permeabilized eggshell (cortical plane). Note that the shape and distribution of PIP₂ cortical structures in *perm-1*(*RNAi*) embryos differs slightly from that of non permeabilized embryos likely due to the pressure applied by the coverslip on these fragile embryos. **(A)** mCherry::PH^PLC1δ1 expressing embryo without Bodipy-FL-PIP₂. **(B)** N2 wild type embryo with addition of Bodipy-FL-PIP₂ (N=9). See also Movie 2. **(C)** mCherry::PH^PLC1δ1 expressing embryo with addition of Bodipy-FL-PIP₂ (N=10). Boxed regions are magnified.

### 3.1.2 PIP₂ cortical structures might be sites of increased PIP₂ generation

We next asked how PIP₂ cortical structures might assemble. PIP₂ cortical structures could either form due to redistribution of existing PIP₂ or because of *de novo* synthesis through a PIP5K1. We thus tested if PIP₂ cortical structures could be sites of increased PIP₂ generation. The sole Type I PI(4)P5-kinase (PIP5K1) in *C. elegans* is PPK-1 (see 1.3.2, page 23) (Weinkove et al., 2008) , which was reported to be enriched at the posterior of one-cell stage embryos based on immunostaining with a PPK-1 antibody (Panbianco et al., 2008). Nevertheless, early in the cell cycle, a transient enrichment of PPK-1 on the anterior is also observed in the published work (Panbianco et al., 2008). Moreover, no cortical imaging of PPK-1 distribution has been performed previously. As we could not preserve cortical structures by immunostaining, we sought to tag PPK-1 with GFP. For this purpose, we generated a monomeric GFP construct (mGFP), introducing an A206K mutation into a GFP construct that is codon adapted for *C. elegans* and contains synthetic introns (Dickinson et al., 2013; von Stetten et al., 2012; Zacharias et al., 2002) (see

Figure 60, page 153). This construct was utilized by Sunybiotech[4] to generate a knock-in strain using CRISPR/Cas-9, in which PPK-1 is endogenously tagged with mGFP. Cortical imaging of embryos expressing endogenously tagged PPK-1 revealed that PPK-1::mGFP forms cortical structures (Figure 15 A, B). On the anterior, PPK-1::mGFP cortical structures overlap with PIP$_2$ cortical structures monitored by mCherry::PH$^{PLC1\delta1}$ during pseudocleavage and mitosis (Figure 15 A, B; Movie 3). In addition, PPK-1::mGFP is present in a distinct cortical meshwork on the posterior, where no PIP$_2$ enrichment is encountered (Figure 15 A, B). If discrete anterior PPK-1::GFP cortical structures are not taken into account, PPK-1 is enriched on the posterior during pseudocleavage and mitosis in N=10/12 embryos. This finding most likely corresponds to the results of Panbianco *et al.*, who reported by imaging the middle plane of fixed embryos that PPK-1 is enriched on the posterior (Panbianco et al., 2008). During mitosis, posterior PPK-1 enrichment is essential for proper spindle positioning (Panbianco et al., 2008), but the function of posterior PPK-1 enrichment during pseudocleavage is unclear. To summarize, these results suggest that *de novo* PIP$_2$ generation by PPK-1 could contribute to the assembly of anteriorly localized PIP$_2$ cortical structures. Nevertheless, we cannot exclude that redistribution of PIP$_2$, or means of PIP$_2$ generation other than through PPK-1, also could play a role in the assembly of PIP$_2$ cortical structures as well.

---

[4] www.SunyBiotech.com
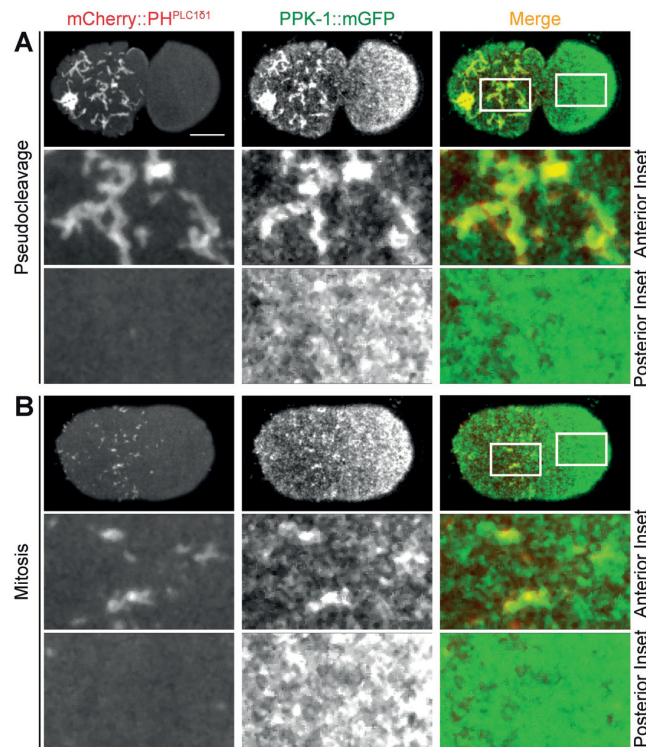
**Figure 15: PPK-1 is enriched at PIP₂ cortical structures. (A, B)** Images acquired by dual color cortical confocal live imaging of *C. elegans* embryos expressing mCherry::PH^PLC1δ1 and PPK-1::mGFP at indicated stages (N=10). Boxed regions of the anterior and posterior regions are magnified below. See also Movie 3.

### 3.1.3 PIP₂ cortical structures do not reside within domains marked by the *bona-fide* raft protein CAV-1::GFP.

We tested if PIP₂ cortical structures might reside within lipid rafts, which are microdomains in the plasma membrane that are enriched in cholesterol and sphingolipids (reviewed in Hooper, 1999; Lajoie and Nabi, 2010). Lipid rafts in *C. elegans* have been detected in the sperm and nervous system (Dou et al., 2012; Sedensky et al., 2004). Nevertheless, sterols are not uniformly distributed in the nematode and generally 20 times les abundant than in mammalian cells. This amount is unlikely to be sufficient to play a structural role in the membrane, and sterols are therefore thought to be only essential as hormone precursors in *C. elegans.* It was therefore hypothesized that rafts may form in the absence of cholesterol with caveolin-1 as a *bona fide* raft protein (Merris et al., 2003; Kurzchalia et al., 1999; reviewed in Entchev and Kurzchalia, 2005; Kurzchalia and Ward, 2003). CAV-1::GFP behaves highly dynamically during oocyte formation, ovulation, fertilization and the first cell cycle of the early embryo. In the one-cell stage embryo, CAV-1::GFP is internalized and degraded after fertilization (Sato et al., 2006). Live imaging of one-cell stage embryos expressing CAV-1::GFP and mCherry::PH^PLC1δ1 during

polarity establishment and pseudocleavage revealed diminishing foci of CAV-1::GFP at the cell cortex that do not overlap with cortical structures of $PIP_2$ (Figure 16). From this result, we conclude that $PIP_2$ cortical structures do not colocalize with putative CAV-1 enriched rafts.
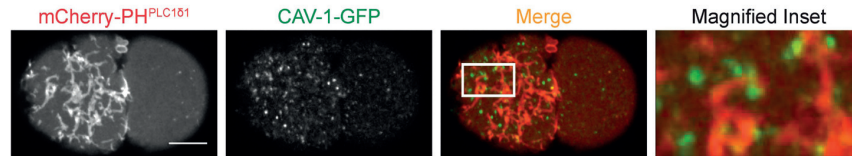


**Figure 16: PIP₂ cortical structures and CAV-1 containing rafts do not overlap.** Images acquired by dual color confocal live imaging of *C. elegans* embryos expressing mCherry::PH$^{PLC1\delta1}$ and CAV-1::GFP (confocal, cortical plane); boxed region is magnified on the right. All images are at the pseudocleavage stage (N=8).

### 3.1.4 AP polarity cues regulate the polarized distribution of PIP₂ cortical structures

We set out to address what regulates the polarized distribution of $PIP_2$ cortical structures, which is particularly apparent during pseudocleavage. We found that $PIP_2$ cortical structures do not overlap with GFP::PAR-2, which marks the posterior cortical domain (Figure 17 A), but do so with GFP::PAR-6, which marks the anterior polarity domain (Figure 17 B; Movie 4). Moreover, we observed that $PIP_2$ cortical structures overlap with elongated GFP::PAR-6 cortical structures (Figure 17 B, arrow), but not with GFP::PAR-6 foci (Figure 17 B, arrowhead), which are two distinct cortical populations of GFP::PAR-6 (see 1.2.7, page 20) (Beers and Kemphues, 2006; Robin et al., 2014; Rodriguez et al., 2017; Wang et al., 2017).
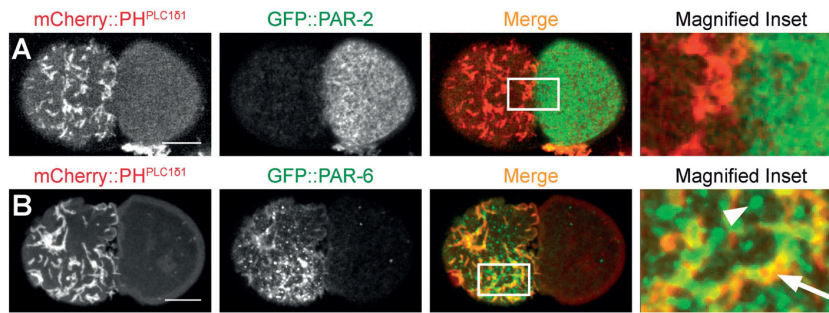
**Figure 17: PIP$_2$ cortical structures partially overlap with PAR-6 but not with PAR-2 cortical structures. (A, B)** Dual color spinning disk confocal cortical imaging of pseudocleavage embryos harboring the indicated pairs of fusion proteins, with high magnification views of the boxed insets. (A) mCherry::PH$^{PLC1\delta1}$/GFP::PAR-2, N=5. (B) mCherry::PH$^{PLC1\delta1}$/GFP::PAR-6, N=5. Note that elongated cortical structures (arrowhead) but not foci (arrow) of GFP::PAR-6 overlap with mCherry::PH$^{PLC1\delta1}$. See also Movie 4.

We next tested whether the polarized distribution of PIP$_2$ cortical structures depends on AP polarity cues. Compared to the control condition, we found that upon *par-3*(*RNAi*), PIP$_2$ cortical structures distribute more uniformly over the cell cortex (compare Figure 18 A, B with C, D), except for the very posterior of the embryo (Figure 18 C), consistent with the known slight posterior clearing of the actomyosin network upon PAR-3 inactivation (Kirby et al., 1990; Munro et al., 2004). Moreover, we found that upon *par-2*(*RNAi*), PIP$_2$ cortical structures first move anteriorly (Figure 18 E, F, Pseudocleavage), but then become distributed in a more uniform manner (Figure 18 E, F, Mitosis). This is in line with PAR-2 being dispensable for polarity establishment, but essential for polarity maintenance (Cuenca et al., 2003; Hao et al., 2006; Munro et al., 2004). The expansion of PIP$_2$ cortical structures towards the posterior in *par-3*(*RNAi*) and *par-2*(*RNAi*) embryos becomes more pronounced when PIP$_2$ cortical structures numbers decrease overall during the polarity maintenance phase and mitosis, making equalization more difficult to observe. We thus magnified the part of the graph corresponding to this stage of the cell cycle (Figure 18 B, D, F). Moreover, we tested the difference in distribution of PIP$_2$ cortical structures between the anterior and posterior during mitosis using the Wilcoxon Rank Sum test / Mann-Whitney test. This revealed a clear statistically significant difference in control embryos, but not in embryos depleted of PAR-2 or PAR-3. Overall these results show that PIP$_2$ cortical structures distribute asymmetrically depending on PAR polarity cues.
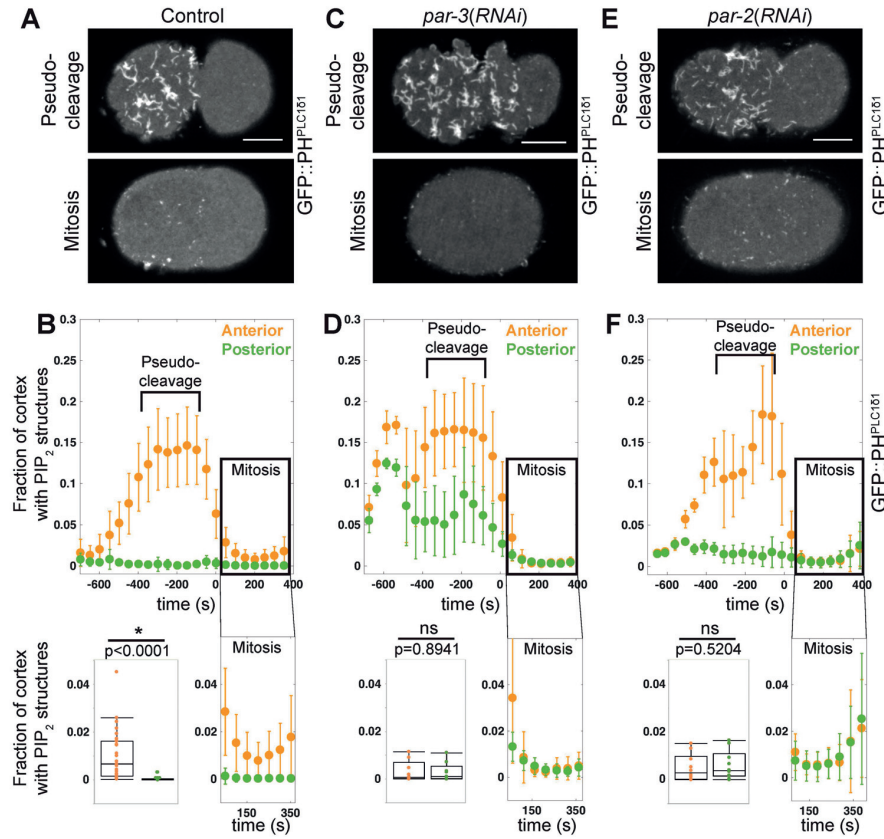
**Figure 18: PIP₂ cortical structures depend on AP polarity. (A, C, E)** Cortical plane at pseudocleavage and mitosis from spinning disk confocal imaging of control (C, N=39), *par-3*(*RNAi*) (E, N=10) or *par-2*(*RNAi*) (G, N=11) embryos expressing GFP::PH^PLC1δ1. **(B, D, F)** Fraction of cell cortex covered by segmented PIP₂ structures in the conditions corresponding to (C, E, G), with expanded view of the evolution during mitosis. The overall cortical area covered at the time point 250 seconds is shown in a boxplot and compared by statistical analysis (Wilcoxon Rank Sum test / Mann-Whitney test).

As stated above, the initial clearing of the posterior from PIP₂ cortical structures during the polarity establishment phase in *par-3*(*RNAi*) and *par-2*(*RNAi*) embryos is consistent with the known behavior of the actomyosin network upon PAR-2 and PAR-3 depletion. To test the hypothesis that PIP₂ cortical structures distribute like F-actin upon PAR-2 and PAR-3 depletion, we depleted PAR-2 or PAR-3 in embryos expressing mNG::PH^PLC1δ1 and Lifeact::mKate-2 (Figure 19 A-F; Movie 5). These experiments established that the boundary of the two domains along the AP axis is similar across the first cell cycle (Figure 19 A-I). This likely also explains why PIP₂ cortical structures do not occupy mutually exclusive territories in *par-3*(*RNAi*) and *par-2*(*RNAi*) embryos, as could be expected (see 1.2.4), since their distribution coincides with the essentially uniform presence of cortical F-actin. Together, these findings further establish that the asymmetric distribution of PIP₂ cortical structures is regulated by PAR-dependent AP polarity cues.
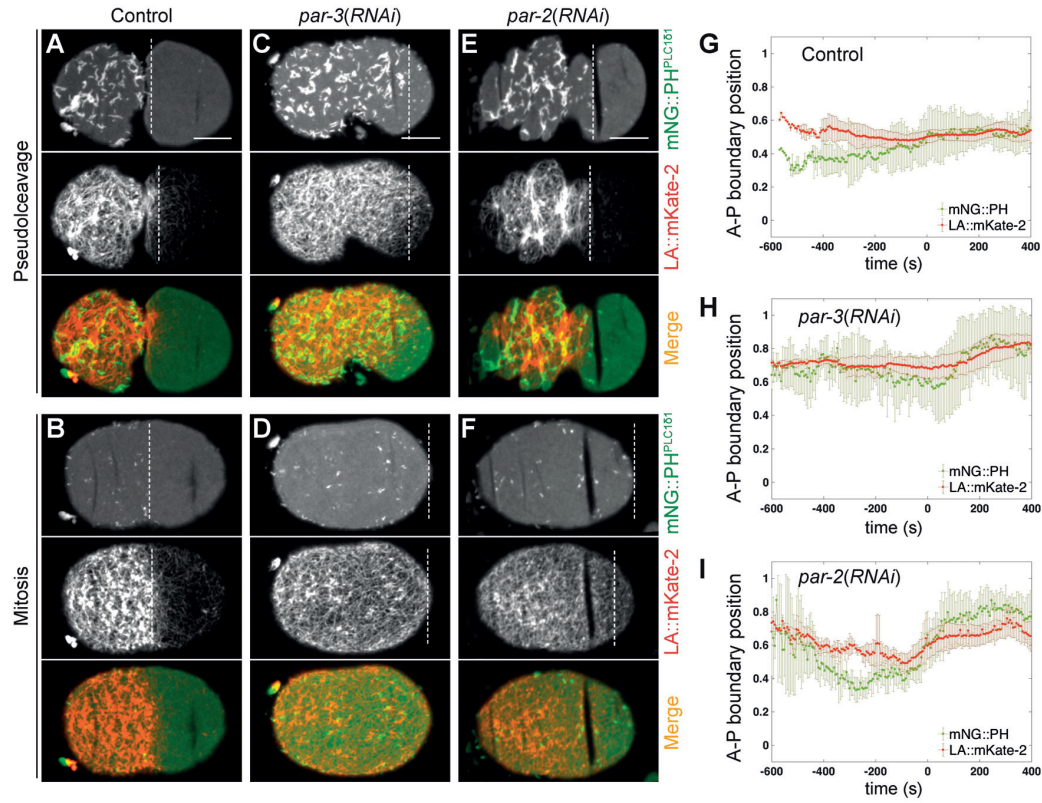
**Figure 19: The distribution of PIP₂ structures along the AP axis upon depletion of PAR-3 and PAR-2 resembles that of F-actin. (A-F)** Cortical images acquired at the indicated stages by spinning disk confocal imaging of embryos expressing mNG::PH$^{PLC1\delta1}$ and Lifeact::mKate-2. (C, D) Embryos upon *par-3*(*RNAi*) (N=7). See also Movie 5. (E, F) Embryos upon *par-2*(*RNAi*) (N=7). **(G-I)** Relative AP boundary position of PIP₂ cortical structures (green, mNG::PH$^{PLC1\delta1}$) and F-actin (red, Lifeact::mKate-2) in control contitions (G) and upon *par-3*(*RNAi*) (H) or *par-2*(*RNAi*) (I). Movies were aligned at t=0. Mean and standard deviation are shown in (A-C) and in similar panels of subsequent figures. Note: movies in the control condition start slightly later than those acquired upon PAR-3 and PAR-2 depletion; as a result, the beginning of the curves in control embryos are less precise.

## 3.1.5 PIP₂ cortical structures colocalize partially with actin and fully with ECT-2, RHO-1 and CDC-42

Since PIP₂ and F-actin are interdependent in many systems (see 1.3.3, page 25), we tested whether these two components overlap at the cell cortex of *C. elegans* embryos using two different markers for F-actin, Lifeact::mKate-2 and GFP::moe (Motegi et al., 2006; Reymann et al., 2016). Lifeact is a 17 amino acid long peptide from the F-actin binding protein Abp140 from *Saccharomyces cerevisiae*, whereas the GFP::moe marker utilizes the F-actin binding domain of moesin from *Drosophila* (Edwards et al., 1997; Riedl et al., 2008). Live imaging of embryos expressing mCherry::PH$^{PLC1\delta1}$ and GFP::moe revealed that PIP₂ cortical structures overlap with sites of dense F-actin (Figure 20 A). We also found a partial overlap of Lifeact::mKate-2 monitoring F-actin and PIP₂ cortical

structures marked by mNeonGreen::PH$^{PLC1\delta1}$ (mNG::PH$^{PLC1\delta1}$) (Figure 20 B; Movie 6). *Drosophila* moesin does not only bind F-actin with its tail domain, but also PIP$_2$ with its head domain (Ben-Aissa et al., 2012). However, GFP::moe contains only the F-actin binding domain of moesin (Edwards et al., 1997). We favored the utilization of Lifeact::mKate-2, because the fluorescence intensities of both Lifeact::mKate-2 and mNG::PH$^{PLC1\delta1}$ are substantially higher than those of GFP::moe and mCherry::PH$^{PLC1\delta1}$. Thus, we performed further experiments that require a PIP$_2$ and F-actin double staining using the Lifeact::mKate-2/mNG::PH$^{PLC1\delta1}$ line. By contrast to the partial overlap of PIP$_2$ cortical structures with F-actin, we detected no substantial overlap between mCherry::PH$^{PLC1\delta1}$ and GFP::NMY-2 (Figure 20 C; Movie 7), the non-muscle myosin that contracts the cortical actomyosin network (Guo and Kemphues, 1996; Hill and Strome, 1988; Hill and Strome, 1990; Munro et al., 2004; Severson and Bowerman, 2003; Shelton et al., 1999). Overall, we conclude that PIP$_2$ cortical structures overlap partially with the F-actin cytoskeleton but not with myosin foci.
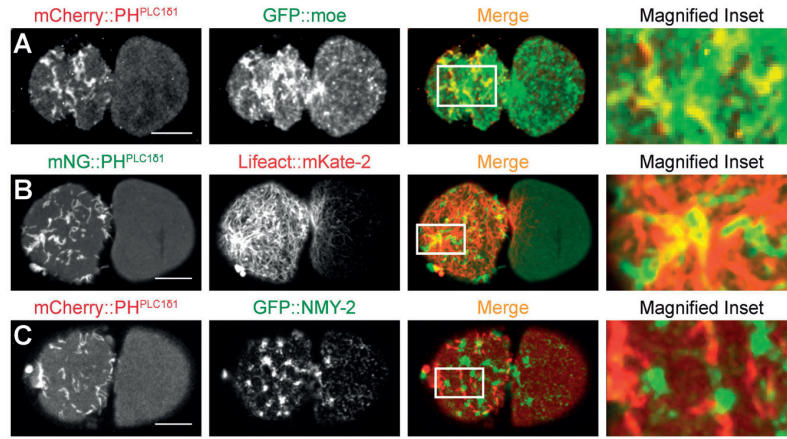


**Figure 20: PIP₂ cortical structures partially overlap with F-actin but not with NMY-2. (A-C)** Dual color spinning disk confocal cortical imaging of pseudocleavage embryos harboring the indicated pairs of fusion proteins, with high magnification views of the boxed regions. (A) mCherry::PH$^{PLC1\delta1}$/ GFP::moe, N=6 (B) mNeonGreen::PH$^{PLC1\delta1}$ /Lifeact::mKate-2, N=46. See also Movie 6. (C) mCherry::PH$^{PLC1\delta1}$/ GFP::NMY-2, N=9. See also Movie 7.

Rho GTPases are well known regulators of the actin cytoskeleton and can be activated or work in concert with PIP$_2$ to perform this function (see 1.3.3.2). Strikingly, we found that PIP$_2$ cortical structures marked by mCherry::PH$^{PLC1\delta1}$ fully colocalize with the RHO-1 GEF GFP::ECT-2, as well as with the Rho GTPases GFP::RHO-1 and GFP::CDC-42 (Figure 21 A-C; Movie 8).
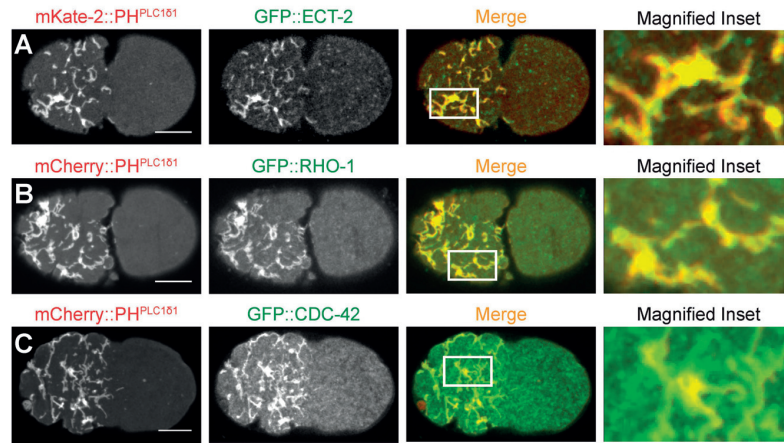
**Figure 21: PIP₂ cortical structures overlap with ECT-2, RHO-1 and CDC-42. (A-C)** Dual color spinning disk confocal cortical imaging of pseudocleavage embryos harboring the indicated pairs of fusion proteins, with high magnification views of the boxed regions. (A) mKate2-PH$^{PLC1\delta1}$/ GFP::ECT-2, N=13. (B) mCherry::PH$^{PLC1\delta1}$/ GFP::RHO-1, N=9. (C) mCherry::PH$^{PLC1\delta1}$/ GFP::CDC-42, N=7. See also Movie 8.

We next aimed to determine if the two Rho GTPases RHO-1 and CDC-42 overlapping with PIP₂ cortical structures are active. To detect active CDC-42, we imaged embryos expressing the *C. elegans* domain of the homologue of the Wiskott-Aldrich Syndrome protein WASP WSP-1 that specifically binds to GTP-bound, active, CDC-42 (Kumfer et al., 2010). Cortical dual color live imaging of GFP::WSP-1 and mCherry::PH$^{PLC1\delta1}$ indeed revealed that elongated structures of GFP::WSP-1 perfectly overlap with mCherry::PH$^{PLC1\delta1}$, indicating that CDC-42 residing at PIP₂ cortical structures is active (Figure 22 A arrow). In addition, we observed foci of active GFP::WSP-1 that do not overlap with PIP₂ cortical structures (Figure 22 arrowhead). Consistent with results reported by Kumfer *et al.*, we also observed a posterior enrichment of GFP::WSP-1 during pseudocleavage, and this pool of active CDC-42 re-localizes to the anterior thereafter (Figure 22 A, B; Movie 9). We also examined the distribution of a biosensor for active RhoA, GFP::AHPH, which contains the C-terminal portion of *C. elegans* anillin, a protein which binds to active RhoA during cytokinesis when it overlaps with NMY-2 (Piekny and Glotzer, 2008; Reymann et al., 2016; Tse et al., 2012). Consistent with the finding that PIP₂ cortical structures do not overlap with NMY-2 (Figure 20 C), live imaging of embryos expressing mCherry::PH$^{PLC1\delta1}$ and GFP::AHPH revealed that a large portion of active RHO-1 does not overlap with PIP₂ cortical structures (Figure 22 C, D, arrowhead; Movie 10). This indicates that the bulk of RHO-1 associated with PIP₂ cortical structures is inactive. Nevertheless, a temporary and partial overlap of active RHO-1 with PIP₂ cortical structures could be observed as well (Figure 22 C, arrow), raising the possibility that a small fraction of RHO-1 at PIP₂ cortical structures is active. Alternatively, given that

GFP::RHO-1 colocalizes perfectly with its activating GEF ECT-2, this particular RhoA biosensor might not detect all active RHO-1 species. Overall, we conclude that CDC-42 residing at PIP$_2$ cortical structures is active, while only a small pool of active RHO-1 temporarily resides at PIP$_2$ cortical structures.
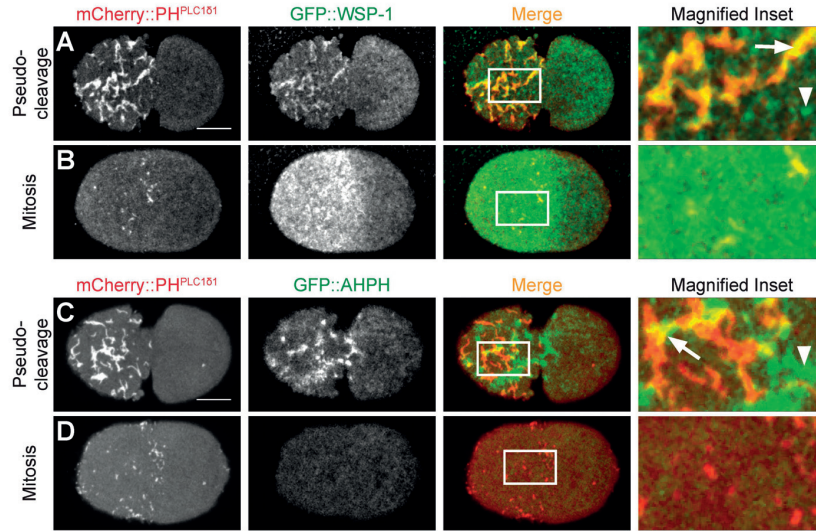


**Figure 22: CDC-42 at PIP$_2$ cortical structures is active and also a small pool of active RHO-1 resides there temporarily.**(A-D)Dual color spinning disk confocal cortical live imaging of embryos at indicated stages harboring the indicated pairs of fusion proteins, with high magnification views of the boxed regions on the right. **(A, B)** mCherry::PH$^{PLC1\delta1}$/ GFP::WSP-1 (active CDC-42 biosensor), N=6. Note elongated GFP::WSP-1 cortical structures that overlap with PIP$_2$ cortical structures (arrow), while foci of GFP::WSP-1 (arrowhead) do not. See also Movie 9. **(C, D)** mCherry::PH$^{PLC1\delta1}$/ GFP::AHPH (active RhoA biosensor), N=7. Note that the bulk of active RhoA (arrowhead) does not overlap with PIP$_2$ cortical structures, although a temporary and partial overlap could be detected (arrow). See also Movie 10.

We tested whether RHO-1 or CDC-42 are needed for PIP$_2$ cortical structures using partial RNAi-mediated depletion, since full depletion leads to sterility in both cases (Schonegg and Hyman, 2006). Upon *rho-1*(*RNAi*), we found that PIP$_2$ structures form normally but distribute symmetrically, in line with the requirement of RHO-1 for AP polarity establishment (Figure 23 A, C, J, K, M, N). Thereafter, PIP$_2$ cortical structures become polarized later than normally (Figure 23 B, D, G, H), most likely through the PAR-2-dependent and actomyosin network-independent polarity establishment pathway (Motegi et al., 2011; Zonies et al., 2010). PIP$_2$ cortical structures also form upon *cdc-42*(*RNAi*), with only minor and variable alterations in shape and size compared to the control (Figure 23 E, F, L, O). The PIP$_2$ structures first segregate towards the anterior in *cdc-42*(*RNAi*) embryos, but then move back towards the posterior (Figure 23 E, F, I), consistent with CDC-42 being required for polarity maintenance (Motegi and Sugimoto, 2006; Schonegg and Hyman, 2006). Overall, we conclude that RHO-1 and CDC-42 are dispensable for PIP$_2$ cortical structure formation and, importantly, that such structures

colocalize partially with F-actin, as well as completely with ECT-2, RHO-1 and active CDC-42.
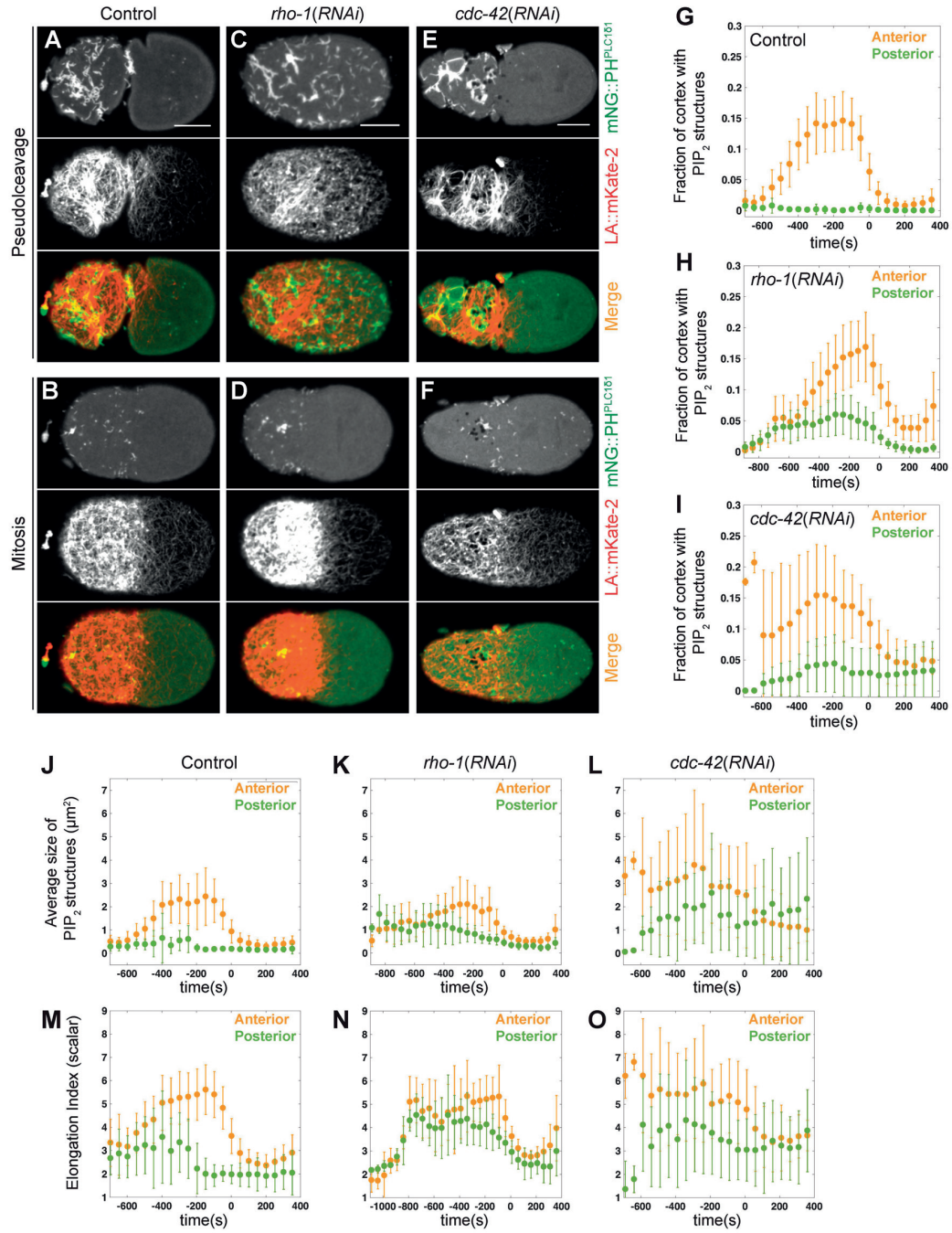
**Figure 23: The formation of PIP₂ cortical structures does not depend on RHO-1 or CDC-42. (A-F)** Cortical images acquired at the indicated stages by spinning disk confocal imaging of embryos expressing mNG::PH^PLC1δ1 and Lifeact::mKate-2. (C, D) Embryos upon *rho-1*(*RNAi*) (N=5). (E, F) Embryos upon *cdc-42*(*RNAi*) (N=8). **(G-I)** Fraction of cell cortex covered by segmented PIP₂ structures over time in control (G), *rho-1*(*RNAi*) (H), and *cdc-42*(*RNAi*) (I) embryos. **(J-L)** Average size of segmented PIP₂ cortical structures over time in control (J), *rho-1*(*RNAi*) (K), and *cdc-42*(RNAi) (L) embryos. **(M-O)** Elongation Index of segmented PIP₂ cortical structures over time in control (M), *rho-1*(*RNAi*) (N) and *cdc-42*(*RNAi*) (O) embryos; larger values correspond to more elongated structures.

### 3.1.6 PIP$_2$ cortical structures and the F-actin cytoskeleton move in concert

The computational part of the PIV and cross-correlation analysis in this section was performed by Kévin Barbieux, in collaboration with me.

Live imaging of control as well as of *par-3*(*RNAi*) and *par-2*(*RNAi*) embryos expressing Lifeact::mKate-2 and mNG::PH$^{PLC1\delta1}$ suggested that movements of PIP$_2$ cortical structures and the F-actin network are coupled (Figure 19). To investigate this potential coupling in a quantitative manner, we used particle image velocimetry (PIV) to simultaneously analyze cortical flows of Lifeact::mKate-2 and mNG::PH$^{PLC1\delta1}$ during polarity establishment until the end of pseudocleavage (Figure 24) (Thielicke and Stamhuis, 2014). PIV has proven to accurately capture the movement of cortical components during polarization in the one-cell stage *C. elegans* embryo in several cases (De Simone et al., 2016; Naganathan et al., 2014; Wang et al., 2017). Correlation of local flows within thresholded areas of Lifeact::mKate-2 and mNeonGreen::PH$^{PLC1\delta1}$ revealed that flow velocities at each time point correlate (Pearson coefficient $\rho = 0.65$) (Figure 24 B, C). Moreover, the direction of flow vectors at each time point is highly similar (Figure 24 D, E). Analogous findings were made when comparing mCherry::PH$^{PLC1\delta1}$ and GFP::CDC-42 (Figure 24 F). By contrast, no strong correlation was found between mCherry::PH$^{PLC1\delta1}$ and the caveolin CAV-1::GFP (Figure 24 F). Together, these results support our hypothesis that the cortical movements of PIP$_2$ cortical structures and the F-actin network are coupled.
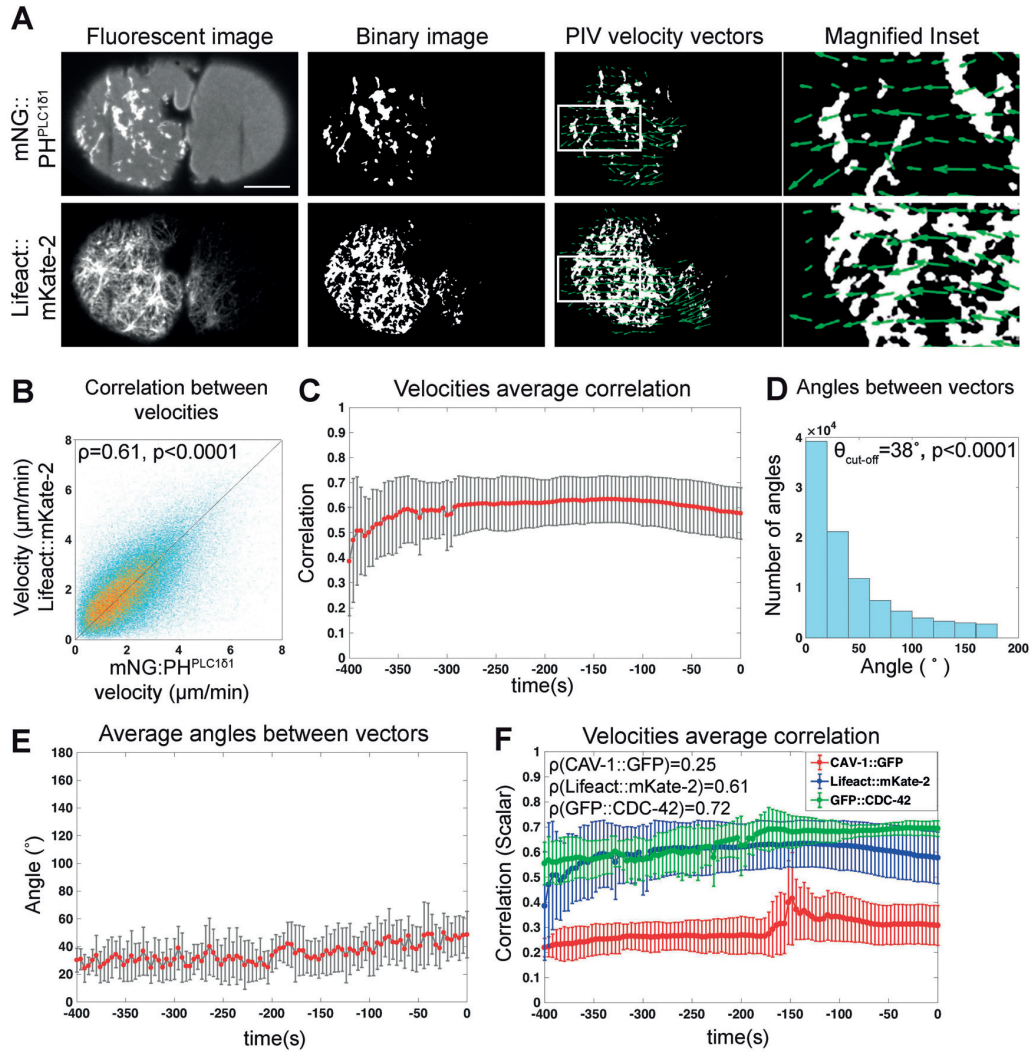
**Figure 24: Coupling between PIP₂ cortical structures and F-actin. (A)** Fluorescent images of spinning disk confocal cortical imaging of embryos expressing mNG::PH$^{PLC1δ1}$ and Lifeact::mKate-2 (first column), corresponding binary thresholded images (second column) and PIV velocity vectors (third column), with high magnification views of boxed regions (arrow direction and length represent flow direction and velocity, respectively). **(B)** Correlation between mNG::PH$^{PLC1δ1}$ and Lifeact::mKate-2 velocities in the same position and time, represented with a color scale dependent on their spatial density, from denser to sparser (red, yellow, light blue). Pearson correlation coefficient: ρ=0.61, p<10E−16 with Matlab precision, unpaired t-test. N=13 embryos for B-D. **(C)** Average correlation of flow velocities of mNG::PH$^{PLC1δ1}$ and Lifeact::mKate-2 in the same position as a function of time. Movies were aligned at t=0 throughout this figure. **(D)** Angle distribution between flow velocity vectors of mNG::PH$^{PLC1δ1}$ and Lifeact::mKate-2 in the same position and time. The angle distribution peaks at θ = 0° and decays exponentially thereafter (cutoff angle: θ=38°). Two independent velocity fields cannot result in the observed angle distribution (p<10E−16 with Matlab precision, X²-test). **(E)** Average correlation of velocity vector angles of mNG::PH$^{PLC1δ1}$ and Lifeact::mKate-2 in the same position as a function of time. Movies were aligned at t=0 throughout this figure. **(F)** Average correlation of velocities over time in the same position. Blue: Lifeact::mKate-2 with mNeonGreen::PH$^{PLC1δ1}$ (Pearson correlation coefficient: ρ=0.61); green: GFP::CDC-42 with mCherry::PH$^{PLC1δ1}$ (ρ=0.72), red: CAV-1::GFP with mCherry::PH$^{PLC1δ1}$ (ρ=0.25). Note that the correlation between GFP::CDC-42 and mCherry::PH$^{PLC1δ1}$ is not higher because there are very small differences in local movements between the two, even though they exhibit very large areas of overlap.

We next addressed whether the movements of PIP$_2$ cortical structures and of F-actin are synchronous or instead exhibit a time shift, which could suggest which component might lead the other. Close examination of embryos expressing Lifeact::mKate-2 and mNG::PH$^{PLC1\delta1}$ suggested that cortical PIP$_2$ structures are ahead of polymerizing F-actin (Figure 25 A; Movie 11). To address this possibility quantitatively, we cross-correlated time-shifted images of Lifeact::mKate-2 and mNG::PH$^{PLC1\delta1}$, and thus determined that maximal overlap between the two signals occurs when mNG::PH$^{PLC1\delta1}$ is ~9.3 +/-1.5 seconds ahead of Lifeact::mKate-2 (Figure 25 B). Overall, we conclude that PIP$_2$ cortical structures move together with, but slightly ahead of, polymerizing F-actin filaments.
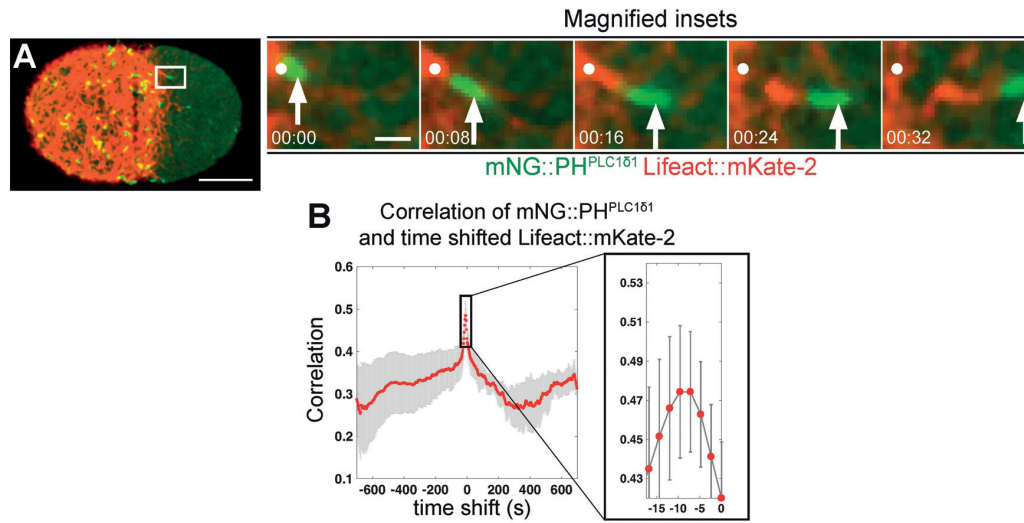


**Figure 25: PIP$_2$ cortical structures move slightly ahead of polymerizing F-actin. (A)** Embryo expressing mNG::PH$^{PLC1\delta1}$ and Lifeact::mKate-2; the boxed region is magnified on the right and shows snapshots from the corresponding movie, illustrating that a PIP$_2$ cortical structure (mNeonGreen::PH$^{PLC1\delta1}$, arrow) moves ahead of polymerizing F-actin (Lifeact::mKate-2). Dot marks the starting point of the PIP$_2$ structure. Note that the brightness adjustment of Lifeact::mKate-2 in this image has been increased to clearly show the polymerizing F-actin behind the PIP$_2$ structures. See also Movie 11. **(B)** Cross-correlation between thresholded binary movies of mNG::PH$^{PLC1\delta1}$ and Lifeact::mKate-2, shifting Lifeact::mKate-2 with different time intervals relative to mNG::PH$^{PLC1\delta1}$. The boxed region is magnified on the right, showing that maximal overlap is achieved with a time shift of -9.3 +/- 1.5 seconds (average and standard deviation), irrespective of the order in which the two signals are recorded (Materials and Methods).

## 3.1.7 Actin polymerization drives the movement and the formation of PIP$_2$ cortical structures

Because F-actin filaments are present behind moving PIP$_2$ cortical structures, we hypothesized that actin polymerization might push PIP$_2$ cortical structures. Compatible with this possibility, we found that the velocity of PIP$_2$ cortical structures is ~0.17 +/-0.03 µm/s (Figure 26 A, B), in the range of actin polymerization driven motility in other systems (Brangbour et al., 2011; Carlsson, 2003; reviewed in Cameron et al., 2000; Carlsson, 2010; Mogilner and Oster, 1996).
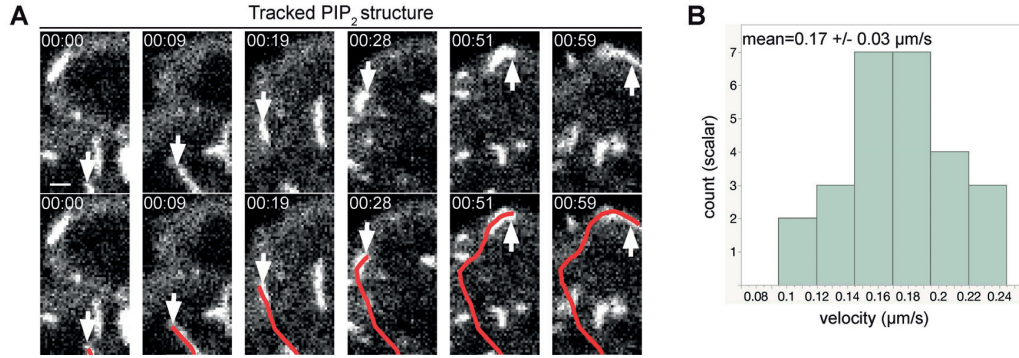
**Figure 26: Velocities of individual PIP₂ cortical structures. (A)** Snapshots of confocal spinning disk imaging of an embryo expressing mNG::PH^PLC1δ1 showing a tracked PIP₂ structure (arrow), with the corresponding track (red, bottom row). Scale bar: 1 μm. **(B)** Histogram of measured velocities of 26 different PIP₂ structures from 5 embryos.

To further test this hypothesis, we aimed to impair F-actin polymerization. We thus depleted different regulators of actin microfilament assembly in the *C. elegans* embryo by RNAi. First, we set out to deplete the arp-2/3 complex proteins ARX-1 and ARX-2. ARX-1 depletion was reported to totally disrupt the formation of the cortical F-actin network in the one-cell stage embryo, but without altering polarity establishment and maintenance (Velarde et al., 2007). Others have reported that depletion of ARX-1, ARX-2, or ARX-1/ARX-2 together does not affect actin microfilament assembly or AP polarity, although membrane blebs suggestive of compromised cortical stability have been observed (Severson et al., 2002). A different conclusion was reached by a study in which ARX-2 depletion was reported to disrupt proper F-actin foci formation and PAR protein distribution during the polarity maintenance phase (Shivas and Skop, 2012). In our experiments, we did not observe any disruption of the actin cortical network as monitored by Lifeact::mKate-2 upon ARX-1 or ARX-2 depletion (Figure 27). However, the localization of the actomyosin network along the AP axis of the embryo as well as the contractility of the embryo changed slightly and variably between embryos (Figure 27). PIP₂ structures were also altered slightly compared to the control condition, but in an extremely variable manner between embryos. Generally, PIP₂ cortical structures became less numerous and appeared larger and patchier (Figure 27 B). Thus, the arp-2/3 complex also plays some role in proper PIP₂ structure formation. Overall, since the F-actin cytoskeleton does not get disrupted in a striking and reproducible manner, the impact of actin polymerization in driving PIP₂ cortical structures cannot be assessed thoroughly using ARX-2 depletion. To achieve depletion of ARX-1 and ARX-2 by other means than RNAi, we added the arp2/3 inhibitors CK666 and CK869 to *perm-1*(*RNAi*) embryos (Hetrick et al., 2013). However even in very high concentrations, these inhibitors did not show any effect compared to control embryos (Materials and methods, data not shown). As we would have expected to find at least a phenotype similar to *arx-2*(*RNAi*),

we conclude that these drugs are most likely not effective in *C. elegans* embryos under these conditions.
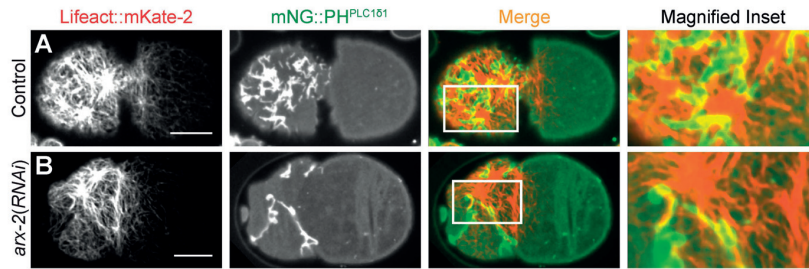


**Figure 27: ARX-2 is dispensable for actin microfilament formation, but slightly changes the F-actin localization along the AP axis and is involved in PIP$_2$ structures formation. (A, B)** Cortical images acquired during pseudocleavage by spinning disk confocal live imaging of embryos expressing mNG::PH$^{PLC1\delta1}$ and Lifeact::mKate-2 with high magnification views of the boxed regions on the right, (A) control and (B) *arx-2*(*RNAi*) embryos (N=12).

As depletion of *C. elegans* members of the arp2/3 complex did not lead to a clear disruption of the F-actin cytoskeleton, we set out to deplete further regulators of actin microfilament formation. Other known regulators of F-actin polymerization in the *C. elegans* one-cell stage embryo are the Formin Homology protein CYK-1 and the profilin PFN-1, which binds to and functions together with CYK-1 (Severson et al., 2002; Velarde et al., 2007). Using RNAi, we could not achieve sufficient depletion of CYK-1 (data not shown), as assessed by cytokinesis being successful in such embryos (Severson et al., 2002). Thus, we next set out to impair actin polymerization by partially depleting the profilin PFN-1 (Figure 28). A clear disruption of F-actin filaments monitored by Lifeact::mKate-2 was observed in *pfn-1*(*RNAi*) embryos (Figure 28 A, top; Movie 12). Importantly, in addition, we found that the overall velocity of PIP$_2$ cortical structures is reduced to ~0.06 +/-0.04 μm/s in *pfn-1*(*RNAi*) embryos (Figure 28 B). Moreover, whereas control embryos exhibit fast and directed movement (Figure 28 C), we noted that in half of the *pfn-1*(*RNAi*) embryos (N=4/8), which are the least affected as judged by cytokinesis still occurring, PIP$_2$ cortical structures move in a somewhat directed manner, albeit at lower velocities (Figure 28 E; Movie 13). In more strongly affected *pfn-1*(*RNAi*) embryos (N=4/8), in which cytokinesis does not occur, PIP$_2$ cortical structures move only very locally and in seemingly random directions with occasional jumps, instead of exhibiting longer range directional movements (Figure 28 D). Together, these findings indicate that PIP$_2$ cortical structure movements are driven by actin polymerization.
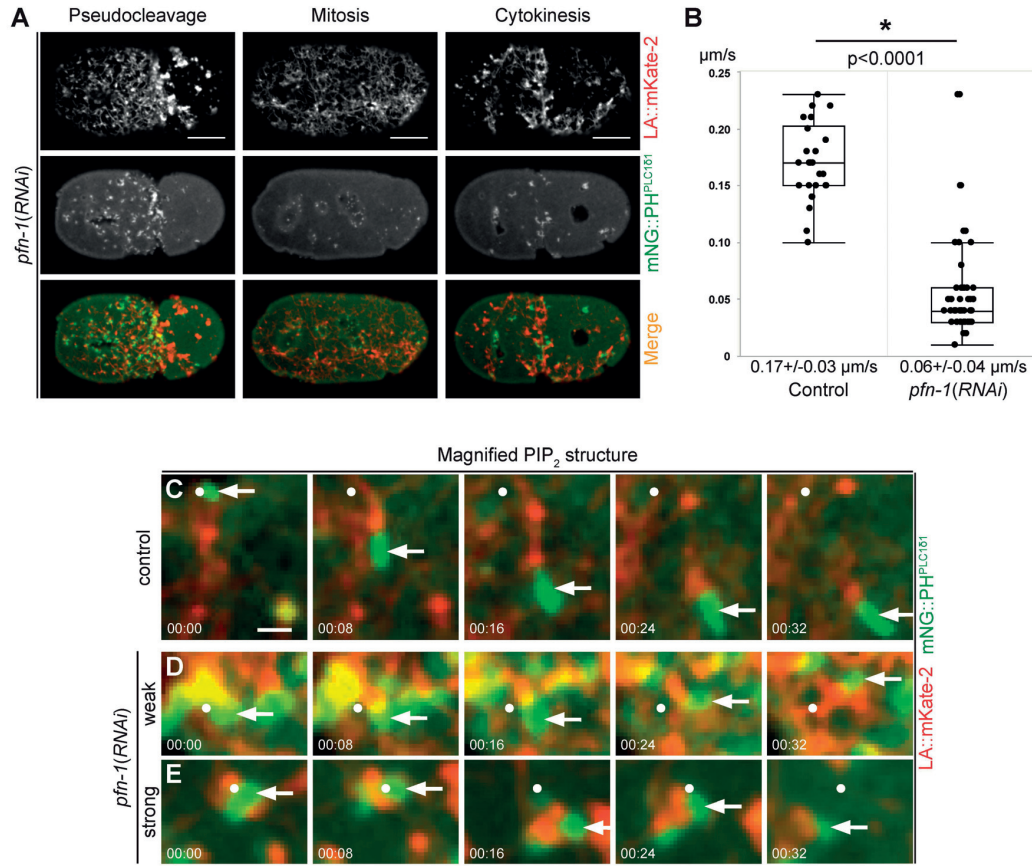
**Figure 28: Disruption of F-actin upon *pfn-1*(*RNAi*) impairs the movement of PIP₂ cortical structures. (A)** Cortical images acquired at the indicated stages by spinning disk confocal imaging of embryos expressing mNG::PH^PLC1δ1 and Lifeact::mKate-2 upon strong *pfn-1*(*RNAi*) (N=4). See also Movie 12. **(B)** Box plot showing the velocity of PIP₂ structures in control conditions (0.17 +/- 0.03 μm/s, Mean and STD, N=26) and upon *pfn-1*(*RNAi*) (0.06 +/- 0.04 μm/s, Mean and STD, N=40 tracks in 8 embryos, pooling strong and weak *pfn-1*(*RNAi*) conditions). p<0.0001 (Wilcoxon Rank Sum test/Mann-Whitney test). **(C-E)** Snapshots of confocal spinning disk imaging of embryos expressing mNG::PH^PLC1δ1 and Lifeact::mKate-2, showing a PIP₂ structure (arrow) next to an actin filament. Dot marks the starting point of the PIP₂ structure, and t=00:00 corresponds to the beginning of the movie sequence. (C) Control embryo -the PIP₂ cortical structure exhibits directional movement. See also Movie 11. (D) Weak *pfn-1*(*RNAi*) -PIP₂ cortical structures move directional, but very slowly (N=4); note the change in direction of the PIP₂ structure, for instance between 00:16 and 00:24, as well as the dense packing of PIP₂ containing entities. (E) Strong *pfn-1*(*RNAi*) -the PIP₂ cortical structure hardly moves, with only occasional jumps (for instance between 00:24 to 00:32) (N=4). See also Movie 13. Scale bar: 1 μm.

Given notably the tight coupling between cortical PIP₂ structures and F-actin, we investigated whether the actomyosin network not only regulates the movement, but also the formation of PIP₂ structures. We found that in *nmy-2*(*RNAi*) embryos, in which actomyosin network contractility is abolished (Munro et al., 2004), PIP₂ cortical structures are present (Figure 29 C, D), although they are more elongated than usual (Figure 29 E, F). Moreover, PIP₂ cortical structures distribute symmetrically in *nmy-2*(*RNAi*) embryos (Figure 29 C, D), as expected from the known requirement of NMY-2 in AP polarity

(Guo and Kemphues, 1996). Therefore, formation of PIP$_2$ cortical structures does not depend on a contractile actomyosin cortex.
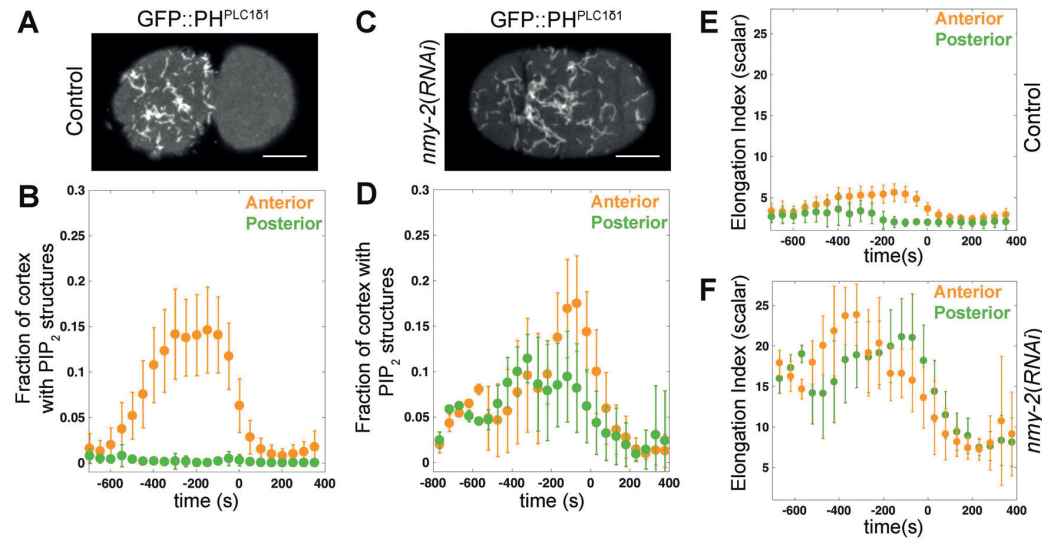


**Figure 29: The formation of PIP$_2$ cortical structures does not depend on myosin. (A, C)** Cortical plane at pseudocleavage from spinning disk confocal imaging of control (A) or *nmy-2*(*RNAi*) (C) embryos express-ing GFP::PH$^{PLC1\delta1}$. **(B, D, E, F)** Fraction of cell cortex covered (B, D) and Elongation Index (E, F larger values correspond to more elongated shapes) of segmented PIP$_2$ cortical structures over time in control (N=39) (B, E) and *nmy-2*(*RNAi*) (N=7) (D, F) embryos.

In stark contrast to the independence of PIP$_2$ cortical structures on myosin, we found that PIP$_2$ cortical structures hardly form in *act-1*(*RNAi*) embryos (Figure 30 A-D, G-J). Moreover, acute impairment of F-actin through treatment of *perm-1*(*RNAi*) embryos with Cytochalasin D led to the disappearance of PIP$_2$ cortical structures and instead to invaginations from the plasma membrane (Redemann et al., 2010) (Figure 30 K, L). By contrast, we found that PIP$_2$ cortical structures remain present upon depletion of the $\alpha$-tubulin TBA-2 (Figure 30 E, F), indicating that they form independently of the microtu-bule cytoskeleton. Overall, we conclude that the formation of PIP$_2$ cortical structures depends on F-actin.
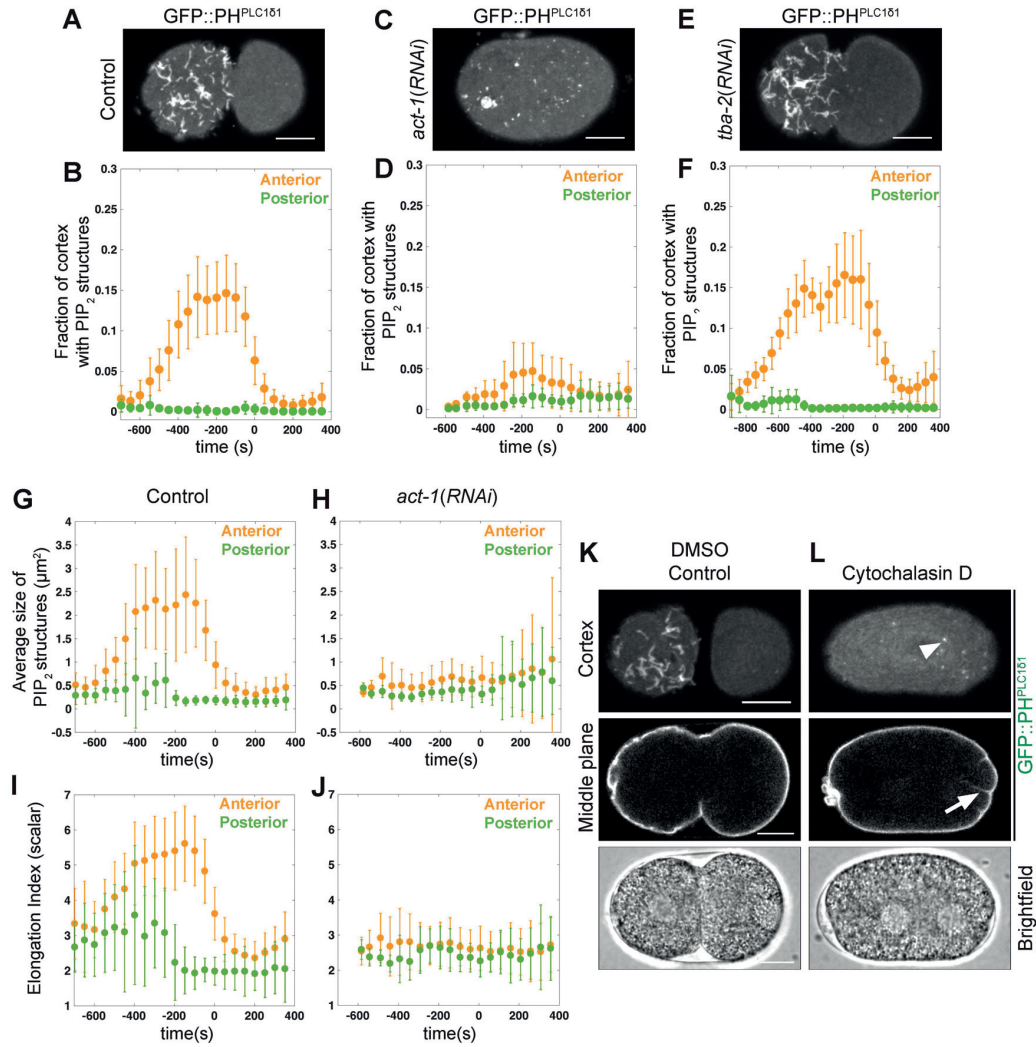
**Figure 30: F-actin is essential for the formation of PIP₂ cortical structures. (A, C, E)** Cortical plane at pseudocleavage from spinning disk confocal imaging of embryos treated as indicated and expressing GFP::PH^PLC1δ1. (A) Control, (C) *act-1*(*RNAi*), (E) *tba-2*(*RNAi*). Note that both *act-1*(*RNAi*) and *tba-2*(*RNAi*) are severe but partial depletion conditions, as more complete depletion results in sterility. **(B, D, F)** Fraction of cell cortex covered by segmented PIP₂ structures in control (B, N=39), *act-1*(*RNAi*) (D, N= 8 at pseudocleavage, N=12 at mitosis) or *tba-2*(*RNAi*) (F, N=10) embryos. (E, F) Note that although PIP₂ cortical structures form normally upon *tba-2*(*RNAi*), there are slightly more numerous on the anterior side of the embryo during mitosis compared to the control condition. **(G-J)** Quantification of segmented PIP₂ cortical structures of control (N=39) and *act-1*(*RNAi*) (N=12) embryos as indicated: average size of PIP₂ cortical structures in µm² (G, H) and elongation Index (larger values correspond to more elongated structures) (I, J). **(K, L)** Confocal live images of *perm-1*(*RNAi*) pseudocleavage embryos expressing GFP::PH^PLC1δ1 upon addition of DMSO (E) or 20 µM Cytochalasin D (F). Top: Maximum intensity z-Projection of 7 cortical planes 0.5 µm apart each; bottom: middle plane; N=7. Note that membrane invaginations form upon F-actin impairment (arrow) (Redemann et al., 2010), which are also visible as foci on the cortex (arrowhead, pointing to a different structure).

## 3.2 PIP$_2$ directs actin and cell polarity

### 3.2.1 Lowering the cellular level of PIP$_2$ impacts F-actin distribution

We set out to address whether, conversely, PIP$_2$ regulates F-actin organization. If this were the case, then changing the level of PIP$_2$ should alter actomyosin network organization. We tested this prediction first by depleting PIP$_2$. To this end, we activated phospholipase C, an enzyme that cleaves PIP$_2$, by delivering Ionomycin and Ca$^{2+}$ into *perm-1(RNAi)* embryos (Figure 31 A) (Hammond et al., 2012; Várnai and Balla, 1998). Cleavage of PIP$_2$ at the plasma membrane was monitored by the gradual loss of GFP::PH$^{PLC1\delta1}$ plasma membrane signal, which enabled us to determine the time t$_{1/2}$ when half of the initial GFP::PH$^{PLC1\delta1}$ plasma membrane fluorescence signal disappeared in the embryo middle plane (Figure 31 B, C).
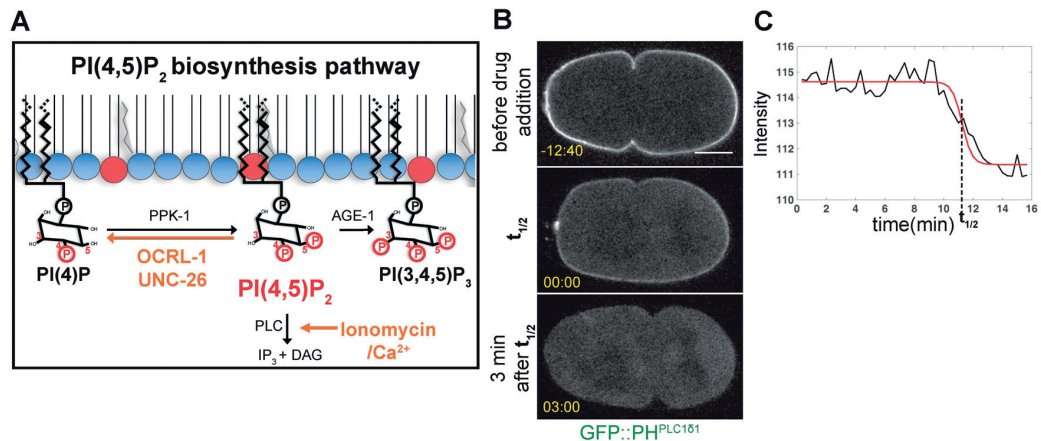


**Figure 31: Depletion of cortical PIP$_2$ by PLC activation. (A)** Schematic representation of the core PIP$_2$ biosynthesis and degradation pathways at the plasma membrane; orange arrows indicate points of experimental intervention in the present study (see text for additional details). **(B)** Snapshots of a movie in the middle plane of an embryo expressing GFP::PH$^{PLC1\delta1}$, before drug addition (top), at time t$_{1/2}$ (middle) and 3 min thereafter (bottom), as indicated. **(C)** Fluorescence intensity of GFP::PH$^{PLC1\delta1}$ at the plasma membrane over time (black curve) in embryo shown in B after addition of Ionomycin/Ca$^{2+}$ (at t=00:00 min:sec), with fitted sigmoidal curve (red). t$_{1/2}$ is the inflection point of the sigmoidal curve when approximately half of the initial GFP::PH$^{PLC1\delta1}$ fluorescence has disappeared from the plasma membrane. Time stamps aligned to t$_{1/2}$=00:00 in yellow (here and in figures below).

We found that PIP$_2$ removal following Ionomycin/Ca$^{2+}$ treatment during pseudocleavage led to a rapid change of embryo shape on the anterior side, coincident with altered F-actin organization (Figure 32 A, B; Figure 33 A, B). An analogous F-actin alteration was observed following Ionomycin/Ca$^{2+}$ treatment during mitosis (Figure 32 C;

Movie 14). Overall, these results establish that PIP$_2$ is essential for proper F-actin reorganization.
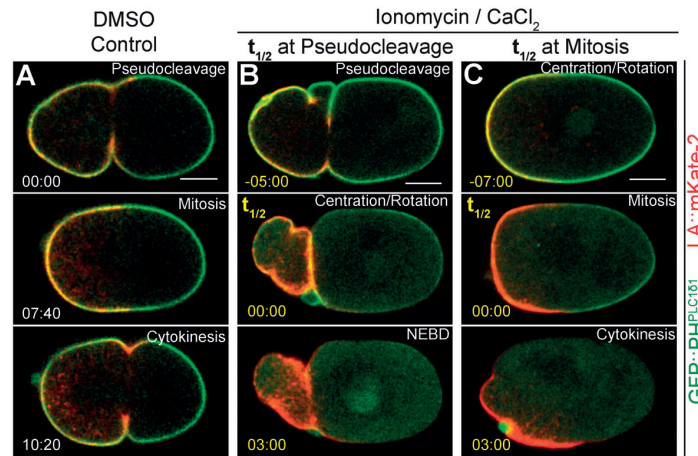


**Figure 32: PIP$_2$ depletion impairs the correct organization of the actin cytoskeleton. (A-C)** Confocal spinning disk imaging of embryos expressing GFP::PH$^{PLC1\delta1}$ and Lifeact::mKate-2 (middle plane). **(A)** DMSO treated *perm-1*(*RNAi*) control embryos. **(B, C)** *perm-1*(*RNAi*) embryos treated with Ionomycin/Ca$^{2+}$. $t_{1/2}$=00:00: time when half of plasma membrane GFP::PH$^{PLC1\delta1}$ fluorescence disappears. N=17, all stages combined. (B) $t_{1/2}$ at pseudocleavage. Note that the absence of coverslip, which is needed to preserve fragile *perm-1*(*RNAi*) embryos, prevents flattening, such that more surface ruffles are apparent. Note also that the pseudocleavage furrow moves towards the anterior and either remains there until the end of the first cell cycle (N=4, as shown) or relaxes (N=4, not shown) (C) $t_{1/2}$ at mitosis. See also Movie 14.

To test whether the embryo shape change following Ionomycin/Ca$^{2+}$ is caused by alterations in F-actin organization, we added Latrunculin A to such embryos, thus depolymerizing the actin network. As shown in Figure 33 C and Movie 15, we found that this results in normally shaped embryos. Therefore, shape changes following PIP$_2$ removal are F-actin dependent. Although we cannot formally rule out that Ionomycin/Ca$^{2+}$ causes these phenotypes for a different reason, these results taken together indicate that PIP$_2$ is critical for the proper distribution of F-actin and thus the shape of the *C. elegans* zygote.
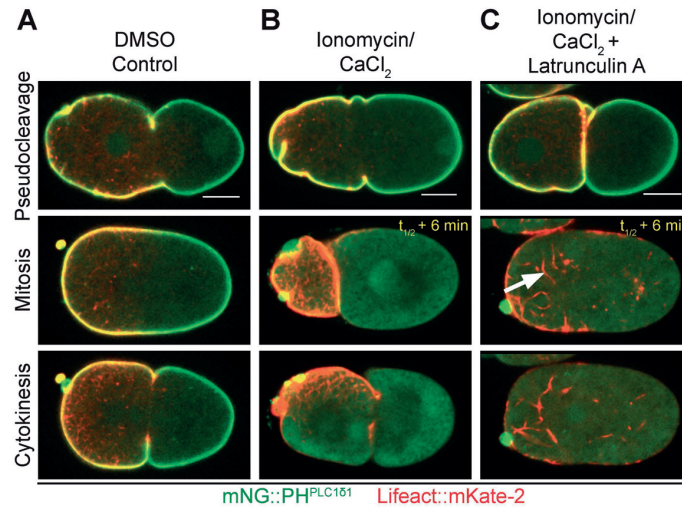
**Figure 33: A proper PIP₂ cellular level is essential for correct organization of the actin cytoskeleton. (A, B, C)** Images acquired by spinning disk confocal imaging of *perm-1*(*RNAi*) embryos expressing mNG::PH and Lifeact::mKate-2, (A) after addition of DMSO (see also Figure 32 A), (B) Ionomycin/$Ca^{2+}$ (see also Figure 32 B), (C) Ionomycin/ $Ca^{2+}$ plus Latrunculin A; N=12); note F-actin spikes in the cytoplasm (arrow) that form after simultaneous depletion of F-actin and PIP₂. See also Movie 15.

PPK-1, which synthesizes PIP₂, and Casein Kinase 1 (CSNK-1), a negative regulator of PPK-1 localization, were reported to be essential for proper spindle positioning in the one-cell stage embryo (Panbianco et al., 2008). Therefore we tested whether depleting PIP₂ influences spindle positioning. Embryos depleted of PIP₂ did not divide in most cases (N=26/36). 10/26 not-dividing embryos even died before mitosis and thus before spindle positioning takes place. In 16/26 non-dividing embryos, spindle positioning was majorly disturbed and could not be tracked properly in most cases. In these embryos, the anterior side was not accessible due to a deformed F-actin cytoskeleton and the spindle had to be placed on the posterior side (Figure 32 B, Figure 34 C). In diving embryos, no significant difference compared to DMSO control embryos could be detected (N=10/36) (Figure 34 A, B, D, E), but the end position of the posterior pole was slightly more variable (Figure 34 F). Together, we conclude that completely depleting PIP₂ from the cell cortex has such an overall strong impact on the embryo that assessing spindle positioning is impossible in most embryos. In the embryos that could be analyzed, PIP₂ depletion happened just before spindle positioning, which might be a too short time interval to detect a phenotype.
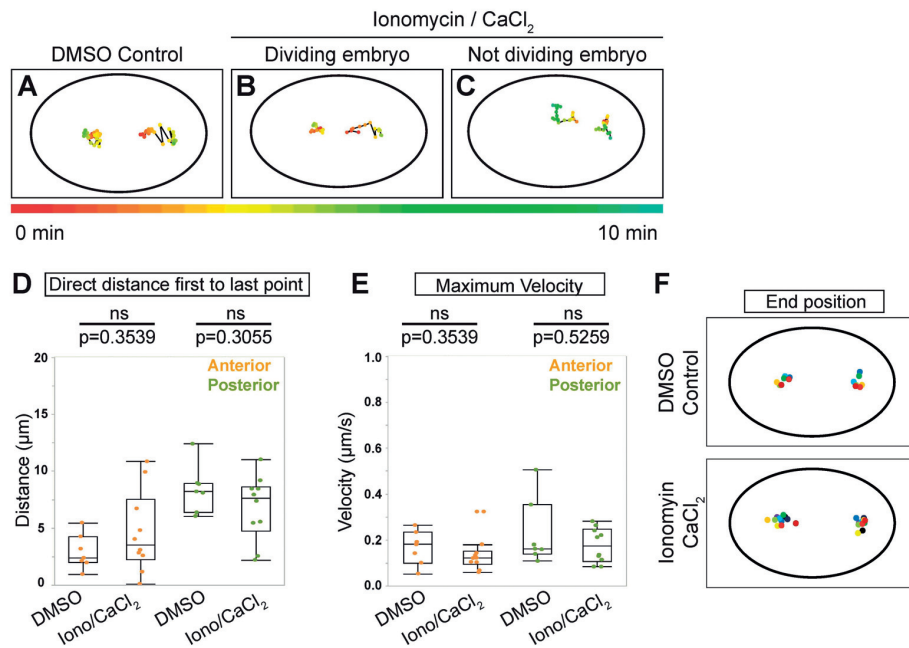
**Figure 34: Depleting PIP₂ influences spindle positioning. (A-C)** Examples of tracks of the anterior (left) and posterior (right) spindle pole of embryos of the indicated conditions during mitosis upon *perm-1*(*RNAi*); tracks were placed into an ellipse fitted to each embryo. Tracked points are colored according to when they were tracked, from nuclear envelope breakdown (NEBD), t=0 min until cytokinesis onset (see color legend below). (A-C) Note that most embryos depleted of PIP₂ could not be scored for spindle positioning because they did not assemble a spindle or were too deformed (N=10/36 and N=16/36, respectively). **(D, E)** Box Plot of distances from first to last tracked point (D) and of maximum velocity (E); only dividing embryos have been analysed. Two group comparison: Wilcoxon Rank Sum test / Mann-Whitney test. Note that there is no difference compared to control embryos in Ionomycin/Ca²⁺ treated embryos that divide. **(F)** End position of anterior (left) and posterior (right) spindle pole at cytokinesis onset; each embryo is represented by a given pair of colored dots. Only dividing embryos have been analysed. Note that the end position of PIP₂ depleted embryos that divided is slightly more variable than that of control embryos. Numbers of tracked anterior and posterior spindle poles used for analysis: *perm-1*(*RNAi*): DMSO control N=7, Ionomycin/Ca²⁺ dividing embryos N=10

## 3.2.2 -Increasing the cellular level of PIP₂ impacts F-actin distribution via enhanced actin polymerization

We sought to test the relationship between PIP₂ and F-actin further by increasing the level of PIP₂. We investigated whether this could be achieved by altering individual enzymes from the PIP₂ biosynthetic pathway using RNAi or mutant animals (Figure 8, Table 1). We first targeted AGE-1, the catalytic subunit of the sole *C. elegans* Class I PI3K, which can generate PIP₃ from PIP₂, using both RNAi and an *age-1*(*m333*) null mutant. We found that *age-1*(*RNAi*) embryos do not exhibit PIP₂ alterations, maybe because of incomplete RNAi-mediated depletion (Table 1). Likewise, whereas null *age-1* mutants arrest as dauer larvae (Larsen et al., 1995; Morris et al., 1996), we found no change in

PIP$_2$ in the corresponding embryos Table 1), perhaps because compensatory mechanisms operate to keep PIP$_2$ level constant. This is in the line with the fact that the expression of hundreds of genes is altered in *age-1* mutant worms (Ayyadevara et al., 2009; Shmookler Reis et al., 2012). Furthermore, we did not find another single RNAi or mutant condition with altered PIP$_2$ (Table 1), maybe due to redundancy amongst enzymes in the PIP$_2$ biosynthesis or degradation pathways.

**Table 1: Genes of the PIP₂ biosynthesis or degradation pathways targeted.** The genes listed below were either depleted by RNAi or using mutant worm lines, singly or in combination, as indicated. Note that genes were selected and targeted not only to find candidates whose depletion leads to an increased PIP$_2$ level as described in this section, but also ones whose depletion would lead to a decreased PIP$_2$ level.

| Depleted gene | Method (Genotype) | Pheno-type on PIP₂ structures | Function of encoded protein / Comments (Source: Wormbase) |
|---|---|---|---|
| *age-1* | *RNAi* | none | Ortholog of the phosphoinositide 3-kinase (PI3K) p110 catalytic subunit |
| *ttx-7* | *RNAi* | none | Myo-inositol monophosphatase (IMPase) |
| *egl-8* | *RNAi* | none | Phospholipase C (PLC) beta |
| *daf-18* | *RNAi* | none | Human PTEN homologous phosphatase |
| *inpp-1* | *RNAi* | none | Ortholog of the human inositol polyphosphate-5-phosphatase Ocrl, member of the Phosphoinositide phosphatase family INPP5E / Very low expression level in the early embryo |
| *ocrl-1* | *RNAi* | none | Inositol-1,4,5-triphosphate 5-phosphatase, homologous to human Ocrl |
| *W09C5.7* | *RNAi* | none | Ortholog of human inositol polyphosphate 5-phosphatase F (INPP5F) |
| *age-1* | mutant *age-1*(*m333*) II. | none | see above / *age-1* null allele (balanced) |
| *unc-26* | mutant *unc-26*(*s1710*) IV. | none | Polyphosphoinositide phosphatase orthologous to human synaptojanin 11 |
| *ppk-1* | *RNAi* | none | Ortholog of human phosphatidylinositol 4-phosphate 5-kinase (PIP5K) / Partial depletion because of sterility |
| *ppk-2* | *RNAi* | none | Ortholog of human phosphatidylinositol 5-phosphate 4-kinase (PIP4K) |
| *inpp-1/ W09C5.9* | *RNAi/RNAi* | none | see above |
| *inpp-1/ocrl-1/ W09C5.9* | *RNAi/RNAi/RNAi* | none | see above |
| *unc-26/age-1* | mutant/*RNAi* *unc-26*(*s1710*) IV. | none | see above |
| *unc-26/ocrl-1* | mutant/*RNAi* *unc-26*(*s1710*) IV. | see Fig. 36,41 | see above |

With this possibility in mind, we jointly inactivated *ocrl-1* and *unc-26*, for the following reasons. OCRL-1 is an inositol 5-phosphatase that hydrolyzes $PIP_2$ to PI4P, and whose depletion leads to increased $PIP_2$ level on *C. elegans* phagosomes (Cheng et al., 2015). Moreover, UNC-26 is homologous to Synaptojanin, a polyphosphoinositide phosphatase that also hydrolyzes $PIP_2$ to PI4P, and whose impairment results in vesicle trafficking defects and cytoskeletal abnormalities in the worm nervous system (Charest et al., 1990; Harris et al., 2000). We jointly depleted the function of these two $PIP_2$ phosphatases, using RNAi for *ocrl-1* and an extant mutant for *unc-26*. We found by comparing cortical mCherry::$PH^{PLC1\delta1}$ mean intensity values that *ocrl-1*(*RNAi*) *unc-26*(*s1710*) embryos exhibit an increased overall level of $PIP_2$ (Figure 35 A, B).
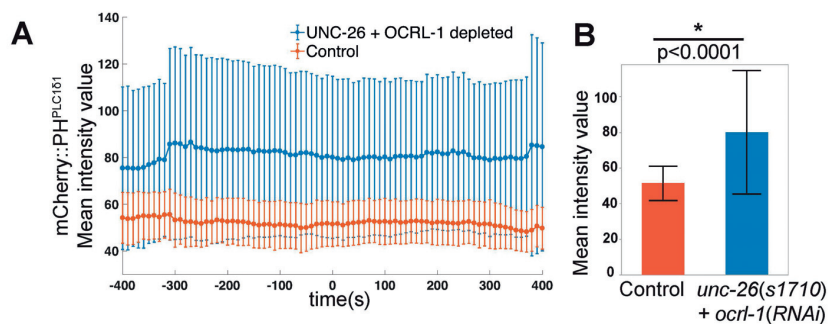


**Figure 35: Depletion of UNC-26 and OCRL-1 increases the level of $PIP_2$.. (A)** Mean intensity values of total cortical area plotted over time in embryos expressing mCherry::$PH^{PLC1\delta1}$. Red: control embryos; N=17; blue: *unc-26*(*s1710*) *ocrl-1*(*RNAi*) embryos; N=32. t=00:00 is at NEBD. **(B)** Mean intensity value and standard deviation of control and *unc-26*(*s1710*) *ocrl-1*(*RNAi*) embryos at t=00:00 (see (A)). Intensities between the two conditions are significantly different (Wilcoxon Rank Sum test / Mann-Whitney test p<0.0001).

Importantly, in addition, this leads to drastic alterations in $PIP_2$ monitored by GFP::$PH^{PLC1\delta1}$ or mCherry::$PH^{PLC1\delta1}$ (Figure 36 A, D and Figure 36 B, C, E, F top; Figure 36 K-P). First, in addition to motile $PIP_2$ structures, we found immotile $PIP_2$ clusters residing between the eggshell and the plasma membrane (Figure 36 B, E, H, arrow; Figure 36 J, arrowhead; Movie 16). Second, motile $PIP_2$ structures do not disappear as readily after pseudocleavage as they normally do (Figure 36 E, F, compare to Figure 36 D; Figure 36 N). Third, we found that motile $PIP_2$ structures exhibit altered distribution in all *ocrl-1*(*RNAi*) *unc-26*(*s1710*) embryos (Figure 36 B, C, L, P). In some cases (hereafter referred as class I embryos, N=43/72), anteriorly-directed movement of $PIP_2$ cortical structures does not stop at pseudocleavage, but instead continue until the end of mitosis, resulting in a very small anterior domain of $PIP_2$ (compare Figure 36 D, G top to Figure 36 E, H top). In class II *ocrl-1*(*RNAi*) *unc-26*(*s1710*) embryos (N=29/72), weak anteriorly-directed movement of cortical $PIP_2$ is initiated, but $PIP_2$ structures then become distributed throughout the cortex, except at the very posterior (Figure 36 F, I). By the very end of

the first cell cycle, improperly sized $PIP_2$ domains in class 1 and class 2 embryos get corrected. Whereas a clear cytokinesis furrow formed in all class 1 embryos, this was the case in only 14/29 class 2 embryos; this subset exhibited the most pronounced anteriorly-directed movements. Overall, we conclude that the extent of depletion of $PIP_2$ 5-phosphatases is weaker in class 1 than in class 2 embryos, with the severe phenotype in the latter perhaps reflecting an impact on multiple cellular processes. Interestingly, imaging *ocrl-1*(*RNAi*) *unc-26*(*s1710*) embryos expressing Lifeact::mKate-2 (class 1 N=3/7, class 2 N=4/7) or Lifeact::mKate-2 and GFP::PH$^{PLC1\delta1}$ (class 1 N=3/7, class 2 N=4/7), revealed that F-actin distributes in the same manner as $PIP_2$ cortical structures (Figure 36 A-I). These findings establish that an increase in $PIP_2$ as achieved in class 1 embryos leads to sustained cortical flows towards the anterior side. Moreover, although there may also be indirect effects of $PIP_2$ 5-phosphatase depletion on phosphoinositides other than $PIP_2$, these results further indicate that $PIP_2$ regulates actin cytoskeletal organization in one-cell *C. elegans* embryos.
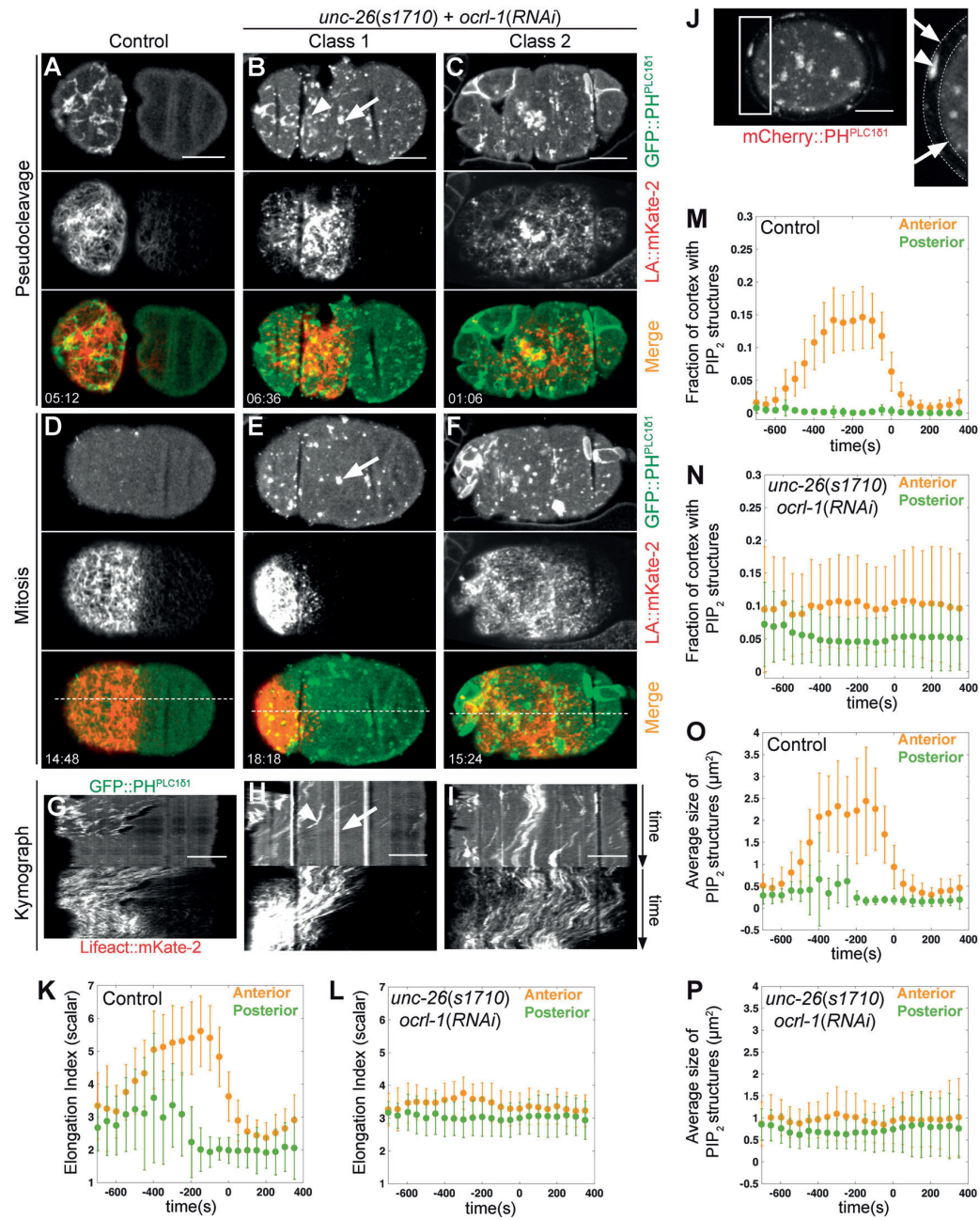
**Figure 36: PIP₂ is involved in the correct organization of the actin cytoskeleton. (A-F)** Confocal spinning disk imaging of embryos expressing GFP::PH$^{PLC1\delta1}$ and Lifeact::mKate-2 (LA::Kate-2) (cortical plane). Control (A, D) and *ocrl-1*(*RNAi*) *unc-26*(*s1710*) (B, C, E, F) embryos during pseudocleavage (A, B, C) or mitosis (D, E, F). (B, E) class 1 phenotype (N=43/72 scored with GFP::PH $^{PLC1\delta1}$ or mCherry::PH$^{PLC1\delta1}$ only, N=3/7 scored by Lifeact::mKate-2 only, N=3/7 scored by both GFP::-PH$^{PLC1\delta1}$/Lifeact::mKate-2); arrow: immotile structure, arrowhead: motile structure. See also Movie 16. (C, F) class 2 phenotype (N=29/72 embryos scored with GFP::PH$^{PLC1\delta1}$ or mCherry::PH$^{PLC1\delta1}$ only, N=4/7 scored by Lifeact::mKate-2 only, N=4/7 scored by both GFP::-PH$^{PLC1\delta1}$/Lifeact::mKate-2). Dashed lines in (D-F) show the positions utilized to create the corresponding kymographs in (G-I). **(G-I)** Corresponding kymographs aligned at cytokinesis. Arrow: immotile structure, arrowhead: motile structure. Note that motile cortical PIP₂ structures eventually move towards the cleavage furrow, partly correcting the aberrant PIP₂ cortical domain distribution, consistent with a cortical domain correction mechanism operating at this stage (Schenk et al., 2010). Entire duration of the kymographs, in min:sec: (J) 16:30, (K) 20:00, (L) 19:00. **(J)** Spinning disk confocal imaging of *unc-26*(*s1710*) *ocrl-1*(*RNAi*) embryo expressing mCherry::PH$^{PLC1\delta1}$. Note large immotile PIP₂ cortical structures (arrowhead) between the eggshell (top arrow) and the embryo proper (bottom arrow), indicating that this PIP₂ containing structure is no longer connected to the plasma membrane. Note also that, had such external structures retained a thin connection to the plasma membrane, they would have been expected to move with the cortical flow and not stay completely immobile, as they do (see H, arrow). **(K-P)** Fraction of cell cortex covered with segmented PIP₂ structures (K, L), their averages size (M, N) and Elongation Index (O, P, larger values correspond to more elongated structures) in control embryos expressing GFP::PH$^{PLC1\delta1}$ (K, M, O, N=39) and *ocrl-1*(*RNAi*) *unc-26*(*s1710*) embryos expressing mCherry::PH$^{PLC1\delta1}$ (L, N, P, N=20).

We sought to investigate whether such regulation of PIP₂ is exerted through promotion of actin polymerization. We reasoned that if this were the case, then enhancing actin polymerization in a different way might mimic the *unc-26*(*s1710*)/*ocrl1*(*RNAi*) phenotype. Therefore, we treated *perm-1*(*RNAi*) embryos with Jasplakinolide, which promotes actin polymerization (Figure 37). Such treatment sometimes led to large actin clumps and to detachment of the actin cytoskeleton from the plasma membrane (N=7/17, data not shown). Usually, however, if treatment occurred during pseudocleavage, the actin cytoskeleton moved exaggeratedly towards the anterior in Jasplakinolide-treated embryos (Figure 37 B, D, H; N=10/17), as in class 1 *unc-26*(*s1710*)/*ocrl1*(*RNAi*) embryos. However, the movement of F-actin to the anterior in Jasplakinolide embryos occurred much faster than in class 1 *unc-26*(*s1710*)/*ocrl1*(*RNAi*) embryos and was not corrected at the end of the first cell cycle. To further test the hypothesis that PIP₂ regulation is exerted through actin polymerization promotion, we treated permeabilized *unc-26*(*s1710*)/*ocrl1*(*RNAi*) embryos with low concentrations of Cytochalasin D (250-500 nM) (Figure 37 A-F). We reasoned that this should ameliorate the *unc-26*(*s1710*)/ *ocrl1*(*RNAi*) phenotype if caused by increased actin polymerization. We found this to be the case indeed: whereas DMSO-treated *perm-1*(*RNAi*)/*unc-26*(*s1710*)/ *ocrl1*(*RNAi*) embryos usually exhibited the class 1 or class 2 phenotypes (N=6 and N=1, respectively, with 1 additional embryo exhibiting no apparent phenotype), all Cytochalasin D-treated *perm-1*(*RNAi*)/*unc-26*(*s1710*)/*ocrl1*(*RNAi*) embryos polarized normally (Figure 37 A, C, E; N=6). Together, these experiments establish that PIP₂ regulation is exerted through the promotion of actin polymerization.
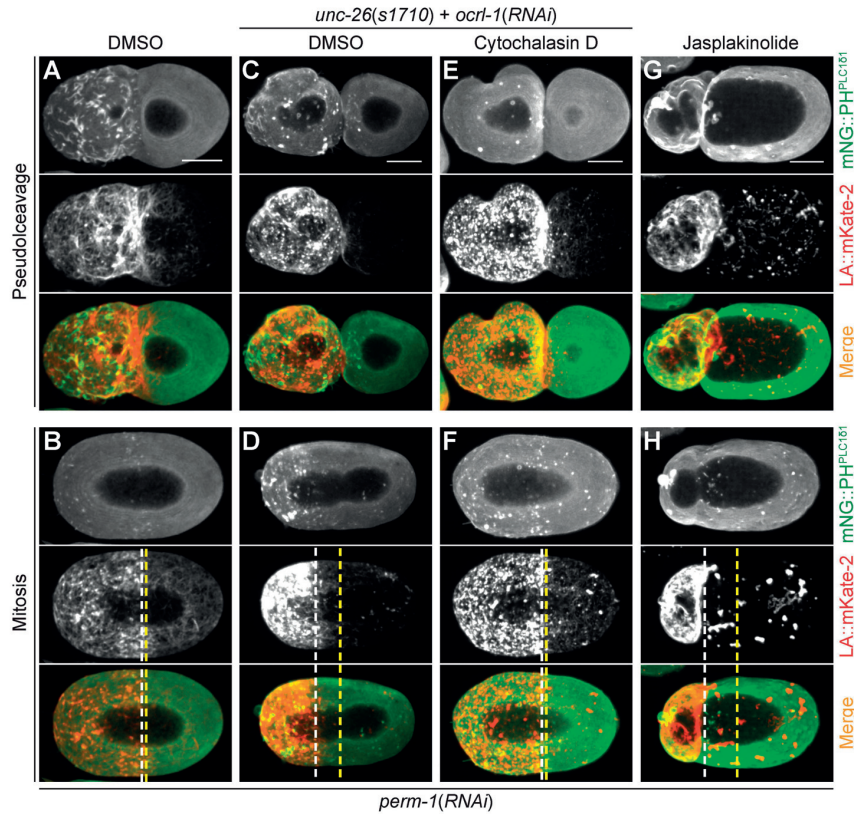
**Figure 37: An increased PIP$_2$ level enhances actin polymerization. (A-H).** Images acquired at the indicated stages by spinning disk confocal imaging of embryos expressing mNG::PH$^{PLC1\delta1}$ and Lifeact::mKate-2 upon *perm-1*(*RNAi*). **(A, B)** DMSO treated control embryos. **(C, D)** DMSO treated *unc-26*(*s1710*)/*ocrl-1*(*RNAi*) class 1 embryos (N=6). **(E, F)** *unc-26*(*s1710*)/*ocrl-1*(*RNAi*) embryos treated with 250 nM Cytochalasin D (N=4 embryos, plus 2 embryos treated with 500 nM Cytochalasin D with the same outcome, N=6 in total). **(G, H)** Embryos treated with 2.5 μM Jasplakinolides (N=10). Note that gravid worms were dissected in the drug-containing solution. As embryos were not flattened, to prevent pressure on these fragile specimens, 17 cortical frames were acquired for each channel every 30 seconds and z-projected. As the shape of the embryos changes in the z-direction over time, the outer most-cortical planes were often not acquired due to having lost the focus in the interval, hence explaining the large dark regions in these z-projected images. The boundary of the F-actin-containing domains during mitosis is indicated with a white dashed line, the yellow dashed line marking the middle of the embryo.

As described above, we had noted that spindle positioning is affected if PIP$_2$ is depleted. We also tracked centrosome position from NEBD to cytokinesis furrow formation after an increase in the PIP$_2$ level, which revealed that spindle positioning is also more variable in both class 1 and class 2 *ocrl-1*(*RNAi*) *unc-26*(*s1710*) embryos than in the control condition (Figure 38), as may be anticipated from such pleiotropic defects. In most class 1 (N=13/16) and class 2 embryos (N=5/8) analyzed, the spindle assembles already in the posterior embryo half and then extends significantly less to the posterior and significantly more to the anterior compared to the control (Figure 38 B, C, D, F).

Moreover, oscillations of the posterior spindle pole, measured as maximum velocity, significantly decrease (Figure 38 G) and the end positions of both spindle poles are more variable (Figure 38 H). In a few class 2 embryos (N=3/8), the spindle assembles in the center of the embryos and then extends symmetrically in both directions, leading to a symmetric end position (Figure 38 E, H). Overall, an increase in PIP$_2$ disturbs proper spindle positioning, whereas strongly increasing the PIP$_2$ level can lead to symmetric divisions.
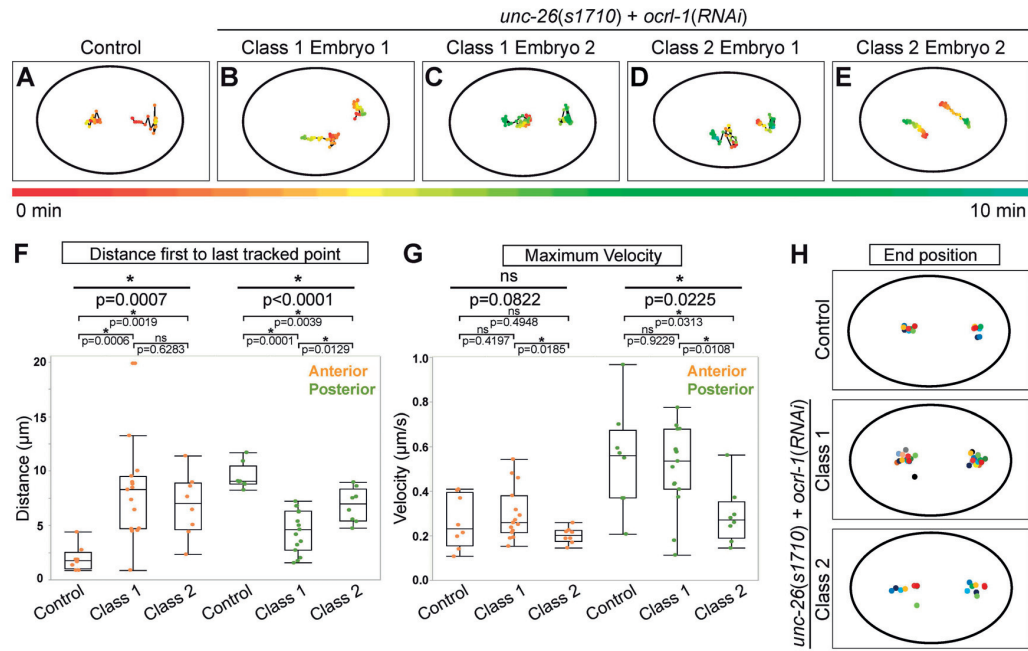


**Figure 38: Increasing the level of PIP$_2$ impacts proper spindle positioning. (A-E).** Examples of tracks of the anterior (left) and posterior (right) spindle poles of embryos of the indicated conditions during mitosis; tracks were placed into an ellipse fitted to each embryo. Tracked points are colored according to when they were tracked, from nuclear envelope breakdown (NEBD), t=0 min until cytokinesis onset (see color legend below). (A-E) Note that an increase in the PIP$_2$ level variably impacts spindle positioning. **(F, G)** Box Plot of distances from first to last tracked point (F) and of maximum velocity (G) in embryos of the indicated conditions. Three group comparison: Kruskal-Wallis test and Wilcoxon Each Pair post-hoc test (F, G). (F) Note that in most class 1 (N=13/16) and class 2 embryos (N=5/8) analyzed, the spindle assembles more posteriorly than normal, and then extends more anteriorly than in the control. (G) Note that oscillations of the posterior spindle pole, measured as maximum velocity, significantly decrease in class 1 and class 2 embryos. **(H)** End position of anterior (left) and posterior (right) spindle poles at cytokinesis onset; each embryo is represented by a given pair of colored dots. Note that the end positions of both spindle poles are more variable than in the control. In some class 2 embryos (N=3/8), the spindle assembles in the center and then extends symmetrically to both sides, leading to a symmetric end position (see also E). Numbers of tracked anterior and posterior spindle poles used for analysis F-H: *ocrl-1*(*RNAi*) *unc-26*(*s1710*): control N=8, class 1 N=15, class 2 N=8.

### 3.2.3 PIP₂ is needed for RHO-1 and CDC-42 cortical structures

The regulation of actin polymerization and F-actin organization by PIP$_2$ could conceivably be mediated through the actin regulators ECT-2, RHO-1 and CDC-42, with which PIP$_2$ cortical structures coincide (see Figure 21). We explored this possibility for RHO-1 and CDC-42 through PIP$_2$ depletion via Ionomycin/Ca$^{2+}$ treatment. We found this to result in the loss of both cortical GFP::RHO-1 (N=5) and GFP::CDC-42 (N=7) if PIP$_2$ depletion occurs before pseudocleavage (Figure 39 A-D). Moreover, PIP$_2$ depletion after pseudocleavage results in cortical GFP::RHO-1 loss (N=2), but generally not in that of GFP::CDC-42 cortical structures (Figure 39 E, N=5/7). Overall, these experiments indicate that PIP$_2$ is needed for RHO-1 cortical structure formation and maintenance during the first cell cycle, and for CDC-42 cortical structure formation, primarily until the pseudocleavage stage. By contrast, the maintenance of CDC-42 structures, once formed, appears to be controlled by other factors than PIP$_2$ cortical structures.
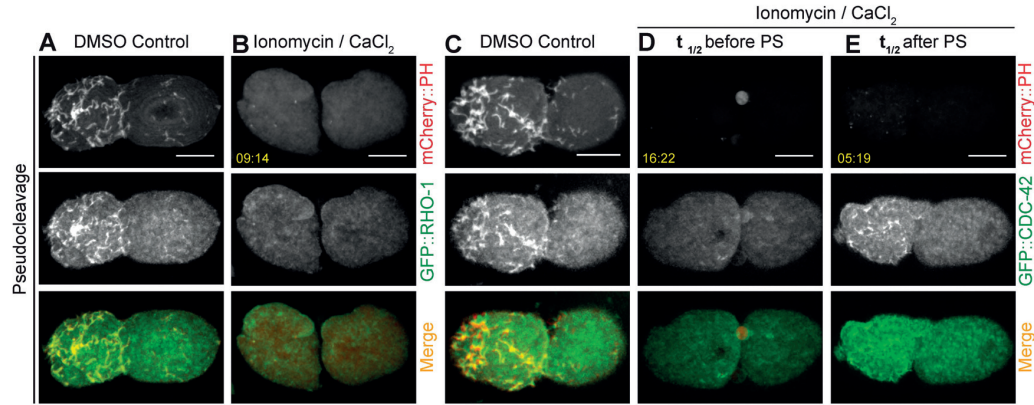


**Figure 39: The formation of GFP::RHO-1 and GFP::CDC-42 cortical structures depends on PIP₂. (A-E)** Confocal spinning disk imaging of embryos expressing mCherry::PHPLC1δ1 and GFP::RHO-1 (A, B) or GFP::CDC-42 (C). z-projection of 9 planes 0.5 µm apart (note that only one image of the GFP channel was acquired in this case, so that the loss of focus issue described in Figure 35 does not apply here). **(A, C)** DMSO treated *perm-1*(*RNAi*) control embryos at pseudocleavage. **(B, D, E)** *perm-1*(*RNAi*) embryos at pseudocleavage treated with Ionomycin/Ca2+. Time stamp in yellow indicates time after t1/2. (B) N=7; (D) t1/2 occurred before pseudocleavage furrow formation (N=7). Note absence of GFP::CDC-42 cortical structures. (E) t$_{1/2}$ occurred after pseudocleavage furrow formation (N=5). Note that GFP::CDC-42 cortical structures are still present to some extent including the embryo shown here (N=5), but in N=2 embryos they seem to have disappeared as well (not shown).

Given that PIP$_2$ cortical structures are essential for CDC-42 and RHO-1 structure formation, altering PIP$_2$ cortical structure distribution might likewise change that of RHO-1 and CDC-42. To test this possibility, we examined the distribution of GFP::RHO-1 and GFP::CDC-42 cortical structures in *unc-26*(*s1710*)/*ocrl1*(*RNAi*) class 1 and class 2 embryos, where PIP$_2$ cortical structure organization is altered (see Figure 36). We found that GFP::RHO-1 and GFP::CDC-42 distributions mirror that of mCherry::PH$^{PLC1δ1}$ in such class 1 and class 2 embryos (Figure 40 A-F). Together, these results further confirm that

PIP$_2$ cortical structures are crucial for the formation and distribution of cortical structures of the actin regulators RHO-1 and CDC-42. Moreover, they also support the speculation that the regulation of F-actin reorganization by PIP$_2$ could be mediated by these actin regulators.
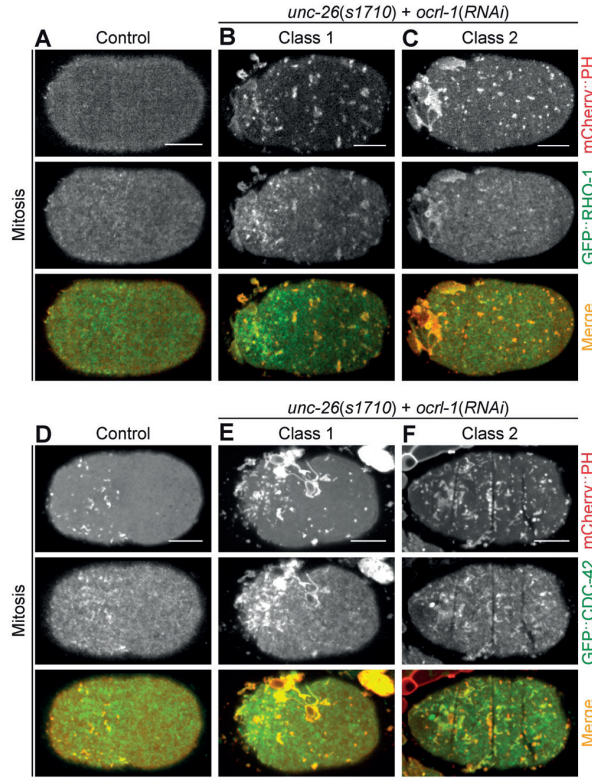


**Figure 40: The localization of GFP::RHO-1 and GFP::CDC-42 cortical structures depends on PIP$_2$. (A-F)** Confocal spinning disk imaging of embryos expressing mCherry::PH$^{PLC1\delta1}$ and GFP::RHO-1 (A-C) or GFP::CDC-42 (D-F). Control (A, D) and *ocrl-1*(*RNAi*)/*unc-26*(*s1710*) (B, C, E, F) embryos during mitosis. Class 1 phenotype: (G) N=6; (J) N=6. Class 2 phenotype: (H) N=4; (K) N=3.

### 3.2.4 An appropriate level of PIP$_2$ is essential for proper PAR polarity establishment and maintenance

It is well known that the actomyosin network is essential for AP polarity in the *C. elegans* zygote (Guo and Kemphues, 1996; Hill and Strome, 1990; Munro et al., 2004; Strome and Wood, 1983). Given that a proper level of PIP$_2$ is essential for correct actomyosin network organization, we tested whether it is also important for AP polarity. We investigated the impact of excess PIP$_2$ on polarity using *ocrl-1*(*RNAi*) *unc-26*(*s1710*) embryos expressing mCherry::PH$^{PLC1\delta1}$ and GFP::PAR-2 or GFP::PAR-6, respectively (Figure 41 A-

L). We found that the distribution of GFP::PAR-2 and GFP::PAR-6 domains changes from early on in a manner consistent with alterations in motile $PIP_2$ structures and the F-actin network. Thus, for GFP::PAR-6, either a small domain formed on the very anterior (Figure 41 B, E; class 1, N=5/9; Movie 17) or else the fusion protein remained present over the entire cortex, except on the very posterior (Figure 41 C, F class 2; N=4/9). As expected, GFP::PAR-2 distributed in a reciprocal manner, either expanding drastically towards the anterior (Figure 41 H, K; class 1, N=12/22; Movie 18) or else remaining restricted to the very posterior (Figure 41 I, L; class 2, N=10/22). Moreover, we observed that spindle positioning is affected in a variable manner in *ocrl-1*(*RNAi*) *unc-26*(*s1710*) embryos (Figure 38), as anticipated from altered AP polarity and potentially other consequences of excess $PIP_2$. Overall, these results indicate that a correct level of $PIP_2$ is needed for proper F-actin network localization and, presumably as a consequence, appropriate PAR polarity and accurate spindle positioning.
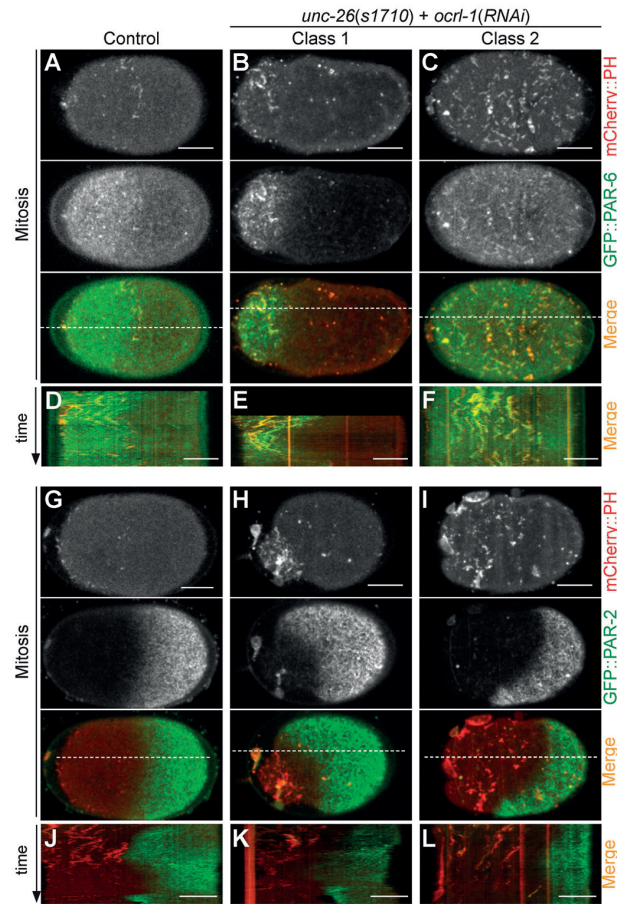
**Figure 41: Increasing the PIP₂ cellular level impacts PAR polarity. (A-C, G-I)** Confocal spinning disk cortical imaging of control (A, G) or *ocrl-1*(*RNAi*) *unc-26*(*s1710*) (B, C, H, I) embryos expressing mCherry::PH$^{PLC1\delta1}$ (mCherry::PH) and GFP::PAR-6 (A-C, N=5/9 class 1, N=4/9 class 2) or GFP::PAR-2 (G-I, N=12/22 class 1; N=10/22 class 2). Dashed lines indicate positions used to create the corresponding kymographs in (D-F). See also Movie 17. **(D-F, J-L)** Corresponding kymographs aligned at cytokinesis. Entire duration of the kymographs, in min:sec: (D) 16:40, (E) 11:20, (F-I) 17:40. See also Movie 18.

In the above experiments, the level of PIP₂ is in excess from the beginning of development, such that the impact on polarity might reflect a role strictly during the establishment phase or else during both establishment and maintenance phases. We reasoned that one could test specifically a potential role for PIP₂ in polarity establishment by adding Ionomycin/Ca$^{2+}$ to *perm-1*(*RNAi*) embryos expressing mCherry::PH$^{PLC1\delta1}$ and GFP::PAR-2 before symmetry breaking. In DMSO treated control embryos, PAR-2 first localizes throughout the entire cortex, then becomes cytoplasmic, and after symmetry breaking is enriched at the posterior (Figure 42 A), as reported (Boyd et al., 1996; Cuenca et al., 2003; Etemad-Moghadam et al., 1995; Hung and Kemphues, 1999; Munro

et al., 2004). Interestingly, depletion of $PIP_2$ before PAR-2 becomes cytoplasmic abolished the detachment of PAR-2 from the cortex. Instead, PAR-2 remained present throughout the cortex and did not get further enriched at the posterior cortex even after pronuclei formation. Together, these results suggest a role of $PIP_2$ during symmetry breaking and polarity establishment.
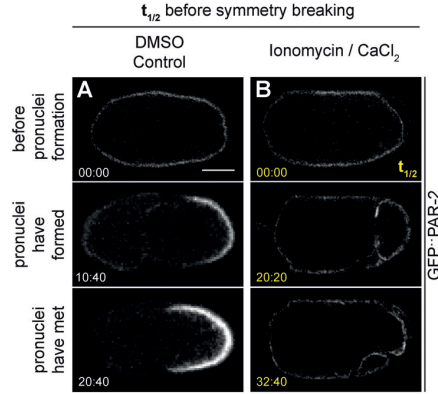


**Figure 42: $PIP_2$ is essential for PAR polarity establishment.(A, B)** Images acquired by confocal imaging of embryos expressing GFP::PAR-2, 4.5 µm below the cortical plane. (A) DMSO treated control *perm-1(RNAi)* embryo. (B) *perm-1(RNAi)* embryo treated with Ionomycin/$Ca^{2+}$ ($t_{1/2}$=00:00) before symmetry breaking (N=4).

Next, we set out to test specifically a potential role for $PIP_2$ in polarity maintenance by adding Ionomycin/$Ca^{2+}$ during pseudocleavage, after polarity establishment, to *perm-1(RNAi)* embryos expressing mCherry::$PH^{PLC1\delta1}$ and GFP::PAR-2. We found that GFP::PAR-2 expands slowly towards the anterior starting ~3 min after $t_{1/2}$ (Figure 43), when the actin cytoskeleton is already disorganized (Figure 32). In these embryos, the pseudocleavage furrow moves anteriorly initially, and then either disappears (Figure 43 B; N=6/14; Movie 19), or remains at the very anterior (Figure 43 C; N=8/14; Movie 20). The same two possible outcomes were also observed for Ionomycin/$Ca^{2+}$ treated *perm-1(RNAi)* embryos expressing GFP::$PH^{PLC1\delta1}$ and Lifeact::mKate-2 (Figure 32). Likewise, the GFP::PAR-2 domain expands slowly towards the anterior when $t_{1/2}$ occurs at nuclear envelope breakdown (NEBD) (Figure 43 D; Movie 21). Together, these results indicate that an appropriate level of $PIP_2$ is essential for proper PAR polarity also during the maintenance phase. Moreover, the fact that actin disorganization happens before the expansion of the PAR-2 domain indicates that $PIP_2$ might regulate polarity through actin reorganization during the maintenance phase.
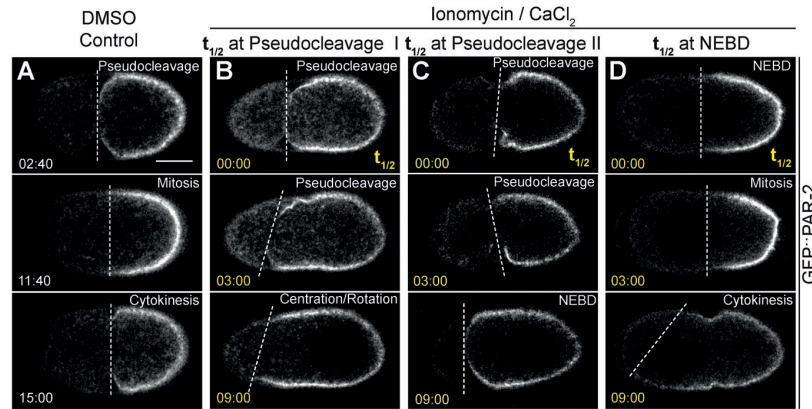
**Figure 43: PIP₂ is essential for correct PAR polarity maintenance. (A-D)** Images acquired by confocal imaging of embryos expressing GFP::PAR-2, 4.5 μm below the cortical plane. The dashed line marks the boundary of the PAR-2 domain. (A) DMSO treated control *perm-1*(*RNAi*) embryo. (B-D) *perm-1*(*RNAi*) embryo treated with Ionomycin/Ca$^{2+}$ ($t_{1/2}$=00:00) during (B) pseudocleavage, when pseudocleavage furrow retract (N=6) (see also Movie 19), (C) pseudocleavage when pseudocleavage furrow does not retract (N=8) (see also Movie 20) or (D) NEBD (N=3) (see also Movie 21).

In principle, PIP₂ could alter PAR polarity during the maintenance phase through an impact on F-actin organization, as suggested by the results above, or else via an actin-independent role. In contrast to its well-known role during polarity establishment, a potential role of F-actin in polarity maintenance is somewhat controversial (Goehring et al., 2011; Hill and Strome, 1990; Liu et al., 2010a; Severson and Bowerman, 2003). In the light of our findings with PIP₂ level alterations, we set out to directly test whether F-actin plays a role in polarity maintenance, first by adding Cytochalasin D to *perm-1*(*RNAi*) embryos expressing Lifeact::mKate-2 and GFP::PAR-2 after polarity establishment (Figure 44 A, B). Consistent with previous studies (Goehring et al., 2011; Hill and Strome, 1990), we found that Cytochalasin D addition at this stage does not significantly alter GFP::PAR-2 distribution (Figure 44 A, B). However, we found also that Cytochalasin D does not fully disrupt F-actin, as clumps of Lifeact::mKate-2 remain on the embryo anterior (Figure 44 B; Movie 22). We hence turned to inhibiting F-actin polymerization using Latrunculin A, which resulted in total depletion of F-actin (Figure 44 C; N=12; Movie 23). We observed membrane invaginations that remove GFP::PAR-2 from the cortex into cytoplasmic aggregates (Figure 44 C, arrowhead), as reported (Goehring et al., 2011; Redemann et al., 2010). Importantly, in addition, we monitored changes in GFP::PAR-2 distribution not as a function of drug addition time, as previously (Goehring et al., 2011), but of the time at which half of the Lifeact::mKate-2 fluorescence disappears from the membrane. In doing so, we found that GFP::PAR-2 domain size decreases after $t_{1/2}$ in all embryos analyzed (Figure 44 C, bottom; N=12), in a manner that is highly correlated with Lifeact::mKate-2 disappearance (Figure 44 D), demonstrating that F-actin is critical for PAR polarity maintenance.
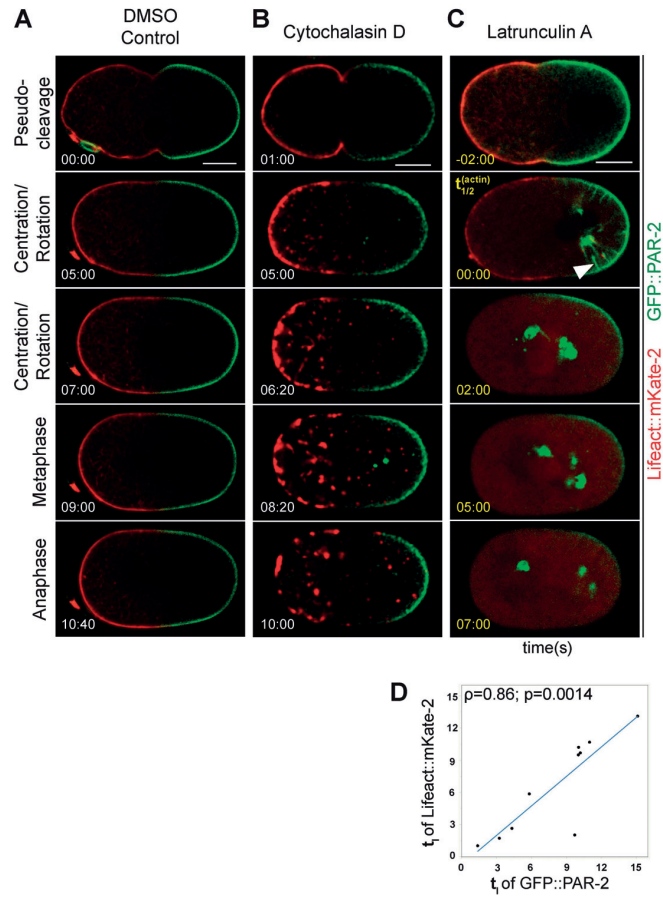
**Figure 44: F-actin impairment affects GFP::PAR-2 also during polarity maintenance. (A-C)** Confocal spinning disk cortical imaging of *perm-1*(*RNAi*) embryos expressing GFP::PAR-2 and Lifeact::mKate-2 (middle plane), treated during early centration/rotation either with DMSO (A, N=6), Cytochalasin D (B, N=5, movie acquired with bining=2, see also Movie 22), or Latrunculin A (C, N=18, see also Movie 23). Arrowhead points to plasma membrane invagination (Redemann et al., 2010). **(D)** Correlation of $t_{1/2}$ of Lifeact::mKate-2 and GFP::PAR-2 upon treatment of *perm-1*(*RNAi*) embryos with Latrunculin A (see Figure 44). Pearson correlation coefficient $\rho=0.86$, $p=0.0014$ (unpaired t-test) (N=10, as the GFP::PAR-2 signal was too weak in 2/12 imaged embryos for the correlation analysis to be conducted). Note that $t_{1/2}$ of GFP::PAR-2 happens on average 0.78 +/- 0.78 min after $t_{1/2}$ of Lifeact::mKate-2 (N=9, after removal of an outlier in which $\Delta t_{1/2}=7.73$ min).

Overall, we uncovered that a proper level of PIP$_2$ is essential for correct sizing of PAR domains, presumably through reorganization of F-actin, not only during polarity establishment but also during the polarity maintenance phase. Moreover, together with the fact that PIP$_2$ cortical structures form in a manner that is dependent on F-actin and

that their movement is driven by actin polymerization (see 3.1), this uncovers reciprocal feedback mechanisms between PIP$_2$ and F-actin (Figure 45, Figure 46).
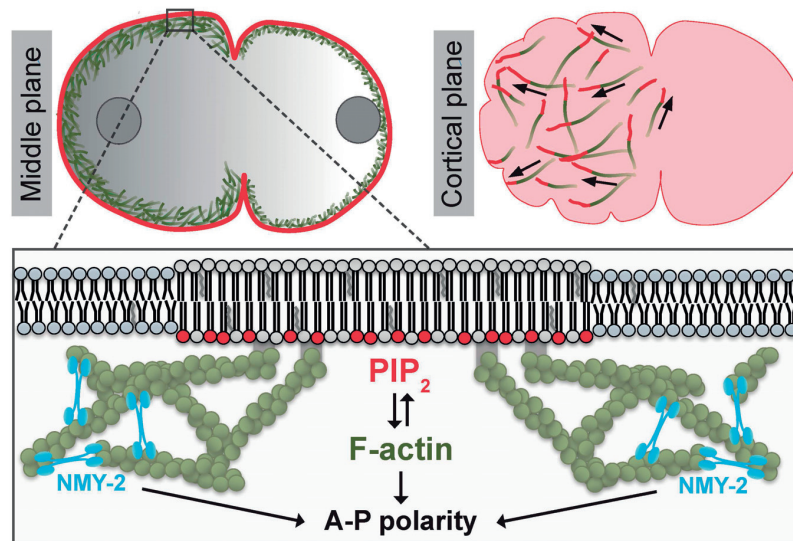


**Figure 45: Schematic working model (not to scale).** PIP$_2$ is enriched in dynamic and polarized structures at the cortex of one-cell *C. elegans* embryos, moving ahead of F-actin. These two components exhibit mutually reciprocal requirements: the formation of PIP$_2$ cortical structures requires F-actin and a proper PIP$_2$ level is essential for F-actin organization. Moreover, through its ability to properly organize the F-actin network, PIP$_2$ is essential for proper sizing of PAR domains and thus AP polarity. See text for further details. Note that only those actin filaments that move in concert with PIP$_2$ cortical structures are represented on the top right, for simplicity.
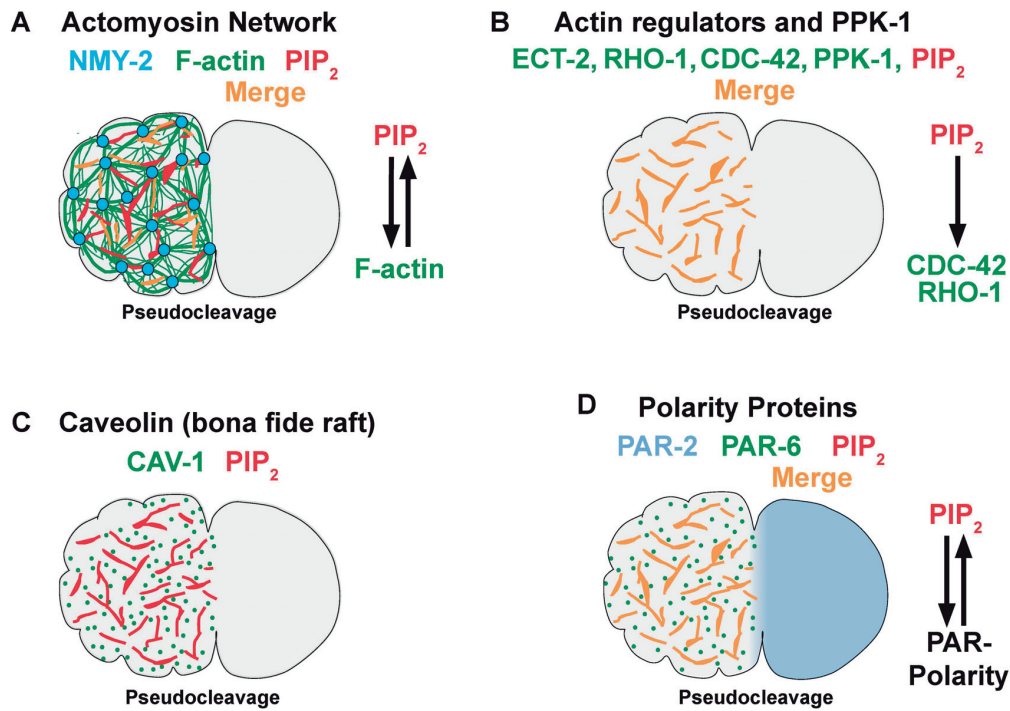
**Figure 46: Schematic summary of PIP$_2$ cortical structures' overlap with further cortical components.** **(A)** PIP$_2$ cortical structures partially overlap with the F-actin network but not with NMY-2. The formation of PIP$_2$ cortical structures depends on F-actin and the correct organization and polymerization of F-actin depends on correct PIP$_2$ levels. **(B)** PIP$_2$ cortical structures fully overlap with the actin regulators RHO-1, CDC-42, the RHO-1 GEF ECT-2, and the PIP$_2$ generating kinase PPK-1. PIP$_2$ cortical structures form mostly independent of RHO-1 and CDC-42, but the formation and localization of RHO-1 and CDC-42 cortical structures depends on correct PIP$_2$ levels. **(C)** PIP$_2$ cortical structures do not overlap with the bona fide lipid raft protein CAV-1. **(D)** PIP$_2$ cortical structures overlap with elongated structures of PAR-6 but not with PAR-6 foci and not with PAR-2. The asymmetric distribution of PIP$_2$ cortical structures depends on PAR polarity and correct PIP$_2$ levels are essential for proper PAR polarity establishment and maintenance.

## 3.3 Cortical structures of force generator components and regulators

### 3.3.1 Positive and negative regulators of force distribute in distinct cortical structures.

In the one-cell stage *C. elegans* embryo, the mitotic spindle is asymmetrically positioned towards the posterior side through the action of asymmetric spindle pulling forces generated by positive and negative force regulators (see 1.2.6, page 15). We set out to test the cortical distribution of the negative force regulators GPB-1, CSNK-1 and CHC-1, as well as of the positive force regulators GPR-1 and LIN-5 using cortical confocal live imaging. Imaging of embryos expressing GFP::GPB-1 (Thyagarajan et al., 2011) revealed that during pseudocleavage GPB-1 forms elongated cortical structures that are present essentially solely on the anterior side (Figure 47 A). Thereafter, during mitosis, GFP::GPB-1 is distributed in foci that are enriched on the anterior (Figure 47 B). These observations are consistent with previous observations that GPB-1 is enriched on the embryo anterior and that GPB-1 foci might correspond to sites of endocytosis of GPB-1-containing vesicles, since GPB-1 traffics through the endosomal system (Thyagarajan et al., 2011). In addition, GFP::GPB-1 foci could be sites of exocytosis. The Gβ protein subunit GPB-1 forms a dimer with the G γ protein subunit GPC-2, and GPC-2 also negatively regulates forces (Afshar et al., 2004; Afshar et al., 2005; Tsou et al., 2003). As expected, cortical imaging of GFP::GPC-2 (Thyagarajan et al., 2011) showed that GPC-2 distributes in the same way as GPB-1 on the cortex (Figure 47 C, D).

Gβγ competes with the force generation mediators GPR-1/2 for Gα-GDP binding and thus negatively regulate pulling forces mainly on the anterior (Afshar et al., 2004; Afshar et al., 2005; Thyagarajan et al., 2011; Tsou et al., 2003). We hypothesized that GPR-1/2 and GPB-1 might reside in distinct cortical structures, thus perhaps explaining their opposite impact on force generation. We therefore imaged embryos in which GPR-1 is endogenously tagged with GFP using CRISPR-Cas9 (Portegijs et al., 2016). During pseudocleavage, instead of clear elongated cortical structures as those observed for GPB-1, GFP::GPR-1 mainly forms small foci (Figure 47 E). During mitosis, GFP::GPR-1 is temporarily enriched on the very posterior of the embryo, as expected from the analysis of fixed specimens (Colombo et al., 2003; Gotta and Ahringer, 2001; Gotta et al., 2003; Srinivasan et al., 2003; Tsou et al., 2003) (Figure 47 F). Overall, we found that GFP::GPR-1 and GFP::GPB-1 are localized in distinct cortical structures during pseudocleavage and mitosis.

The force generation mediator LIN-5 functions together with GPR-1/2 in a ternary complex (see 1.2.6). We thus expected that LIN-5 cortical distribution resembles that of GPR-1/2. To test this hypothesis, we imaged embryos expressing endogenously tagged LIN-5 (Portegijs et al., 2016), which indeed revealed that GFP::LIN-5 distributes in cortical structures resembling those of GFP::GPR-1, both during pseudocleavage and mitosis (Figure 47 G, H). The tenary complex anchors the minus end directed molecular motor dynein to the cortex (see 1.2.6). Consistent with this, we found that, as GFP::GPR-1 and GFP::LIN-5, also GFP::DHC-1 forms small cortical foci during pseudocleavage (Figure 47 I) and mitosis (Figure 47 J) and these foci are enriched on the very posterior during mitosis. Next, we tested if two other negative force regulators, CSNK-1 and CHC-1, also reside in cortical structures resembling those of GPB-1 and GPC-2. We imaged embryos expressing a fusion protein between GFP and CSNK-1, a kinase that negatively regulates forces on the anterior (Panbianco et al., 2008). Interestingly, we found that during pseudocleavage, GFP::CSNK-1 forms elongated structures on the anterior resembling those of GFP::GPB-1 (Figure 47 K). During mitosis, just like for GPB-1, CSNK-1 is present in foci localized on the anterior, but these foci are less numerous and seem to slightly differ in shape compared to GFP::GPB-1 foci (Figure 47 L). We also imaged the cortical distribution of the clathrin heavy chain CHC-1, which has also been reported to negatively regulate pulling forces (Spiro et al., 2014). In contrast to GPB-1 and CSNK-1, we found that GFP::CHC-1 does not distribute in elongated structures during pseudocleavage, but instead forms foci enriched on the anterior (Figure 47 M). Likewise, CHC-1 distributes in foci enriched on the embryo anterior during mitosis (Figure 47 N). Such a focal distribution is not surprising considering the role of CHC-1 in receptor-mediated endocytosis (Grant et al., 1999). Overall, these results establish that, during pseudocleavage, the negative force regulators GPB-1 and CSNK-1 distribute in elongated cortical structures resembling each other, while the force generation mediators GPR-1 and LIN-5 distribute in foci also resembling each other.
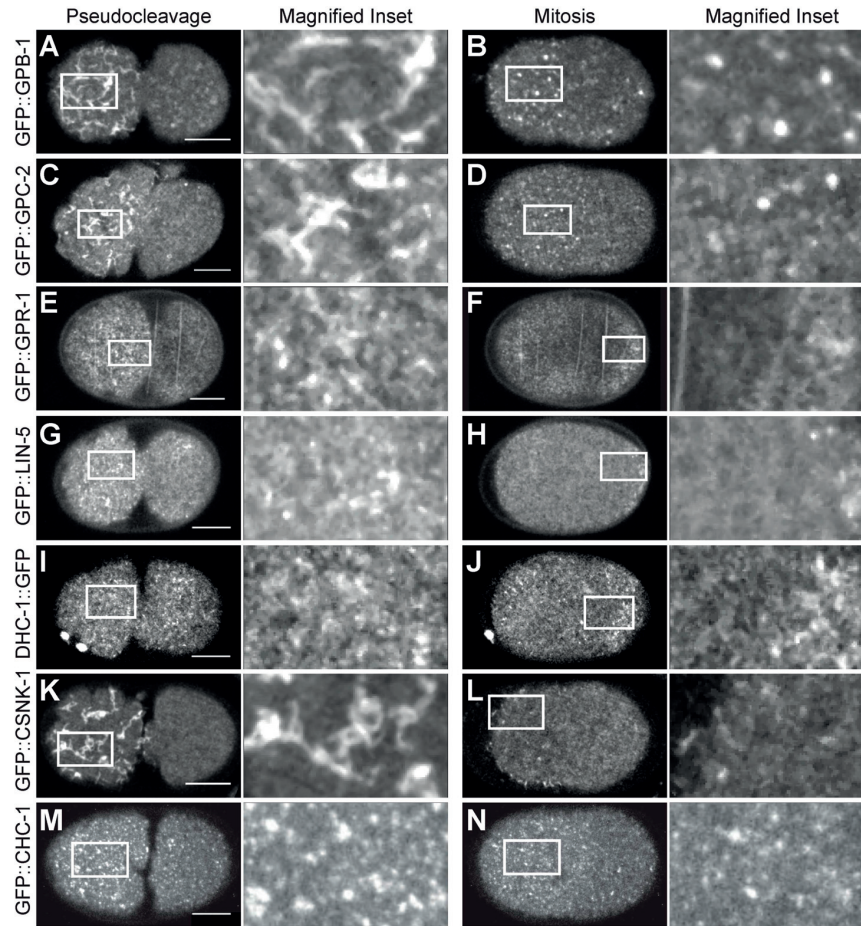
**Figure 47: Cortical distribution of force generation mediators and negative force regulators. (A-N)** Confocal spinning disk cortical imaging of embryos during pseudocleavage and mitosis harboring the indicated fusion protein, with high magnification views of the boxed regions shown on the right. (A, B) GFP::GPB-1, N=18. (C, D) GFP::GPC-2, N=3. (E, F) GFP::GPR-1 (endogenously tagged), N=15. (G, H) GFP::LIN-5 (endogenously tagged), N=8. (I, J) DHC-1::GFP (endogenously tagged), N=3 (K,L) GFP::CSNK-1, N=4. (M, N) GFP::CHC-1, N=4.

Next, we aimed to test whether GPB-1 and GPR-1 or LIN-5 cortical structures overlap. We thus sought to generate worm lines expressing mCherry::GPB-1 either as an integrated transgene by bombardment, or by tagging the endogenous component using CRISPR-Cas9 (see 7.2). As these efforts were unfortunately not met with success, we decided instead to assess the colocalization of GPB-1 with GPR-1 and LIN-5 in an indirect manner. During pseudocleavage, GFP::GPB-1 elongated cortical structures resemble cortical structures of $PIP_2$, suggesting that they may colocalize (see 3.1.1, Figure 10). To address this possibility, we imaged embryos expressing simultaneously mCherry::PH$^{PLC1\delta1}$ and GFP::GPB-1, and found that the two signals indeed perfectly overlap during pseudocleavage (Figure 48 A; Movie 24). The situation differs somewhat dur-

ing mitosis: although there is a weak enrichment of GFP::GPB-1 at $PIP_2$ cortical structures, most GPB-1 foci do not overlap with $PIP_2$ cortical structures (Figure 48 B). However, both GFP::GPB-1 and $PIP_2$ cortical structures are enriched at the embryo anterior (Figure 48 B). We conclude that during pseudocleavage at the least, $PIP_2$ cortical structures can be utilized as a proxy to monitor the localization of GPB-1 containing cortical structures, and thus assess their localization with respect to that of GPR-1 and LIN-5. Imaging of embryos expressing mCherry::PH$^{PLC1\delta1}$ and GFP::GPR-1 revealed that although a subset of GPR-1 cortical structures overlaps with elongated $PIP_2$ cortical structures during pseudocleavage, the bulk of GPR-1 foci does not (Figure 48 C; Movie 25). It appears that GFP::GPR-1 does not form clear elongated structures by itself but nevertheless some of the GFP::GPR-1 foci overlap with elongated $PIP_2$ cortical structures (Figure 47 E; Movie 26). Furthermore, during mitosis, GPR-1 foci form on the posterior, while $PIP_2$ cortical structures reside on the anterior (Figure 48 D). We also performed cortical imaging of embryos expressing GFP::LIN-5 and mCherry:PH$^{PLC1\delta1}$, obtaining similar results. Thus, during pseudocleavage, only some LIN-5 cortical structures overlap with $PIP_2$ cortical structures, while most do not (Figure 48 E). During mitosis, LIN-5 foci are localized to the very posterior, while $PIP_2$ cortical structures reside on the anterior (Figure 48 F). Overall, we conclude that the force generation mediators LIN-5 and GPR-1 not only form cortical structures distinct in shape from GPB-1 cortical structures, but also that they occupy distinct cortical territories.
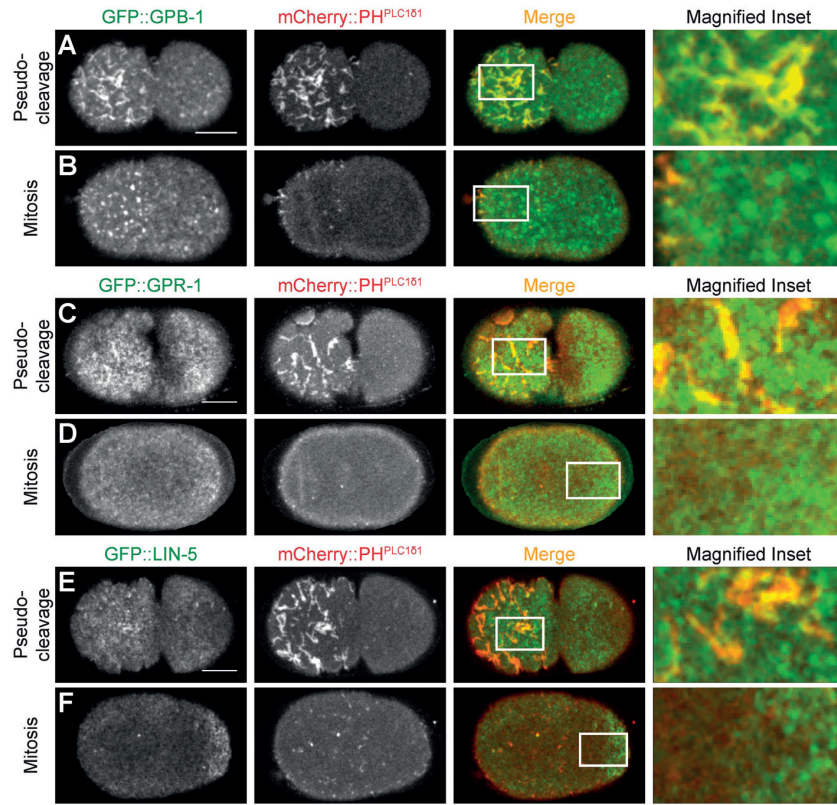
**Figure 48: PIP$_2$ cortical structures overlap with GPB-1 during pseudocleavage but only marginally with GPR-1 and LIN-5. (A-F)** Dual color confocal spinning disk cortical imaging of embryos harboring the indicated pairs of fusion proteins at the indicated stages, with high magnification views of the boxed regions shown on the right. (A, B) GFP::GPB-1/ mCherry::PH$^{PLC1\delta1}$, N=7. See also Movie 24. (C, D) GFP::GPR-1/ mCherry::PH$^{PLC1\delta1}$, N=10. See also Movie 25. (E, F) GFP:LIN-5/ mCherry::PH$^{PLC1\delta1}$, N=3. See also Movie 26.

### 3.3.2  GPR-1 contributes to the cortical recruitment of LIN-5

As described above, we found that GPR-1 and LIN-5 distribute in foci on the cortex that resemble each other (see 3.3.1; Figure 47). In murine mammary stem cells, the GPR-1/2 homolog LGN and the LIN-5 homolog NUMA form hetero-hexamers, which are functional oligomeric units that drive spindle positioning (Mapelli, M; Mechanisms of asymmetric cell division, Theo Murphy Meeting, November 2016). We thus speculated that GPR-1/2 and LIN-5 foci could also arise from higher order oligomers of GPR-1 and LIN-5. To test this possibility, we depleted GPR-1/2 by RNAi in embryos expressing GFP::LIN-5 (Figure 49 A-E). Measuring the total cortical fluorescence intensity of GFP::LIN-5, we found that cortical enrichment of GFP::LIN-5 is significantly diminished in *gpr-1/2*(*RNAi*) embryos compared to the control (Figure 49 E). This is consistent with the known role of GPR-1/2 in recruiting LIN-5 to the cortex (Couwenbergs et al., 2007; Nguyen-Ngoc et

al., 2007; Park and Rose, 2008). Moreover, less GFP::LIN-5 foci seem to be present on the cortex upon depletion of GPR-1/2 compared to control embryos, however, we cannot distinguish if this reflects a role of GPR-1/2 specifically in LIN-5 foci formation or simply LIN-5 cortical recruitment(Figure 49 A-D). Overall, we found that GRP-1/2 contributes to the cortical recruitment of LIN-5 and, directly or indirectly, for LIN-5 foci formation.
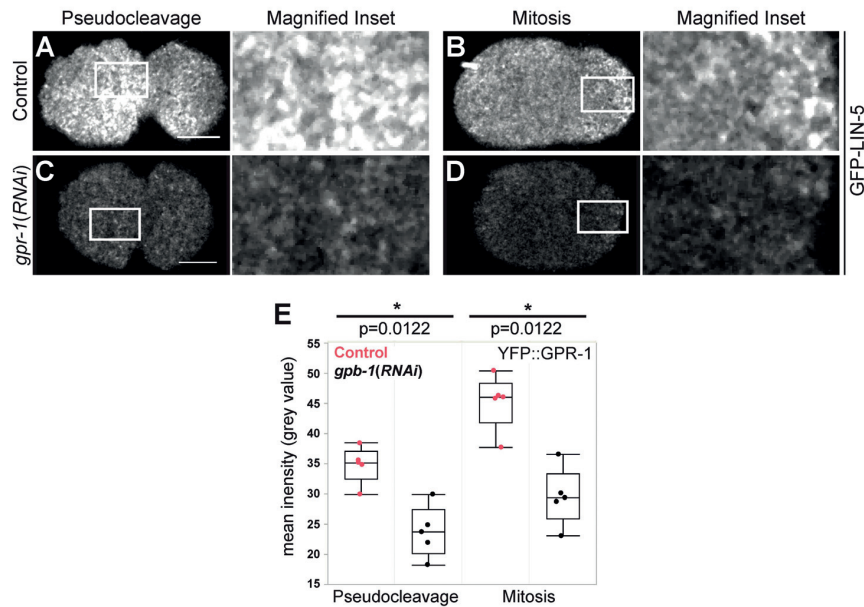


**Figure 49: GPR-1 contributes to LIN-5 cortical recruitment. (A-D)** Confocal spinning disk cortical live imaging of embryos during indicated stages expressing GFP::LIN-5, with high magnification views of the boxed regions shown on the right. (A, B) in control conditions, N=5 and (C, D) upon *gpr-1/2*(*RNAi*) N=5. **(E)** Box plot of mean intensities of total cortical intensity (16 bit grey values) of embryos shown in (A-D). Two group statistical comparisons were performed using the Wilcoxon Rank Sum test/Mann-Whitney test.

### 3.3.3 PIP$_2$ cortical structures determine the formation and localization of GPB-1 cortical structures

As described above, we found that PIP$_2$ and GPB-1 cortical structures perfectly overlap during pseudocleavage. To better establish the relationship between PIP$_2$ and GPB-1 cortical structures, we set out to test if one determines the formation and localization of the other, and reciprocally. First, we imaged embryos expressing GFP::PH$^{PLC1\delta1}$ upon depletion of GPB-1, and found that PIP$_2$ cortical structures form and distribute as in control embryos (Figure 50 A-D). In addition, we found that PIP$_2$ cortical structures form and distribute largely independent of GPR-1/2 and CHC-1 (Figure 50 E-H). Overall, these results establish that GPB-1 cortical structures, although perfectly overlapping

with PIP$_2$ cortical structures during pseudocleavage, are not needed for their formation and distribution.
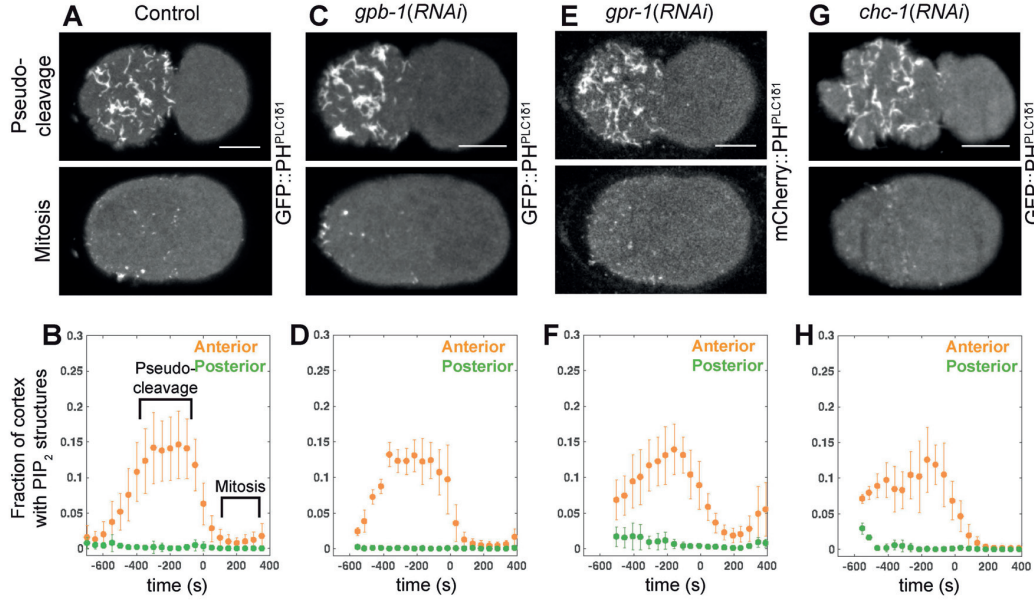


**Figure 50: The formation and localization of PIP$_2$ cortical structures does not depend on GPB-1, GPR-1/2, or CHC-1. (A, C, E, G)** Cortical plane at pseudocleavage and mitosis from spinning disk confocal imaging of control (A, N=39), *gpb-1(RNAi)* (C, N=4), *gpr-1/2(RNAi)* (E, N=4) or *chc-1(RNAi)* (G, N=9) embryos expressing GFP::PH$^{PLC1\delta1}$ (A, C, G) or mCherry::PH$^{PLC1\delta1}$ (E). **(B, D, F, H)** Fraction of anterior (orange) and posterior (green) cell cortex covered by segmented PIP$_2$ structures in the conditions corresponding to (A, C, E, G) side over time. Here and in similar panels in Figure 56: quantification for anterior (orange) and posterior (green) embryo side is shown, with the mean and the standard deviation.

We tested next whether GPB-1 cortical structures depend on PIP$_2$. As described above, we found that combined depletion of the function of the PIP$_2$ 5-phosphatases UNC-26 and OCRL-1 increases the level of cortical PIP$_2$ and changes the shape and localization of PIP$_2$ cortical structures (see 3.2.2). Cortical imaging of *ocrl-1(RNAi) unc-26(s1710)* embryos expressing mCherry::PH$^{PLC1\delta1}$ and GFP::GPB-1 during pseudocleavage revealed that GPB-1 cortical structures are altered in the same way as PIP$_2$ cortical structures in class 1 and class 2 embryos (Figure 51 A, C, E; Movie 27). Likewise, during mitosis, GPB-1 cortical structures form a much smaller anterior domain in class 1 embryos compared to control embryos (Figure 51 B, D). Moreover, in class 2 embryos, GPB-1 essentially does not get polarized and is cleared only from the very posterior (Figure 51 F). As described above, increasing the level of PIP$_2$ alters PAR polarity (see 3.2.4, page 81). This probably results in the altered distribution of GPB-1 cortical structures observed here, since the asymmetric distribution of GPB-1 during mitosis depends on PAR polarity (Thyagarajan et al., 2011). Together, these experiments establish that PIP$_2$ is essential for the formation and localization of GPB-1 cortical structures, while PIP$_2$ cortical structures form independently of GPB-1.
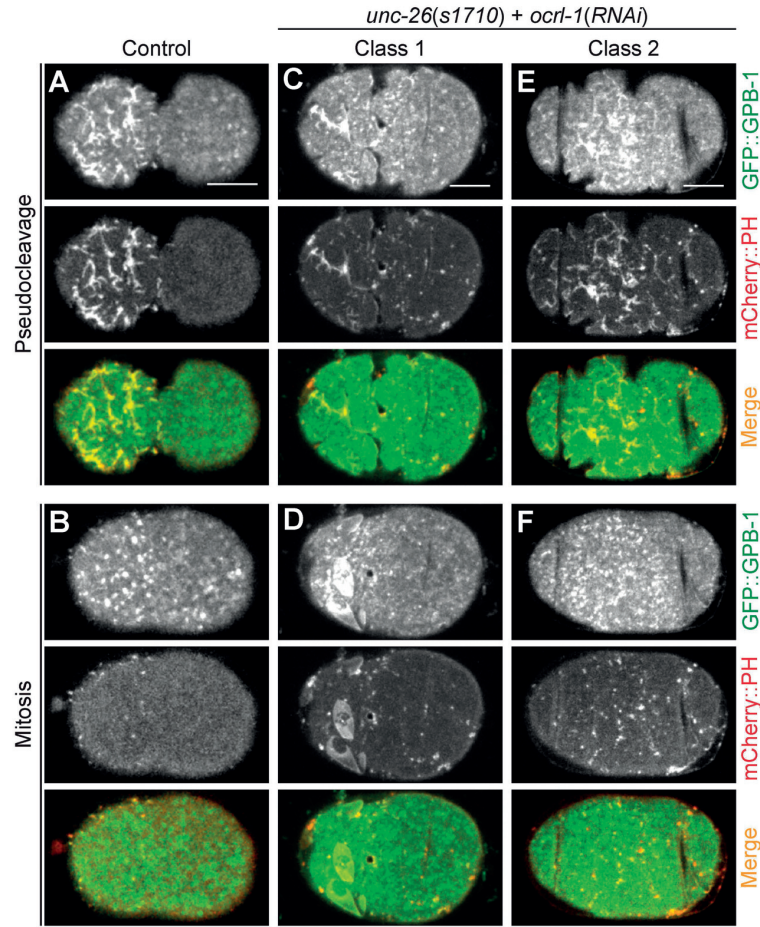
**Figure 51: The formation and distribution of GPB-1 cortical structures depends on PIP$_2$. (A-F)** Cortical confocal spinning disk imaging of embryos expressing mCherry::PH$^{PLC1\delta1}$ and GFP::GPB-1. Control (A, D) and *ocrl-1(RNAi) unc-26(s1710)* (B, C, E, F) embryos during pseudocleavage (A, B, C) or mitosis (D, E, F). (B, E) class 1 phenotype N=4/7. (C, F) class 2 phenotype N=3/7. See also Movie 27.

Next, we set out to test whether PIP$_2$ also regulates the formation and localization of ternary complex cortical structures, even though cortical structures of PIP$_2$ and of GPR-1 and LIN-5 only partially overlap. Preliminary experiments imaging *unc-26(s1710)/ocrl-1(RNAi)* embryos expressing GFP::GPR-1 and mCherry::PH$^{PLC1\delta1}$ indicated that GFP::GPR-1 foci still form unabated (data not shown). However, a subset of GFP::GPR-1 cortical structures changed their localization in a variable manner amongst embryos. This is to be expected given that GPR-1/2 localization depends on PAR polarity (Colombo et al., 2003; Gotta and Ahringer, 2001; Gotta et al., 2003; Srinivasan et al., 2003; Tsou et al., 2003), which is affected in *unc26(s1710)/ocrl-1(RNAi)* embryos (see 3.2.4).

### 3.3.4 The formation of GPR-1 and GPB-1 cortical structures is independent from one another.

We set out to test whether the formation of GPR-1 cortical structures depends on GPB-1 function, and vice versa. To test the dependency of GPR-1 cortical structures on GPB-1, one would ideally image endogenously tagged GFP::GPR-1 upon GPB-1 depletion. As such a worm line was not available when performing the experiments, we depleted instead GPB-1 from embryos overexpressing transgenic YFP::GPR-1. First, we imaged control embryos expressing YFP::GPR-1. Intriguingly, we found that YFP::GPR-1 also forms elongated structures during pseudocleavage similar to elongated cortical structures of GFP::GPB-1 (Figure 52 A). Likewise, during mitosis cortical YFP::GPR-1 resembles cortical GFP::GPB-1, with foci being present on the anterior cortex (Figure 52 B). Again, this cortical distribution of YFP::GPR-1 is very distinct from the cortical distribution of endogenous GPR-1/2 (Figure 47 E-F). YFP::GPR-1 is strongly overexpressed (Redemann et al., 2011), which likely causes the difference in distribution compared to endogenous GPR-1/2. Consistent with this hypothesis, we found that during mitosis, YFP::GPR-1 is enriched on the embryo anterior instead of the posterior (Figure 52 B), as is the case for endogenous GPR-1/2 (Colombo et al., 2003; Gotta and Ahringer, 2001; Gotta et al., 2003; Srinivasan et al., 2003; Tsou et al., 2003) and endogenously tagged GFP::GPR-1 (see Figure 47 F). Perhaps in the wild-type, negative regulators of pulling forces enriched on the anterior side such as GPB-1 limit cortical GPR-1/2 binding on that side. YFP::GPR-1 overexpression might outcompete all such negative regulators on the anterior and thus bind to all binding sites available in that location. In contrast, binding sites on the posterior might already be saturated at endogenous levels of GPR-1/2 and might not be able to increase further. We depleted GPB-1 from embryos expressing YFP::GPR-1 and found that such fluorescently marked cortical structures form unabated during pseudocleavage and mitosis (Figure 52 A-D). However, during mitosis, the overall cortical level of GPR-1 increased significantly in embryos upon *gpb-1*(*RNAi*) (Figure 52 I), consistent with the known role of GPB-1 in negatively regulating GPR-1 cortical levels (Thyagarajan et al., 2011; Tsou et al., 2003). Overall, this experiment suggests that the formation of GPR-1 cortical structures is independent of GPB-1, but this tentative conclusion remains to be verified for endogenous GPR-1 structures.

To test the dependency of GPB-1 cortical structures on GPR-1/2, we imaged GFP::GPB-1 embryos upon GPR-1/2 depletion. We found that GPB-1 cortical structures form unaltered (Figure 52 E-H). Moreover, overall cortical levels of GFP::GPB-1 remained the same (Figure 52 J). Overall, we conclude that the formation of GPB-1 and GPR-1 cortical structures is independent from one another.
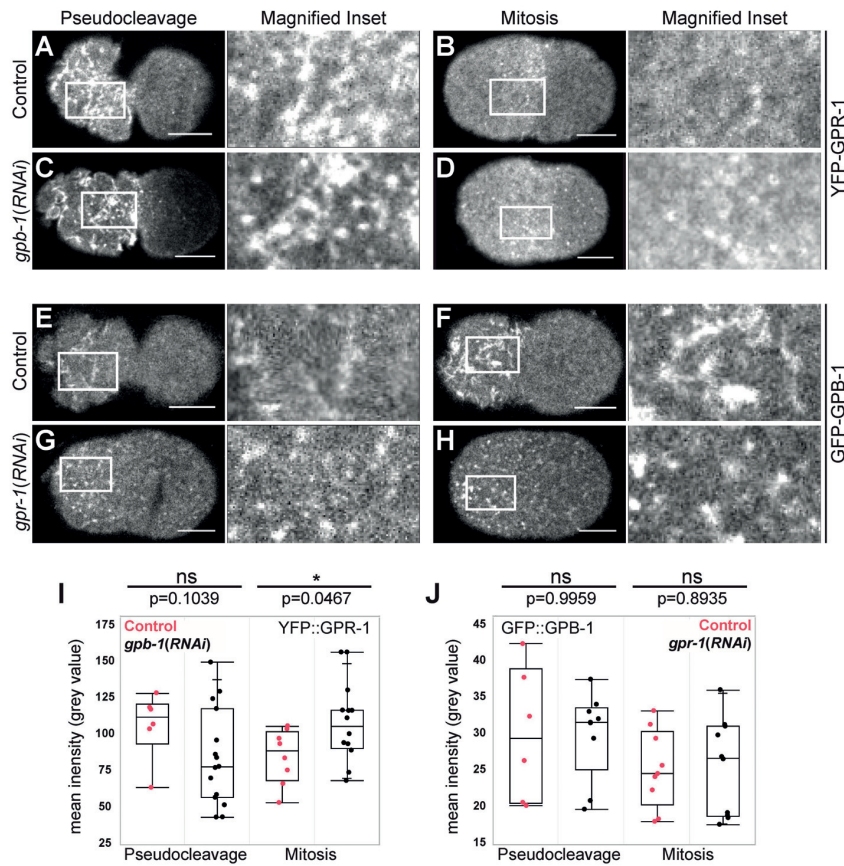
**Figure 52: GPB-1 and GPR-1 (overexpressed) cortical structures form independently from one another. (A-H)** Confocal spinning disk cortical live imaging of embryos harboring the indicated fusion proteins, with high magnification views of the boxed regions shown on the right. (A, B) YFP::GPR-1 control embryos during (A) pseudocleavage, N=6 or (B) mitosis, N=8. (C, D) YFP::GPR-1 embryos upon *gpb-1*(*RNAi*) during (C) pseudocleavage, N=15 or (D) mitosis, N=6. (E, F) GFP::GPB-1 control embryos during (E) pseudocleavage, N=6 or (F) mitosis, N=9. (G, H) GFP::GPB-1 embryos upon *gpr-1/2*(*RNAi*) during (G) pseudocleavage, N=11 or (H) mitosis, N=9. **(I, J)** Box plots of mean intensities of total cortical intensity of embryos shown in (A-H). Statistical analysis was performed using an unpaired t-test.

Although GPR-1 cortical structures form normally upon GPB-1 depletion, we found that their distribution along the AP axis is altered. In control embryos, during centration/rotation, YFP::GPR-1 foci are mainly enriched on the anterior and on the very posterior, but do not localize in a posterior band, likely where LET-99 resides (Figure 53 A, C) (see also 1.2.6, Figure 6) (Krueger et al., 2010; Park and Rose, 2008; Rose and Kemphues, 1998; Tsou et al., 2002). In contrast, upon GPB-1 depletion, YFP::GPR-1 foci enrichment gradually decreases along the AP axis (Figure 53 B, C). Thus, GPB-1 is essential for the proper distribution of YFP::GPR-1 foci along the AP axis, possibly in an indirect manner by determining the proper localization of LET-99 in a posterior band. This has not been observed previously in immunofluorescence stainings of endogenous GPR-1/2,

although the posterior GPR-1/2 domain in $P_1$ was found to be larger in some embryos (Tsou et al., 2003).
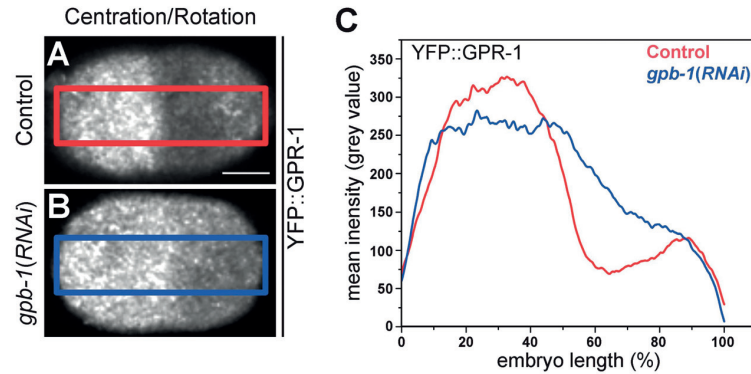


**Figure 53: GPB-1 determines the localization of YFP::GPR-1 foci along the AP axis.(A, B)** Confocal spinning disk cortical live imaging of embryos during centration/rotation expressing YFP::GPR-1 (A) in control conditions, N=11 and (B) upon *gpb-1*(*RNAi*) N=8. Boxed regions indicate areas in which the total cortical intensity of YFP::GPR-1 was determined for the plot profile shown in (C). **(C)** Mean cortical YFP::GPR-1 intensity (16 bit grey value) of control (red) and GPB-1 depleted (blue) embryos plotted along embryo length in %.

### 3.3.5 GPR-1 overexpression increases the amount of and overlap with PIP$_2$ cortical structures

As shown above, we found that GPR-1/2 depletion does not impact PIP$_2$ or GPB-1 cortical structures (Figure 50 E, F and Figure 52 E-H, J). However, we wondered if the overlap of PIP$_2$ cortical structures and GFP::GPB-1 cortical structures might depend on GPR-1. We thus imaged *gpr-1/2*(*RNAi*) embryos expressing mCherry::PH$^{PLC1\delta1}$ and GFP::GPB-1 and found that the overlap does not change during either pseudocleavage or mitosis (Figure 54 A-D).
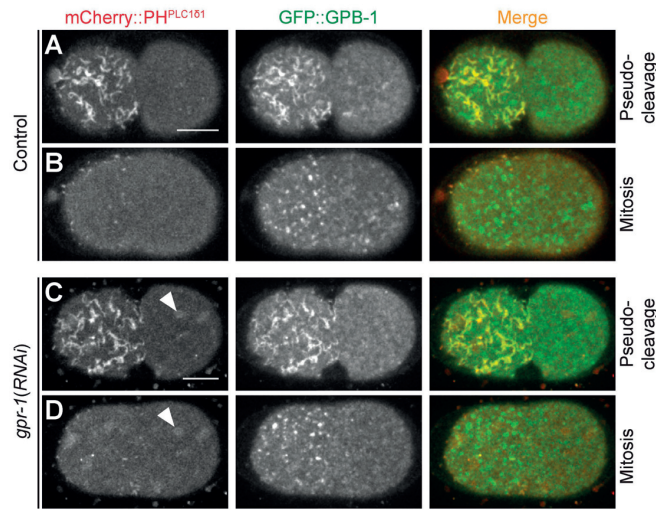
**Figure 54: The overlap of PIP₂ and GPB-1 cortical structures does not depend on GPR-1/2. (A-D)** Dual color confocal spinning disk cortical imaging of embryos expressing mCherry::PH$^{PLC1\delta1}$ and GFP::GPB-1, N=4. Note that the big light blobs in mCherry::PH$^{PLC1\delta1}$ (C, D, arrowheads) correspond to background signals stemming from the coverslip.

We reasoned that we could use mCherry::PH$^{PLC1\delta1}$ to monitor the impact of GPR-1/2 overexpression on GPB-1 cortical structures. We thus imaged embryos overexpressing YFP::GPR-1 (Redemann et al., 2011) crossed to mCherry::PH$^{PLC1\delta1}$. As described above, we found that during pseudocleavage, overexpressed YFP::GPR-1 forms much more elongated cortical structures than endogenously tagged GFP::GPR-1 (Figure 55 A, B; Figure 47 E, G). Hence, the overlap with PIP₂/GPB-1 cortical structures increases; moreover, PIP₂/GPB-1 cortical structures seem to be more abundant compared to control embryos (Figure 55 A, B; Movie 28). YFP::GPR-1 remains strongly enriched on the anterior side also during centration/rotation and mitosis (Figure 55 D, F, H). Moreover, in contrast to GFP::GPR-1 embryos (Figure 55 G, arrowhead), no enrichment is observed on the posterior side in YFP::GPR-1 embryos (Figure 55 H), as shown also above (see Figure 47 E-H). In addition, PIP₂/GPB-1 cortical structures seem more abundant than normal also from the time of centration/rotation until anaphase in YFP::GPR-1 expressing embryos (Figure 55 E-H). During cytokinesis, there is strong ectopic accumulation of YFP::GPR-1 cortical structures close to the anterior of the forming cleavage furrow (Figure 55 J, arrow); such accumulation does not happen in GFP::GPR-1 embryos (Figure 55 I). Intriguingly, PIP₂/GPB-1 cortical structures also start to accumulate at this location, overlapping with YFP::GPR-1 cortical structures (Figure 55 I). Overall, we conclude that YFP::GPR-1 overexpression increases not only the formation of ectopic YFP::GPR-1-containing structures, but also of PIP₂/GPB-1 cortical structures, at sites coincident with

YFP::GPR-1. As GPB-1 is a negative regulator of GPR-1/2, one possibility is that this represents a feedback mechanism whereby $PIP_2$/GPB-1 counteracts the increased forces produced by YFP::GPR-1 overexpression.
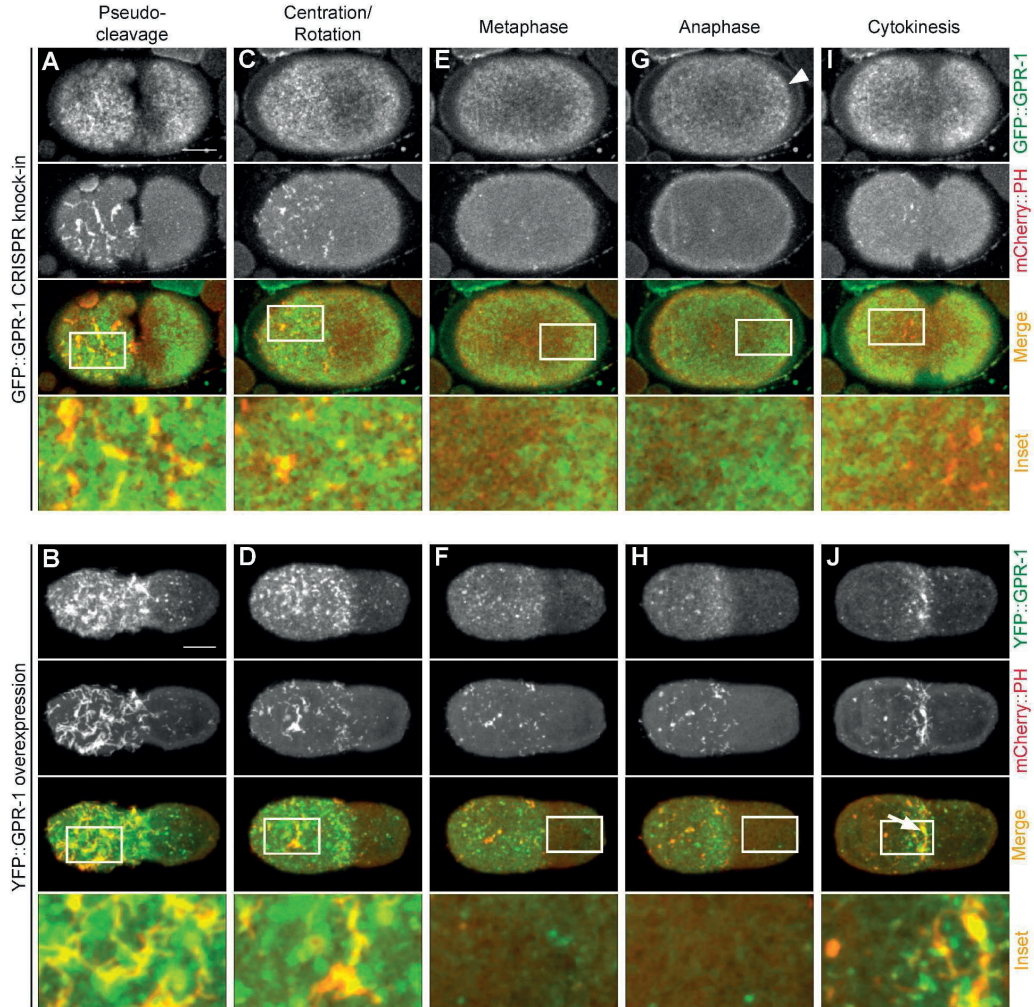


**Figure 55: GPR-1 overexpression leads to the formation of ectopic GPR-1 and PIP₂ cortical structures. (A-J)** Dual color confocal spinning disk cortical imaging of embryos expressing mCherry::PH$^{PLC1\delta1}$ and endogenously tagged GFP::GPR-1, N=10. Magnified insets are shown below. (A, C, E, G, I) or mCherry::PH$^{PLC1\delta1}$ and overexpressed YFP::GPR-1, N=6 (B, D, F, H, J) at indicated stages. Note that GPR-1 clearly enriches at the posterior only during anaphase and only in embryos expressing endogenously tagged GFP::GPR-1 (G, arrowhead). Also note the clear formation of ectopic cortical structures harboring both GPR-1 and PIP₂ during cytokinesis (J, arrow). See also Movie 28.

We next quantified the apparent increase in $PIP_2$/GPB-1 cortical structures upon YFP::GPR-1 overexpression. We found that $PIP_2$/GPB-1 cortical structures cover approximately twice as much of the anterior cortex as in control embryos, and this during both pseudocleavage and mitosis (Figure 56 A-H). In addition, the size of $PIP_2$/GPB-1 cortical structures increases slightly, and becomes somewhat more elongated upon YFP::GPR-1

overexpression (Figure 56 C, G, D, H). We also found that in embryos overexpressing YFP::GPR-1, mitosis takes approximately twice as long as in control embryos (Figure 56 B, F). Previous findings showed that abnormal mitotic spindle assembly can delay mitosis in the early *C. elegans* embryo by activating the spindle assembly checkpoint (Encalada et al., 2004). Maybe too much spindle pulling forces in embryos overexpressing GPR-1 damage the spindle or result in attachement issues of microtubules to kinetochores, which then activates the spindle assembly checkpoint. Overall, these results confirm that upon YFP::GPR-1 overexpression, the formation of $PIP_2$/GPB-1 cortical structures increases.
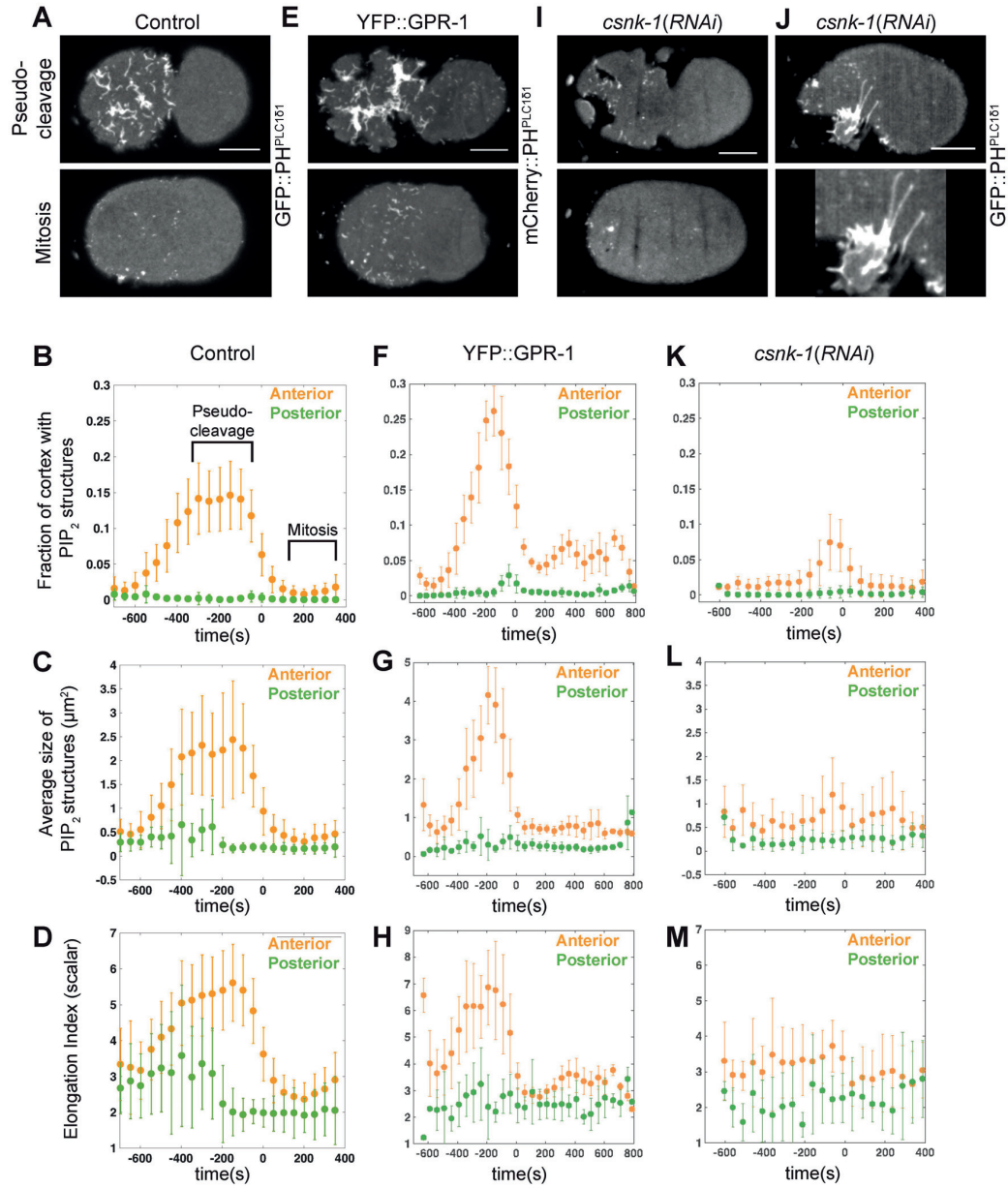
**Figure 56: GPR-1 overexpression increases and CSNK-1 depletion decreases the formation of PIP₂ cortical structures.(A, E, I, J)** Cortical plane at pseudocleavage and mitosis from spinning disk confocal imaging of control (A, N=39), *gpr-1/2*(*RNAi*) (E, N=6), *csnk-1*(*RNAi*) (I, N=12/15, see also Movie 29) or *csnk1-1*(*RNAi*) (J, N=3/15, see also Movie 30) embryos expressing GFP::PH$^{PLC1\delta1}$ (A, I, J) or mCherry::PH$^{PLC1\delta1}$ (E). **(B, F, K)** Fraction of cell cortex covered by segmented PIP₂ structures over time in control (B), YFP::GPR-1 overexpressed (F), and *csnk-1*(*RNAi*) (K) embryos. **(C, G, L)** Average size of segmented PIP₂ cortical structures over time in control (C), YFP::GPR-1 overexpressed (G), and *csnk-1*(*RNAi*) (L) embryos. **(D, H, M)** Elongation Index of segmented PIP₂ cortical structures over time in control (D), YFP::GPR-1 overexpressed (H), and *csnk-1*(*RNAi*) (M) embryos; larger values correspond to more elongated structures.

The increase of PIP$_2$/GPB-1 cortical structures in YFP::GPR-1 overexpressing embryos could either result from too much GPR-1 protein being present, or else as a consequence of too much cortical forces generated as a consequence. We reasoned that depleting CSNK-1, which also leads to increased cortical forces, might enable us to distinguish between these possibilities. Surprisingly, instead of an increase in PIP$_2$/GPB-1 cortical structures, we found that the amount of PIP$_2$/GPB-1 cortical structures decreases in a dramatic manner (Figure 56 I, K; Movie 29). In addition, PIP$_2$/GPB-1 cortical structures become smaller and rounder in *csnk-1*(*RNAi*) embryos (Figure 56 L, M). Interestingly, in 3/15 embryos, we also found very elongated PIP$_2$/GPB-1 cortical structures, which seem to connect different parts of the overly contractile cortex (Figure 56 J; Movie 30). Overall, we found that CSNK-1 positively regulates the formation of PIP$_2$ cortical structures. Moreover, these results show that the increase of PIP$_2$ cortical structures upon YFP::GPR-1 overexpression is not observed in all cases with increased cortical forces, leading us to speculate that is might be caused by an increase in GPR-1 protein itself.

### 3.3.6 CSNK-1 regulates the cortical distribution of PPK-1.

CSNK-1 was reported to negatively regulate the localization of PPK-1 at the anterior cortex (Panbianco et al., 2008). It is thus surprising that the depletion of CSNK-1 should lead to a decrease of PIP$_2$ cortical structures. We set out to test the cortical distribution of PPK-1::mGFP in *csnk-1*(*RNAi*) embryos. This analysis revealed that, during pseudocleavage, PPK-1 cortical structures are indeed strongly decreased in such embryos, as is the case for PIP$_2$ cortical structures (Figure 57 A, B; Movie 31). From this, we conclude that CSNK-1 positively regulates the enrichment of PPK-1 at anterior cortical structures during pseudocleavage, which might promote local PIP$_2$ generation. In contrast to the decreased localization of PPK-1::mGFP at anterior cortical structures, we found an increase of overall PPK-1 cortical levels on the anterior at locations devoid of PIP$_2$ cortical structures during pseudocleavage (Figure 57 B, arrowhead). Moreover, during mitosis, while 10/12 control embryos exhibit a posterior enrichment of PPK-1 enrichment, we found that in CSNK-1 depleted embryos, only 1/6 embryos had a very weak PPK-1 posterior enrichment (Figure 57 C-F). In contrast, mCherry::PH$^{PLC1\delta1}$ remained essentially evenly distributed along the AP axis in control and CSNK-1-depleted embryos during pseudocleavage and mitosis if PIP$_2$ cortical structures are not taken into account (Figure 57 G, H). To summarize, we conclude that CSNK-1 positively regulates the localization of PPK-1 to cortical structures in the anterior and to the posterior cortex. Moreover, while PPK-1 levels at cortical structures in the anterior side correlate with the level of PIP$_2$, this is not the case in cortical areas around them.
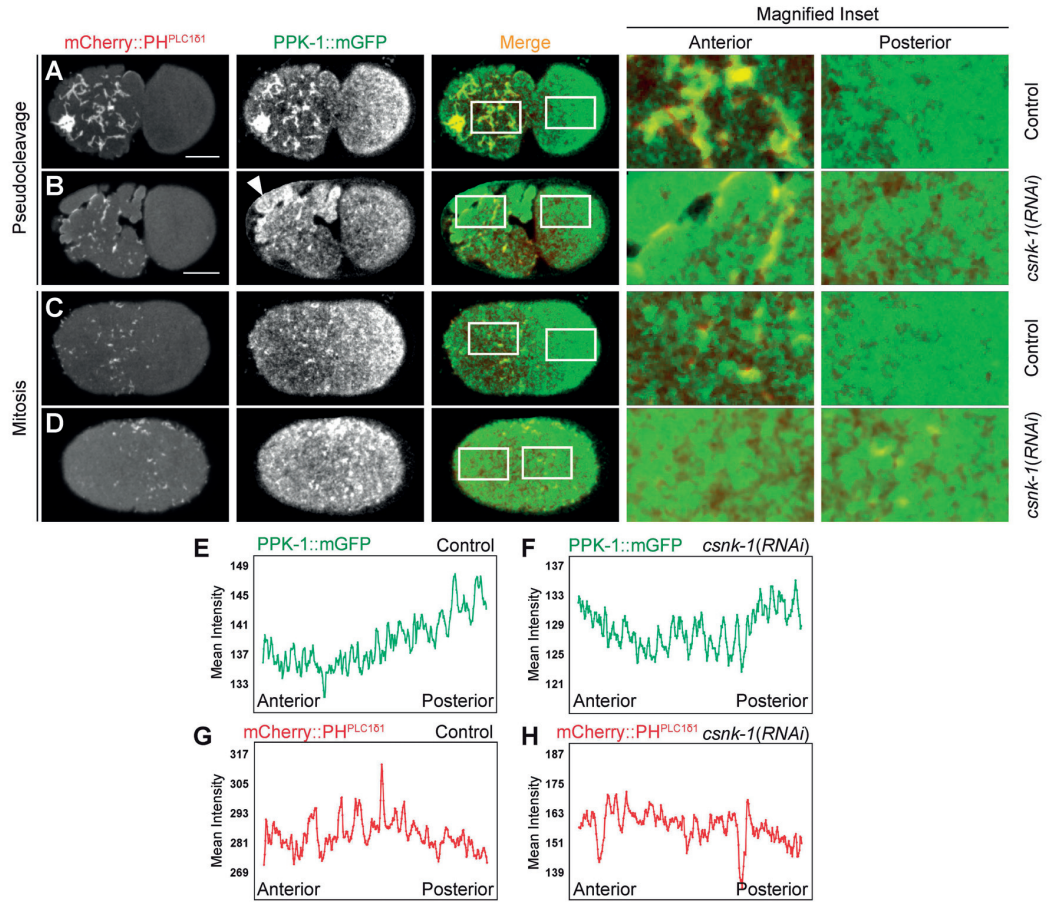
**Figure 57: CSNK-1 depletion changes the cortical distribution of PPK-1.(A-D)** Images acquired by dual color cortical confocal live imaging of *C. elegans* embryos expressing mCherry::PH$^{PLC1\delta1}$ and PPK-1::mGFP at indicated stages of control (A,C; N=10) and *csnk-1*(*RNAi*) (B, D; N=6, see also Movie 31) embryos. Boxed regions in the anterior and posterior are magnified on the right. **(E-H)** Mean intensity (grey values) of PPK-1::mGFP (E, F) mCherry::PH$^{PLC1\delta1}$ and mCherry::PH$^{PLC1\delta1}$ (G, H) measured along the AP axis in control (E,G; N=12) and *csnk-1*(*RNAi*) (F, H; N=6) embryos.

Altogether, positive force generator components and negative regulators form distinct cortical structures that do not overlap in large part. Thus, their opposite function is also largely represented in their cortical distribution (Figure 58 A-E). Elongated cortical structures of the negative force regulator GPB-1 perfectly overlap with PIP$_2$ cortical structures monitored by mCherry-PH$^{PLC1\delta1}$ during pseudocleavage and depend on the correct level of PIP$_2$ (Figure 58 F). Moreover, the formation of GPB-1/PIP$_2$ cortical structures depends on GPR-1 overexpression and CSNK-1 depletion in the opposite manner, although both conditions lead to increased spindle pulling forces (Figure 58 G).
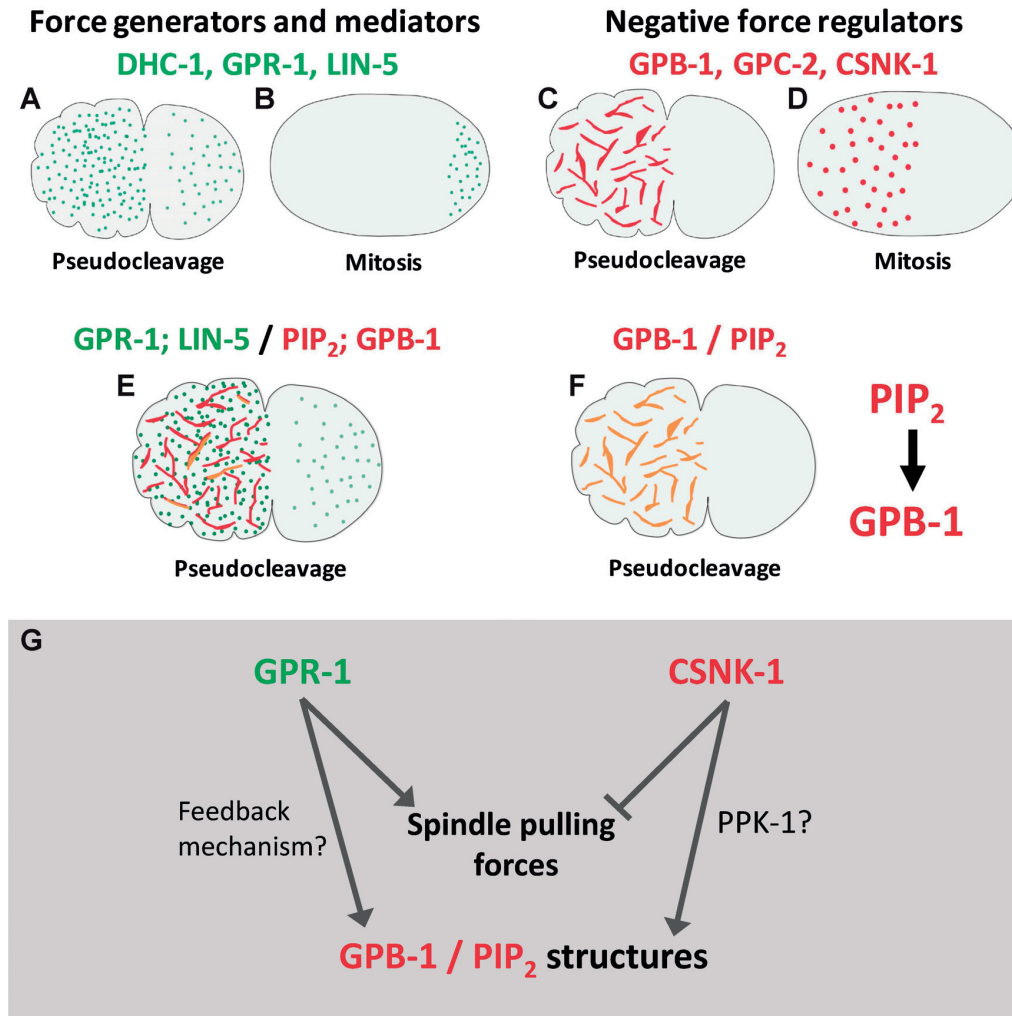
**Figure 58: Schematic summary of cortical structures of force generation components and regulators.**
**(A, B)** Positive force generation components such as DHC-1, GPR-1, and LIN-5 form small cortical foci during pseudocleavage and mitosis, which are enriched on the very posterior during mitosis. **(C, D)** Negative force regulators, such as GPB-1, GPC-1, and CSNK-1, form elongated cortical structures on the anterior during pseudocleavage and foci enriched on the anterior during mitosis. **(E)** Cortical structures of positive force generation components and negative regulators show no substantial overlap. **(F)** Elongated cortical structures during pseudocleavage of GFP::GPB-1 and PIP$_2$ monitored by mCherry::PH$^{PLC1\delta1}$ perfectly overlap. PIP$_2$ cortical structures form and distribute independent of GPB-1, while the formation and localization of GFP::GPB-1 cortical structurs depends on the correct level of PIP$_2$. **(G)** Strong overexpression of YFP::GPR-1 increases the formation of GPR-1 cortical structures and PIP$_2$/GPB-1 cortical structures, which overlap in large part. However, depletion of CSNK-1, which increases spindle pulling forces in a similar manner to YFP::GPR-1 overexpression, decreases the formation of PIP$_2$/GPB-1 cortical structures. This might be mediated by the regulation of PPK-1 through CSNK-1.

# 4. Discussion

In this thesis work, we demonstrate that $PIP_2$ forms cortical structures in the one-cell *C. elegans* embryo. We show that the formation and movement of these structures depend on F-actin and, reciprocally, that $PIP_2$ regulates F-actin organization, revealing an interdependence of these two components in the worm zygote (Figure 45). Moreover, likely through its impact on the actin cytoskeleton, $PIP_2$ is also needed for the correct sizing of PAR domains, demonstrating that a plasma membrane lipid component participates in setting AP polarity in the *C. elegans* embryo.

In addition, we reveal that force generation mediators and negative force regulators, which are essential for proper positioning of the mitotic spindle, also form distinct cortical structures. $PIP_2$ cortical structures fully overlap with elongated cortical structures of the negative force regulators GPB-1 and CSNK-1 during pseudocleavage, but not with cortical foci of GPR-1 and LIN-5. Furthermore, we find that an increase of GPR-1 cortical structures causes a likewise increase of overlapping $PIP_2$/GPB-1 cortical structures, possibly possibly through a negative feedback mechanism.

## 4.1 $PIP_2$ is present in discrete cortical structures in *C. elegans* zygotes

The distribution and dynamics of $PIP_2$ at the plasma membrane of early *C. elegans* embryos were not clear prior to this work, primarily because the middle embryo plane was analyzed in past investigations. Here, we assayed subcellular distributions at the cortex, where the function of PAR proteins and components critical for asymmetric division is exerted. We thus discovered that $PIP_2$ is present in dynamic polarized cortical structures marked by the $PIP_2$ biomarker GFP::PH$^{PLC1\delta1}$ and Bodipy-FL-$PIP_2$, in line with recent observations mentioning a non-uniform distribution of the fusion protein (Rodriguez et al., 2017; Wang et al., 2017). Although patches of plasma membrane enriched in $PIP_2$ have been observed in other systems (Golub and Caroni, 2005; reviewed in Chierico et al., 2015; McLaughlin et al., 2002; Zhang et al., 2012), the stereotyped progression through the first cell cycle of the large worm zygote enabled us to probe such cortical structures with unprecedented resolution. Why were these structures not observed in previous studies in the worm? In addition to the fact that they are not noticeable when imaging the middle plane of the embryo, other plausible reasons are that $PIP_2$

cortical structures appear only transiently during the cell cycle and that they are not preserved upon fixation.

How do $PIP_2$ cortical structures assemble? $PIP_2$ cortical structures could form either by redistribution of existing $PIP_2$ or by *de novo* synthesis through PIP5K1. In other systems, $PIP_2$ has been suggested to diffuse much faster than it is synthesized (reviewed in McLaughlin et al., 2002), such that potential local synthesis alone is unlikely to dictate restricted $PIP_2$ localization. However, we found that PPK-1, the sole PIP5K1 in *C. elegans*, is enriched at $PIP_2$ cortical structures, which suggests that $PIP_2$ generation contributes to enhancing $PIP_2$ cortical structures formation. This view is supported by the finding that a decrease of PPK-1 enrichment at $PIP_2$ cortical structures upon CSNK-1 depletion coincides with a decrease of $PIP_2$ cortical structures. Previously, PPK-1 has been reported to be enriched in the posterior of the embryo (Panbianco et al., 2008), but the distribution of the protein had not been assessed at the cortex, but solely in the middle plane of the embryo. The enrichment of PPK-1 at anteriorly localized $PIP_2$ cortical structures, in addition to its posterior enrichment, could only been uncovered by cortical live imaging. This emphasizes again the importance of assaying the subcellular distributions of such proteins at the embryo cortical plane, where they exert their function.

Interestingly, we find also that $PIP_2$ cortical structures form and move independently of actomyosin contractions powered by NMY-2. Nevertheless, it remains possible that $PIP_2$ cortical structures form at membrane protrusions or ruffles. This would be consistent with $PIP_2$ stimulating F-actin polymerization in curved but not flat membranes (Gallop et al., 2013), and accumulating in membrane ruffles, nascent phagosomes and the leading edge of motile cells, which are all sites of actin reorganization (reviewed in McLaughlin et al., 2002; Zhang et al., 2012). Moreover, in curved membranes, $PIP_2$ stimulates F-actin polymerization, functioning in this role together with Cdc42 (Gallop et al., 2013). Interestingly, we find also CDC-42 and a biosensor for active CDC-42 to be enriched at $PIP_2$ cortical structures. In other systems, increased $PIP_2$ induces actin polymerization around membrane vesicles, generating actin comets that then propel vesicles forward (Ma et al., 1998; Rozelle et al., 2000). We also observed occasional vesicles and connected local F-actin accumulation upon increasing $PIP_2$, although no actin comets were observed in these embryos (data not shown). In summary, we propose that $PIP_2$ cortical structures form in the *C. elegans* zygote through $PIP_2$ generation by PPK-1, maybe supported by the redistribution of existing $PIP_2$ at the plasma membrane, perhaps preferentially at membrane protrusions or ruffles.

## 4.2 Interdependence of PIP$_2$ and F-actin

PIP$_2$ and F-actin exhibit a reciprocal relationship in a number of systems, and we uncover here that this is the case also in *C. elegans*. We find that PIP$_2$ cortical structures and F-actin movements are coupled, with PIP$_2$ structures moving slightly ahead, at velocities compatible with actin polymerization driving these movements. Moreover, impairing the profilin PFN-1, which is essential for microfilament assembly (Severson et al., 2002; Velarde et al., 2007), reveals that PIP$_2$ structure movements are actin driven. This leads us to propose that actin polymerization pushes PIP$_2$ cortical structures, in a manner reminiscent of other actin-dependent motility processes such as that of *Listeria monocytogenes* (reviewed in Mogilner and Oster, 1996). While being pushed ahead of F-actin in *C. elegans*, PIP$_2$ structures might recruit factors promoting actin polymerization and branching, such as ECT-1, RHO-1 and CDC-42, thus guiding F-actin network reorganization, as in other systems (Desrivières et al., 1998; reviewed in McLaughlin et al., 2002; De Craene et al., 2017; Brown, 2015; Yin and Janmey, 2003; Zhang et al., 2012; Wu et al., 2014; Di Paolo and De Camilli, 2006). Intriguingly, a biosensor for active CDC-42 distributes on the cortex like PIP$_2$ in other systems (Cheng et al., 2015; Kumfer et al., 2010). Consistent with this result, we found that the active CDC-42 biosensor is enriched at PIP$_2$ cortical structures, indicating that CDC-42 at PIP$_2$ structures is active. By contrast, the distribution of a biosensor for active RhoA overlaps with that of NMY-2 (Reymann et al., 2016; Tse et al., 2012). The fact that we show here that PIP$_2$ cortical structures do not overlap with NMY-2, whereas they overlap with GFP::RHO-1, suggests that the bulk of RHO-1 associated with PIP$_2$ cortical structures is inactive. However, we found a partial and very temporary overlap of active RHO-1 with PIP$_2$ cortical structures, raising the possibility that a subpopulation of RHO-1 at PIP$_2$ cortical structures is active. Nevertheless, it is surprising that the bulk of RHO-1 at PIP$_2$ cortical structures might be inactive, given that RHO-1 colocalizes with its activating GEF ECT-2, suggesting that the RhoA biosensor might not detect all active RHO-1 species. Furthermore, it is interesting that non-muscle myosin 2 contributes to actin network disassembly in fish keratinocytes (Wilson et al., 2010). Extrapolating from this observation, it is tempting to speculate that PIP$_2$, by promoting F-actin assembly, and NMY-2, by promoting F-actin disassembly (Wilson et al., 2010), in addition to powering network contractility, may together ensure proper F-actin dynamics in *C. elegans* embryos.

## 4.3 PIP$_2$ and PAR-dependent polarity

PAR proteins are also distributed unevenly within their domain. Thus, cortical PAR-6 exists in two populations, one diffuse that depends on CDC-42, and one punctate that colocalizes with PAR-3 (Beers and Kemphues, 2006; Robin et al., 2014). Moreover, PAR-3

forms clusters crucial for proper polarity that assemble in a manner dependent on PCK-3, CDC-42, as well as actomyosin contractility (Rodriguez et al., 2017; Wang et al., 2017). Intriguingly, we find that PIP$_2$ cortical structures colocalize within the more diffuse cortical PAR-6 population, which lacks PAR-3 (Beers and Kemphues, 2006; Robin et al., 2014; Rodriguez et al., 2017; Wang et al., 2017). Moreover, we establish that increasing PIP$_2$ augments the segregation of both populations of PAR-6 to the anterior. As clustering of PAR-3 depends on actomyosin reorganization (Rodriguez et al., 2017; Wang et al., 2017), we propose that increasing the level of PIP$_2$ might reorganize the actin cytoskeleton in a way that promotes PAR-3 clustering and thereby aids segregation.

PAR proteins and the actomyosin network are established players that regulate cell polarity in the *C. elegans* zygote. In contrast, how plasma membrane components such as phospholipids might be involved in polarity regulation has been only poorly investigated. Here, we show that a correct PIP$_2$ level is essential for proper polarity establishment and maintenance. We found that increasing the level of PIP$_2$ by the simultaneous depletion of two PIP$_2$ 5-phosphatases leads to two possible outcomes, with intermediate situations. In some embryos, the actomyosin flow cannot be initiated properly (class 2) and therefore the posterior domain stays very small, whereas the anterior domain is very expanded. Such class 2 embryos often do not divide, and thus the root of this phenotype may be thought of as being rather unspecific. If, on the other hand, an actomyosin flow towards the anterior can be generated properly (class 1), PAR polarity domains are continuously resized. Since most embryos showing the class 1 phenotype divide successfully, the increase of PIP$_2$ level in these embryos is most likely more moderate than in class 2 embryos. Overall, we think that the class 1 phenotype shows more specifically the impact of increased PIP$_2$ levels on cortical flows. The continuous flow towards the anterior in class 1 embryos constantly alters the relative size of anterior and posterior PAR domains also during the maintenance phase. Hence, in a way, the maintenance phase becomes an extension of the establishment phase. This is reminiscent of changes in PAR domain sizing that occur upon RGA-3/4 depletion (Schonegg et al., 2007). However, whereas *rga-3/4*(*RNAi*) embryos exhibit a hypercontractile actomyosin network, this is not the case of embryos with increased PIP$_2$ level. We thus propose that actomyosin contractility regulated by NMY-2, and F-actin organization regulated by PIP$_2$, together contribute in concert to correct movements of the actomyosin network, and, therefore, proper sizing of PAR polarity domains.

Given that moderately increasing total PIP$_2$ levels increases the cortical flow towards the anterior, one could imagine that depleting PIP$_2$ from the embryo would do the opposite, namely diminishing cortical flows. When we deplete PIP$_2$, we observe that the pseudocleavage furrow remains ingressed for much longer than in the control condition. Moverover, the pseudocleavage furrow continuously keeps moving towards the anterior side. Therefore, surprisingly, embryo flows superficially seem to increase also in PIP$_2$ depleted embryos. We hypothesize that in such embryos the pseudocleavage

furrow keeps moving towards the anterior because proper F-actin polymerization regulated by $PIP_2$ does not take place anymore after $PIP_2$ depletion and, therefore, that the F-actin network just "collapses" towards the anterior side, with the contracted pseudo-cleavage furrow following it. Together, we suggest that moderately increasing $PIP_2$ level increases F-actin polymerization and reorganization, leading to increased flow towards the anterior. In contrast, depletion of $PIP_2$ leads to decrease of proper actin polymerization and thus F-actin "collapses" because of NMY-2-depending contractions exerted on this network.

Moreover, we suggest that $PIP_2$ is essential for symmetry breaking and polarity establishment, as depletion of $PIP_2$ before these events abolishes PAR-2 removal from the cortex and formation of a posterior PAR-2 domain. CDC-42 is essential to remove PAR-2 from the cortex and to localize PAR-6 to the cortex during meiosis II (Schonegg et al., 2007). Maybe $PIP_2$ function upstream of, or together with, CDC-42 during this initial process. In the 8-cell stage mouse embryo, PLC-mediated cleavage of $PIP_2$ is essential to trigger symmetry breaking and establishment of actomyosin and PAR polarity (Zhu et al., 2017). Perhaps $PIP_2$ functions in an analogous manner in the *C. elegans* embryo.

## 4.4 On the role of the actomyosin network in polarity establishment and maintenance

The actomyosin network plays a well-established role during polarity establishment, whereas its role during polarity maintenance has been a matter of debate (Goehring et al., 2011; Hill and Strome, 1990; Liu et al., 2010a; Severson and Bowerman, 2003). Our results, together with those of others, indicate that the actomyosin network regulates PAR domains in two ways. First, when the actomyosin network moves anteriorly during the establishment phase, PAR domains alter their distribution accordingly. This relationship was clear prior to this work, and we demonstrate here that this is also the case during polarity maintenance. Second, actin has been suggested to play merely a passive role during the maintenance phase in preventing cortical PAR-2 removal through membrane invaginations driven by microtubules (Goehring *et al.,* 2011). We reveal here that this can lead to the near total disappearance of cortical GFP::PAR-2, further emphasizing the critical importance of actin also during the maintenance phase.

Overall, our results in *C. elegans* are consistent with the role of $PIP_2$ in F-actin reorganization and polarity in other organisms. Previous work in *C. elegans* showed that depletion of CSNK-1, which negatively regulates PPK-1 localization, although perturbing spindle positioning, does not impact cell polarity during cytokinesis (Panbianco et al., 2008). By contrast, we establish here that alterations in the level of $PIP_2$ impair polarity

establishment and maintenance during the first asymmetric division of *C. elegans* embryos. Depleting CSNK-1, we observed that after polarity establishment, a flow from the anterior to the posterior is initiated in embryos expressing GFP::PH$^{PLC1\delta1}$, YFP::GPR-1, and GFP::moe, leading to the disappearance of the anterior PIP$_2$, GPR-1, and F-actin domain (data not shown). Thereafter, a flow from the posterior back to the anterior is initiated, altogether leading to a variable distribution of cortical PIP$_2$, GPR-1 and F-actin from embryo to embryo. The result that CSNK-1 depletion impacts cortical flows are consistent with findings that *csnk-1*(*RNAi*) embryos have excess cortical activity (Fievet et al., 2013), disturbed rotational cortical flows during the first and second cell division (Singh and Pohl, 2014), and increased cortical invaginations during meiosis caused by defective myosin patches disassembly (Flynn and McNally, 2017). Together, these findings strongly suggest that PAR polarity is also defective in embryos depleted of CSNK-1, as cortical flows of the actomyosin network determine PAR polarity. Moreover, PAR domains can be transported and even PAR polarity can be inverted by cortical flows alone (Mittasch et al., 2018). The finding of Panbianco *et al.* that PAR polarity is normal in *csnk-1*(*RNAi*) embryos is thus very surprising and should be re-visited.

## 4.5 Cortical structures of force generation mediators and regulators.

We found that the force generation mediators GPR-1 and LIN-5, as well as the negative force regulators GPB-1 and CSNK-1, form distinct cortical structures. GPB-1 and CSNK-1 elongated cortical structures only partially overlap with a subpopulation of cortical GPR-1 and LIN-5. Thus, force generation promoters and negative force regulators are not only distinct in their activity during mitotic spindle positioning, but also in their subcortical localization, which could be a prerequisite for their proper function. Interestingly, PIP$_2$ distributes essentially in the same way as negative force regulators at the cortex during pseudocleavage, which suggests that the PIP$_2$ population enriched at cortical structures could also negatively regulate forces. However, during mitosis, when spindle positioning takes place, cortical structures of GPB-1 and PIP$_2$ do not show much overlap. In addition, decreasing the level of PIP$_2$ did not suggest a major impact on cortical pulling forces, as merely the end position of the spindle was more variable (Figure 34). Nevertheless, in most embryos completely depleted of PIP$_2$, spindle positioning could not be assessed (see 3.2.1). Moreover, when PIP$_2$ level is increased, the oscillations of the posterior spindle pole, as determined from their maximum velocity, decrease significantly (Figure 38 G). This would again argue for a negative regulation of spindle pulling forces by PIP$_2$. GPB-1 and GPR-1 compete for Gα binding (Afshar et al., 2004; Afshar et al., 2005; Tsou et al., 2003). Thus, the sites at which GPB-1 and GPR-1 partially overlap might represent areas where such competition is happening. To monitor the cortical distribution of Gα,

we set out to generate a fluorescently tagged Gα worm line (see 7.3), but did not find the time to actually produce it during the course of this thesis work. In the absence of such a line, we would predict Gα to localize all over the cortex, but being enriched at the minimum at the following three subcortical domains: first, where there are only GPB-1 cortical structures; second, where there are only GPR-1 cortical structures; and third, in places where GPB-1 and GPR-1 overlap. In human cells, live imaging of GFP-tagged Gα revealed that Gα is localized throughout the cortex. In addition, in some cases distinct patches of Gα in the plasma membrane were observed (Hughes et al., 2001; Sheridan et al., 2002). Overexpression of YFP::GPR-1, which increased GPR-1 cortical structures, also increased GPB-1 cortical structures monitored by mCherry-PH$^{PLC1\delta1}$, with a significant overlap with GPR-1 cortical structures. Thus, we speculate that an increase in GPR-1 cortical structures might engage a feedback mechanism that increases GPB-1 cortical structures in an attempt to compensate for the increase in cortical forces. However, depletion of CSNK-1, which also increases cortical pulling forces, has the opposite effect and instead decreases GPB-1/PIP$_2$ cortical structures. Thus, the increase of GPB-2/PIP$_2$ cortical structures might be a specific response to an increase of GPR-1 protein, and not to an increase in cortical pulling forces. It should be stated also that YFP::GPR-1 overexpression and CSNK-1 depletion might increase cortical forces through different mechanisms, and the two conditions thus might not be fully comparable. Moreover, in contrast to the merely partial overlap of GPB-1 and GPR-1, anterior cortical structures of GPB-1 and CSNK-1 fully overlap during pseudocleavage. Therefore, the fact that depletion of CSNK-1 decreases GPB-1/PIP$_2$ cortical structures could reflect instead the fact that GPB-1 and CSNK-1 are coupled and interdependent for their localization.

Overexpressed YFP::GPR-1 exhibits a different cortical localization than endogenously tagged GFP::GPR-1. Thus, one could imagine that other transgenic fusion proteins, including GFP::GPB-1, might also exhibit altered cortical distribution compared to the endogenous proteins. However, this issue likely pertains solely to YFP::GPR-1, since this fusion protein was designed purposefully to be strongly overexpressed, through codon usage optimization and insertion of synthetic introns. In contrast, all other transgenic fusion proteins analyzed in this work were generated by micro-particle bombardment using the cognate sequence corresponding to the mRNA. This usually leads to single-copy or low-copy number chromosomal insertions. Moreover, large extrachromosomal arrays are silenced in the germline due to repetitive sequences (Praitis et al., 2001; Wilm et al., 1999; reviewed in Green et al., 2008). The above considerations indicate that, in contrast to YFP::GPR-1, the other transgenic fusion proteins are not overexpressed and suggests that their cortical distributions resembles that of the corresponding endogenous proteins. This inference is supported for GFP::GPB-1 by the following facts. First, GFP::GPB-1 and GFP::GPC-2 distribute in the same way (Figure 47 A-D). Second, in immunofluorescence stainings using GPB-1 antibodies of GFP::GPB-1 and endogenous GPB-1, imaged in the middle plane, proteins levels appear to be similar (Thyagarajan et al., 2011). Third, embryos expressing transgenic GFP::GPB-1 do not exhibit a

phenotype (Thyagarajan et al., 2011), whereas embryos with excess GPB-1 function would be expected to exhibit less pulling forces. Overall, we conclude that the expression levels of transgenic GFP::GPB-1 are likely to be comparable to those of endogenous GPB-1.

We found that GPR-1 and LIN-5 form foci that could conceivably be sites of active force generation. The fact that negative force regulators do not overlap with these foci supports this hypothesis. Partial depletion of the actomyosin network leads to cortical invagination that mark sites of force generation (Redemann et al., 2010). We found that these invaginations appear as foci at the cell cortex. Testing the overlap of these foci with GPR-1 and LIN-5 foci could reveal if GPR-1 and LIN-5 foci are indeed place of force generation. How do GPR-1 and LIN-5 foci form? One possibility is that GPR-1 and LIN-5 form higher order oligomers similar to their mammalian homologues LGN and NUMA that form functional hetero-hexamers in mammary stem cells driving spindle positioning (Mapelli, M; Mechanisms of asymmetric cell division, Theo Murphy Meeting, November 2016).

GPR-1 cortical structures form normally upon GPB-1 depletion, but their distribution is altered since the clear cortical band usually devoid of GPR-1 is not visible (Krueger et al., 2010; Park and Rose, 2008; Rose and Kemphues, 1998; Tsou et al., 2002). Therefore, GPB-1 is essential for the proper distribution of YFP::GPR-1 foci, probably due to LET-99-dependent exclusion. LET-99 was shown to be a negative regulator of cortical GPB-1 levels (Tsou et al., 2003). Here, we show indirectly, that vice versa, GPB-1 seems also important for proper cortical LET-99 distribution.

Increasing the level of $PIP_2$ reveals that proper $PIP_2$ level is essential for the formation of GPB-1 cortical structures, but not for GPR-1 foci. This is not surprising given that $PIP_2$ cortical structures overlap with the former, but not with the latter. Moreover, the $PIP_2$ level regulates the distribution of GPB-1 cortical structures, but seems to influence only partially the distribution of GPR-1 along the AP axis (data not shown). Altogether, this supports the hypothesis that $PIP_2$ cortical structures, together with GPB-1, negatively regulate forces rather than promoting them. In contrast, PPK-1 enriched on the embryo posterior might positively contribute to force generation, perhaps through its role in $PIP_2$ generation (Panbianco et al., 2008). Although PPK-1 is enriched on the posterior, we did not detect posterior $PIP_2$ enrichment, suggesting that the function of PPK-1 in recruiting GPR-1 to the posterior might be independent of $PIP_2$ generation.

$PIP_2$ cortical structures form independent of GPB-1 but the formation and localization of GPB-1 cortical structures depends on $PIP_2$. How could Gβ be recruited to $PIP_2$ cortical structures? Together with $PIP_2$, purified bovine Gβ binds in a cooperative manner to the PH domain of purified bovine β-Adrenergic Receptor Kinase *in vitro* (Pitcher et al., 1995; Touhara, 1997; Touhara et al., 1994). Moreover, in human cells, Gβ proteins can interact with different Rho GEFs, which then activate Rho GTPases such as Cdc42,

leading to actin polymerization and reorganization (Niu et al., 2003; Runne and Chen, 2013; Ueda et al., 2008; reviewed in Aittaleb et al., 2010). Altogether, it could thus be possible that GPB-1 is recruited to $PIP_2$ cortical structures by binding to the PH domain of a protein or interacting in another way with a protein that also binds $PIP_2$.

CSNK-1 negatively regulates forces (Panbianco et al., 2008). Consistent with its function, CSNK-1 subcortical distribution resembles that of $PIP_2$ and also of GPB-1 during pseudocleavage. Moreover, CSNK-1 was reported to negatively regulate PPK-1 localization on the anterior, leading to a PPK-1 enrichment at the posterior (Panbianco et al., 2008). Also in yeast, the casein kinase I homologues Yck1/2 negatively regulate plasma membrane association of the yeast PI4P5K Mss4 by direct phosphorylation of Mss4 (Audhya and Emr, 2003). Surprisingly, we found that both PPK-1 and CSNK-1 are enriched at $PIP_2$ cortical structures. Moreover depletion of CSNK-1 leads to a decrease of PPK-1 cortical structures and $PIP_2$ cortical structures, while at the same time increasing the overall level of anterior PPK-1. This overall increase of the PPK-1 level at the anterior, however, is not correlated with an increase in the overall $PIP_2$ level at the anterior. Perhaps a cue activating PPK-1 is present at $PIP_2$/PPK-1 cortical structures. Alternatively, a cue inhibiting PPK-1 kinase activity at the cortex is absent at $PIP_2$/PPK-1 cortical structures. Overall, CSNK-1 does not only positively regulate PPK-1 enrichment at the posterior, as previously reported (Panbianco et al., 2008), but also at anteriorly localized cortical structures, as uncovered here. In fact, the localization of PPK-1 at anterior cortical structures as well as the regulation of this PPK-1 localization by CSNK-1 were not observed by imaging the embryos' middle plane (Panbianco et al., 2008). This emphasizes again the importance of cortical imaging, as performed here.

# 5. Conclusion

Confocal cortical live imaging revealed that many important factors regulating different aspects of asymmetric cell division in the early *C. elegans* embryo have an interesting dynamic subcortical distribution, forming elongated structures and foci. Such subcortical distribution could only been found and studied by cortical live imaging. Hence, this work emphasizes the importance of assaying the subcellular distributions of proteins at the cortical plane, where they exert their function. We describe for the first time the subcortical distribution of a plasma membrane lipid, $PIP_2$, as well as of force generation mediator components, such as GPR-1, and negative force regulators, such as GPB-1. We found that positive and negative force regulators form distinct and mostly non-overlapping cortical structures. Thus, their opposite function is largely represented also by their subcortical distribution. Interestingly, we found that increasing GPR-1 cortical structures leads to an increase in overlapping GPB-1 cortical structures, as monitored by $PIP_2$ cortical structures. This could reveal a counter-regulatory feedback mechanism between positive and negative force components. Moreover, we found that the formation of $PIP_2$ cortical structures depends on F-actin and their movement on F-actin polymerization. Vice versa, $PIP_2$ is essential for proper F-actin reorganization, revealing a reciprocal positive feedback regulation between the two components. In addition, $PIP_2$ regulates proper PAR polarity establishment and maintenance most likely through its impact on the F-actin cytoskeleton. Overall, results of this work reveal for the first time that a plasma membrane lipid component participates in regulating AP polarity in the one-cell stage *C. elegans* embryo.

# 6. References

**Aceto, D., Beers, M. and Kemphues, K. J.** (2006). Interaction of PAR-6 with CDC-42 is required for maintenance but not establishment of PAR asymmetry in C. elegans. *Developmental biology* **299**, 386–97.

**Afshar, K., Willard, F. S., Colombo, K., Johnston, C. A., McCudden, C. R., Siderovski, D. P. and Gönczy, P.** (2004). RIC-8 Is Required for GPR-1/2-Dependent Gα Function during Asymmetric Division of C. elegans Embryos. *Cell* **119**, 219–230.

**Afshar, K., Willard, F. S., Colombo, K., Siderovski, D. P. and Gönczy, P.** (2005). Cortical localization of the Galpha protein GPA-16 requires RIC-8 function during C. elegans asymmetric cell division. *Development (Cambridge, England)* **132**, 4449–59.

**Afshar, K., Werner, M. E., Tse, Y. C., Glotzer, M. and Gönczy, P.** (2010). Regulation of cortical contractility and spindle positioning by the protein phosphatase 6 PPH-6 in one-cell stage C. elegans embryos. *Development (Cambridge, England)* **137**, 237–47.

**Aittaleb, M., Boguth, C. A. and Tesmer, J. J. G.** (2010). Structure and function of heterotrimeric G protein-regulated Rho guanine nucleotide exchange factors. *Mol. Pharmacol.* **77**, 111–125.

**Albertson, D. G.** (1984). Formation of the first cleavage spindle in nematode embryos. *Developmental biology* **101**, 61–72.

**Aroian, R. V., Field, C., Pruliere, G., Kenyon, C. and Alberts, B. M.** (1997). Isolation of actin-associated proteins from Caenorhabditis elegans oocytes and their localization in the early embryo. *The EMBO journal* **16**, 1541–9.

**Audhya, A. and Emr, S. D.** (2003). Regulation of PI4,5P2 synthesis by nuclear–cytoplasmic shuttling of the Mss4 lipid kinase. *The EMBO Journal* **22**, 4223–4236.

**Audhya, A., Hyndman, F., McLeod, I. X., Maddox, A. S., Yates, J. R., Desai, A. and Oegema, K.** (2005). A complex containing the Sm protein CAR-1 and the RNA helicase CGH-1 is required for embryonic cytokinesis in Caenorhabditis elegans. *The Journal of cell biology* **171**, 267–79.

**Ayyadevara, S., Tazearslan, Ã., Bharill, P., Alla, R., Siegel, E. and Shmookler Reis, R. J.** (2009). *Caenorhabditis elegans* PI3K mutants reveal novel genes underlying exceptional stress resistance and lifespan. *Aging Cell* **8**, 706–725.

**Ayyadevara, S., Balasubramaniam, M., Johnson, J., Alla, R., Mackintosh, S. G., Shmookler Reis, R. J., Ayyadevara, S., Balasubramaniam, M., Johnson, J., Alla, R., et al.** (2016). PIP$_3$-binding proteins promote age-dependent protein aggregation and limit survival in *C. elegans*; *Oncotarget* **7**, 48870–48886.

**Azoury, J., Lee, K. W., Georget, V., Hikal, P. and Verlhac, M.-H.** (2011). Symmetry breaking in mouse oocytes requires transient F-actin meshwork destabilization. *Development (Cambridge, England)* **138**, 2903–8.

**Bamburg, J. R., Harris, H. E. and Weeds, A. G.** (1980). Partial purification and characterization of an actin depolymerizing factor from brain. *FEBS letters* **121**, 178–82.

**Bastiani, C.** (2006). Heterotrimeric G proteins in C. elegans. *WormBook*.

**Beatty, A., Morton, D. and Kemphues, K.** (2010). The C. elegans homolog of Drosophila Lethal giant larvae functions redundantly with PAR-2 to maintain polarity in the early embryo. *Development* **137**, 3995–4004.

**Beers, M. and Kemphues, K.** (2006). Depletion of the co-chaperone CDC-37 reveals two modes of PAR-6 cortical association in C. elegans embryos. *Development* **133**, 3745–3754.

**Bellaïche, Y., Radovic, A., Woods, D. F., Hough, C. D., Parmentier, M. L., O'Kane, C. J., Bryant, P. J. and Schweisguth, F.** (2001). The Partner of Inscuteable/Discs-large complex is required to establish planar polarity during asymmetric cell division in Drosophila. *Cell* **106**, 355–66.

**Ben-Aissa, K., Patino-Lopez, G., Belkina, N. V., Maniti, O., Rosales, T., Hao, J.-J., Kruhlak, M. J., Knutson, J. R., Picart, C. and Shaw, S.** (2012). Activation of moesin, a protein that links actin cytoskeleton to the plasma membrane, occurs by phosphatidylinositol 4,5-bisphosphate (PIP2) binding sequentially to two sites and releasing an autoinhibitory linker. *J. Biol. Chem.* **287**, 16311–16323.

**Berends, C. W. H., Muñoz, J., Portegijs, V., Schmidt, R., Grigoriev, I., Boxem, M., Akhmanova, A., Heck, A. J. R. and van den Heuvel, S.** (2013). F-actin asymmetry and the endoplasmic reticulum-associated TCC-1 protein contribute to stereotypic spindle movements in the Caenorhabditis elegans embryo. *Molecular biology of the cell* **24**, 2201–15.

**Bienkowska, D. and Cowan, C. R.** (2012). Centrosomes Can Initiate a Polarity Axis from Any Position within One-Cell C. elegans Embryos. *Current Biology* **22**, 583–589.

**Blanchoin, L. and Pollard, T. D.** (1998). Interaction of actin monomers with Acanthamoeba actophorin (ADF/cofilin) and profilin. *The Journal of biological chemistry* **273**, 25106–11.

**Blanchoin, L. and Pollard, T. D.** (2002). Hydrolysis of ATP by polymerized actin depends on the bound divalent cation but not profilin. *Biochemistry* **41**, 597–602.

**Blanchoud, S., Budirahardja, Y., Naef, F. and Gönczy, P.** (2010). ASSET: A robust algorithm for the automated segmentation and standardization of early Caenorhabditis elegans embryos. *Developmental Dynamics* **239**, 3285–3296.

**Botelho, R. J., Scott, C. C. and Grinstein, S.** (2004). Phosphoinositide involvement in phagocytosis and phagosome maturation. *Current topics in microbiology and immunology* **282**, 1–30.

**Bowie, M. B., Kent, D. G., Dykstra, B., McKnight, K. D., McCaffrey, L., Hoodless, P. A. and Eaves, C. J.** (2007). Identification of a new intrinsically timed developmental checkpoint that reprograms key hematopoietic stem cell properties. *Proc. Natl. Acad. Sci. U.S.A.* **104**, 5878–5882.

**Bowman, S. K., Neumüller, R. A., Novatchkova, M., Du, Q. and Knoblich, J. A.** (2006). The Drosophila NuMA Homolog Mud Regulates Spindle Orientation in Asymmetric Cell Division. *Developmental Cell* **10**, 731–742.

**Boyd, L., Guo, S., Levitan, D., Stinchcomb, D. T. and Kemphues, K. J.** (1996). PAR-2 is asymmetrically distributed and promotes association of P granules and PAR-1 with the cortex in C. elegans embryos. *Development (Cambridge, England)* **122**, 3075–84.

**Brangbour, C., du Roure, O., Helfer, E., Démoulin, D., Mazurier, A., Fermigier, M., Carlier, M.-F., Bibette, J. and Baudry, J.** (2011). Force-Velocity Measurements of a Few Growing Actin Filaments. *PLoS Biology* **9**, e1000613.

**Brenner, S.** (1974). The genetics of Caenorhabditis elegans. *Genetics* **77**, 71–94.

**Brown, D. A.** (2015). PIP2Clustering: From model membranes to cells. *Chemistry and Physics of Lipids* **192**, 33–40.

**Bunce, M. W., Boronenkov, I. V and Anderson, R. A.** (2008). Coordinated activation of the nuclear ubiquitin ligase Cul3-SPOP by the generation of phosphatidylinositol 5-phosphate. *The Journal of biological chemistry* **283**, 8678–86.

**Burn, P., Kupfer, A. and Singer, S. J.** (1988). Dynamic membrane-cytoskeletal interactions: specific association of integrin and talin arises in vivo after phorbol ester treatment of peripheral blood lymphocytes. *Proceedings of the National Academy of Sciences of the United States of America* **85**, 497–501.

**Burridge, K. and Connell, L.** (1983). Talin: a cytoskeletal component concentrated in adhesion plaques and other sites of actin-membrane interaction. *Cell motility* **3**, 405–17.

**Bustelo, X. R.** (2000). Regulatory and signaling properties of the Vav family. *Molecular and cellular biology* **20**, 1461–77.

**Calderwood, D. A., Yan, B., de Pereda, J. M., Alvarez, B. G., Fujioka, Y., Liddington, R. C. and Ginsberg, M. H.** (2002). The phosphotyrosine binding-like domain of talin activates integrins. *The Journal of biological chemistry* **277**, 21749–58.

**Cameron, L. A., Giardini, P. A., Soo, F. S. and Theriot, J. A.** (2000). Secrets of actin-based motility revealed by a bacterial pathogen. *Nature Reviews Molecular Cell Biology* **1**, 110–119.

**Canman, J. C., Lewellyn, L., Laband, K., Smerdon, S. J., Desai, A., Bowerman, B. and Oegema, K.** (2008). Inhibition of Rac by the GAP activity of centralspindlin is essential for cytokinesis. *Science (New York, N.Y.)* **322**, 1543–6.

**Cantley, L. C.** (2002). The Phosphoinositide 3-Kinase Pathway. *Science* **296**, 1655–1657.

**Cao, W., Goodarzi, J. P. and De La Cruz, E. M.** (2006). Energetics and kinetics of cooperative cofilin-actin filament interactions. *Journal of molecular biology* **361**, 257–67.

**Carlsson, A. E.** (2003). Growth velocities of branched actin networks. *Biophysical journal* **84**, 2907–18.

**Carlsson, A. E.** (2010). Actin dynamics: from nanoscale to microscale. *Annual review of biophysics* **39**, 91–110.

**Carvalho, A., Olson, S. K., Gutierrez, E., Zhang, K., Noble, L. B., Zanin, E., Desai, A., Groisman, A. and Oegema, K.** (2011). Acute Drug Treatment in the Early C. elegans Embryo. *PLoS ONE* **6**, e24656.

**Chang, J. T., Palanivel, V. R., Kinjyo, I., Schambach, F., Intlekofer, A. M., Banerjee, A., Longworth, S. A., Vinup, K. E., Mrass, P., Oliaro, J., et al.** (2007). Asymmetric T Lymphocyte Division in the Initiation of Adaptive Immune Responses. *Science* **315**, 1687–1691.

**Charest, D. L., Clark, D. V, Green, M. E. and Baillie, D. L.** (1990). Genetic and fine structure analysis of unc-26(IV) and adjacent regions in Caenorhabditis elegans. *Molecular & general genetics : MGG* **221**, 459–65.

**Chartier, N. T., Salazar Ospina, D. P., Benkemoun, L., Mayer, M., Grill, S. W., Maddox, A. S. and Labbé, J.-C.** (2011). PAR-4/LKB1 mobilizes nonmuscle myosin through anillin to regulate C. elegans embryonic polarization and cytokinesis. *Current biology : CB* **21**, 259–69.

**Chen, F., Ma, L., Parrini, M. C., Mao, X., Lopez, M., Wu, C., Marks, P. W., Davidson, L., Kwiatkowski, D. J., Kirchhausen, T., et al.** (2000). Cdc42 is required for PIP(2)-induced actin polymerization and early development but not for cell viability. *Current biology : CB* **10**, 758–65.

**Cheng, S., Wang, K., Zou, W., Miao, R., Huang, Y., Wang, H. and Wang, X.** (2015). PtdIns(4,5)P $_2$ and PtdIns3P coordinate to regulate phagosomal sealing for apoptotic cell clearance. *The Journal of Cell Biology* **210**, 485–502.

**Chichili, G. R. and Rodgers, W.** (2009). Cytoskeleton–membrane interactions in membrane raft structure. *Cellular and Molecular Life Sciences* **66**, 2319–2328.

**Chierico, L., Joseph, A. S., Lewis, A. L. and Battaglia, G.** (2015). Live cell imaging of membrane / cytoskeleton interactions and membrane topology. *Scientific Reports* **4**, 6056.

**Claret, S., Jouette, J., Benoit, B., Legent, K. and Guichet, A.** (2014). PI(4,5)P2 produced by the PI4P5K SKTL controls apical size by tethering PAR-3 in Drosophila epithelial cells. *Current biology : CB* **24**, 1071–9.

**Clarke, J. H., Emson, P. C. and Irvine, R. F.** (2008). Localization of phosphatidylinositol phosphate kinase IIγ in kidney to a membrane trafficking compartment within specialized cells of the nephron. *American Journal of Physiology-Renal Physiology* **295**, F1422–F1430.

**Colombo, K., Grill, S. W., Kimple, R. J., Willard, F. S., Siderovski, D. P. and Gönczy, P.** (2003). Translation of Polarity Cues into Asymmetric Spindle Positioning in Caenorhabditis elegans Embryos. *Science* **300**, 1957–1961.

**Conklin, E.** (1905). The organization and cell-lineage of the ascidian egg. *J. Acad. Natl. Sci. Phil.* **13**,.

**Courtemanche, N. and Pollard, T. D.** (2013). Interaction of Profilin with the Barbed End of Actin Filaments. *Biochemistry* **52**, 6456–6466.

**Couwenbergs, C., Labbé, J.-C., Goulding, M., Marty, T., Bowerman, B. and Gotta, M.** (2007). Heterotrimeric G protein signaling functions with dynein to promote spindle positioning in C. elegans. *The Journal of cell biology* **179**, 15–22.

**Cowan, C. R. and Hyman, A. A.** (2004). Centrosomes direct cell polarity independently of microtubule assembly in C. elegans embryos. *Nature* **431**, 92–96.

**Cuenca, A. A., Schetter, A., Aceto, D., Kemphues, K. and Seydoux, G.** (2003). Polarization of the C. elegans zygote proceeds via distinct establishment and maintenance phases. *Development (Cambridge, England)* **130**, 1255–65.

**Czech, M. P.** (2003). Dynamics of Phosphoinositides in Membrane Retrieval and Insertion. *Annual Review of Physiology* **65**, 791–815.

**Daste, F., Walrant, A., Holst, M. R., Gadsby, J. R., Mason, J., Lee, J.-E., Brook, D., Mettlen, M., Larsson, E., Lee, S. F., et al.** (2017). Control of actin polymerization via the coincidence of phosphoinositides and high membrane curvature. *The Journal of Cell Biology* **216**, 3745–3765.

**De Craene, J.-O., Ripp, R., Lecompte, O., Thompson, J. D., Poch, O. and Friant, S.** (2012). Evolutionary analysis of the ENTH/ANTH/VHS protein superfamily reveals a co-evolution between membrane trafficking and metabolism. *BMC Genomics* **13**, 297–297.

**De Craene, J.-O., Bertazzi, D., Bär, S. and Friant, S.** (2017). Phosphoinositides, Major Actors in Membrane Trafficking and Lipid Signaling Pathways. *International Journal of Molecular Sciences* **18**, 634.

**De Simone, A., Nédélec, F. and Gönczy, P.** (2016). Dynein Transmits Polarized Actomyosin Cortical Flows to Promote Centrosome Separation. *Cell Reports* **14**, 2250–2262.

**Desrivières, S., Cooke, F. T., Parker, P. J. and Hall, M. N.** (1998). MSS4, a phosphatidylinositol-4-phosphate 5-kinase required for organization of the actin cytoskeleton in Saccharomyces cerevisiae. *The Journal of biological chemistry* **273**, 15787–93.

**Dey-Guha, I., Wolfer, A., Yeh, A. C., G. Albeck, J., Darp, R., Leon, E., Wulfkuhle, J., Petricoin, E. F., Wittner, B. S. and Ramaswamy, S.** (2011). Asymmetric cancer cell division regulated by AKT. *Proceedings of the National Academy of Sciences* **108**, 12845–12850.

**Di Paolo, G. and De Camilli, P.** (2006). Phosphoinositides in cell regulation and membrane dynamics. *Nature* **443**, 651–657.

**Dickinson, D. J. and Goldstein, B.** (2016). CRISPR-based methods for Caenorhabditis elegans genome engineering. *Genetics Soc America*.

**Dickinson, D. J., Ward, J. D., Reiner, D. J. and Goldstein, B.** (2013). Engineering the Caenorhabditis elegans genome using Cas9-triggered homologous recombination. *Nature methods* **10**, 1028–34.

**Dickinson, D. J., Schwager, F., Pintard, L., Gotta, M. and Goldstein, B.** (2017). A Single-Cell Biochemistry Approach Reveals PAR Complex Dynamics during Cell Polarization. *Developmental Cell* **42**, 416-434.e11.

**Dodgson, J., Chessel, A., Yamamoto, M., Vaggi, F., Cox, S., Rosten, E., Albrecht, D., Geymonat, M., Csikasz-Nagy, A., Sato, M., et al.** (2013). Spatial segregation of polarity factors into distinct cortical clusters is required for cell polarity control. *Nature Communications* **4**, 1834.

**Dou, J., Chen, L., Hu, Y. and Miao, L.** (2012). Cholesterol and the biosynthesis of glycosphingolipids are required for sperm activation in Caenorhabditis elegans. *Biochimica et biophysica acta* **1821**, 934–42.

**Edwards, K. A., Demsky, M., Montague, R. A., Weymouth, N. and Kiehart, D. P.** (1997). GFP-Moesin Illuminates Actin Cytoskeleton Dynamics in Living Tissue and Demonstrates Cell Shape Changes during Morphogenesis inDrosophila. *Developmental Biology* **191**, 103–117.

**Edwards, M., Zwolak, A., Schafer, D. A., Sept, D., Dominguez, R. and Cooper, J. A.** (2014). Capping protein regulators fine-tune actin assembly dynamics. *Nature reviews. Molecular cell biology* **15**, 677–89.

**Encalada, S. E., Willis, J., Lyczak, R. and Bowerman, B.** (2004). A Spindle Checkpoint Functions during Mitosis in the Early Caenorhabditis elegans Embryo. *MBoC* **16**, 1056–1070.

**Entchev, E. V. and Kurzchalia, T. V.** (2005). Requirement of sterols in the life cycle of the nematode Caenorhabditis elegans. *Seminars in cell & developmental biology* **16**, 175–82.

**Etemad-Moghadam, B., Guo, S. and Kemphues, K. J.** (1995). Asymmetrically distributed PAR-3 protein contributes to cell polarity and spindle alignment in early C. elegans embryos. *Cell* **83**, 743–52.

**Fabian, L., Wei, H. C., Rollins, J., Noguchi, T., Blankenship, J. T., Bellamkonda, K., Polevoy, G., Gervais, L., Guichet, A., Fuller, M. T., et al.** (2010). Phosphatidylinositol 4,5-bisphosphate Directs Spermatid Cell Polarity and Exocyst Localization in Drosophila. *Molecular Biology of the Cell* **21**, 1546–1555.

**Fievet, B. T., Rodriguez, J., Naganathan, S., Lee, C., Zeiser, E., Ishidate, T., Shirayama, M., Grill, S. and Ahringer, J.** (2013). Systematic genetic interaction screens uncover cell polarity regulators and functional redundancy. *Nature cell biology* **15**, 103–12.

**Fire, A., Albertson, D., Harrison, S. W. and Moerman, D. G.** (1991). Production of antisense RNA leads to effective and specific inhibition of gene expression in C. elegans muscle. *Development (Cambridge, England)* **113**, 503–14.

**Fire, A., Xu, S., Montgomery, M. K., Kostas, S. A., Driver, S. E. and Mello, C. C.** (1998). Potent and specific genetic interference by double-stranded RNA in Caenorhabditis elegans. *Nature* **391**, 806–811.

**Flynn, J. R. and McNally, F. J.** (2017). A casein kinase 1 prevents expulsion of the oocyte meiotic spindle into a polar body by regulating cortical contractility. *Mol. Biol. Cell* **28**, 2410–2419.

**Ford, M. G. J., Pearse, B. M., Higgins, M. K., Vallis, Y., Owen, D. J., Gibson, A., Hopkins, C. R., Evans, P. R. and McMahon, H. T.** (2001). Simultaneous Binding of PtdIns(4,5)P2 and Clathrin by AP180 in the Nucleation of Clathrin Lattices on Membranes. *Science* **291**, 1051–1055.

**Fortin, S. M., Marshall, S. L., Jaeger, E. C., Greene, P. E., Brady, L. K., Isaac, R. E., Schrandt, J. C., Brooks, D. R. and Lyczak, R.** (2010). The PAM-1 aminopeptidase regulates centrosome positioning to ensure anterior-posterior axis specification in one-cell C. elegans embryos. *Developmental biology* **344**, 992–1000.

**Fraser, A. G., Kamath, R. S., Zipperlen, P., Martinez-Campos, M., Sohrmann, M. and Ahringer, J.** (2000). Functional genomic analysis of C. elegans chromosome I by systematic RNA interference. *Nature* **408**, 325–330.

**Fujiwara, I., Vavylonis, D. and Pollard, T. D.** (2007). Polymerization kinetics of ADP- and ADP-Pi-actin determined by fluorescence microscopy. *Proceedings of the National Academy of Sciences* **104**, 8827–8832.

**Gaidarov, I. and Keen, J. H.** (1999). Phosphoinositide-AP-2 interactions required for targeting to plasma membrane clathrin-coated pits. *The Journal of cell biology* **146**, 755–64.

**Galli, M., Muñoz, J., Portegijs, V., Boxem, M., Grill, S. W., Heck, A. J. R. and van den Heuvel, S.** (2011). aPKC phosphorylates NuMA-related LIN-5 to position the mitotic spindle during asymmetric division. *Nature cell biology* **13**, 1132–8.

**Gallop, J. L., Walrant, A., Cantley, L. C. and Kirschner, M. W.** (2013). Phosphoinositides and membrane curvature switch the mode of actin polymerization via selective recruitment of toca-1 and Snx9. *Proceedings of the National Academy of Sciences* **110**, 7193–7198.

**Garcia, P., Gupta, R., Shah, S., Morris, A. J., Rudge, S. A., Scarlata, S., Petrova, V., McLaughlin, S. and Rebecchi, M. J.** (1995). The pleckstrin homology domain of phospholipase C-.delta.1 binds with high affinity to phosphatidylinositol 4,5-bisphosphate in bilayer membranes. *Biochemistry* **34**, 16228–16234.

**Gateff, E.** (1978). Malignant neoplasms of genetic origin in Drosophila melanogaster. *Science (New York, N.Y.)* **200**, 1448–59.

**Gateff, E.** (1994). Tumor suppressor and overgrowth suppressor genes of Drosophila melanogaster: developmental aspects. *The International journal of developmental biology* **38**, 565–90.

**Gervais, L., Claret, S., Januschke, J., Roth, S. and Guichet, A.** (2008). PIP5K-dependent production of PIP2 sustains microtubule organization to establish polarized transport in the Drosophila oocyte. *Development* **135**, 3829–3838.

**Giet, R., Petretti, C. and Prigent, C.** (2005). Aurora kinases, aneuploidy and cancer, a coincidence or a real link? *Trends Cell Biol.* **15**, 241–250.

**Gil, E. B., Malone Link, E., Liu, L. X., Johnson, C. D. and Lees, J. A.** (1999). Regulation of the insulin-like developmental pathway of Caenorhabditis elegans by a homolog of the PTEN tumor suppressor gene. *Proceedings of the National Academy of Sciences of the United States of America* **96**, 2925–30.

**Goehring, N. W. and Grill, S. W.** (2013). Cell polarity: mechanochemical patterning. *Trends Cell Biol.* **23**, 72–80.

**Goehring, N. W., Hoege, C., Grill, S. W. and Hyman, A. A.** (2011). PAR proteins diffuse freely across the anterior–posterior boundary in polarized C. elegans embryos. *The Journal of Cell Biology* **193**.

**Goldenson, B. and Crispino, J. D.** (2015). The aurora kinases in cell cycle and leukemia. *Oncogene* **34**, 537–545.

**Goldstein, B. and Hird, S. N.** (1996). Specification of the anteroposterior axis in Caenorhabditis elegans. *Development (Cambridge, England)* **122**, 1467–74.

**Golebiewska, U., Nyako, M., Woturski, W., Zaitseva, I. and McLaughlin, S.** (2008). Diffusion coefficient of fluorescent phosphatidylinositol 4,5-bisphosphate in the plasma membrane of cells. *Molecular biology of the cell* **19**, 1663–9.

**Golub, T. and Caroni, P.** (2005). PI(4,5)P2-dependent microdomain assemblies capture microtubules to promote and control leading edge motility. *The Journal of cell biology* **169**, 151–65.

**Golub, T. and Pico, C.** (2005). Spatial control of actin-based motility through plasmalemmal PtdIns (4, 5) P2-rich raft assemblies. *Biochemical Society Symposia*.

**Gómez-López, S., Lerner, R. G. and Petritsch, C.** (2014). Asymmetric cell division of stem and progenitor cells during homeostasis and cancer. *Cellular and Molecular Life Sciences* **71**, 575–597.

**Gönczy, P.** (2008). Mechanisms of asymmetric cell division: flies and worms pave the way. *Nature Reviews Molecular Cell Biology* **9**, 355–366.

**Gönczy, P. and Rose, L. S.** (2005). Asymmetric cell division and axis formation in the embryo. *WormBook : the online review of C. elegans biology* 1–20.

**Gönczy, P., Schnabel, H., Kaletta, T., Amores, A. D., Hyman, T. and Schnabel, R.** (1999). Dissection of cell division processes in the one cell stage Caenorhabditis elegans embryo by mutational analysis. *The Journal of cell biology* **144**, 927–46.

**Gönczy, P., Echeverri, C., Oegema, K., Coulson, A., Jones, S. J. M., Copley, R. R., Duperon, J., Oegema, J., Brehm, M., Cassin, E., et al.** (2000). Functional genomic analysis of cell division in C. elegans using RNAi of genes on chromosome III. *Nature* **408**, 331–336.

**Gong, L.-W., Di Paolo, G., Diaz, E., Cestra, G., Diaz, M.-E., Lindau, M., De Camilli, P. and Toomre, D.** (2005). Phosphatidylinositol phosphate kinase type I regulates dynamics of large dense-core vesicle fusion. *Proceedings of the National Academy of Sciences* **102**, 5204–5209.

**Gotta, M. and Ahringer, J.** (2001). Distinct roles for Gα and Gβγ in regulating spindle position and orientation in Caenorhabditis elegans embryos. *Nature Cell Biology* **3**, 297–300.

**Gotta, M., Abraham, M. C., Ahringer, J., Cheng, N. S., Stinchcomb, D. T., Bagrodia, S. and al., et** (2001). CDC-42 controls early cell polarity and spindle orientation in C. elegans. *Current biology : CB* **11**, 482–8.

**Gotta, M., Dong, Y., Peterson, Y. K., Lanier, S. M. and Ahringer, J.** (2003). Asymmetrically distributed C. elegans homologs of AGS3/PINS control spindle position in the early embryo. *Current biology : CB* **13**, 1029–37.

**Grant, B., Hirsh, D. and Kimble, J.** (1999). Receptor-mediated Endocytosis in the Caenorhabditis elegans Oocyte. *MBoC* **10**, 4311–4326.

**Green, R. A., Audhya, A., Pozniakovsky, A., Dammermann, A., Pemble, H., Monen, J., Portier, N., Hyman, A., Desai, A. and Oegema, K.** (2008). Expression and Imaging of Fluorescent Proteins in the C. elegans Gonad and Early Embryo. In *Methods in Cell Biology*, pp. 179–218. Academic Press.

**Greener, T., Grant, B., Zhang, Y., Wu, X., Greene, L. E., Hirsh, D. and Eisenberg, E.** (2001). *Caenorhabditis elegans* auxilin: a J-domain protein essential for clathrin-mediated endocytosis *in vivo*. *Nature Cell Biology* **3**, 215–219.

**Grill, S. W., Gönczy, P., Stelzer, E. H. K. and Hyman, A. A.** (2001). Polarity controls forces governing asymmetric spindle positioning in the Caenorhabditis elegans embryo. *Nature* **409**, 630–633.

**Grill, S. W., Howard, J., Schäffer, E., Stelzer, E. H. K. and Hyman, A. A.** (2003). The Distribution of Active Force Generators Controls Mitotic Spindle Position. *Science* **301**, 518–521.

**Guglielmi, G., Barry, J. D., Huber, W. and De Renzis, S.** (2015). An Optogenetic Method to Modulate Cell Contractility during Tissue Morphogenesis. *Developmental Cell* **35**, 646–660.

**Gunning, P. W., Ghoshdastider, U., Whitaker, S., Popp, D. and Robinson, R. C.** (2015). The evolution of compositionally and functionally distinct actin filaments. *Journal of Cell Science* **128**, 2009–2019.

**Guo, S. and Kemphues, K. J.** (1995). par-1 a Gene Required for Establishing Polarity in C. elegans Embryos, Encodes a Putative Ser/Thr Kinase That Is Asymmetrically Distributed. *Cell* **61**, 61–620.

**Guo, S. and Kemphues, K. J.** (1996). A non-muscle myosin required for embryonic polarity in Caenorhabditis elegans. *Nature* **382**, 455–458.

**Hammond, G. R. V., Sim, Y., Lagnado, L. and Irvine, R. F.** (2009). Reversible binding and rapid diffusion of proteins in complex with inositol lipids serves to coordinate free movement with spatial information. *The Journal of Cell Biology* **184**.

Hammond, G. R. V., Fischer, M. J., Anderson, K. E., Holdich, J., Koteci, A., Balla, T. and Irvine, R. F. (2012). PI4P and PI(4,5)P2 Are Essential But Independent Lipid Determinants of Membrane Identity. *Science* **337**.

Hao, Y., Boyd, L. and Seydoux, G. (2006). Stabilization of cell polarity by the C. elegans RING protein PAR-2. *Developmental cell* **10**, 199–208.

Harris, T. W., Hartwieg, E., Horvitz, H. R. and Jorgensen, E. M. (2000). Mutations in synaptojanin disrupt synaptic vesicle recycling. *The Journal of cell biology* **150**, 589–600.

Harris, T. W., Antoshechkin, I., Bieri, T., Blasiar, D., Chan, J., Chen, W. J., De La Cruz, N., Davis, P., Duesbury, M., Fang, R., et al. (2010). WormBase: a comprehensive resource for nematode research. *Nucleic Acids Research* **38**, D463–D467.

Heppert, J. K., Dickinson, D. J., Pani, A. M., Higgins, C. D., Steward, A., Ahringer, J., Kuhn, J. R. and Goldstein, B. (2016). Comparative assessment of fluorescent proteins for in vivo imaging in an animal model system. *Molecular biology of the cell* **27**, 3385–3394.

Hess, H. A., Röper, J.-C., Grill, S. W. and Koelle, M. R. (2004). RGS-7 Completes a Receptor-Independent Heterotrimeric G Protein Cycle to Asymmetrically Regulate Mitotic Spindle Positioning in C. elegans. *Cell* **119**, 209–218.

Hetrick, B., Han, M. S., Helgeson, L. A. and Nolen, B. J. (2013). Small molecules CK-666 and CK-869 inhibit actin-related protein 2/3 complex by blocking an activating conformational change. *Chem. Biol.* **20**, 701–712.

Higgs, H. N. and Pollard, T. D. (2000). Activation by Cdc42 and PIP(2) of Wiskott-Aldrich syndrome protein (WASp) stimulates actin nucleation by Arp2/3 complex. *The Journal of cell biology* **150**, 1311–20.

Hilgemann, D. W., Feng, S. and Nasuhoglu, C. (2001). The Complex and Intriguing Lives of PIP2 with Ion Channels and Transporters. *Science Signaling* **2001**, re19–re19.

Hill, D. P. and Strome, S. (1988). An analysis of the role of microfilaments in the establishment and maintenance of asymmetry in Caenorhabditis elegans zygotes. *Developmental biology* **125**, 75–84.

Hill, D. P. and Strome, S. (1990). Brief cytochalasin-induced disruption of microfilaments during a critical interval in 1-cell C. elegans embryos alters the partitioning of developmental instructions to the 2-cell embryo. *Development (Cambridge, England)* **108**, 159–72.

Hird, S. N. and White, J. G. (1993). Cortical and cytoplasmic flow polarity in early embryonic cells of Caenorhabditis elegans. *The Journal of cell biology* **121**, 1343–55.

**Hobro, A. J. and Smith, N. I.** (2017). An evaluation of fixation methods: Spatial and compositional cellular changes observed by Raman imaging. *Vibrational Spectroscopy* **91**, 31–45.

**Hoege, C., Constantinescu, A.-T., Schwager, A., Goehring, N. W., Kumar, P. and Hyman, A. A.** (2010). LGL can partition the cortex of one-cell Caenorhabditis elegans embryos into two domains. *Current biology : CB* **20**, 1296–303.

**Hokin, M. and Hokin, L.** (1964). Interconversions of phosphatidylinositol and phosphatidic acid involved in the response to acetylcholine in the salt gland. *Wiley New York* **Metabolism**, 423–434.

**Höning, S., Ricotta, D., Krauss, M., Späte, K., Spolaore, B., Motley, A., Robinson, M., Robinson, C., Haucke, V. and Owen, D. J.** (2005). Phosphatidylinositol-(4,5)-Bisphosphate Regulates Sorting Signal Recognition by the Clathrin-Associated Adaptor Complex AP2. *Molecular Cell* **18**, 519–531.

**Hooper, N. M.** (1999). Detergent-insoluble glycosphingolipid/cholesterol-rich membrane domains, lipid rafts and caveolae (Review). *Molecular Membrane Biology* **16**, 145–156.

**Horikoshi, Y., Hamada, S., Ohno, S. and Suetsugu, S.** (2011). Phosphoinositide binding by par-3 involved in par-3 localization. *Cell structure and function* **36**, 97–102.

**Horvitz, H. R. and Herskowitz, I.** (1992). Mechanisms of asymmetric cell division: Two Bs or not two Bs, that is the question. *Cell* **68**, 237–255.

**Hughes, T. E., Zhang, H., Logothetis, D. E. and Berlot, C. H.** (2001). Visualization of a functional Galpha q-green fluorescent protein fusion in living cells. Association with the plasma membrane is disrupted by mutational activation and by elimination of palmitoylation sites, but not be activation mediated by receptors or AlF4-. *J. Biol. Chem.* **276**, 4227–4235.

**Humphries, A. C., Donnelly, S. K. and Way, M.** (2014). Cdc42 and the Rho GEF intersectin-1 collaborate with Nck to promote N-WASP-dependent actin polymerisation. *Journal of cell science* **127**, 673–85.

**Hung, T. J. and Kemphues, K. J.** (1999). PAR-6 is a conserved PDZ domain-containing protein that colocalizes with PAR-3 in Caenorhabditis elegans embryos. *Development (Cambridge, England)* **126**, 127–35.

**Hynes, T. R., Hughes, T. E. and Berlot, C. H.** (2004). Cellular localization of GFP-tagged alpha subunits. *Methods Mol. Biol.* **237**, 233–246.

**Idevall-Hagren, O., Dickson, E. J., Hille, B., Toomre, D. K. and De Camilli, P.** (2012). Optogenetic control of phosphoinositide metabolism. *Proceedings of the National Academy of Sciences of the United States of America* **109**, E2316-23.

**Ishihara, H., Shibasaki, Y., Kizuki, N., Wada, T., Yazaki, Y., Asano, T. and Oka, Y.** (1998). Type I phosphatidylinositol-4-phosphate 5-kinases. Cloning of the third isoform and deletion/substitution analysis of members of this novel lipid kinase family. *The Journal of biological chemistry* **273**, 8741–8.

**Itoh, T. and Takenawa, T.** (2002). Phosphoinositide-binding domains: Functional units for temporal and spatial regulation of intracellular signalling. *Cellular Signalling* **14**, 733–743.

**Izumi, Y., Hirose, T., Tamai, Y., Hirai, S., Nagashima, Y., Fujimoto, T., Tabuse, Y., Kemphues, K. J. and Ohno, S.** (1998). An atypical PKC directly associates and colocalizes at the epithelial tight junction with ASIP, a mammalian homologue of Caenorhabditis elegans polarity protein PAR-3. *The Journal of cell biology* **143**, 95–106.

**Izumi, Y., Ohta, N., Hisata, K., Raabe, T. and Matsuzaki, F.** (2006). Drosophila Pins-binding protein Mud regulates spindle-polarity coupling and centrosome organization. *Nature cell biology* **8**, 586–93.

**Jamur, M. C. and Oliver, C.** (2010). Permeabilization of Cell Membranes. In *Methods in molecular biology (Clifton, N.J.)*, pp. 63–66.

**Janetopoulos, C., Jin, T. and Devreotes, P.** (2001). Receptor-mediated activation of heterotrimeric G-proteins in living cells. *Science* **291**, 2408–2411.

**Jégou, A., Niedermayer, T., Orbán, J., Didry, D., Lipowsky, R., Carlier, M.-F. and Romet-Lemonne, G.** (2011). Individual Actin Filaments in a Microfluidic Flow Reveal the Mechanism of ATP Hydrolysis and Give Insight Into the Properties of Profilin. *PLoS Biology* **9**, e1001161.

**Jenkins, N., Saam, J. R. and Mango, S. E.** (2006). CYK-4/GAP Provides a Localized Cue to Initiate Anteroposterior Polarity upon Fertilization. *Science* **313**, 1298–1301.

**Joberty, G., Petersen, C., Gao, L. and Macara, I. G.** (2000). The cell-polarity protein Par6 links Par3 and atypical protein kinase C to Cdc42. *Nature Cell Biology* **2**, 531–539.

**Johnson, J. L., Erickson, J. W. and Cerione, R. A.** (2012). C-terminal Di-arginine Motif of Cdc42 Protein Is Essential for Binding to Phosphatidylinositol 4,5-Bisphosphate-containing Membranes and Inducing Cellular Transformation. *Journal of Biological Chemistry* **287**, 5764–5774.

**Kakumoto, T. and Nakata, T.** (2013). Optogenetic Control of PIP3: PIP3 Is Sufficient to Induce the Actin-Based Active Part of Growth Cones and Is Regulated via Endocytosis. *PLoS ONE* **8**, e70861–e70861.

**Kamath, R. S. and Ahringer, J.** (2003). Genome-wide RNAi screening in Caenorhabditis elegans. *Methods* **30**, 313–321.

**Kamath, R. S., Martinez-Campos, M., Zipperlen, P., Fraser, A. G. and Ahringer, J.** (2001). Effectiveness of specific RNA-mediated interference through ingested double-stranded RNA in Caenorhabditis elegans. *Genome biology* **2**, RESEARCH0002.

**Kamath, R. S., Fraser, A. G., Dong, Y., Poulin, G., Durbin, R., Gotta, M., Kanapin, A., Le Bot, N., Moreno, S., Sohrmann, M., et al.** (2003). Systematic functional analysis of the Caenorhabditis elegans genome using RNAi. *Nature* **421**, 231–237.

**Kang, H., Bradley, M. J., Elam, W. A. and De La Cruz, E. M.** (2013). Regulation of Actin by Ion-Linked Equilibria. *Biophysical Journal* **105**, 2621–2628.

**Kelley, L. A., Mezulis, S., Yates, C. M., Wass, M. N. and Sternberg, M. J. E.** (2015). The Phyre2 web portal for protein modeling, prediction and analysis. *Nature Protocols* **10**, 845.

**Kemphues, K. J., Priess, J. R., Morton, D. G. and Cheng, N. S.** (1988). Identification of genes required for cytoplasmic localization in early C. elegans embryos. *Cell* **52**, 311–20.

**Kennedy, M. J., Hughes, R. M., Peteya, L. A., Schwartz, J. W., Ehlers, M. D. and Tucker, C. L.** (2010). Rapid blue-light-mediated induction of protein interactions in living cells. *Nat. Methods* **7**, 973–975.

**Kiel, M. J., Yilmaz, Ö. H., Iwashita, T., Yilmaz, O. H., Terhorst, C. and Morrison, S. J.** (2005). SLAM Family Receptors Distinguish Hematopoietic Stem and Progenitor Cells and Reveal Endothelial Niches for Stem Cells. *Cell* **121**, 1109–1121.

**Kimura, K. and Kimura, A.** (2011). Intracellular organelles mediate cytoplasmic pulling force for centrosome centration in the Caenorhabditis elegans early embryo. *Proceedings of the National Academy of Sciences* **108**, 137–142.

**Kirby, C., Kusch, M. and Kemphues, K.** (1990). Mutations in the par genes of Caenorhabditis elegans affect cytoplasmic reorganization during the first cell cycle. *Developmental biology* **142**, 203–15.

**Knoblich, J. A.** (2008). Mechanisms of Asymmetric Stem Cell Division. *Cell* **132**, 583–597.

**Knoblich, J. A.** (2010). Asymmetric cell division: recent developments and their implications for tumour biology. *Nature Reviews Molecular Cell Biology* **11**, 849–860.

**Korn, E. D., Carlier, M. F. and Pantaloni, D.** (1987). Actin polymerization and ATP hydrolysis. *Science (New York, N.Y.)* **238**, 638–44.

**Korotkevich, E., Niwayama, R., Courtois, A., Friese, S., Berger, N., Buchholz, F. and Hiiragi, T.** (2017). The Apical Domain Is Required and Sufficient for the First Lineage Segregation in the Mouse Embryo. *Developmental Cell* **40**, 235-247.e7.

**Kotak, S. and Gönczy, P.** (2013). Mechanisms of spindle positioning: cortical force generators in the limelight. *Current Opinion in Cell Biology* **25**, 741–748.

**Kotak, S., Busso, C. and Gönczy, P.** (2012). Cortical dynein is critical for proper spindle positioning in human cells. *The Journal of cell biology* **199**, 97–110.

**Kotak, S., Busso, C. and Gönczy, P.** (2014). NuMA interacts with phosphoinositides and links the mitotic spindle with the plasma membrane. *The EMBO Journal* **33**, 1815–1830.

**Kotak, S., Afshar, K., Busso, C. and Gönczy, P.** (2016). Aurora A kinase regulates proper spindle positioning in C. elegans and in human cells. *Journal of cell science* **129**, 3015–25.

**Kozlowski, C., Srayko, M. and Nedelec, F.** (2007). Cortical Microtubule Contacts Position the Spindle in C. elegans Embryos. *Cell* **129**, 499–510.

**Krahn, M. P., Klopfenstein, D. R., Fischer, N. and Wodarz, A.** (2010). Membrane Targeting of Bazooka/PAR-3 Is Mediated by Direct Binding to Phosphoinositide Lipids. *Current Biology* **20**, 636–642.

**Kraut, R., Chia, W., Jan, L. Y., Jan, Y. N. and Knoblich, J. A.** (1996). Role of inscuteable in orienting asymmetric cell divisions in Drosophila. *Nature* **383**, 50–55.

**Krueger, L. E., Wu, J.-C., Tsou, M.-F. B. and Rose, L. S.** (2010). LET-99 inhibits lateral posterior pulling forces during asymmetric spindle elongation in C. elegans embryos. *The Journal of cell biology* **189**, 481–95.

**Kuchinke, U., Grawe, F. and Knust, E.** (1998). Control of spindle orientation in Drosophila by the Par-3-related PDZ-domain protein Bazooka. *Current Biology* **8**, 1357–1365.

**Kumar, S., Xu, J., Perkins, C., Guo, F., Snapper, S., Finkelman, F. D., Zheng, Y. and Filippi, M.-D.** (2012). Cdc42 regulates neutrophil migration via crosstalk between WASp, CD11b, and microtubules. *Blood* **120**, 3563–3574.

**Kumfer, K. T., Cook, S. J., Squirrell, J. M., Eliceiri, K. W., Peel, N., O'Connell, K. F. and White, J. G.** (2010). CGEF-1 and CHIN-1 Regulate CDC-42 Activity during Asymmetric Division in the Caenorhabditis elegans Embryo. *Molecular Biology of the Cell* **21**, 266–277.

**Kurzchalia, T. V. and Ward, S.** (2003). Why do worms need cholesterol? *Nature cell biology* **5**, 684–8.

**Kurzchalia, T. V., Scheel, J., Srinivasan, J., Honnert, U. and Henske, A.** (1999). Involvement of caveolin-1 in meiotic cell-cycle progression in Caenorhabditis elegans. *Nature Cell Biology* **1**, 127–129.

**Labbé, J.-C., McCarthy, E. K. and Goldstein, B.** (2004). The forces that position a mitotic spindle asymmetrically are tethered until after the time of spindle assembly. *The Journal of cell biology* **167**, 245–56.

**Lackner, M. R., Nurrish, S. J. and Kaplan, J. M.** (1999). Facilitation of Synaptic Transmission by EGL-30 Gqα and EGL-8 PLCβ: DAG Binding to UNC-13 Is Required to Stimulate Acetylcholine Release. *Neuron* **24**, 335–346.

**Lajoie, P. and Nabi, I. R.** (2010). Lipid Rafts, Caveolae, and Their Endocytosis. In *International review of cell and molecular biology*, pp. 135–163.

**Lang, C. F. and Munro, E.** (2017). The PAR proteins: from molecular circuits to dynamic self-stabilizing cell polarity. *Development* **144**, 3405–3416.

**Larsen, P. L., Albert, P. S. and Riddle, D. L.** (1995). Genes that regulate both development and longevity in Caenorhabditis elegans. *Genetics* **139**.

**Lathia, J. D., Hitomi, M., Gallagher, J., Gadani, S. P., Adkins, J., Vasanji, A., Liu, L., Eyler, C. E., Heddleston, J. M., Wu, Q., et al.** (2011). Distribution of CD133 reveals glioma stem cells self-renew through symmetric and asymmetric cell divisions. *Cell Death & Disease* **2**, e200–e200.

**Lee, C.-Y., Andersen, R. O., Cabernard, C., Manning, L., Tran, K. D., Lanskey, M. J., Bashirullah, A. and Doe, C. Q.** (2006). Drosophila Aurora-A kinase inhibits neuroblast self-renewal by regulating aPKC/Numb cortical polarity and spindle orientation. *Genes Dev.* **20**, 3464–3474.

**Lee, R. Y. N., Howe, K. L., Harris, T. W., Arnaboldi, V., Cain, S., Chan, J., Chen, W. J., Davis, P., Gao, S., Grove, C., et al.** (2018). WormBase 2017: molting into a new stage. *Nucleic Acids Research* **46**, D869–D874.

**Lemmon, M. A., Ferguson, K. M., O'Brien, R., Sigler, P. B. and Schlessinger, J.** (1995). Specific and high-affinity binding of inositol phosphates to an isolated pleckstrin homology domain. *Proceedings of the National Academy of Sciences of the United States of America* **92**, 10472–6.

**Lewis, K. and Petritsch, C.** (2013). Asymmetric cell division: Implications for glioma development and treatment. *Translational Neuroscience* **4**, 484–503.

**Li, J., Kim, H., Aceto, D. G., Hung, J., Aono, S. and Kemphues, K. J.** (2010). Binding to PKC-3, but not to PAR-3 or to a conventional PDZ domain ligand, is required for PAR-6 function in C. elegans. *Developmental Biology* **340**, 88–98.

**Li, S., Wang, H. and Groth, C.** (2014). Drosophila neuroblasts as a new model for the study of stem cell self-renewal and tumour formation. *Biosci Rep* **34**.

**Lin, D., Edwards, A. S., Fawcett, J. P., Mbamalu, G., Scott, J. D. and Pawson, T.** (2000). A mammalian PAR-3-PAR-6 complex implicated in Cdc42/Rac1 and aPKC signalling and cell polarity. *Nature cell biology* **2**, 540–7.

**Liu, Y. and Bankaitis, V. A.** (2010). Phosphoinositide phosphatases in cell biology and disease. *Progress in Lipid Research* **49**, 201–217.

**Liu, J., Maduzia, L. L., Shirayama, M. and Mello, C. C.** (2010a). NMY-2 maintains cellular asymmetry and cell boundaries, and promotes a SRC-dependent asymmetric cell division. *Developmental Biology* **339**, 366–373.

**Liu, Z., Klaavuniemi, T. and Ono, S.** (2010b). Distinct Roles of Four Gelsolin-like Domains of *Caenorhabditis elegans* Gelsolin-like Protein-1 in Actin Filament Severing, Barbed End Capping, and Phosphoinositide Binding. *Biochemistry* **49**, 4349–4360.

**Liu, Z., Kanzawa, N. and Ono, S.** (2011). Calcium-sensitive Activity and Conformation of *Caenorhabditis elegans* Gelsolin-like Protein 1 Are Altered by Mutations in the First Gelsolin-like Domain. *Journal of Biological Chemistry* **286**, 34051–34059.

**Lyczak, R., Zweier, L., Group, T., Murrow, M. A., Snyder, C., Kulovitz, L., Beatty, A., Smith, K. and Bowerman, B.** (2006). The puromycin-sensitive aminopeptidase PAM-1 is required for meiotic exit and anteroposterior polarity in the one-cell Caenorhabditis elegans embryo. *Development* **133**, 4281–4292.

**Ma, L., Cantley, L. C., Janmey, P. A. and Kirschner, M. W.** (1998). Corequirement of specific phosphoinositides and small GTP-binding protein Cdc42 in inducing actin assembly in Xenopus egg extracts. *The Journal of cell biology* **140**, 1125–36.

**Maddox, A. S., Habermann, B., Desai, A. and Oegema, K.** (2005). Distinct roles for two C. elegans anillins in the gonad and early embryo. *Development* **132**, 2837–2848.

**Martel, V., Racaud-Sultan, C., Dupe, S., Marie, C., Paulhe, F., Galmiche, A., Block, M. R. and Albiges-Rizo, C.** (2001). Conformation, localization, and integrin binding of talin depend on its interaction with phosphoinositides. *The Journal of biological chemistry* **276**, 21217–27.

**Marumoto, T., Zhang, D. and Saya, H.** (2005). Aurora-A — A guardian of poles. *Nature Reviews Cancer* **5**, 42–50.

**Mayer, M., Depken, M., Bois, J. S., Jülicher, F. and Grill, S. W.** (2010). Anisotropies in cortical tension reveal the physical basis of polarizing cortical flows. *Nature* **467**, 617–621.

**McCarthy Campbell, E. K., Werts, A. D. and Goldstein, B.** (2009). A cell cycle timer for asymmetric spindle positioning. *PLoS biology* **7**, e1000088.

**McCloskey, R. J. and Kemphues, K. J.** (2012). Deubiquitylation Machinery Is Required for Embryonic Polarity in Caenorhabditis elegans. *PLoS Genetics* **8**, e1003092.

**McLaughlin, S., Wang, J., Gambhir, A. and Murray, D.** (2002). PIP $_2$ and Proteins: Interactions, Organization, and Information Flow. *Annual Review of Biophysics and Biomolecular Structure* **31**, 151–175.

**McNally, F. J.** (2013). Mechanisms of spindle positioning. *The Journal of cell biology* **200**, 131–40.

**Meng, J., Vardar, D., Wang, Y., Guo, H.-C., Head, J. F. and McKnight, C. J.** (2005). High-resolution crystal structures of villin headpiece and mutants with reduced F-actin binding activity. *Biochemistry* **44**, 11963–73.

**Merdes, A., Ramyar, K., Vechio, J. D. and Cleveland, D. W.** (1996). A complex of NuMA and cytoplasmic dynein is essential for mitotic spindle assembly. *Cell* **87**, 447–58.

**Merris, M., Wadsworth, W. G., Khamrai, U., Bittman, R., Chitwood, D. J. and Lenard, J.** (2003). Sterol effects and sites of sterol accumulation in Caenorhabditis elegans: developmental requirement for 4alpha-methyl sterols. *Journal of lipid research* **44**, 172–81.

**Merritt, C., Rasoloson, D., Ko, D. and Seydoux, G.** (2008). 3' UTRs Are the Primary Regulators of Gene Expression in the C. elegans Germline. *Current Biology* **18**, 1476–1482.

**Mihaylova, V. T., Borland, C. Z., Manjarrez, L., Stern, M. J. and Sun, H.** (1999). The PTEN tumor suppressor homolog in Caenorhabditis elegans regulates longevity and dauer formation in an insulin receptor-like signaling pathway. *Proceedings of the National Academy of Sciences of the United States of America* **96**, 7427–32.

**Miller, K. G. and Rand, J. B.** (2000). A role for RIC-8 (Synembryn) and GOA-1 (G(o)alpha) in regulating a subset of centrosome movements during early embryogenesis in Caenorhabditis elegans. *Genetics* **156**, 1649–60.

**Miller, K. G., Emerson, M. D. and Rand, J. B.** (1999). Goα and Diacylglycerol Kinase Negatively Regulate the Gqα Pathway in C. elegans. *Neuron* **24**, 323–333.

**Milosevic, I., Sørensen, J. B., Lang, T., Krauss, M., Nagy, G., Haucke, V., Jahn, R. and Neher, E.** (2005). Plasmalemmal Phosphatidylinositol-4,5-Bisphosphate Level Regulates the Releasable Vesicle Pool Size in Chromaffin Cells. *Journal of Neuroscience* **25**, 2557–2565.

**Mittasch, M., Gross, P., Nestler, M., Fritsch, A. W., Iserman, C., Kar, M., Munder, M., Voigt, A., Alberti, S., Grill, S. W., et al.** (2018). Non-invasive perturbations of intracellular flow reveal physical principles of cell organization. *Nat. Cell Biol.* **20**, 344–351.

**Mockrin, S. C. and Korn, E. D.** (1980). Acanthamoeba profilin interacts with G-actin to increase the rate of exchange of actin-bound adenosine 5'-triphosphate. *Biochemistry* **19**, 5359–62.

**Mogilner, A. and Oster, G.** (1996). Cell Motility Driven by Actin Polymerization. *Biophysical Journal* **71**, 3030–3045.

**Morais-de-Sa, E., Mukherjee, A., Lowe, N. and St Johnston, D.** (2014). Slmb antagonises the aPKC/Par-6 complex to control oocyte and epithelial polarity. *Development* **141**, 2984–2992.

**Moravcevic, K., Mendrola, J. M., Schmitz, K. R., Wang, Y.-H., Slochower, D., Janmey, P. A. and Lemmon, M. A.** (2010). Kinase associated-1 domains drive MARK/PAR1 kinases to membrane targets by binding acidic phospholipids. *Cell* **143**, 966–77.

**Morris, J. Z., Tissenbaum, H. A. and Ruvkun, G.** (1996). A phosphatidylinositol-3-OH kinase family member regulating longevity and diapause in Caenorhabditis elegans. *Nature* **382**, 536–539.

**Motegi, F. and Sugimoto, A.** (2006). Sequential functioning of the ECT-2 RhoGEF, RHO-1 and CDC-42 establishes cell polarity in Caenorhabditis elegans embryos. *Nature Cell Biology* **8**, 978–985.

**Motegi, F., Velarde, N. V., Piano, F., Sugimoto, A., Malone, C. J., White, J., Seydoux, G., Saxton, W. and Salmon, E. D.** (2006). Two Phases of Astral Microtubule Activity during Cytokinesis in C. elegans Embryos. *Developmental Cell* **10**, 509–520.

**Motegi, F., Zonies, S., Hao, Y., Cuenca, A. A., Griffin, E. and Seydoux, G.** (2011). Microtubules induce self-organization of polarized PAR domains in Caenorhabditis elegans zygotes. *Nature Cell Biology* **13**, 1361–1367.

**Munro, E., Nance, J. and Priess, J. R.** (2004). Cortical Flows Powered by Asymmetrical Contraction Transport PAR Proteins to Establish and Maintain Anterior-Posterior Polarity in the Early C. elegans Embryo. *Developmental Cell* **7**, 413–424.

**Nag, S., Larsson, M., Robinson, R. C. and Burtnick, L. D.** (2013). Gelsolin: the tail of a molecular gymnast. *Cytoskeleton (Hoboken, N.J.)* **70**, 360–84.

**Naganathan, S. R., Fürthauer, S., Nishikawa, M., Jülicher, F. and Grill, S. W.** (2014). Active torque generation by the actomyosin cell cortex drives left-right symmetry breaking. *eLife* **3**, e04165.

**Nakaya, M., Fukui, A., Izumi, Y., Akimoto, K., Asashima, M. and Ohno, S.** (2000). Meiotic maturation induces animal-vegetal asymmetric distribution of aPKC and ASIP/PAR-3 in Xenopus oocytes. *Development (Cambridge, England)* **127**, 5021–31.

**Neumüller, R. A. and Knoblich, J. A.** (2009). Dividing cellular asymmetry: asymmetric cell division and its implications for stem cells and cancer. *Genes & development* **23**, 2675–99.

**Nguyen-Ngoc, T., Afshar, K. and Gönczy, P.** (2007). Coupling of cortical dynein and G alpha proteins mediates spindle positioning in Caenorhabditis elegans. *Nature cell biology* **9**, 1294–302.

**Nishida, E.** (1985). Opposite effects of cofilin and profilin from porcine brain on rate of exchange of actin-bound adenosine 5'-triphosphate. *Biochemistry* **24**, 1160–4.

**Niu, J., Profirovic, J., Pan, H., Vaiskunaite, R. and Voyno-Yasenetskaya, T.** (2003). G Protein betagamma subunits stimulate p114RhoGEF, a guanine nucleotide exchange factor for RhoA and Rac1: regulation of cell shape and reactive oxygen species production. *Circ. Res.* **93**, 848–856.

**Niwayama, R., Shinohara, K. and Kimura, A.** (2011). Hydrodynamic property of the cytoplasm is sufficient to mediate cytoplasmic streaming in the Caenorhabditis elegans embryo. *Proceedings of the National Academy of Sciences of the United States of America* **108**, 11900–5.

**Nung Jan, Y. and Yeh Jan, L.** (1998). Asymmetric cell division. *NATURE* **392**.

**Oegema, K.** (2006). Cell division. *WormBook*.

**Ogg, S. and Ruvkun, G.** (1998). The C. elegans PTEN Homolog, DAF-18, Acts in the Insulin Receptor-like Metabolic Signaling Pathway. *Molecular Cell* **2**, 887–893.

**Ohno, H., Kato, S., Naito, Y., Kunitomo, H., Tomioka, M. and Iino, Y.** (2014). Role of synaptic phosphatidylinositol 3-kinase in a behavioral learning response in C. elegans. *Science* **345**, 313–317.

**Ohshiro, T., Matsuzaki, F., Yagami, T. and Zhang, C.** (2000). Role of cortical tumour-suppressor proteins in asymmetric division of Drosophila neuroblast. *Nature* **408**, 593–596.

**Ojala, P. J., Paavilainen, V. and Lappalainen, P.** (2001). Identification of Yeast Cofilin Residues Specific for Actin Monomer and PIP $_2$ Binding [†]. *Biochemistry* **40**, 15562–15569.

**Oliaro, J., Ham, V. V., Sacirbegovic, F., Pasam, A., Bomzon, Z., Pham, K., Ludford-Menting, M. J., Waterhouse, N. J., Bots, M., Hawkins, E. D., et al.** (2010). Asymmetric Cell Division of T Cells upon Antigen Presentation Uses Multiple Conserved Mechanisms. *The Journal of Immunology* **185**, 367–375.

**Olson, S. K., Greenan, G., Desai, A., Müller-Reichert, T. and Oegema, K.** (2012). Hierarchical assembly of the eggshell and permeability barrier in C. elegans. *The Journal of cell biology* **198**, 731–48.

**Orlando, K., Zhang, J., Zhang, X., Yue, P., Chiang, T., Bi, E. and Guo, W.** (2008). Regulation of Gic2 Localization and Function by Phosphatidylinositol 4,5-Bisphosphate during the Establishment of Cell Polarity in Budding Yeast. *Journal of Biological Chemistry* **283**, 14205–14212.

**Pacquelet, A.** (2017). Asymmetric Cell Division in the One-Cell C. elegans Embryo: Multiple Steps to Generate Cell Size Asymmetry.pp. 115–140. Springer, Cham.

**Paix, A., Wang, Y., Smith, H. E., Lee, C.-Y. S., Calidas, D., Lu, T., Smith, J., Schmidt, H., Krause, M. W. and Seydoux, G.** (2014). Scalable and versatile genome editing using linear DNAs with microhomology to Cas9 Sites in Caenorhabditis elegans. *Genetics* **198**, 1347–1356.

**Paix, A., Folkmann, A., Rasoloson, D. and Seydoux, G.** (2015). High Efficiency, Homology-Directed Genome Editing in Caenorhabditis elegans Using CRISPR-Cas9 Ribonucleoprotein Complexes. *Genetics* **201**, 47–54.

**Paix, A., Schmidt, H. and Seydoux, G.** (2016). Cas9-assisted recombineering in C. elegans : genome editing using in vivo assembly of linear DNAs. *Nucleic Acids Research* **44**, gkw502–gkw502.

**Panbianco, C., Weinkove, D., Zanin, E., Jones, D., Divecha, N., Gotta, M. and Ahringer, J.** (2008). A casein kinase 1 and PAR proteins regulate asymmetry of a PIP(2) synthesis enzyme for asymmetric spindle positioning. *Developmental cell* **15**, 198–208.

**Park, D. H. and Rose, L. S.** (2008). Dynamic localization of LIN-5 and GPR-1/2 to cortical force generation domains during spindle positioning. *Developmental biology* **315**, 42–54.

**Patalano, S., Prulière, G., Prodon, F., Paix, A., Dru, P., Sardet, C. and Chenevert, J.** (2006). The aPKC–PAR-6–PAR-3 cell polarity complex localizes to the centrosome attracting body, a macroscopic cortical structure responsible for asymmetric divisions in the early ascidian embryo. *Journal of Cell Science* **119**, 1592–1603.

**Paul, A. S. and Pollard, T. D.** (2009). Review of the mechanism of processive actin filament elongation by formins. *Cell Motility and the Cytoskeleton* **66**, 606–617.

**Payrastre, B., Missy, K., Giuriato, S., Bodin, S., Plantavid, M. and Gratacap, M.-P.** (2001). Phosphoinositides : key players in cell signalling, in time and space. *Cellular Signalling* **13**, 377–387.

**Peng, C. Y., Manning, L., Albertson, R. and Doe, C. Q.** (2000). The tumour-suppressor genes lgl and dlg regulate basal protein targeting in Drosophila neuroblasts. *Nature* **408**, 596–600.

**Petronczki, M. and Knoblich, J. A.** (2001). DmPAR-6 directs epithelial polarity and asymmetric cell division of neuroblasts in Drosophila. *Nature Cell Biology* **3**, 43–49.

**Piano, F., Schetter†, A. J., Mangone, M., Stein, L. and Kemphues, K. J.** (2000). RNAi analysis of genes expressed in the ovary of Caenorhabditis elegans. *Current Biology* **10**, 1619–1622.

**Piekny, A. J. and Glotzer, M.** (2008). Anillin Is a Scaffold Protein That Links RhoA, Actin, and Myosin during Cytokinesis. *Current Biology* **18**, 30–36.

## 6. References

**Pintard, L. and Bowerman, B.** (2018). Cell Division in Caenorhabditis elegans. *WormBook*.

**Pitcher, J. A., Touhara, K., Payne, E. S. and Lefkowitz, R. J.** (1995). Pleckstrin homology domain-mediated membrane association and activation of the beta-adrenergic receptor kinase requires coordinate interaction with G beta gamma subunits and lipid. *J. Biol. Chem.* **270**, 11707–11710.

**Pollard, T. D.** (2016). Actin and Actin-Binding Proteins. *Cold Spring Harbor Perspectives in Biology* **8**, a018226–a018226.

**Portegijs, V., Fielmich, L.-E., Galli, M., Schmidt, R., Muñoz, J., van Mourik, T., Akhmanova, A., Heck, A. J. R., Boxem, M. and van den Heuvel, S.** (2016). Multisite Phosphorylation of NuMA-Related LIN-5 Controls Mitotic Spindle Positioning in C. elegans. *PLOS Genetics* **12**, e1006291–e1006291.

**Praitis, V., Casey, E., Collar, D. and Austin, J.** (2001). Creation of Low-Copy Integrated Transgenic Lines in Caenorhabditis elegans. *Genetics* **157**, 1217–1226.

**Prehoda, K. E., Scott, J. A., Mullins, R. D. and Lim, W. A.** (2000). Integration of multiple signals through cooperative regulation of the N-WASP-Arp2/3 complex. *Science (New York, N.Y.)* **290**, 801–6.

**Pring, M., Evangelista, M., Boone, C., Yang, C. and Zigmond, S. H.** (2003). Mechanism of Formin-Induced Nucleation of Actin Filaments. *Biochemistry* **42**, 486–496.

**Rao, J. N., Madasu, Y. and Dominguez, R.** (2014). Mechanism of actin filament pointed-end capping by tropomodulin. *Science (New York, N.Y.)* **345**, 463–7.

**Redemann, S., Pecreaux, J., Goehring, N. W., Khairy, K., Stelzer, E. H. K., Hyman, A. A. and Howard, J.** (2010). Membrane Invaginations Reveal Cortical Sites that Pull on Mitotic Spindles in One-Cell C. elegans Embryos. *PLoS ONE* **5**, e12301–e12301.

**Redemann, S., Schloissnig, S., Ernst, S., Pozniakowsky, A., Ayloo, S., Hyman, A. A. and Bringmann, H.** (2011). Codon adaptation-based control of protein expression in C. elegans. *Nat. Methods* **8**, 250–252.

**Reymann, A.-C., Staniscia, F., Erzberger, A., Salbreux, G. and Grill, S. W.** (2016). Cortical flow aligns actin filaments to form a furrow. *eLife* **5**.

**Rhee, S. G. and Bae, Y. S.** (1997). Regulation of phosphoinositide-specific phospholipase C isozymes. *The Journal of biological chemistry* **272**, 15045–8.

**Rhyu, M. S., Jan, L. Y. and Jan, Y. N.** (1994). Asymmetric distribution of numb protein during division of the sensory organ precursor cell confers distinct fates to daughter cells. *Cell* **76**, 477–91.

**Riddle, D. L.** (1988). The dauer larva. In *TheNematode Caenorhabditis elegans* (ed. W. B. WOODC. old Spring Harbor Laboratory, Cold Spring Harbor, N. Y.), pp. 393–412.

Riedl, J., Crevenna, A. H., Kessenbrock, K., Yu, J. H., Neukirchen, D., Bista, M., Bradke, F., Jenne, D., Holak, T. A., Werb, Z., et al. (2008). Lifeact: a versatile marker to visualize F-actin. *Nature Methods* **5**, 605–607.

Robin, F. B., McFadden, W. M., Yao, B. and Munro, E. M. (2014). Single-molecule analysis of cell surface dynamics in Caenorhabditis elegans embryos. *Nature Methods* **11**, 677–682.

Rodriguez, J., Peglion, F., Martin, J., Hubatsch, L., Reich, J., Hirani, N., Gubieda, A. G., Roffey, J., Fernandes, A. R., St Johnston, D., et al. (2017). aPKC Cycles between Functionally Distinct PAR Protein Assemblies to Drive Cell Polarity. *Developmental Cell*.

Rodriguez-Boulan, E. and Macara, I. G. (2014). Organization and execution of the epithelial polarity programme. *Nature reviews. Molecular cell biology* **15**, 225–42.

Rolls, M. M., Albertson, R., Shih, H.-P., Lee, C.-Y. and Doe, C. Q. (2003). Drosophila aPKC regulates cell polarity and cell proliferation in neuroblasts and epithelia. *The Journal of cell biology* **163**, 1089–98.

Rose, L. and Gönczy, P. (2014). Polarity establishment, asymmetric division and segregation of fate determinants in early C. elegans embryos. *WormBook* 1–43.

Rose, L. S. and Kemphues, K. (1998). The let-99 gene is required for proper spindle orientation during cleavage of the C. elegans embryo. *Development (Cambridge, England)* **125**, 1337–46.

Rose, L. S., Lamb, M. L., Hird, S. N. and Kemphues, K. J. (1995). Pseudocleavage Is Dispensable for Polarity and Development in C. elegans Embryos. *Developmental Biology* **168**, 479–489.

Rottner, K., Hänisch, J. and Campellone, K. G. (2010). WASH, WHAMM and JMY: regulation of Arp2/3 complex and beyond. *Trends in Cell Biology* **20**, 650–661.

Rouault, J.-P., Kuwabara, P. E., Sinilnikova, O. M., Duret, L., Thierry-Mieg, D. and Billaud, M. (1999). Regulation of dauer larva development in Caenorhabditis elegans by daf-18, a homologue of the tumour suppressor PTEN. *Current Biology* **9**, 329–334.

Rouiller, I., Xu, X.-P., Amann, K. J., Egile, C., Nickell, S., Nicastro, D., Li, R., Pollard, T. D., Volkmann, N. and Hanein, D. (2008). The structural basis of actin filament branching by the Arp2/3 complex. *The Journal of Cell Biology* **180**, 887–895.

Rozelle, A. L., Machesky, L. M., Yamamoto, M., Driessens, M. H., Insall, R. H., Roth, M. G., Luby-Phelps, K., Marriott, G., Hall, A. and Yin, H. L. (2000). Phosphatidylinositol 4,5-bisphosphate induces actin-based movement of raft-enriched vesicles through WASP-Arp2/3. *Current biology : CB* **10**, 311–20.

**Rual, J.-F., Ceron, J., Koreth, J., Hao, T., Nicot, A.-S., Hirozane-Kishikawa, T., Vanden-haute, J., Orkin, S. H., Hill, D. E., van den Heuvel, S., et al.** (2004). Toward improving Caenorhabditis elegans phenome mapping with an ORFeome-based RNAi library. *Genome research* **14**, 2162–8.

**Runne, C. and Chen, S.** (2013). PLEKHG2 promotes heterotrimeric G protein βγ-stimulated lymphocyte migration via Rac and Cdc42 activation and actin polymerization. *Mol. Cell. Biol.* **33**, 4294–4307.

**Russo, J., Snider, K., Pereira, J. S. and Russo, I. H.** (2010). Estrogen-induced breast cancer is the result of disruption of asymmetric cell division of the stem cell. *Hormone Molecular Biology and Clinical Investigation* **1**, 53–65.

**Sadler, P. L. and Shakes, D. C.** (2000). Anucleate Caenorhabditis elegans sperm can crawl, fertilize oocytes and direct anterior-posterior polarization of the 1-cell embryo. *Development (Cambridge, England)* **127**, 355–66.

**Sailer, A., Anneken, A., Li, Y., Lee, S. and Munro, E.** (2015). Dynamic Opposition of Clustered Proteins Stabilizes Cortical Polarity in the C. elegans Zygote. *Developmental Cell* **35**, 131–142.

**Sato, K., Sato, M., Audhya, A., Oegema, K., Schweinsberg, P. and Grant, B. D.** (2006). Dynamic regulation of caveolin-1 trafficking in the germ line and embryo of Caenorhabditis elegans. *Molecular biology of the cell* **17**, 3085–94.

**Schaefer, M., Shevchenko, A., Shevchenko, A. and Knoblich, J. A.** (2000). A protein complex containing Inscuteable and the Galpha-binding protein Pins orients asymmetric cell divisions in Drosophila. *Current biology : CB* **10**, 353–62.

**Schaefer, M., Petronczki, M., Dorner, D., Forte, M. and Knoblich, J. A.** (2001). Heterotrimeric G proteins direct two modes of asymmetric cell division in the Drosophila nervous system. *Cell* **107**, 183–94.

**Schenk, C., Bringmann, H., Hyman, A. A. and Cowan, C. R.** (2010). Cortical domain correction repositions the polarity boundary to match the cytokinesis furrow in C. elegans embryos. *Development (Cambridge, England)* **137**, 1743–53.

**Schmidt, D. J., Rose, D. J., Saxton, W. M. and Strome, S.** (2005). Functional Analysis of Cytoplasmic Dynein Heavy Chain in Caenorhabditis elegans with Fast-acting Temperature-sensitive Mutations. *Molecular Biology of the Cell* **16**, 1200–1212.

**Schmökel, V., Memar, N., Wiekenberg, A., Trotzmüller, M., Schnabel, R. and Döring, F.** (2016). Genetics of Lipid-Storage Management in Caenorhabditis elegans Embryos. *Genetics* **202**.

**Schmutz, C., Stevens, J. and Spang, A.** (2007). Functions of the novel RhoGAP proteins RGA-3 and RGA-4 in the germ line and in the early embryo of C. elegans. *Development (Cambridge, England)* **134**, 3495–505.

**Schober, M., Schaefer, M. and Knoblich, J. A.** (1999). Bazooka recruits Inscuteable to orient asymmetric cell divisions in *Drosophila* neuroblasts. *Nature* **402**, 548–551.

**Schonegg, S. and Hyman, A. A.** (2006). CDC-42 and RHO-1 coordinate acto-myosin contractility and PAR protein localization during polarity establishment in C. elegans embryos. *Development (Cambridge, England)* **133**, 3507–16.

**Schonegg, S., Constantinescu, A. T., Hoege, C. and Hyman, A. A.** (2007). The Rho GTPase-activating proteins RGA-3 and RGA-4 are required to set the initial size of PAR domains in Caenorhabditis elegans one-cell embryos. *Proceedings of the National Academy of Sciences of the United States of America* **104**, 14976–81.

**Schroeder, T.** (2007). Asymmetric Cell Division in Normal and Malignant Hematopoietic Precursor Cells. *Cell Stem Cell* **1**, 479–481.

**Sedensky, M. M., Siefker, J. M., Koh, J. Y., Miller, D. M. and Morgan, P. G.** (2004). A stomatin and a degenerin interact in lipid rafts of the nervous system of Caenorhabditis elegans. *AJP: Cell Physiology* **287**, C468–C474.

**Severson, A. F. and Bowerman, B.** (2003). Myosin and the PAR proteins polarize microfilament-dependent forces that shape and position mitotic spindles in Caenorhabditis elegans. *The Journal of Cell Biology* **161**.

**Severson, A. F., Baillie, D. L. and Bowerman, B.** (2002). A Formin Homology Protein and a Profilin Are Required for Cytokinesis and Arp2/3-Independent Assembly of Cortical Microfilaments in C. elegans. *Current Biology* **12**, 2066–2075.

**Shelton, C. A. and Bowerman, B.** (1996). Time-dependent responses to glp-1-mediated inductions in early C. elegans embryos. *Development (Cambridge, England)* **122**, 2043–50.

**Shelton, C. A., Carter, J. C., Ellis, G. C. and Bowerman, B.** (1999). The nonmuscle myosin regulatory light chain gene mlc-4 is required for cytokinesis, anterior-posterior polarity, and body morphology during Caenorhabditis elegans embryogenesis. *The Journal of cell biology* **146**, 439–51.

**Sheridan, D. L., Berlot, C. H., Robert, A., Inglis, F. M., Jakobsdottir, K. B., Howe, J. R. and Hughes, T. E.** (2002). A new way to rapidly create functional, fluorescent fusion proteins: random insertion of GFP with an in vitro transposition reaction. *BMC Neurosci* **3**, 7.

**Shivas, J. M. and Skop, A. R.** (2012). Arp2/3 mediates early endosome dynamics necessary for the maintenance of PAR asymmetry in Caenorhabditis elegans. *Mol. Biol. Cell* **23**, 1917–1927.

**Shmookler Reis, R. J., Ayyadevara, S., Crow, W. A., Lee, T. and Delongchamp, R. R.** (2012). Gene Categories Differentially Expressed in C. elegans Age-1 Mutants of Extraordinary Longevity: New Insights From Novel Data-Mining Procedures. *The Journals of Gerontology: Series A* **67A**, 366–375.

**Siller, K. H., Cabernard, C. and Doe, C. Q.** (2006). The NuMA-related Mud protein binds Pins and regulates spindle orientation in Drosophila neuroblasts. *Nature cell biology* **8**, 594–600.

**Singh, D. and Pohl, C.** (2014). Coupling of Rotational Cortical Flow, Asymmetric Midbody Positioning, and Spindle Rotation Mediates Dorsoventral Axis Formation in C. elegans. *Developmental Cell* **28**, 253–267.

**Skwarek, L. C., Windler, S. L., de Vreede, G., Rogers, G. C. and Bilder, D.** (2014). The F-box protein Slmb restricts the activity of aPKC to polarize epithelial cells. *Development* **141**, 2978–2983.

**Small, L. E. and Dawes, A. T.** (2017). PAR proteins regulate maintenance-phase myosin dynamics during *Caenorhabditis elegans* zygote polarization. *Molecular Biology of the Cell* **28**, 2220–2231.

**Solari, F., Bourbon-Piffaut, A., Masse, I., Payrastre, B., Chan, A. M.-L. and Billaud, M.** (2005). The human tumour suppressor PTEN regulates longevity and dauer formation in Caenorhabditis elegans. *Oncogene* **24**, 20–27.

**Sonneville, R. and Gönczy, P.** (2004). Zyg-11 and cul-2 regulate progression through meiosis II and polarity establishment in C. elegans. *Development* **131**, 3527–3543.

**Sönnichsen, B., Koski, L. B., Walsh, A., Marschall, P., Neumann, B., Brehm, M., Alleaume, A.-M., Artelt, J., Bettencourt, P., Cassin, E., et al.** (2005). Full-genome RNAi profiling of early embryogenesis in Caenorhabditis elegans. *Nature* **434**, 462–469.

**Spector, A. A. and Yorek, M. A.** (1985). Membrane lipid composition and cellular function. *Journal of lipid research* **26**, 1015–35.

**Spiga, F. M., Prouteau, M. and Gotta, M.** (2013). The TAO kinase KIN-18 regulates contractility and establishment of polarity in the C. elegans embryo. *Developmental biology* **373**, 26–38.

**Spiro, Z., Thyagarajan, K., De Simone, A., Trager, S., Afshar, K. and Gonczy, P.** (2014). Clathrin regulates centrosome positioning by promoting acto-myosin cortical tension in C. elegans embryos. *Development* **141**, 2712–2723.

**Srinivasan, D. G., Fisk, R. M., Xu, H. and van den Heuvel, S.** (2003). A complex of LIN-5 and GPR proteins regulates G protein signaling and spindle function in C. elegans. *Genes & Development* **17**, 1225–1239.

**Strome, S. and Wood, W. B.** (1983). Generation of asymmetry and segregation of germline granules in early C. elegans embryos. *Cell* **35**, 15–25.

**Sugiarto, S., Persson, A. I., Munoz, E. G., Waldhuber, M., Lamagna, C., Andor, N., Hanecker, P., Ayers-Ringler, J., Phillips, J., Siu, J., et al.** (2011). Asymmetry-Defective Oligodendrocyte Progenitors Are Glioma Precursors. *Cancer Cell* **20**, 328–340.

**Sugioka, K., Fielmich, L.-E., Mizumoto, K., Bowerman, B., van den Heuvel, S., Kimura, A. and Sawa, H.** (2018). Tumor suppressor APC is an attenuator of spindle-pulling forces duringC. elegansasymmetric cell division. *Proceedings of the National Academy of Sciences of the United States of America* **115**, E954–E963.

**Suh, B.-C. and Hille, B.** (2005). Regulation of ion channels by phosphatidylinositol 4,5-bisphosphate. *Current Opinion in Neurobiology* **15**, 370–378.

**Sunahara, R. K., Tesmer, J. J., Gilman, A. G. and Sprang, S. R.** (1997). Crystal structure of the adenylyl cyclase activator Gsalpha. *Science* **278**, 1943–1947.

**Tabuse, Y., Izumi, Y., Piano, F., Kemphues, K. J., Miwa, J. and Ohno, S.** (1998). Atypical protein kinase C cooperates with PAR-3 to establish embryonic polarity in Caenorhabditis elegans. *Development (Cambridge, England)* **125**, 3607–14.

**Tan, J., Oh, K., Burgess, J., Hipfner, D. R. and Brill, J. A.** (2014). PI4KIII is required for cortical integrity and cell polarity during Drosophila oogenesis. *Journal of Cell Science* **127**, 954–966.

**Thielicke, W. and Stamhuis, E. J.** (2014). PIVlab – Towards User-friendly, Affordable and Accurate Digital Particle Image Velocimetry in MATLAB. *Journal of Open Research Software* **2**.

**Thyagarajan, K., Afshar, K. and Gonczy, P.** (2011). Polarity mediates asymmetric trafficking of the G heterotrimeric G-protein subunit GPB-1 in C. elegans embryos. *Development* **138**, 2773–2782.

**Tissenbaum, H. A. and Ruvkun, G.** (1998). An insulin-like signaling pathway affects both longevity and reproduction in Caenorhabditis elegans. *Genetics* **148**, 703–17.

**Tosoni, D., Zecchini, S., Coazzoli, M., Colaluca, I., Mazzarol, G., Rubio, A., Caccia, M., Villa, E., Zilian, O., Di Fiore, P. P., et al.** (2015). The Numb/p53 circuitry couples replicative self-renewal and tumor suppression in mammary epithelial cells. *The Journal of Cell Biology* **211**, 845–862.

**Touhara, K.** (1997). Binding of multiple ligands to pleckstrin homology domain regulates membrane translocation and enzyme activity of beta-adrenergic receptor kinase. *FEBS Lett.* **417**, 243–248.

**Touhara, K., Inglese, J., Pitcher, J. A., Shaw, G. and Lefkowitz, R. J.** (1994). Binding of G protein beta gamma-subunits to pleckstrin homology domains. *J. Biol. Chem.* **269**, 10217–10220.

**Tse, Y. C., Werner, M., Longhini, K. M., Labbe, J.-C., Goldstein, B. and Glotzer, M.** (2012). RhoA activation during polarization and cytokinesis of the early Caenorhabditis elegans embryo is differentially dependent on NOP-1 and CYK-4. *Molecular biology of the cell* **23**, 4020–31.

**Tsou, M.-F. B., Hayashi, A., DeBella, L. R., McGrath, G. and Rose, L. S.** (2002). LET-99 determines spindle position and is asymmetrically enriched in response to PAR polarity cues in C. elegans embryos. *Development (Cambridge, England)* **129**, 4469–81.

**Tsou, M.-F. B., Hayashi, A. and Rose, L. S.** (2003). LET-99 opposes G /GPR signaling to generate asymmetry for spindle positioning in response to PAR and MES-1/SRC-1 signaling. *Development* **130**, 5717–5730.

**Tsukita, S., Yonemura, S. and Tsukita, S.** (1997). ERM proteins: head-to-tail regulation of actin-plasma membrane interaction. *Trends in biochemical sciences* **22**, 53–8.

**Ueda, H., Nagae, R., Kozawa, M., Morishita, R., Kimura, S., Nagase, T., Ohara, O., Yoshida, S. and Asano, T.** (2008). Heterotrimeric G protein betagamma subunits stimulate FLJ00018, a guanine nucleotide exchange factor for Rac1 and Cdc42. *J. Biol. Chem.* **283**, 1946–1953.

**Várnai, P. and Balla, T.** (1998). Visualization of Phosphoinositides That Bind Pleckstrin Homology Domains: Calcium- and Agonist-induced Dynamic Changes and Relationship to Myo-[3H]inositol-labeled Phosphoinositide Pools. *The Journal of Cell Biology* **143**.

**Velarde, N., Gunsalus, K. C. and Piano, F.** (2007). Diverse roles of actin in C. elegans early embryogenesis. *BMC Developmental Biology* **7**, 142–142.

**Verbist, K. C., Guy, C. S., Milasta, S., Liedmann, S., Kamiński, M. M., Wang, R. and Green, D. R.** (2016). Metabolic maintenance of cell asymmetry following division in activated T lymphocytes. *Nature* **532**, 389–393.

**Vernay, A., Schaub, S., Guillas, I., Bassilana, M. and Arkowitz, R. A.** (2012). A steep phosphoinositide bis-phosphate gradient forms during fungal filamentous growth. *The Journal of Cell Biology* **198**, 711–730.

**Vertii, A., Kaufman, P. D., Hehnly, H. and Doxsey, S.** (2018). New dimensions of asymmetric division in vertebrates. *Cytoskeleton* **75**, 87–102.

**Vinot, S., Le, T., Ohno, S., Pawson, T., Maro, B. and Louvet-Vallée, S.** (2005). Asymmetric distribution of PAR proteins in the mouse embryo begins at the 8-cell stage during compaction. *Developmental Biology* **282**, 307–319.

**Vinson, V. K., De La Cruz, E. M., Higgs, H. N. and Pollard, T. D.** (1998). Interactions of Acanthamoeba profilin with actin and nucleotides bound to actin. *Biochemistry* **37**, 10871–80.

**von Stetten, D., Noirclerc-Savoye, M., Goedhart, J., Gadella, T. W. J. and Royant, A.** (2012). Structure of a fluorescent protein from *Aequorea victoria* bearing the obligate-monomer mutation A206K. *Acta Crystallographica Section F Structural Biology and Crystallization Communications* **68**, 878–882.

**Wall, M. A., Coleman, D. E., Lee, E., Iniguez-Lluhi, J. A., Posner, B. A., Gilman, A. G. and Sprang, S. R.** (1995). The structure of the G protein heterotrimer Gi alpha 1 beta 1 gamma 2. *Cell* **83**, 1047–1058.

**Wang, H., Somers, G. W., Bashirullah, A., Heberlein, U., Yu, F. and Chia, W.** (2006). Aurora-A acts as a tumor suppressor and regulates self-renewal of Drosophila neuroblasts. *Genes Dev.* **20**, 3453–3463.

**Wang, S.-C., Low, T. Y. F., Nishimura, Y., Gole, L., Yu, W. and Motegi, F.** (2017). Cortical forces and CDC-42 control clustering of PAR proteins for Caenorhabditis elegans embryonic polarization. *Nature Cell Biology* **19**, 988–995.

**Watts, J. L., Etemad-Moghadam, B., Guo, S., Boyd, L., Draper, B. W., Mello, C. C., Priess, J. R. and Kemphues, K. J.** (1996). par-6, a gene involved in the establishment of asymmetry in early C. elegans embryos, mediates the asymmetric localization of PAR-3. *Development (Cambridge, England)* **122**, 3133–40.

**Weeds, A. G., Harris, H., Gratzer, W. and Gooch, J.** (1986). Interactions of pig plasma gelsolin with G-actin. *European journal of biochemistry* **161**, 77–84.

**Wegner, A. M., Nebhan, C. A., Hu, L., Majumdar, D., Meier, K. M., Weaver, A. M. and Webb, D. J.** (2008). N-wasp and the arp2/3 complex are critical regulators of actin in the development of dendritic spines and synapses. *The Journal of biological chemistry* **283**, 15912–20.

**Weinkove, D., Bastiani, M., Chessa, T. A. M., Joshi, D., Hauth, L., Cooke, F. T., Divecha, N. and Schuske, K.** (2008). Overexpression of PPK-1, the Caenorhabditis elegans Type I PIP kinase, inhibits growth cone collapse in the developing nervous system and causes axonal degeneration in adults. *Developmental Biology* **313**, 384–397.

**Whitman, C.** (1878). The embryology of Clepsine. *Q.J.Micrisc.Sci.* **18**.

**Wilm, T., Demel, P., Koop, H.-U., Schnabel, H. and Schnabel, R.** (1999). Ballistic transformation of Caenorhabditis elegans. *Gene* **229**, 31–35.

**Wilson, C. A., Tsuchida, M. A., Allen, G. M., Barnhart, E. L., Applegate, K. T., Yam, P. T., Ji, L., Keren, K., Danuser, G. and Theriot, J. A.** (2010). Myosin II contributes to cell-scale actin network treadmilling through network disassembly. *Nature* **465**, 373–7.

**Wodarz, A., Ramrath, A., Grimm, A. and Knust, E.** (2000). Drosophila atypical protein kinase C associates with Bazooka and controls polarity of epithelia and neuroblasts. *The Journal of cell biology* **150**, 1361–74.

**Wu, M., Kwon, H. Y., Rattis, F., Blum, J., Zhao, C., Ashkenazi, R., Jackson, T. L., Gaiano, N., Oliver, T. and Reya, T.** (2007a). Imaging Hematopoietic Precursor Division in Real Time. *Cell Stem Cell* **1**, 541–554.

**Wu, H., Feng, W., Chen, J., Chan, L.-N., Huang, S. and Zhang, M.** (2007b). PDZ Domains of Par-3 as Potential Phosphoinositide Signaling Integrators. *Molecular Cell* **28**, 886–898.

**Wu, C.-Y., Lin, M.-W., Wu, D.-C., Huang, Y.-B., Huang, H.-T. and Chen, C.-L.** (2014). The role of phosphoinositide-regulated actin reorganization in chemotaxis and cell migration. *British journal of pharmacology* **171**, 5541–54.

**Xian, W. and Janmey, P. A.** (2002). Dissecting the gelsolin-polyphosphoinositide interaction and engineering of a polyphosphoinositide-sensitive gelsolin C-terminal half protein. *Journal of molecular biology* **322**, 755–71.

**Xu, X., Guo, H., Wycuff, D. L. and Lee, M.** (2007). Role of phosphatidylinositol-4-phosphate 5' kinase (ppk-1) in ovulation of Caenorhabditis elegans. *Experimental cell research* **313**, 2465–75.

**Xu, W., Jin, M., Hu, R., Wang, H., Zhang, F., Yuan, S. and Cao, Y.** (2017). The Joubert Syndrome Protein Inpp5e Controls Ciliogenesis by Regulating Phosphoinositides at the Apical Membrane. *Journal of the American Society of Nephrology : JASN* **28**, 118–129.

**Yi, K. and Li, R.** (2012). Actin cytoskeleton in cell polarity and asymmetric division during mouse oocyte maturation. *Cytoskeleton* **69**, 727–737.

**Yin, H. L. and Janmey, P. A.** (2003). Phosphoinositide Regulation of the Actin Cytoskeleton. *Annual Review of Physiology* **65**, 761–789.

**Yu, J.-Z. and Rasenick, M. M.** (2002). Real-time visualization of a fluorescent G(alpha)(s): dissociation of the activated G protein from plasma membrane. *Mol. Pharmacol.* **61**, 352–359.

**Yu, F., Morin, X., Cai, Y., Yang, X. and Chia, W.** (2000). Analysis of partner of inscuteable, a novel player of Drosophila asymmetric divisions, reveals two distinct steps in inscuteable apical localization. *Cell* **100**, 399–409.

**Zacharias, D. A., Violin, J. D., Newton, A. C. and Tsien, R. Y.** (2002). Partitioning of Lipid-Modified Monomeric GFPs into Membrane Microdomains of Live Cells. *Science* **296**, 913–916.

**Zeiser, E., Frøkjær-Jensen, C., Jorgensen, E. and Ahringer, J.** (2011). MosSCI and Gateway Compatible Plasmid Toolkit for Constitutive and Inducible Expression of Transgenes in the C. elegans Germline. *PLOS ONE* **6**, e20082.

**Zhang, D. and Glotzer, M.** (2015). The RhoGAP activity of CYK-4/MgcRacGAP functions non-canonically by promoting RhoA activation during cytokinesis. *eLife* **4**,.

**Zhang, L., Mao, Y. S., Janmey, P. A. and Yin, H. L.** (2012). Phosphatidylinositol 4, 5 Bisphosphate and the Actin Cytoskeleton.pp. 177–215. Springer, Dordrecht.

**Zhang, L., Ward, J. D., Cheng, Z. and Dernburg, A. F.** (2015). The auxin-inducible degradation (AID) system enables versatile conditional protein depletion in C. elegans. *Development* **142**, 4374–4384.

**Zhu, M., Leung, C. Y., Shahbazi, M. N. and Zernicka-Goetz, M.** (2017). Actomyosin polarisation through PLC-PKC triggers symmetry breaking of the mouse embryo. *Nature Communications* **8**, 921.

**Ziel, J. W., Hagedorn, E. J., Audhya, A. and Sherwood, D. R.** (2009). UNC-6 (netrin) orients the invasive membrane of the anchor cell in C. elegans. *Nature Cell Biology* **11**, 183–189.

**Ziomek, C. A. and Johnson, M. H.** (1980). Cell surface interaction induces polarization of mouse 8-cell blastomeres at compaction. *Cell* **21**, 935–42.

**Zon, L. I.** (2008). Intrinsic and extrinsic control of haematopoietic stem-cell self-renewal. *Nature* **453**, 306–313.

**Zonies, S., Motegi, F., Hao, Y. and Seydoux, G.** (2010). Symmetry breaking and polarization of the C. elegans zygote by the polarity protein PAR-2. *Development (Cambridge, England)* **137**, 1669–77.

# 7. Appendix

## 7.1 Attempts at developing an optogenetic tool to change cortical PIP$_2$ structures in a spatially and temporally controlled manner

We decreased and increased the PIP$_2$ level in the whole embryo by activating Phospholipase C or depleting the PIP$_2$ 5-phosphatases OCRL-1 and UNC-26, respectively (see 3.2.1 and 3.2.2). This gave us interesting new insights about the function of PIP$_2$ in reorganizing the actin cytoskeleton and polarity in the *C. elegans* embryo. Nevertheless, to specifically test the function of given PIP$_2$ cortical structures, we aimed at changing them in a spatiotemporally controlled manner without altering overall PIP$_2$ cellular levels. In principle, this could be achieved by controlling phosphoinositide metabolism with optogenetics. Two proteins from *Arabidopsis thaliana*, cryptochrome 2 (CRY2) and the transcription factor CIB1, dimerize upon blue light illumination (Kennedy et al., 2010). The PIP$_2$ 5-phosphatase domain of OCRL can be fused to the photolyase homology region domain of CRY2 (CRY2PHR), and this construct then interacts upon light exposure with the N-terminal domain of CIB1 (CIBN), which can be targeted to the plasma membrane by fusing it to a CaaX domain (Idevall-Hagren et al., 2012). Thus, upon blue light illumination, OCRL-CRY2PHR should be recruited to plasma membrane bound CIBN-CaaX, and there OCRL acts to dephosphorylate PIP$_2$ to PI4P within seconds. This could be monitored by the release of a PH$^{PLC1\delta1}$ PIP$_2$ marker (Figure 59 top). This dephosphorylation event is reversible within minutes after blue light illumination (Idevall-Hagren et al., 2012). This system is thus well suited to rapidly, locally and reversibly change PIP$_2$ levels at the plasma membrane and has been successfully used in different systems to this end. Thus, in COS-7 cells, cleavage of PIP$_2$ with this system causes loss of peripheral actin and decreased membrane ruffling (Idevall-Hagren et al., 2012). Moreover, during *Drosophila* embryogenesis, this causes loss of actin and of apical constriction (Guglielmi et al., 2015). A similar system, fusing PI3K to CRY2PHR for blue-light induced membrane recruitment to CIBN-CaaX, can achieve phosphorylation of PIP$_2$ to PIP$_3$, leading to the formation of actin-based structures in mouse hippocampal neurons (Kakumoto and Nakata, 2013); this second system was also already used in *C. elegans* neurons (Ohno et al., 2014).

We decided to set up the first system described above in the one cell stage *C. elegans* embryo, aiming to dephosphorylate PIP$_2$ locally and temporarily at cortical

structures to specifically address the function of PIP$_2$ at these structures. We cloned three constructs under the control of the *pie-1* promoter for germline expression with the *pie-1* 3`UTR (Merritt et al., 2008). Using the MultiSite Gateway$^{TM}$ system, the constructs were set up in a way that promoter and 3`UTR are easily exchangeable in case of expression problems (Zeiser et al., 2011). Moreover, the constructs can be easily either put into a vector for bombardment or for MosSCI transgenic line generation, dependent on the desired method for generation of a worm line. We started with the constructs for bombardment.
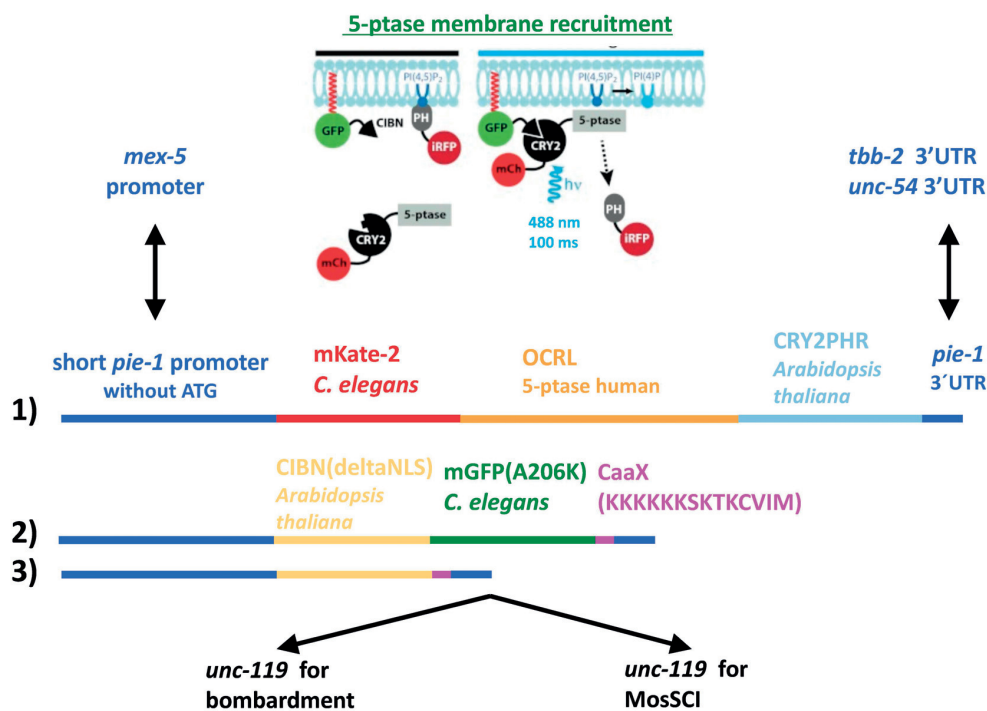


**Figure 59: Schematic of the CRY-2/CIBN optogenetic system and constructs designed.** Schematic on the top adapted from (Idevall-Hagren et al., 2012). Designed constructs for generation of *C. elegans* worm lines and possible ways to change them. The *unc-119* gene was utilized as a selection marker to determine rescued *unc-119* mutant worms, which successfully integrated the vector containing the transgene and the *unc-119* gene into their genome or as extrachromosomal array.

The first construct contains mKate-2 codon adapted for *C. elegans* (Dickinson et al., 2013), the 5-ptase domain of human OCRL, and CRY2PHR from *Arabidopsis thaliana* (Figure 59 (1)). The second construct we cloned contains CIBN from *Arabidopsis thaliana*, GFP codon adapted for *C. elegans,* in which we inserted the A206K mutation needed for GFP to stay monomeric (Figure 60) (Dickinson et al., 2013; von Stetten et al., 2012; Zacharias et al., 2002), and a CaaX domain for membrane localization (Figure 59 (2)). We planned to use these two constructs to set up the system. We also generated a third construct containing only CIBN and a CaaX domain without a fluorescent protein for

later use together with GFP::PH$^{PLC1δ1}$ to monitor PIP₂ cleavage at the plasma membrane (Figure 59 (3)). Alternatively, a far-red fluorescent protein could have been used as a third color.

**wild type GFP**

MSKGEELFTGVVPILVELDGDVNGHKFSVSGEGEGDATYGKLTLKFICTT
GKLPVPWPTLVTT**FS**YGVQCFSRYPDHMK**Q**HD**E**FKSAMPEGYVQERTI
FFKDDGNYKTRAEVKFEGDTLVNRIELKGIDFKEDGNILGHKLEYNYNSH
NVYIMADKQKNGIKVNFKIRHNIEDGSVQLADHYQQNTPIGDGPVLLP
DNHYLSTQS**A**LSKDPNEKRDHMVL**LEF**VTAAGITHGMDELYK

**GFP from Dickinson D. *et al.*, Genetics, 2015**

- Codon adapted ✓
- Introns ✓
- S65T drastic enhancement of green fluorescence ✓
- **F64L** mutation ✗ (EGFP, increased folding efficiency at 37 °C)
- Q80R ✓ Present in most GFP cDNAs, no function
- E83F ✓
- **A206K monomeric GFP:** not present originally: mutated ✓
  hydrophobic to positive (alternative: F223K, L221K)

**Figure 60: Sequence and introduced mutations of GFP used in this study.** On the top: original wild type GFP sequence from *Aequorea Victoria*. Amino acids that are usually mutated in GFP transgenes are marked in red. The mutations are named and their purpose explained below. GFP used for *C. elegans* worm line generation in this study is based on the GFP constructed by Dickinson *et al.*, which contains the mutations and characteristics marked with a green check mark (Dickinson et al., 2013). The A206K mutation to obtain monomeric GFP (mGFP) was added. The F64L mutation commonly used for EGFP in mammalian cells was not added as worms are not cultured at 37°C.

We bombarded *unc-119* mutant worms with the three constructs. We could obtain worm lines from all three bombardments, with successfully integration in the genome as screened by PCR. Unfortunately, however, the construct containing mKate-2::OCRL::CRY2PHR did not get expressed in any of the 12 worm lines obtained from 2 rounds of bombardment that were screened for fluorescence. However, we could obtain one line expressing CIBN::mGFP::CaaX in the germline and early embryos, and the construct is successfully localized to the plasma membrane (Figure 61). However, the mKate-2::OCRL::CRY2PHR construct would probably need to be changed in a substantial way to obtain expression. Exchange of the promoter, 3`UTR, as well as codon adaptation, insertion of synthetic introns, and usage of MosSCI or CRISPR instead of bombardment to generate the worm line can be considered in future attempts.
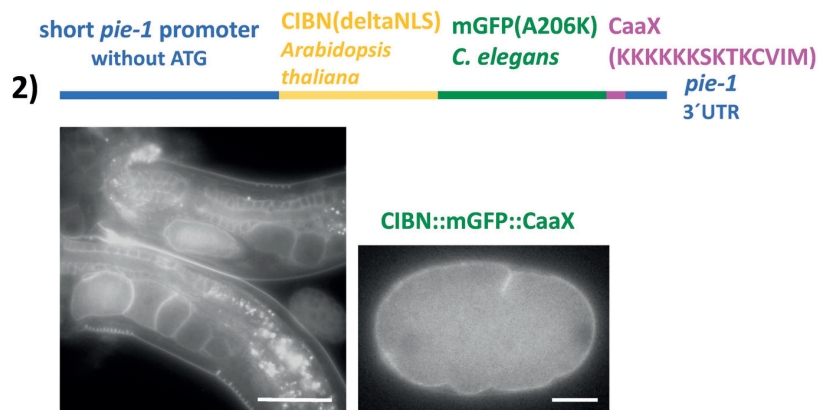
**Figure 61: The CIBN::mGFP::CaaX domain is expressed in the gonad and early embryos and localizes to the plasma membrane.** Design of construct 2) (CIBN::mGFP::CaaX) and its expression in the *C. elegans* gonad and early embryo, with plasma membrane localization, imaged using epi-fluorescent live microscopy. Scale bar left: 50 µm, scale bar right: 10 µm.

## 7.2 Attempts to generate an endogenous knock-in line of mKate-2::GPB-1 by CRISPR/Cas9

We aimed to generate a worm line expressing endogenously tagged mKate-2::GPB-1 for the following two reasons. First, we wanted to be able to monitor the colocalization of GPB-1 and GPR-1 by dual color imaging of embryos expressing GFP::GPR-1 and mKate-2::GPB-1. Second, in this manner, we could test the cortical distribution of endogenous GPB-1. Various strategies to generate endogenous knock-in lines by CRISPR/Cas9 are available for *C. elegans* (reviewed in Dickinson and Goldstein, 2016). We decided to use a Co-CRISPR method using the *dpy-10* mutation as a marker and linear DNA as repair template (Paix et al., 2014). Guide RNA sequences and primer sequences to generate linear repair templates to obtain C-terminal or N-terminal mKate-2 tagged GPB-1 are listed in Figure 62. Guide RNA sequences were obtained using an online available CRISPR design tool (crispr.mit.edu). We then generated linear repair templates and introduced the respective sgRNA sequence into a Cas9 expression vector (Dickinson et al., 2013) (Figure 63). To set up the method, we first aimed to reproduce the generation of a line expressing GTBP-1::GFP in the same way as reported by Paix *et al.* (Figure 63). We injected 100 worms in 3 rounds of injection with the required DNA constructs and repair templates as described (Paix et al., 2014) and screened the F1 offspring of those worms for so called "Jackpot broods" containing many worms with Roller phenotype (Figure 64, Table 2). Only the offspring of 21 worms contained very few Rollers, thus recombination had worked successfully, but not very efficient. One of the 21 plates contained 18 F1 Rollers and the other 20 plates contained 1 to 5 Rollers each. In addition, 11 of the 21 plates contained some worms with Dpy phenotype. We screened all 44 obtained

Roller and 28 Dpy worms for fluorescence, but could not obtain any fluorescent worm. Thus, the recombination events had only taken place for the *dpy-10* Co-CRISPR marker, but not for GTBP-1::GFP. Genome editing using linear DNA as a repair template with the *dpy-10* Co-CRISPR strategy has been reported later to be much more efficient if instead of expression of Cas9 and the respective sgRNA from an injected plasmid, a Cas9 ribo-nucleoprotein complex assembled *in vitro* is injected (Paix et al., 2015). To improve the efficiency of a recombination event, synthetic crRNA, tracrRNA and purified Cas9 protein should be injected next (Figure 65).

**Fluorescent protein constructs:**

      **mKate-2::GPB-1**
      **GPB-1::mKate-2**
      **GFP::GPR-1**

**homology arm + sequence between cut and insert + mkate-2 primer**
**homology arm + sequence between cut and insert + GFP primer**

| Gene | guide RNA | Sequence (5' to 3') |
|------|-----------|---------------------|
| GPB-1 N | TTCGCTCATCTTGCTGCT**GG**TGG | atcagtaccatcctccggagcacgcacc a*cc acc agc agc aag ATG*GTCTCCGAGCTCATTAAAG TCAGCCTCCTGTCGAAGTTGGTCAAG*TTCGCTCAT*ACGGTGTCCGAGCTTGGATG |
| GPB-1 C | TTTCTTAATTCCAGATCTT**G**AGG | GCCGTGTGCACAGGATCATGGGACTCGTT***T CTC AAG** ATC TGG AAT* ATGGTCTCCGAGCTCATTAAAG ggagaataattaaggaagacatttgatg*tttcTTA*ACGGTGTCCGAGCTTGGATG |
| GPR-1 N | GTCCATTCGTTTTGCGAAT**G**TGG | ttgcaattttcgattcatttcagaagtt t*cg aca ttc gca aaa cga ATG*AGTAAAGGAGAAGAATTG TCATCCTTGGGACCATCGTAATAAGAGACGTCCATCTTGTAGAGCTCGTCCATTCC |

**Figure 62: Design of primers for repair templates and chosen guide sequences.** The described guide RNA sequences were chosen for the knock-in of fluorescent proteins by CRISPR-Cas9 to the N and C terminus of GPB-1, and to the N terminus of GPR-1. The sequences of primers used to generate linear repair templates by RNAi are listed also, with homology arms in blue, sequence between cut and insert in grey and primers for mKate-2 in red and for GFP in green. As a GFP::GPR-1 knock-in line by CRISPR-Cas9 has been published in the meantime (Portegijs et al., 2016), only the generation of an endogenously tagged mKate-2::GPB-1 was followed up.

**Repair templates:**

- **1_**GFP::GPR-1 (N-terminus) (in pGEMT)
- **2_**GFP_F64L_A206K::GPR-1 (N-terminus) (in pGEMT)
- **3_**GFP_A206K::GPR-1 (N-terminus) (in pGEMT)

- **4_**mKate-2::GPB-1 (C-terminus) (in pGEMT):
- **5_**GPB-1::mKate-2 (N-terminus) (only PCR product)

- **6_**GTBP-1(K08F4.2)::GFP (at cut site near C-Terminus) (only PCR product)
- **7_**GTBP-1-GFP_F64L_A206K
- **8_**GTBP-1_GFP_F64L

- *dpy-10* (ssODN) (for co-CRISPR)

**Cas-9-sgRNA-vector:**

- For GFP::GPR-1 (N-terminus)
- For mKate-2::GPB-1 (C-terminus)
- For GPB-1::mKate-2 (N-terminus)
- For GTBP-1(K08F4.2)::GFP
- For *dpy-10* (ssODN)

***gtbp-1:*** non essential gene expressed in most tissues, insertion site directly at cut site (near C-terminus)



K08F4.2::GFP
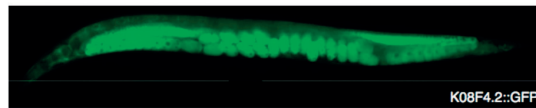
**Figure 63: Generated repair templates and Cas9-sgRNA vectors.** The following repair templates and Cas9-sgRNA vectors were generated and are ready to use. The knock-in of GFP near the C-terminus of GTBP-1 has proven to be very efficient (Paix et al., 2014). All repair templates and Cas9-sgRNA-vectors listed above were thus generated for setting up the *dpy-10* Co marker based Co-CRISPR strategy as described (Paix et al., 2014). Image of worm expressing GTBP-1::GFP reprinted by permission from the Genetics Society of America (Paix et al., 2014).

**Phenotpyes:**
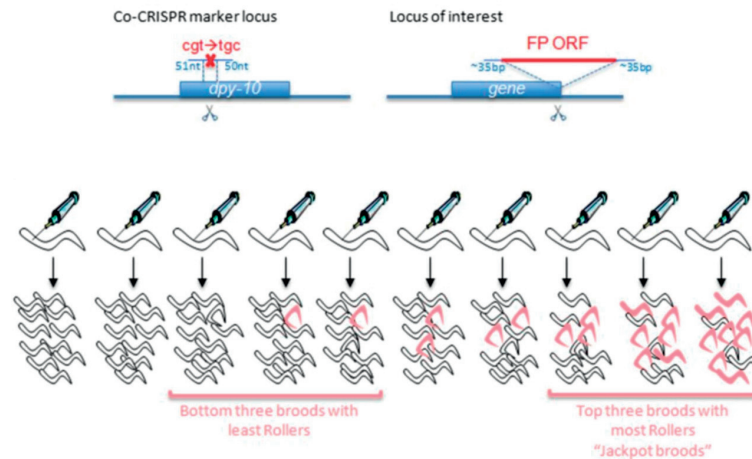
| | |
|---|---|
| *dpy-10*(*cn64*)/+ | *rol* |
| *dpy-10*(*cn64*)/ *dpy-10*(*cn64*) | *dpy* |
| *dpy-10*(*cn64*)/0 | *rol/dpy* |

**Figure 64: Co-CRISPR strategy using linear DNA repair templates and dpy-10 as selection marker.** Schematic of Co-CRISPR strategy based on *dpy-10* as a co-selection marker, reprinted by permission from the Genetics Society of America (Paix et al., 2015). Expected phenotypes resulting from homozygote or heterozygote *dpy-10* mutation are listed below.

**Table 2: Injection rounds and obtained phenotypes of F1 offspring of injected P0 worms.** Number of P0 worms injected per round. Injected P0 worms were singled to have one P0 worm per plate. Obtained phenotypes of F1 offspring per plate are listed.

### 1st round → 56 worms injected

| Injected P0: | F1 Phenotypes: |
|---|---|
| Plate 1: | 1 *dpy* |
| Plate 2: | 1 *rol* / 1 *dpy* |
| Plates 3-8: | 1 or 2 *rol* |
| Plates 9-10: | 5 *rol* |
| Plates 11-56 | all wild type |

### 2nd round → 13 worms injected

| Injected P0: | F1 Phenotypes: |
|---|---|
| Plate 1: | 2 *rol* / 9 *dpy* / 1 *dpy/rol* |
| Plate2: | 5 *rol* / 1 *dpy* |
| Plates 3-13 | all wild type |

### 3rd round → 31 worms injected

| Injected P0: | F1 Phenotypes: |
|---|---|
| **Plate 1:** | **18 *rol* / 2 *dpy*** |
| Plate 2: | 2 *dpy* |
| Plate 3: | 1 *rol* |
| Plate 4: | 1 *rol* / 1 *dpy* |
| Plate 5: | 3 *rol* / 2 *dpy* |
| Plate 6: | 2 *rol* / 1 *dpy* |
| Plate 7: | 3 *rol* / 5 *dpy* |
| Plate 8: | 1 *rol* |
| Plate 9: | 3 *dpy* |
| Plates 10-31 | all wild type |

- **Synthetic tracrRNA** 5 nmol
  stock solution: 4 µg/µl (0.17 nmol/µl) in Tris pH 7.5
  final concentration: 42.5 µM

- **Synthetic crRNA  *dpy-10*** 20 nmol
  stock solution: 8 µg/µl (0.6 nmol/µl) in Tris pH 7.5
  final concentration: 11.8 µM

- **Synthetic crRNA  *gtbp-1*** 20 nmol
  stock solution: 8 µg/µl (0.6 nmol/µl) in Tris pH 7.5
  final concentration: 29.6 µM

- **Cas9**
  Stock solution: 10 µg/µl
  final concentration: 15.5 µM

- ***dpy-10* ssODN** (500 ng/µl)
  final concentration: 0.42 µM

- **PCR template *gpbt-1***
  Final concentration: 500 ng/µl (0.5 µM)

**Figure 65: Injection mix for new strategy.** Injection mix with respective final concentrations of purified CAS9 protein and synthetic tracrRNA and crRNA instead of plasmid for Cas9-sgRNA expression (Paix et al., 2015). The respective stock solution and required final concentrations are listed.

## 7.3  A possible way to generate a GFP-tagged Gα line

The ternary complex generating pulling forces is anchored to the plasma membrane through myristoylation by two partially redundant Gα subunits, GOA-1 and GPA-16, with GPR-1 binding with its GoLoco motif to GDP bound Gα. GPB-1 competes with GPR-1 for Gα binding (see 1.2.6). The sub-cortical distribution of Gα could thus give interesting insights about places of force generation and its regulation, but no fluorescently tagged Gα *C. elegans* worm line for live imaging is available. Gα has to be internally tagged by GFP, as the C-terminus is needed for its interaction with the receptor GPCR and the N-terminus is essential for the association of Gα with Gβγ and for myristoylation and palmitoylation. There have been numerous successful approaches to tag Gα internally in other systems (Hughes et al., 2001; Janetopoulos et al., 2001; Sheridan et al., 2002; Yu and Rasenick, 2002; reviewed in Hynes et al., 2004) (Figure 66).
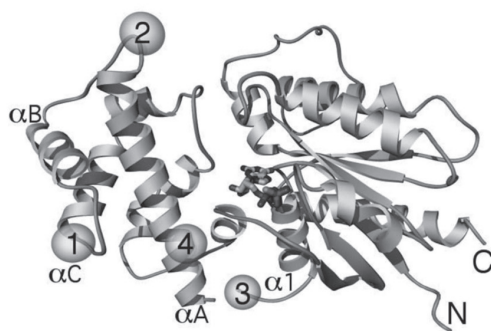
Insertion sites for GFP that resulted in functional α subunits:

**Site 1,** F124-S-G-G-G-G-S-[GFP]-S-G-G-G-G-S-E125, was used for αq-GFP
(Hughes, T.E. *et al*., 2001)

**Site 2**, G90-T-[CFP]-S-M91, was used for Dictyostelium discoideum Gα2-CFP
(Janetopolous, C. *et al*., 2001)

**Site 3**, E71-[GFP]-S82 (Yu, J.Z. 2001) or G72-S-G-G-G-G-S-[GFP]-S-G-G-G-G-S-
D85 (HYNES, T.R. *et al*., 2004), was used for αs-GFP.

**Site 4**, V92-Q93-D94-L-S-L-I-H-I-[GFP]-G-G-G-P-G-L-D-V-Y-K-R-Q-V92- Q93-
D94, is another αs-GFP fusion site generated by an in vitro
transposition reaction (Sheridan, D. L. *et al*., 2002). Note that this
site is within an α helix (αA). This surprising location demonstrates
the usefulness of a random-insertion approach

**Figure 66: Possible internal sites of Gα for GFP tagging.** Possible internal sites for
Gα tagging with GFP that have been previously used successfully for GFP tagging
in other systems are listed and marked in a crystal structures of adenylyl cylase
activator Gsα (Sunahara et al., 1997). Adapted and reprinted by permission from
Springer Nature. © Humana Press Inc. 2004.

*C. elegans* has 21 genes encoding for Gα proteins, including at least one homolog
of each mammalian Gα family (reviewed in Bastiani, 2006). GPA-16 and GOA-1 are most
similar to mammalian Gαi proteins (reviewed in Bastiani, 2006). We used the web-based
protein structure prediction tool Phyre2 to predict the 3D structures of GOA-1 and GPA-
16 because no solved protein structure exists for Gα proteins in *C. elegans* (Kelley et al.,
2015). We then aligned the predicted structures of *C. elegans* GPA-16 and GOA-1 with
the solved crystal structures of a mammalian GDP-bound Gαi protein in complex with
Gβγ (1GP2) in PyMOL to determine suitable sites for GFP tagging (Figure 67) (Wall et al.,
1995). We found that site 1 and site 2 used previously for tagging of Gα proteins aligned
well with GOA-1 and GPA-16 of *C. elegans* (Figure 66, Figure 67)*.* Potential attachment
sites, to be tested in future experiments, are listed in Table 3.
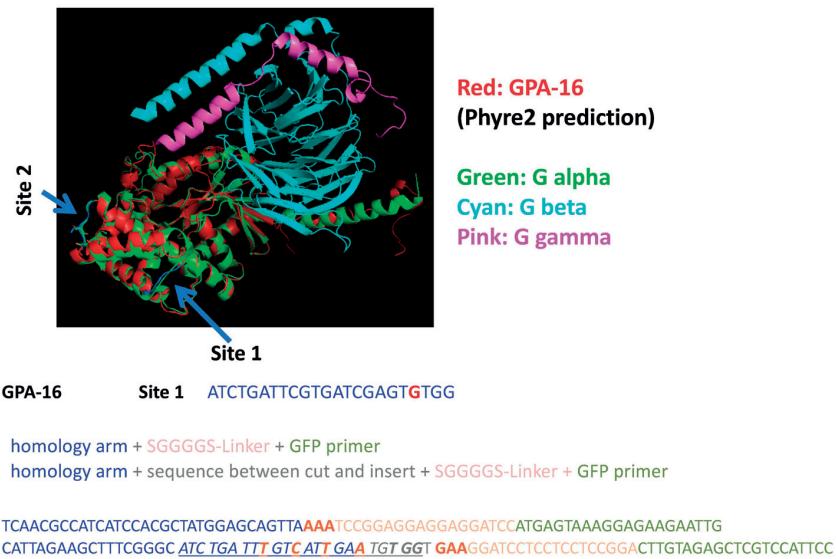
**Figure 67: Predicted structure of GPA-16 aligned to a mammalian GDP-bound Gαi protein in complex with Gβγ.** The tertiary protein structures of *C. elegans* GPA-16 (red) was predicted with Phyre2 and aligned to a GDP-bound Gαi protein (green) in complex with Gβ (cyan) and Gγ (pink) (PDB: 1GP2). Two possible sites for GFP attachment (Site 1 and Site 2) are marked.

**Table 3: Possible sites for GFP tagging of GPA-16 and GOA-1.**

| GPA-16 | | |
|---|---|---|
| Site 1 | K92-SGGGGS-GFP-SGGGGS-F95 | Removed: I93, S94 |
| Site 2 | E115-SGGGGS-GFP-SGGGGS-E118 | Removed: E116, D117 |
| GOA-1 | | |
| Site 1 | G92-SGGGGS-GFP-SGGGGS-F95 | Removed: V93, S94 |
| Site 2 | D116-SGGGGS-GFP-SGGGGS-P119 | Removed:T117, E118 |

## 7.4 Movie legends

All movies can be found at the following link:
https://www.youtube.com/channel/UC8DaMJafa_Ase107jkeGbRg/videos

**Movie 1:** Cortical confocal spinning disk imaging of PIP$_2$ structures monitored using GFP::PH$^{PLC1\delta1}$. In this and other movies, scale bar is 10 µm, time is indicated in minutes:seconds, and embryo anterior is to the left.

**Movie 2:** Cortical confocal spinning disk imaging of a *perm-1*(*RNAi*) wild-type (N2) embryo upon addition of Bodipy-PL-PIP$_2$.

**Movie 3:** Cortical confocal spinning disk imaging of PIP$_2$ monitored by mCherry::PH$^{PLC1\delta1}$ (red) and of mGFP::PPK-1 (green). (complete overlap of structures). Note: enrichment of PPK-1 on posterior.

**Movie 4:** Cortical confocal spinning disk imaging of PIP$_2$ structures monitored by mCherry::PH$^{PLC1\delta1}$ (red) and of GFP::PAR-6 (green) during pseudocleavage.

**Movie 5:** Cortical confocal spinning disk imaging of PIP$_2$ monitored by mNeon-Green::PH$^{PLC1\delta1}$ (green) and of F-actin monitored by Lifeact::mKate-2 (red) upon *par-3*(*RNAi*).

**Movie 6:** Cortical confocal spinning disk imaging of PIP$_2$ monitored by mNeon-Green::PH$^{PLC1\delta1}$ (green) and of F-actin monitored by Lifeact::mKate-2 (red) (partial overlap).

**Movie 7:** Cortical confocal spinning disk imaging of PIP$_2$ monitored by mCherry::PH$^{PLC1\delta1}$ (red) and of GFP::NMY-2 (green) (no overlap).

**Movie 8:** Cortical confocal spinning disk imaging of PIP$_2$ cortical structures monitored by mCherry::PH$^{PLC1\delta1}$ (red) and of GFP::CDC-42 (green) during pseudoclavage (complete overlap).

**Movie 9:**   Cortical confocal spinning disk imaging of $PIP_2$ cortical structures monitored by mCherry::PH$^{PLC1\delta1}$ (red) and of the active CDC-42 biomarker GFP::WSP-1 (green) (complete overlap).

**Movie 10:**   Cortical confocal spinning disk imaging of $PIP_2$ cortical structures monitored by mCherry::PH$^{PLC1\delta1}$ (red) and of the active RhoA biomarker GFP::AHPH (green) (temporary partial overlap).

**Movie 11:**   Confocal spinning disk imaging of a $PIP_2$ cortical structure monitored with mNeonGreen::PH$^{PLC1\delta1}$ moving ahead of F-actin monitored with Lifeact::mKate-2. Scale bar: 1 μm

**Movie 12:**   Cortical confocal spinning disk imaging of $PIP_2$ monitored by mNeon-Green::PH$^{PLC1\delta1}$ (green) and of F-actin monitored by Lifeact::mKate-2 (red) upon *pfn-1*(*RNAi*).

**Movie 13:**   Cortical confocal spinning disk imaging of $PIP_2$ monitored by mNeon-Green::PH$^{PLC1\delta1}$ (green) and of F-actin monitored by Lifeact::mKate-2 (red) upon *pfn-1*(*RNAi*) with slower frame rate than Movie 12. Note the slight back and forth movement with occasional jumps, in contrast to the directed movement of $PIP_2$ cortical structures and F-actin. Scale bar: 5 μm.

**Movie 14:**   Middle plane confocal spinning disk imaging of a *perm-1*(*RNAi*) embryo expressing GFP::PH$^{PLC1\delta1}$ and Lifeact::mKate-2upon Ionomycin/Ca$^{2+}$ treatment. $t_{1/2}$ at mitosis. Note disorganization of F-actin.

**Movie 15:**   Middle plane confocal spinning disk imaging of a *perm-1*(*RNAi*) embryo expressing mNeonGreen::PH$^{PLC1\delta1}$ and Lifeact::mKate-2 upon Ionomycin/Ca$^{2+}$ plus Latrunculin A treatment; note F-actin spikes in the cytoplasm.

**Movie 16:**   Cortical confocal spinning disk imaging of *ocrl-1*(*RNAi*) *unc-26*(*s1710*) class 1 embryo expressing GFP::PH$^{PLC1\delta1}$ and Lifeact::mKate-2.

**Movie 17:**   Cortical confocal spinning disk imaging of *ocrl-1*(*RNAi*) *unc-26*(*s1710*) class 1 embryo expressing mCherry::PH$^{PLC1\delta1}$ and GFP::PAR-6.

**Movie 18:** Cortical confocal spinning disk imaging of a *ocrl-1*(*RNAi*) *unc-26*(*s1710*) class 1 embryo expressing mCherry::PH$^{PLC1\delta1}$ and GFP::PAR-2.

**Movie 19:** Middle plane confocal spinning disk imaging of *perm-1*(*RNAi*) embryo expressing mCherry::PH$^{PLC1\delta1}$ and GFP::PAR-2 upon Ionomycin/Ca$^{2+}$ treatment. $t_{1/2}$ at pseudocleavage.

**Movie 20:** Middle plane confocal spinning disk imaging of *perm-1*(*RNAi*) embryo expressing mCherry::PH$^{PLC1\delta1}$ and GFP::PAR-2 upon Ionomycin/Ca$^{2+}$ treatment. $t_{1/2}$ at pseudoclavage. Note that the pseudocleavage does not retract.

**Movie 21:** Middle plane confocal spinning disk imaging of a *perm-1*(*RNAi*) embryo expressing mCherry::PH$^{PLC1\delta1}$ and GFP::PAR-2 upon Ionomycin/Ca$^{2+}$ treatment. $t_{1/2}$ at mitosis.

**Movie 22:** Middle plane confocal spinning disk imaging of a *perm-1*(*RNAi*) embryo expressing mCherry::PH$^{PLC1\delta1}$ and GFP::PAR-2 upon Ionomycin/ Ca$^{2+}$ and Cytochalasin D treatment. Note that this movie was acquired with binning=2.

**Movie 23:** Middle plane confocal spinning disk imaging of a *perm-1*(*RNAi*) embryo, expressing mCherry::PH$^{PLC1\delta1}$ and GFP::PAR-2 upon Ionomycin/Ca$^{2+}$ and Latrunculin D treatment. Note embryo movement caused by flow of the buffer after Latrunculin A addition.

**Movie 24:** Cortical confocal spinning disk imaging of PIP$_2$ monitored by mCherry::PH$^{PLC1\delta1}$ (red) and of GFP::GPB-1 (green).

**Movie 25:** Cortical confocal spinning disk imaging of PIP$_2$ monitored by mCherry::PH$^{PLC1\delta1}$ (red) and of GFP::GPR-1 (green) (endogenously tagged).

**Movie 26:** Cortical confocal spinning disk imaging of PIP$_2$ monitored by mCherry::PH$^{PLC1\delta1}$ (red) and of GFP::LIN-5 (green) (endogenously tagged).

**Movie 27:** Cortical confocal spinning disk imaging of *ocrl-1*(*RNAi*) *unc-26*(*s1710*) class 1 embryo expressing mCherry::PH$^{PLC1\delta1}$ and GFP::GPB-1.

**Movie 28:** Cortical confocal spinning disk imaging of PIP$_2$ monitored by mCherry::PH$^{\text{PLC1}\delta\text{1}}$ (red) and of YFP::GPR-1 (green) (strongly overexpressed).

**Movie 29:** Cortical confocal spinning disk imaging of PIP$_2$ structures monitored using GFP::PH$^{\text{PLC1}\delta\text{1}}$ upon *csnk-1*(*RNAi*).

**Movie 30:** Cortical confocal spinning disk imaging of PIP$_2$ structures monitored using GFP::PH$^{\text{PLC1}\delta\text{1}}$ upon *csnk-1*(*RNAi*). Note the extremely elongated PIP$_2$ cortical structures.

**Movie 31:** Cortical confocal spinning disk imaging of PIP$_2$ monitored by mCherry::PH$^{\text{PLC1}\delta\text{1}}$ (red) and of mGFP::PPK-1 (green) upon *csnk-1*(*RNAi*).

# 8. Curriculum vitae

**Melina Scholze**
Nationality: German
Marital Status: not married, no child

Avenue de France 18C
1004 Lausanne
+41 78 912 30 06
melina.scholze@gmail.com

| | EDUCATION |
|---|---|

| 11/2013 – 09/2018 | **EPFL Lausanne (Switzerland), PhD in Molecular Life Sciences.** Research area: Asymmetric cell division, development, basic cancer research. Thesis subject: Probing the distribution of cortical components, including PtdIns(4,5)P$_2$, during asymmetric division of *C. elegans* embryos. |
|---|---|
| 2007 – 2010 / 2011 – 2013 | **Eberhard Karls University Tübingen (Germany), Diploma in Biochemistry.** <ul><li>09/2013: Diploma of biochemistry (Master equivalent).</li><li>01/2013 – 09/2013: Diploma thesis: "Identification and Characterization of a Potassium Channel in *T. brucei*".</li><li>2012: Diploma examinations: Pharmaceutical Chemistry; Pathobiochemistry, Biochemistry</li><li>10/2009: Intermediate diploma (Bachelor equivalent).</li></ul> |
| 04/2010 – 03/2011 | **Capital Normal University, College of Life Science (Beijing, China).** Biochemistry (2 semesters). |
| 1998 – 2007 | **Parler Gymnasium, Schwäbisch Gmünd, Germany.** Abitur;  German university entry diploma |

| | EXPERIENCE |
|---|---|

---
TEACHING
---

| 2016 – 2017 | Supervision of Bachelor students for semester projects. |
|---|---|
| 2014 – 2017 | Teaching assistant for four courses: Introduction to Life Science, Integrated Laboratory in Life Science (I and II) and Scientific project design in cell and developmental biology. |
| 01/2013 – 07/2013 | Teacher for Biochemistry labs and seminars for medicine students. |
| 2013 | Supervision of interns for occupational orientation. |

---
INTERSHIPS
---

| 10/2011 – 11/2011 | **Participation on the project "Combinatorial Chemistry"** EMC microcollections GMBH, Tübingen, Germany |
|---|---|
| 07/2011 – 09/2011 | **Ectopic Fat Accumulation in primary human Astrocytes** University Hospitals Tübingen, Germany, Laboratory of patho-mechanisms of the peripheral and central insulin resistance. |

| | |
|---|---|
| 08/2010 – 11/2010 | **Interaction of Checkpoint Kinase 2 (Chk2) and Myosin targeting Phosphatase 1 (MYPT1) in Mitotic Entry.**<br>Capital Normal University, College of Life Science, Beijing, China<br>Beijing Key Laboratory of DNA Damage Response and Cancer Biology. |
| 05/2010 – 07/2010 | **Analysis of Gluten in *Brachypodium distachyon* and Wheat.**<br>Capital Normal University, College of Life Science, Beijing, China. |

## PUBLICATIONS

- Scholze, M. J., Barbieux, K. S., De Simone, A., Boumasmoud, M., Suess, C. C., Wang, R., & Gönczy, P. (2018). **PI(4,5)P$_2$ forms dynamic cortical structures and directs actin distribution and cell polarity in *Caenorhabditis elegans* embryos.** *Development*, 145, dev164988 doi: 10.1242/dev.164988. PMID: 29724757
- Stein, J., Mogk, S., Mudogo, C. N., Sommer, B. P., Scholze, M., Meiwes, A., Huber, M., Gray, A. & Duszenko, M. (2014). Drug development against sleeping sickness: old wine in new bottles?. *Current medicinal chemistry*, *21*(15), 1713-1727. PMID: 24251577

## SCIENTIFIC SKILLS

- Advanced microscopy for life science: wide field fluorescence, scanning confocal, spinning disk confocal, live imaging, DIC
- Image processing and analysis using Image J
- Molecular biology, cell biology, biochemistry, chemical biology, pharmaceutical chemistry, pathobiochemistry, genetics`
- Laboratory experiments:  design, management and execution

## COMPUTER SKILLS

- Experienced (+4 years) with ImageJ.
- Experienced (+1 year) with Adobe InDesign and Photoshop.
- "Microsoft Office Word, Excel and Power Point Specialist" (official certification since 2006).

## SCHOLARSHIPS

| | |
|---|---|
| 04/2010 – 01/2011 | **DAAD scholarship (ISAP Program)**<br>German academic exchange service. |
| Since 2007 | **e-fellows.net scholarship** |

## LANGUAGES

- German: native speaker.
- English: fluent.
- French: very good command.
- Chinese: basic knowledge.
- Latin: advanced Latinum certificate.

## EXTRACURRICULAR ACTIVITIES

- Trainer license for professional table tennis (C) and for table tennis as a therapeutic sport (since 2008 respectively 2012).
- 10 years of guitar lessons. First prize "Jugend musiziert" regional level.
- Since 2016, coach for new PhD students in Life sciences at EPFL.
- Hiking, Swimming, Traveling, Reading, Singing